Mobile Node-Aided Localization and Tracking in Terrestrial and Underwater Networks

by

© *Zijun Gong*, BEng, MEng

A thesis submitted to the

School of Graduate Studies

in partial fulfilment of the

requirements for the degree of

Doctor of Philosophy

Faculty of Engineering & Applied Science

Memorial University of Newfoundland

St. John's, NL.

May 2021

Abstract

In large-scale wireless sensor networks (WSNs), the position information of individual sensors is very important for many applications. Generally, there are a small number of position-aware nodes, referred to as the anchors. Every other node can estimate its distances to the surrounding anchors, and then employ trilateration or triangulation for self-localization. Such a system is easy to implement, and thus popular for both terrestrial and underwater applications, but it suffers from some major drawbacks. First, the density of the anchors is generally very low due to economical considerations, leading to poor localization accuracy. Secondly, the energy and bandwidth consumptions of such systems are quite significant. Last but not the least, the scalability of a network based on fixed anchors is not good. Therefore, whenever the network expands, more anchors should be deployed to guarantee the required performance. Apart from these general challenges, both terrestrial and underwater networks have their own specific ones. For example, real-time channel parameters are generally required for localization in terrestrial WSNs. For underwater networks, the clock skew between the target sensor and the anchors must be considered. That is to say, time synchronization should be performed together with localization, which makes the problem complicated.

An alternative approach is to employ mobile anchors to replace the fixed ones. For terrestrial networks, commercial drones and unmanned aerial vehicles (UAVs) are very good choices, while autonomous underwater vehicles (AUVs) can be used for underwater applications. Mobile anchors can move along a predefined trajectory and broadcast beacon signals. By listening to the messages, the other nodes in the network can localize themselves passively. This architecture has three major advantages: first, energy and bandwidth

consumptions can be significantly reduced; secondly, the localization accuracy can be much improved with the increased number of virtual anchors, which can be boosted at negligible cost; thirdly, the coverage can be easily extended, which makes the solution and the network highly scalable.

Motivated by this idea, this thesis investigates the mobile node-aided localization and tracking in large-scale WSNs. For both terrestrial and underwater WSNs, the system design, modeling, and performance analyses will be presented for various applications, including: (1) the drone-assisted localization in terrestrial networks; (2) the ToA-based underwater localization and time synchronization; (3) the Doppler-based underwater localization; (4) the underwater target detection and tracking based on the convolutional neural network and the fractional Fourier transform. In these applications, different challenges will present, and we will see how these challenges can be addressed by replacing the fixed anchors with mobile ones. Detailed mathematical models will be presented, and extensive simulation and experimental results will be provided to verify the theoretical results. Also, we will investigate the channel estimation for the fifth generation (5G) wireless communications. A pilot decontamination method will be presented for the massive multiple-input-multiple-output communications, and the data-aided channel tracking will be discussed for millimeter wave communications. We will see that the localization problem is highly coupled with the channel estimation in wireless communications.

Acknowledgements

Time flies and I find it very difficult to believe that I have been working on this for five years. When I proofread the thesis, I can remember every equation, table, and figure, that I have been working on. Now I am at the end of this long journey, and I would like to take this opportunity to acknowledge the help and support from my supervisors, friends, and family.

First of all, I would like to thank Dr. Cheng Li, my supervisor, for his great help and support through the whole program. He is very open to new ideas and gives me great freedom to explore. Because of him, I gradually falled in love with academia and enjoyed the program a lot.

Also, I would like to thank Dr. R. Venkatesan and Dr. H. Heys, who are on my supervisory committee. They are both exemplary scholars in their respective fields, and they gave me a lot of valuable comments on my thesis proposal.

I would like to thank the School of Graduate Studies at the Memorial University of Newfoundland for their financial support, without which I won't be here today.

During my program, I also got great help from Dr. Cecilia Moloney. She was the instructor of *Digital Signal Processing* during my first year. I learned a lot from that course, and got inspirations for my research.

I met many friends at MUN, and they assisted me in so many ways during my work and life. In our WineMocol research group, I learned a lot from the excellent members, including Dr. Chen, Fan Jiang, Chen Zhang, Ruoyu Su, Yuhui Song, Xiaolin Pang, Sipan Ye, Yi Zhang, and many friends whose names are not mentioned. They are all good friends and excellent researchers. When I first came here, my English was not good, and

the WineMocol group discussions gave me great opportunities to practice my speaking. Now I can confidently present my research in front of many people, and I really own my thanks to the WineMocol members. During my study, I enjoyed the inspiring discussions with these friends.

Lastly, I would like to say thanks to my families. Five years ago, when I decided to come to Canada and work on my PhD, they were worried, but very supportive. Thanks to the high-speed Internet, I can talk to them "face to face" every week, even when we are on opposite sides of this planet. This was my greatest comfort at the beginning of my study, and endless fuel for my work, especially when things are not going well.

— Zijun Gong

Contents

List of Figures

List of Tables

List of Notations and Abbreviations

5G	Fifth Generation
AWGN	additive white Gaussian noise
DFT	discrete Fourier transform
FFT	fast Fourier transform
IDFT	inverse-DFT
IFFT	inverse-FFT
LTE	long-term evolution
LTE-A	LTE-advanced
MAP	maximum *a posteriori*
MIMO	multiple-input-multiple-output
ML	maximum likelihood
MMSE	minimum mean-square error
MSE	mean-square error
OFDM	orthogonal frequency division multiplexing
WSN	wireless sensor networks
GPS	Global Positioning System
AUV	autonomous underwater vehicle
RSS	received signal strength
DoA	direction of arrival
RSS	received signal strength
ToA	time of arrival

TDoA	time difference of arrival
LoS	line-of-sight
NLoS	non-line-of-sight
BS	base station
CSI	channel state information
CRLB	Cramér-Rao lower bound
FIM	Fisher information matrix
GDOP	geometrical dilution of precision
ML	maximum likelihood
MF	matched filter
LS	least square
PDF	probability density function
SINR	signal to interference-plus-noise ratio
SNR	signal to noise ratio
TDD	time division duplex
$(\cdot)^T$	matrix transpose
$(\cdot)^H$	matrix conjugate transpose
$(\cdot)^*$	element-wise conjugate
$(\cdot)^{-1}$	matrix inversion
$\lfloor \cdot \rfloor$	the floor function
$E\{\cdot\}$	mathematical expectation
$\exp(\cdot)$	exponential function

$\ln(\cdot)$	natural logarithmic function
$\mathbf{I}_L$	the size L identity matrix
$\mathrm{tr}\{\mathbf{A}\}$	the trace of matrix $\mathbf{A}$
$\mathrm{diag}\{\mathbf{A}\}$	a column vector with diagonal elements in $\mathbf{A}$
$\mathrm{diag}\{\mathbf{v}\}$	a diagonal matrix with diagonal elements in $\mathbf{v}$

Chapter 1

Introduction

1.1 Background

Large-scale wireless sensor networks (WSNs) are crucial for environmental, military, commercial, and scientific purposes, and have gained increasing attention in the past decade [2,3]. The underwater sensor networks are of particular interest to academia and industry, due to the rapid growth of human ambition on ocean exploration. With underwater sensors, ocean monitoring, tsunami warning, and resource exploration will become easier and more efficient. However, in order to exploit the full potentials of the large-scale WSNs, one important technical challenge must be properly addressed is how to obtain the location information of individual sensors in real time. In many network applications, location information of sensors is critical for decision making. For example, for environmental monitoring applications, environmental data without the corresponding location information is meaningless. However, how to effectively obtain such information remains as a challenging

problem in both terrestrial and underwater applications.

As we know, the GPS (Global Positioning System) is playing a dominant role in outdoor applications. However, GPS signals are not available for underwater sensor networks, due to water's absorption of electromagnetic waves. Under the terrestrial scenario, GPS may not be necessarily a good choice for some applications. For example, for a large sensor network in deep forests for environmental and fire monitoring, the GPS signals can be easily blocked. On the other hand, even when the GPS signal is available, it might be uneconomical and impractical to equip a GPS chip on every node for the following considerations: first, a GPS receiver is sometimes more expensive than the rest of the sensor node; secondly, the node number in a large-scale WSN can be very big, as the name suggests [3]. Besides, it is unrealistic to collect sensors' location information manually, due to the massive quantity and the movement of wireless sensors. Therefore, a practical strategy is to install GPS chips on a small number of sensors, and use them as reference nodes, i.e., anchors. Then, the other nodes localize themselves with reference to these location-aware anchors through geometric methods. These anchors can work independently or cooperatively, and the cooperative localization systems can improve positioning accuracy at the cost of more communication overheads and higher computational complexity.

For the underwater scenario, one possible solution is to deploy buoys on the sea surface of the target area [4]. The buoys are equipped with the GPS receivers, and they can localize themselves in real time. Then, they serve as location-aware anchors, and broadcast their positions and timing information through hydrophones. The underwater acoustic devices can receive the signals for self-localization. This system is not economic for large underwater acoustic sensor networks, because the density of buoys should be comparable

to that of the underwater sensors to ensure coverage. Another choice is to manually localize some of the sensors, and use them as anchors for the localization of other sensors. Once a sensor is localized, it can also serve as an anchor. This process repeats until the location information of all sensors is obtained. The major issue of such a system is the low accuracy, as has been pointed out by [5]. To be specific, the positioning accuracy of this system is highly dependent on the density of anchors, which is generally very low.

As we can see, the localization in large-scale WSNs is challenging. Fortunately, the surge of UAVs such as small consumer drones and AUVs provides us with another possible solution. Drones have been applied to many areas, such as photography, radar imaging [6], telepresence platform [7], and even express delivery [8]. In [9] and [10], the energy efficiency and throughput of drone-assisted WSNs are discussed. Drones provide a favorable platform for many applications because they are affordable, agile and versatile. Taking the DJI INSPIRE 2 as example, each of the four rotors can provide a thrust of two kilograms, and we can install all kinds of sensors on it conveniently [11]. Therefore, drones can serve as mobile anchors for localization in large-scale WSNs. For underwater WSNs, the AUVs can serve as mobile anchors as well as mobile data collector and aggregator [12–17]. When the AUVs move close to the sensors, they can collect the data through optical communications or magnetic induction methods, which support very high data rates. However, the AUVs must localize the sensors before that. To achieve this goal, the AUVs travel on the predefined trajectories, and broadcast beacon signals periodically. Any acoustic device within the communication range of the AUVs can receive the beacon signals and localize themselves through trilateration. This system can also work in the opposite way, that is, the target devices generate beacon signals, whereas the AUVs stay silent. From the received signals,

the AUVs can localize and track the target devices. Nowadays, some AUVs are solar-powered and suitable for long-endurance missions [18]. By employing AUVs, the number (or density, equivalently) of anchors can be boosted at a negligible cost, leading to much improved localization accuracy [5]. The AUVs can greatly extend the network coverage by moving around in the area of interest. The positioning and timing error caused by the AUVs' movement is negligible, because their typical velocity is only around 1.5 m/s [18,19].

1.2 Challenges and Problem Description

In large-scale WSNs, by replacing the fixed anchors with drones and AUVs, better coverage and higher localization accuracy can be achieved at very low cost. However, there are still some challenges in system design, and depending on the applications, the challenges lie in different aspects. In this section, we will briefly review these challenges.

1.2.1 Challenges in Terrestrial Localization

Most terrestrial localization techniques are ranging-based, and the underlying idea is trilateration or triangulation. To be specific, a target node estimates its distances to the anchors in its communication range and employs trilateration to localize itself. Therefore, a major problem is how to estimate the distances. For ranging purposes, four common choices are ToA (Time of Arrival), TDoA (Time Difference of Arrival), RTD (Round-Trip Delay) and RSS (Received Signal Strength). The ToA-based ranging method can be very accurate, but it requires high-precision time synchronization between the transmitters and receivers, which is expensive in practical implementation. Thus, it is not suitable for low-

cost WSNs. TDoA is adopted in GPS, where only time synchronization among anchors is required. The RTD can be estimated by sending a small packet to an anchor and receiving the corresponding reply packet. By doing that, a target node can easily estimate the distance without expensive time synchronization. However, the RTD-based method still experiences heavy communication burden since the target nodes need to send/receive packets to/from all anchors within the communication range.

For terrestrial localization, the RSS-based ranging method is attractive among the four candidates since it does not have the above mentioned deficiencies. The basic idea is to estimate the distance between the transmitter and receiver based on the RSS. For this method, a LoS (Line-of-Sight) path between the transmitter and receiver is generally assumed. Nevertheless, how to apply the RSS-based method to NLoS (None-Line-of-Sight) scenarios is studied in many literatures [20–22]. For example, the authors of [22] proposed to rule out the NLoS RSS values by setting a predefined threshold. The radio propagation model is an essential component in RSS-ranging based localization systems. Generally, RSS is affected by many factors, such as shadowing and the multi-path effect, corresponding to the slow and fast fading, respectively. These factors introduce vigorous fluctuations in RSS, which causes large ranging errors. Fortunately, shadowing and multi-path fading can be ignored in wide open fields, where large-scale WSNs are generally deployed. Nevertheless, RSS measurements still fluctuate due to the imperfections of the radio propagation model and the devices used for measurements.

In the radio propagation model, the model parameters vary with environments and time, which means we need to update them in real time. To address this issue, a possible solution has been proposed in [23], where the central node periodically estimates those

parameters by collecting the RSS measurements among anchors and broadcasts the estimated parameters. Then, the other nodes in the network can utilize those parameters to localize themselves by measuring the RSS of anchors.

The RSS-ranging based localization method is easy to implement, however, it suffers from several major defects as follows. Firstly, it is difficult to obtain unbiased estimates of distances from RSS measurements in practical scenarios [24]. Even with perfect channel parameters, an estimator that achieves the Cramér-Rao lower bound (CRLB) is still absent [25]. Secondly, because positioning error is proportional to ranging error, inaccurate distance estimates will lead to poor localization accuracy. Thirdly, due to economic considerations, the density of anchors is generally kept very low. In later discussions, we will see that by employing a drone as a mobile anchor, most of these problems can be very well addressed.

1.2.2 Challenges in Underwater Localization

For underwater large-scale WSNs, ToA and TDoA are the most common choices, because they achieve great balance between performance and complexity. Employing AUVs as mobile anchors, the sensors can estimate ToA or TDoA by receiving the beacon messages from AUVs. Generally, there will be a time bias between the AUVs and the sensors. As a result, time synchronization must be conducted through bi-directional message exchange. For the localization and time synchronization system based on fixed anchors, a huge number of anchors are required, because every target sensor needs at least three or four anchors in its communication range, depending on whether the average sound speed is known or not. Besides, because the anchors are fixed, their coverage will be quite limited. Therefore, the

authors of [12] proposed to deploy an AUV as a mobile anchor in the area of interest. The AUV travels on the predefined trajectories, and broadcasts beacon signals periodically. By receiving the beacons, all sensors in the network localize themselves. In [17], the sequential time-synchronization and localization (STSL) algorithm is proposed for the AUV-based system, in which time synchronization and localization are conducted iteratively. This method has two problems: firstly, extra estimation error is introduced by assuming the AUV is static in a short period of time; secondly, according to the simulation results, it converges slowly.

Apart from ToA and TDoA, Doppler shrift is another choice for underwater localization. As known, Doppler shift is generally used to estimate radial velocities of targets. However, it can also be used for three dimensional localization. Compared with the ToA-based method, the Doppler-based one has advantages in some applications. For example, suppose we employ AUVs to find a flight recorder in a specific water area, like in the search of the missing aircraft MA370. For the ToA-based method, the flight recorder should be equipped with a modem to broadcast beacon messages. For the Doppler-based method, it only needs to broadcast a sinusoidal wave at a fixed frequency. However, the mathematical model of the localization problem based on Doppler shift is more complicated.

After localization and time synchronization of the underwater sensor network, the sensors can work collaboratively to scan a target area and identify the objects in this area. The location and velocities of these targets can be estimated simultaneously. In recent years, the continuous active sonar (CAS) is getting more research interest, because it allows the sonar to transmit probe signals at very low power for a long period of time, and the reflected waves will be received by the other nodes. Based on the received signals,

distance and radial velocity of the target can be estimated. With enough observations, the sensor network can localize and track the target. In this system, a major challenge is the real-time processing of large volume of data.

1.3 Motivations and Research Contributions

Based on the previous discussions, RSS is a good choice for ranging in terrestrial WSNs. When we employ a drone as a mobile anchor, the major challenge is how to get the real-time parameters of the propagation model. To solve this issue, an intuitive idea is to jointly estimate the model parameters and sensor's location. By doing this, the communications burdens of the conventional localization framework can be alleviated. Meanwhile, the mobility of drones makes it possible to boost the number of virtual anchors at low cost, leading to much improved localization accuracy.

For underwater localization, AUVs can serve as mobile anchors. ToA and Doppler shift can be employed for localization, and they both have certain advantages in specific applications. The advantage of the ToA-based approach is that localization and time synchronization of the sensors in a network can be simultaneously conducted. On the other hand, Doppler shift contains both location and velocity information, and is a good choice for mobile target tracking. Similar to the terrestrial scenario, the mobility of the AUV can significantly improve system performance and reduce the cost.

With the above mentioned motivations, we will investigate the design, modeling, and analyses of mobile node-assisted localization in large-scale WSNs in this thesis. Also, motivated by the channel modeling needs for the localization problems, the channel estimation

and channel tracking are investigated for massive multiple-input-multiple-output (MIMO) and millimeter wave (mmWave) communications, which are two key enabling techniques for the fifth-generation (5G) cellular networks. The major contributions are summarized below.

(1) Algorithm design and comprehensive analyses are conducted for the drone-assisted localization framework. The theoretical results are supported by simulations and experiments.

(2) A two-phase low-complexity algorithm is presented for ToA-based underwater localization and time synchronization. Based on the theoretical and simulation results, the CRLB can be closely achieved.

(3) It is shown that we can exclusively depend on the Doppler shift measurements for underwater localization, and the positioning accuracy grows cubically with the sampled sequence length.

(4) The convolutional neural network-based target detection and localization framework is designed for CAS, and the accuracy can be as high as 97 percent.

(5) The spatial sparsity of signals in massive MIMO systems is thoroughly analyzed, and a pilot decontamination method based on spatial filter is proposed.

(6) A data-aided channel tracking scheme is proposed for mmWave communications. Theoretical and simulation results show that the CRLB can be achieved, and the communication redundancy is significantly reduced.

1.4 Thesis Organization

The topics of different chapters are briefly summarized in this section.

In Chapter 2, the fundamentals of the related techniques in localization and communications are introduced, including the RSS-ranging based terrestrial localization, the ToA-based underwater localization, the massive MIMO technique, and the millimeter wave communications. Also, challenges and problems concerning these techniques are also presented in detail.

In Chapter 3, a drone-assisted zero-configuration localization framework will be presented. A drone will be employed as a mobile anchor and the RSS is used for rangingo. An algorithm is introduced to jointly estimate the unknown parameters of the propagation model and the target node's distance to the drone. The closed-form positioning error is derived for the Newton's method and the CRLB is closely achieved. This new framework has two advantages over the conventional one: 1) offline measurements are totally unnecessary; 2) the number of virtual anchors can be vastly increased at negligible cost, leading to very high positioning accuracy.

In Chapter 4, an AUV-aided joint localization and synchronization algorithm will be presented for underwater WSNs. Similar to the terrestrial scenario, an AUV serves as a mobile anchor, and keeps broadcasting beacon messages. The nodes in the WSN achieve self-localization by receiving the beacon messages from the AUV. A two-phase joint time synchronization and localization algorithm is presented. In the first phase, the relative clock skew is ignored, because it is generally very small. Then, the nonlinear equations are transformed into linear ones, and the least square (LS) algorithm is employed to obtain

coarse time synchronization and localization results. In the second phase, the coarse estimation is refined by another LS estimator. Compared with the existing algorithms, the proposed one achieves the CRLB with much lower computational complexity.

In Chapter 5, the passive localization of acoustic devices based on Doppler shift measurements will be investigated. It can be easily shown that the Doppler shifts not only contain speed information, but also position information. Therefore, we will discuss the localization accuracy of systems exclusively dependent on Doppler shift. A low-complexity Doppler estimation algorithm is employed and the probability density function of its estimation error is derived. Based on Doppler shift measurements, a two-phase linear algorithm is presented for Doppler-based underwater localization, and its closed-form localization error is given. As a benchmark, the CRLB of the proposed system is analyzed.

In Chapter 6, the focus will be the proactive tracking of underwater objects/events based on underwater sensor network. After obtaining the position information of the nodes in an underwater WSN, we can employ the network for surveillance of the target water area. Some proactive nodes will periodically broadcast linear frequency modulated (LFM) signals, which will hit the targets, get reflected and received by the other nodes. Depending on the target's position and velocity, the received signals will also be LFM signals of different frequencies and frequency rates. We can use the Fractional Fourier Transform (FrFT) to analyze the received signal's spectrum and find the peak. Based on the location of the peak, the target's distance and radial velocity can be estimated. However, the accuracy is highly dependent on the sampling interval of the spectrum. Smaller sampling interval leads to higher accuracy but also induces considerable complexity. To overcome this issue, a machine learning-based approach is presented to automatically detect the existence of the

target, and roughly estimate the peak's location if targets exist. Then over-sampling can be conducted for a small area around the peak, leading to improved accuracy and reduced complexity. The idea is based on the following observation: if a target exists, we will be able to observe an "X" pattern on the spectrum. Extensive simulations are conducted to verify the effectiveness of the presented architecture.

In Chapter 7, a pilot decontamination method based on spatial filter will be presented for massive MIMO communications. To employ massive MIMO for high-speed data transmission from drones to BSs, the pilot contamination issue must be resolved. Due to pilot reuse, every user will experience interference from users in adjacent cells who employ the same pilot sequence. In massive MIMO systems, the communication protocols are generally divided into four phases: pilot transmission, processing, uplink data transmission, and downlink data transmission. In the first phase, the BS receives both the desired signal and the pilot contaminated signal. In the second phase, all users in the target cell stay silent for one symbol period and the BS only receives interference from adjacent cells. The fast Fourier transform can then be employed to analyze the spatial spectrums of the received signals. The spatial sparsity of the massive MIMO channels makes it possible to identify the pilot contamination components by comparing the two spectrums on different spatial signatures (or angles of arrival). A spatial filter can then be constructed to eliminate pilot contamination. Both theoretical analysis and simulation results demonstrate the effectiveness of the proposed method, whose complexity is comparable to that of the conventional LS channel estimator.

In Chapter 8, a data-aided fast channel tracking algorithm will be introduced for millimeter wave communications. The mmWave channels are generally very sparse, and the

CSI in adjacent data blocks are highly correlated. Therefore, it is possible to employ the CSI from the previous data block for the data detection in the current block. Then, based on the detected data, the CSI can be updated. By doing this, we only need to transmit pilot sequence at the very beginning, and exclusively depend on detected data for channel tracking. The channel estimation overhead can thus be significantly reduced. We will see that the data-aided channel tracking algorithm has very high accuracy and low cost in sparse channels.

The last chapter summarizes the thesis and presents the future work.

1.5 Publications and Awards

This section contains the list of publications and obtained awards during my PhD program at Memorial University of Newfoundland. Most of the published papers are very closely related to the topic of this thesis, while the others can serve as supplementary material, such as the work in [J12] on weak signal processing. Over the past five years, the research has led to 23 published journal papers, two book chapters, and 16 conference papers. The work in [C6] was awarded the Best Paper Award at the 2017 IEEE International Conference on Communications (Globecom'17) which was selected from over 3000 submissions, and the work in [C15] was awarded the Best Poster Award on the 28th Annual Newfoundland Electrical and Computer Engineering Conference.

■ Book Chapters

[B1] *Zijun Gong*, Fan Jiang, *Encyclopedia of Wireless Networks*, Chapter 2, "Ad hoc Network", Springer International Publishing, ISBNs: 978-3-31-932903-1, Jan. 2018.

[B2] *Zijun Gong* and Cheng Li, *Smart Ships*, Chapter "Smart AUV-Assisted Localization and Time Synchronization of Underwater Acoustic Devices", CRC press, accepted, to appear.

■ Journal Papers Published or Accepted

[J1] *Zijun Gong*, Cheng Li and Fan Jiang, "A Machine Learning-based Approach for Auto-Detection and Localization of Targets in Underwater Acoustic Array Networks," *IEEE Transactions on Vehicular Technologies, accepted, to appear in 2020.*

[J2] *Zijun Gong*, Cheng Li, Moe Z. Win and Fan Jiang, "Data-Aided Doppler Compensation for High-Speed Railway Communications on Millimeter Wave Frequency," *IEEE Transactions on Wireless Communications, accepted, to appear in 2020.*

[J3] *Zijun Gong*, Cheng Li and Fan Jiang, "The Analysis of the Muti-path Effect in Underwater Doppler Estimation," *IEEE Wireless Communications Letters*, vol. 9, no. 10, pp. 1758-1762, June 2020.

[J4] *Zijun Gong*, Cheng Li, Fan Jiang, and Jun Zheng, "AUV-Aided Localization of Underwater Acoustic Devices Based on Doppler Shift Measurements," *IEEE Transactions on Wireless Communications*, vol. 19, no. 4, pp. 2226-2239, April 2020.

[J5] *Zijun Gong*, Fan Jiang, and Cheng Li, "Angle Domain Channel Tracking with Large

Antenna Array for High Mobility V2I Millimeter Wave Communications," *IEEE Journal of Selected Topics in Signal Processing*, vol. 13, no. 5, pp. 1077-1089, Sept. 2019.

[J6] Kun Hao, Kaicheng Yu and *Zijun Gong*, Xiujuan Du, Yonglei Liu, and Lu Zhao, "An Enhanced AUV-Aided TDoA Localization Algorithm for Underwater Acoustic Sensor Networks," *Mobile Networks and Applications*, vol. 25, pp. 1673-1682, June 2020.

[J7] Fan Jiang, Cheng Li, and *Zijun Gong*, "MMSE-based Iterative Processing With Imperfect Channel and Parity Check in MIMO Systems," *IET Communications*, vol. 13, no. 17, pp. 2660-2667, Oct. 2019.

[J8] Ruoyu Su, D. Zhang, R. Venkatesan, *Zijun Gong*, Cheng Li, F. Ding, Fan Jiang, and Ziyang Zhu "Resource Allocation for Network Slicing in 5G Telecommunication Networks: A Survey of Principles and Models," *IEEE Network Magazine*, vol. 33, no. 6, pp. 172-179, Nov. 2019.

[J9] Ruoyu Su, D. Zhang, Cheng Li, *Zijun Gong*, R. Venkatesan, and Fan Jiang, "Localization and Data Collection in AUV-aided Underwater Sensor Networks: Challenges and Opportunities," *IEEE Network*, vol. 33, no. 6, pp. 86-93, Nov. 2019.

[J10] Fan Jiang, Cheng Li and *Zijun Gong*, "An Iterative Approach for Massive MIMO Uplink Processing under Imperfect Channel Conditions," *IEEE Transactions on Vehicular Technology*, vol. 68, no. 4, pp. 3642-3654, Feb. 2019.

[J11] *Zijun Gong*, Cheng Li and Fan Jiang, "Pilot Decontamination in Noncooperative

Massive MIMO Cellular Networks Based on Spatial Filter," *IEEE Transactions on Wireless Communications*, vol. 18, no. 2, pp. 1419-1433, Feb. 2019.

[J12] *Zijun Gong*, Cheng Li and Fan Jiang, "Channel Estimation for Sparse Massive MIMO Channels in Low SNR Regime," *IEEE Transactions on Cognitive Communications and Networking*, vol. 4, no. 4, pp. 883-893, Dec. 2018.

[J13] Fan Jiang, Cheng Li, and *Zijun Gong*, "Extrinsic Information Analysis of A New Iterative Method Using the Stair Matrix for Massive MIMO Uplink Signal Detection," *IEEE Wireless Communications Letters*, vol. 7, no. 6, pp. 1022-1025, Dec. 2018.

[J14] Fan Jiang, Cheng Li, and *Zijun Gong*, "Low Complexity and Fast Processing Algorithms for V2I Massive MIMO Uplink Detection," *IEEE Transactions on Vehicular Technology*, vol. 67, no. 6, pp. 5054-5068, June 2018.

[J15] Fan Jiang, Cheng Li, and *Zijun Gong*, "Accurate Analytical BER Performance for ZF Receivers under Imperfect Channel in Large Receiving Antennas and Low SNR Region," *IEEE Signal Processing Letters*, vol. 25, no. 8, pp. 1246-1250, Aug. 2018.

[J16] *Zijun Gong*, Cheng Li and Fan Jiang, "AUV-Aided Joint Localization and Time Synchronization for Underwater Acoustic Sensor Networks," *IEEE Signal Processing Letters*, vol. 25, no. 4, pp. 477-481, April 2018.

[J17] Fan Jiang, Cheng Li, *Zijun Gong*, and Ruoyu Su, "Stair Matrix and its Applications to Massive MIMO Uplink Data Detection," *IEEE Transactions on Communications*, vol. 66, no. 6, pp. 2437-2455, June 2018.

[J18] *Zijun Gong*, Cheng Li and Fan Jiang, "Pilot contamination mitigation strategies in massive MIMO systems," *IET Communications*, vol. 11, no. 16, pp. 2403-2409, Nov. 2017.

[J19] *Zijun Gong*, Cheng Li, Fan Jiang, Ruoyu Su *et al* "Design, Analysis, and Field Testing of an Innovative Drone-Assisted Zero-Configuration Localization Framework for Wireless Sensor Networks," *IEEE Transactions on Vehicular Technology,* vol. 66, no. 11, pp. 10322-10335, Nov. 2017.

[J20] Cheng Li, Fan Jiang, Cheng Meng and *Zijun Gong*, "A New Turbo Equalizer Conditioned on Estimated Channel for MIMO MMSE Receiver," *IEEE Communications Letters,* vol. 21, no. 4, pp. 957-960, April 2017.

[J21] Shuai Han, *Zijun Gong*, Weixiao Meng, and Cheng Li, "Towards Future Techniques for Alternative Positioning, Navigation and Timing," *IEEE Wireless Communications Magazine*, vol. 23, no. 6, pp. 154-160, Dec. 2016.

[J22] Shuai Han, *Zijun Gong*, Weixiao Meng, Cheng Li, D. Zhang and W. Tang, "Automatic Precision Control Positioning for Wireless Sensor Network," in *IEEE Sensors Journal,* vol. 16, no. 7, pp. 2140-2150, April 2016.

[J23] Shuai Han, *Zijun Gong*, Weixiao Meng, and Cheng Li, "An Indoor Radio Propagation Model Considering Angles for WLAN Infrastructures," *Wireless Communications and Mobile Computing,* vol. 15, no. 16, pp. 2038-2048, Nov. 2016.

■ Journal Papers Under Review

[JR1] Fan Jiang, *Zijun Gong*, Zhenyu Liu, Cheng Li, and Moe Z. Win, "Estimation and Tracking for Wideband mmWave Massive MIMO Channels," *Submitted to IEEE Transactions on Wireless Communications, under review.*

[JR2] Yuhui Song, *Zijun Gong*, Cheng Li, and Yuanzhu Chen, "Sparse Channel Estimation of DLA for Wideband Communications," *Submitted to IEEE Transactions on Communications, under review.*

[JR3] Ruoyu Su, *Zijun Gong*, Cheng Li, Yuanzhu Chen and Dengyin Zhang, "An Adaptive Asynchronous Wake-up Scheme for Underwater Acoustic Sensor Networks using Deep Reinforcement Learning," *Submitted to IEEE Transactions on Vehicular Technology, under review.*

■ Published Conference Paper

Full Paper Referred Conference Papers

[C1] *Zijun Gong*, Cheng Li and Fan Jiang,"Passive Underwater Event and Object Detection Based on Time Difference of Arrival", in *Proceedings of 2019 IEEE GLOBECOM*, Big Island, Hawaii, USA, Dec. 2019.

[C2] Fan Jiang, Cheng Li and *Zijun Gong*, "Efficient and Fast Processing Large Array Signal Detection in Underwater Acoustic Communications", in *Proceedings of 2019 IEEE ICC*, Shanghai, China, May 2019.

[C3] Cheng Li, Fan Jiang, *Zijun Gong* and Yan Zhang, "Massive MIMO for Future Ve-

hicular Networks: Compressed-Sensing and Low-complexity Detection Schemes," in *Proceedings of 2017 Springer WiCon,* Tianjin, China, Dec. 2017.

[C4] *Zijun Gong*, Cheng Li and Fan Jiang, "Pilot Decontamination for Cell-Edge Users in Multi-Cell Massive MIMO Based on Spatial Filter," in *Proceedings of 2018 IEEE ICC* , Kansas City, MO, USA, May 2018.

[C5] Fan Jiang, Cheng Li and *Zijun Gong*, "A Low Complexity Soft-Output Data Detection Scheme Based on Jacobi Method for Massive MIMO Uplink Transmission," in *Proceedings of 2017 IEEE ICC*, Paris, May 2017.

[C6] Fan Jiang, Cheng Li and *Zijun Gong*, "Block Gauss-Seidel Method Based Detection in Vehicle-to-Infrastructure Massive MIMO Uplink," in *Proceedings of 2017 IEEE GLOBECOM,* Singapore, Dec. 2017. (**Best Paper Award**)

[C7] Lei Chen, Shuai Han, Weixiao Meng and *Zijun Gong*, "A Spoofing Mitigation Algorithm Based on Subspace Projection for GNSS Receiver," in *Proceedings of 2015 CSNC,* Xi'an, China, May 2015.

[C8] Wanlong Zhao, Shuai Han, Weixiao Meng and *Zijun Gong*, "RSSI Based Positioning Fusion Algorithm in Wireless Sensor Network Using Factor Graph," in *Proceedings of 2016 ChinaCom*, Chongqing, China, Sept. 2016.

[C9] Deyue Zou, Weixiao Meng, Shuai Han and *Zijun Gong*, "User Aided Self-Growing Approach on Radio Map Construction for WLAN Based Localization," in *Proceedings of the 2013 ION GNSS+,* Nashville, TN, USA, Sept. 2013.

[C10] Lei Chen, Shuai Han, Weixiao Meng and *Zijun Gong*, "A Spoofing Mitigation Algorithm based on Subspace Projection for GNSS Receiver," in *Proceedings of 2015 CSNC,* Xi'an, China, May 2015.

Abstract Referred Conference Papers

[C11] *Zijun Gong*, Cheng Li and Fan Jiang, "AUV Aided Localization of Underwater Sensors", in *Proceedings of 27th IEEE NECEC,* St. John's, NL, Canada, Nov. 2018.

[C12] *Zijun Gong* and Cheng Li, "An Innovative Channel Estimation Method for Very Large Antenna Arrays in Low SNR Regime," in *Proceedings of 24th IEEE NECEC,* St. John's, NL, Canada, Nov. 2016.

[C13] *Zijun Gong*, Cheng Li and Shuai Han, "A Robust Positioning Algorithm for WSN" in *Proceedings of 23rd IEEE NECEC,* St. John's, NL, Canada, Nov. 2015.

[C14] Yuhui Song, Cheng Li, Yuanzhu Chen, and *Zijun Gong*, "Beamspace Channel Estimation for Wideband Millimeter Wave MIMO Systems" in *Proceedings of 29th IEEE NECEC,* St. John's, NL, Canada, Nov. 2020.

[C15] Xiaolin Pang, Cheng Li, and *Zijun Gong*, "The Outage Probability Analysis in Millimeter Wave Communications for Highway Application" in *Proceedings of 28th IEEE NECEC,* St. John's, NL, Canada, Nov. 2019. (**Best Poster Award**)

[C16] Xiaolin Pang, Cheng Li, and *Zijun Gong*, "The Analysis of Co-Channel Issue in DLA-based Millimeter Wave Communications for Highway Applications," in *Proceedings of 29th IEEE NECEC,* St. John's, NL, Canada, Nov. 2020.

■ Awards

- The **Best Paper Award** on the 2017 IEEE International Conference on Communications (ICC'17).
- The **Best Poster Award** on the the 28th Annual Newfoundland Electrical and Computer Engineering Conference (NECEC'19).
- The **Annual Research Day Award** on the 4th Annual Research Day, 2019.

Chapter 2

Fundamentals of Localization and Communications in Terrestrial and Underwater Networks

In this chapter, several important localization and communication techniques in terrestrial and underwater networks will be introduced. The localization and communication are deeply coupled, especially in the era of 5G. To be specific, both Massive MIMO and mmWave demand high accuracy channel estimation, and the channel state information (CSI) contains ToA and DoA information, which can be used for positioning. For localization of terrestrial WSNs, the RSS-ranging based method is very popular, while ToA or TDoA are more common choices in underwater applications. For the wireless communications, the discussion will be focused on massive MIMO and mmWave, because they are believed to be the most important techniques for the next generation wireless commu-

nication systems. The system model and channel estimation process will be presented, and the major challenges will be discussed.

2.1 Fundamentals of Terrestrial Localization

2.1.1 Related work

Currently, terrestrial localization is mainly based on radio signals [21,22,26–30]. In [31–33], the fundamental limits of radio based localization systems on positioning accuracy are discussed. Generally, a small number of location-aware nodes are deployed in the network, referred to as anchors. The localization system can work in passive or proactive mode. In the proactive mode, the anchors broadcast beacon signals periodically. The other nodes in the network can receive the beacon signals, estimate the DoA, RSS, ToA, TDoA, etc., and employ these measurements to localize themselves. In the passive mode, the anchors will stay silent, detect signals from other nodes, and extract their position information. Generally, these systems can be roughly divided into two categories: the ranging-based methods and the ranging-free methods, depending on whether they need to calculate the distances between anchors and target nodes or not.

The basic idea underlying the ranging-based methods is trilateration. To be specific, a target node estimates its distances to the anchors in its communication range and employs trilateration to localize itself. Therefore, the major problem is how to estimate the distances. The ranging process can be based on ToA, TDoA, RTD and RSS, as we have mentioned in the previous chapter. The ranging-free localization methods can also be implemented with various kinds of measurements [26, 34–37]. For example, DoA is a com-

mon choice for positioning systems [34]. Using DoA instead of distance, two anchors are sufficient for 2D or even 3D positioning. Besides, angular information can be combined with ranging results to improve positioning accuracy [26]. However, antenna arrays, the indispensable elements for DoA-based systems, are both clumsy and costly for small and cheap sensors. Another kind of appealing measurement is often referred to as *connectivity*. The underlying idea is that if a target sensor receives signals from several surrounding anchors, it must lie in their intersection [35, 36]. According to the experimental and theoretical results in [37], the connectivity-based positioning system can even outperform its peer based on RSS-ranging in noisy environments. Fingerprint-based algorithms are also very popular, but mainly for indoor applications. For example, fingerprint is combined with deep learning in [38–40] for indoor localization, and the positioning error can be very close to or even smaller than one meter.

Not all the above mentioned positioning techniques are suitable for WSNs due to the following considerations. First, the cost of the positioning system should be acceptable. Second, due to limited power supply, the communication traffic of the positioning system and the computation complexity of the localization scheme are restricted. Last but not the least, the expected positioning accuracy should be achieved. Considering all these factors, the RSS-ranging based localization system is widely acknowledged to achieve good compromise between performance and cost.

2.1.2 RSS-Ranging based Localization

In RSS-ranging based localization systems, the anchors are periodically broadcasting beacon signals, and every other node can estimate its distances to surrounding anchors ac-

cording to the RSS. Then, trilateration can be employed for self-localization.

The radio propagation model is an essential component in RSS-ranging based localization systems, and it is given by

$$P(d) = P_0 - 10 \cdot \alpha \cdot \lg(d) + n,^{1} \tag{2.1}$$

where $P(d)$ and P_0 represent the RSS (in dBm) at distances of d (in meters) and d_0 ($d_0 = 1$ m is the reference distance throughout the paper), respectively. α denotes the path loss exponent, and its value in free space is 2. n is the measurement error of $P(d)$ and can be modeled by the zero-mean Gaussian distribution, i.e., $n \sim \mathcal{N}(0, \sigma_n^2)$. This model has been extensively verified by field experiments and adopted in many studies [37, 41, 42]. To simplify notations, we rewrite (2.1) as

$$P(d) = P_0 - \beta \cdot \ln(d) + n, \tag{2.2}$$

where $\beta = 10 \cdot \alpha / \ln 10$.

The RSS-ranging based localization systems are very popular in large-scale WSNs, and three major research directions in this field are summarized in the following paragraphs.

The first research direction is how to improve ranging accuracy [30, 43], which is crucial for any trilateration based positioning methods. Based on the assumptions of perfect channel parameters and log-normal distribution of RSS values, the CRLB of ranging error has been discussed in many literatures [37, 41, 44]. In [41], an unbiased range estimator is proposed, and ranging error is proven to be proportional to the transmitter-receiver (T-R) distance. However, to the best of our knowledge, the optimal estimator that achieves the

[1] Throughout the thesis, $\lg(\cdot)$ and $\ln(\cdot)$ represent base-10 and natural logarithms, respectively.

CRLB is still absent, even with full knowledge of the channel parameters, i.e., P_0 and β. In [24], imperfect channel parameters are considered, which is more realistic.

The second major research direction is how to estimate the target's position based on the ranging results. By viewing the target's coordinate as unknown parameters, a series of circular equations can be established according to the radio propagation model. The solutions of these equations provide the positioning result, where the positioning error is inevitable due to the ranging error. The CRLB of positioning error has been discussed in many literatures [28, 29, 41]; nevertheless, how to achieve that is still under investigation. In [28], a low complexity algorithm based on the least square method is presented for circular equations. In [29], an extended centroid localization algorithm is proposed to remedy the positioning error caused by biased range estimators. Newton's method is proposed as a solution in [41], and the authors have demonstrated that CRLB of positioning error can be achieved under perfect channel parameters, by assigning smaller weights to further anchors. Similar to other trilateration based localization systems (e.g., GPS), the performance of RSS-ranging based positioning system is highly dependent on the number and geometrical distribution of anchors. As a result, the positioning accuracy of target sensors can be quite different [41, 45]. We will show in the next section that the density of anchors puts a fundamental limit on positioning error.

The third direction concentrates on how to get channel parameters. An intuitive idea is to calculate them based on off-line measurements. In fact, the ML estimate of these parameters can be obtained through the LS method [41]. However, these parameters should be timely and automatically updated because they vary with time and environments. To address this issue, a possible solution is proposed in [23]. The basic idea is to collect

the RSS measurements among anchors, and use a central node to estimate and broadcast channel parameters automatically and periodically. Nevertheless, a major problem of this system is the extra communication burden for the purpose of collecting RSS measurements and broadcasting channel parameters.

2.1.3 Deficiencies of the Conventional Architecture

The RSS-ranging based localization system is easy to implement; nevertheless, it suffers from several major defects as follows.

First of all, due to economic considerations, the density of anchors is quite limited, which leads to poor positioning precision. In [25], the variance of positioning error of the RSS-ranging based method is given as:

$$\sigma_p^2 = \mathrm{tr}\left\{(\mathbf{H}^T\mathbf{D}^{-1}\mathbf{H})^{-1}\right\} \cdot \exp\left(\frac{\sigma_n^2}{\beta^2 \cdot \ln 10} - 1\right), \tag{2.3}$$

where the i-th row of $\mathbf{H}$ is the unit vector pointing from the i-th anchor to the target node. $\mathbf{D}$ is a diagonal matrix, and the i-th element is the square of the distance between the target node and the i-th anchor. The first component in the right hand side of Equation (2.3) is defined as GDOP (Geometrical Dilution of Precision) since matrixes $\mathbf{H}$ and $\mathbf{D}$ are determined by the geometrical distribution of anchors. Using the results in *Lemma 1* (given in Appendix A.1), we have the lower bound of $GDOP$ as

$$GDOP = \mathrm{tr}\left\{(\mathbf{H}^T\mathbf{D}^{-1}\mathbf{H})^{-1}\right\} \geq \frac{4}{\sum_{i=1}^{N} 1/d_i^2}, \tag{2.4}$$

where d_i is the distance between the i-th anchor and the target node. The equality of Equation (2.4) holds when the two eigenvalues of $\mathbf{H}^T\mathbf{D}^{-1}\mathbf{H}$ are equal (considering 2-dimensional localization). Statistically, the lower bound of positioning error is inversely proportional

to anchor number, as we will show in latter discussions. In the conventional localization systems based on fixed anchors, N is very small and the lower bound of positioning error is quite high. Besides, due to the limited number of anchors, $GDOP$ varies vigorously with the geometrical distribution of the network, which makes this system unstable [25], i.e., some nodes may have high positioning accuracy, while others may experience large positioning error.

The second problem is that it is difficult to obtain unbiased estimates of distances from RSS measurements in practical scenarios [24]. Even with perfect channel parameters, an estimator that can achieve the CRLB is still absent [25]. Because positioning error is proportional to ranging error, inaccurate distance estimates will lead to poor localization accuracy.

The last problem is the real-time update of the channel parameters, including P_0, α, and σ_n^2. To address this issue, a possible solution has been proposed in [23], where the central node periodically estimates those parameters by collecting the RSS measurements among anchors and broadcasts. The three phases of this solution can be summarized as:

a) the central node estimates channel parameters according to the RSS measurements among anchors, and broadcasts periodically;

b) the target node receives channel parameters and measures RSS values of anchors within its communication range;

c) after receiving signals from three or more anchors, the target node can estimate its distances to anchors based on RSS values and localize itself through trilateration.

This method is very straight forward and effective. However, it will inevitably aggravate

communication burdens and battery consumption on sensor nodes. This is quite obvious because of the following communication links dedicated to the localization purpose: 1) anchors report RSS measurements to the central node; 2) the central node broadcasts channel parameters to the network. Therefore, the central node needs to be very powerful, so as to cover the whole network.

2.2 Fundamentals of Underwater Localization

With the growth of human ambition on ocean exploration, more and more underwater devices are deployed. These devices are used for environmental monitoring, resource exploitation, tsunami warning, wreck salvage, and so on. For many applications, a reliable underwater localization technique is very important. In underwater WSNs, ToA is the most common choice for localization and time synchronization of the nodes. In this section, we will first survey related work in this area, and then introduce the underwater acoustic channel model and the ToA-based localization technique. After localization and time synchronization, the WSN can be used for silent object detection in the coverage area, and this topic will be briefly discussed in the last part of this section.

2.2.1 Related work

During the past several decades, many localization systems for underwater WSNs have been proposed, including various system architectures and the localization algorithms. We will briefly review the existing work from these two aspects.

For the system architecture, the first choice is to deploy buoys on the sea surface of the

target area [4]. These buoys are equipped with the GPS receivers, and they can localize themselves at very low cost. Then, they serve as location-aware anchors, and broadcast their position and timing information through hydrophones. Another choice is to manually localize and synchronize some of the sensors, and use them as anchors for the localization of other sensors. Once a sensor is localized and synchronized, it can also serve as an anchor. This process iterates until the location information of all sensors is available. The major issue of this system is the low accuracy, as has been pointed out by [5]. To be specific, the positioning and timing accuracy of this system is highly dependent on the density of anchors, similar to the terrestrial scenario. Due to the small number of initial anchors, the system performance is quite limited. Another problem of this architecture is that the positioning and timing error propagates in iterations [31, 32, 46].

An alternative is to deploy AUVs as mobile anchors [12–17]. The AUVs travel on the predefined trajectories, and broadcast beacon signals periodically. Any acoustic device in the communication range of the AUVs can receive the beacon signals and localize themselves through trilateration. By employing AUVs, the number (or density, equivalently) of anchors can be boosted at negligible cost, leading to much improved accuracy [5]. Also, the AUVs can provide very good coverage by moving around in the area of interest.

The localization algorithms are generally independent from the system architecture. These algorithms can be based on DoA, ToA, TDoA, RSS, etc [47]. The ToA-based or TDoA-based ones are the most common, because the timing error is reported to be at the level of millisecond (ms) [48], leading to high positioning accuracy. The major challenges include the stratification effect, long propagation delays, and energy constraints [49].

In [50], it was argued that RSS-ranging based method should work better in aquatic

environments than on ground. The reason is that RSS decreases faster with distance in underwater scenarios due to absorption, which leads to a strong correlation between distance and RSS. In [15], the authors installed directional antennas on an AUV. On every side of the AUV, there are two beams. When a target device receives signals from the AUV for two consecutive beams, triangulation can be employed for localization. The largest advantage of this system is that sensor nodes are passive, which will save energy and prolong battery life. In [51], the authors discussed the possibility of employing Doppler for target course estimation, based on the assumption that the Doppler velocity log is available. In [52], the authors employed Doppler shift measurements for node tracking.

Information fusion is also an interesting topic in this area. For example, the authors of [53] combined ToA and DoA for object localization through the Bayesian method. To be specific, the localization result is the coordinate that maximizes the likelihood density of the measurements. In [54], the authors discussed the possibility of employing both ToA and Doppler shift for localization. In [55], the Doppler and ToA measurements were combined for localization.

2.2.2 Underwater Acoustic Channel Model

For underwater localization applications, the underwater acoustic channel model plays a very important role in system design, and it is generally given as [56–59]:

$$h(\tau, t) = \sum_{l=0}^{L-1} A_l(t)\delta(\tau - \tau_l(t)), \tag{2.5}$$

where L denotes the number of paths between the transmitter and the receiver, and these paths are indexed from 0 to $L-1$. $\tau_l(t)$ represents the propagation delay of the l-th path

at time t, and it can be approximated by

$$\tau_l(t) = \tau_l - a_l t, \tag{2.6}$$

where a_l is often referred to as Doppler rate, and it describes how fast the delay of the l-th path varies. The arriving paths are ordered based on the time of arrival, i.e., $\tau_l(t) < \tau_{l+1}(t)$ for an arbitrary $l \in \{0, 1, \cdots, L-2\}$.

$A_l(t)$ is the real-time propagation loss of the l-th path, and we can assume it as a constant for a relatively short period of time, because the coherence time for underwater acoustic channels is on the level of seconds [57,58]. The path loss model is given as [50,60]

$$A(d, f_c) = (d/d_0)^{\gamma} a(f_c)^{d-d_0}, \tag{2.7}$$

where d is the T-R distance, and d_0 is a reference distance. γ indicates the spreading loss, and it varies between 1 and 2, for cylindrical and spherical spreading, respectively. $a(f_c)$ is often referred to as the absorption coefficient, and it is a function of the carrier frequency f_c. For $f_c = 10\,\text{kHz}$, $a(f_c)$ is around $2\,\text{dB/km}$. In [60], we can see that the absorption coefficient increases with frequency piece-wise linearly. However, the bandwidth of underwater acoustic system is only around several kHz (e.g.,The AquaSeNT OFDM modem works on the frequency ranging from $14\,\text{kHz}$ to $20\,\text{kHz}$ [61]), and $a(f_c)$ can be viewed as a constant for given f_c. Therefore, the path loss model in dB is

$$A_{lg} = 10 \lg A(d, f_c) = 10\gamma \lg (d/d_0) + 10(d - d_0) \lg a(f_c). \tag{2.8}$$

Generally, only the LoS signal provides useful information in localization systems, while the multi-path components are interference. Therefore, the receiving nodes need to find a way to decide whether a specific signal component is from LoS or NLoS path. This is indeed an important topic, and has been investigated in literatures such as [62].

2.2.3 ToA-based Localization

As we have mentioned, ToA and TDoA are the most common choices for underwater localization. For WSNs, the anchors are generally assumed to be synchronized, while the other nodes are not. In such systems, there are several major challenges and we will discuss them in the following paragraphs.

First, underwater sound speed is not constant due to the heterogeneous salinity, density and temperature of seawater, leading to the well known stratification effect [49, 63]. Generally, the underwater sound speed ranges from 1420 m/s to 1560 m/s [64]. Although an algorithm has been proposed to compensate for the stratification effect in [63], it is computationally intense. In [17], the authors showed that a small uncertainty in acoustic speed will cause significant positioning error. Also, the authors showed that the stratification effect can be ignored by viewing the average acoustic speed as an extra unknown. This approach has been widely utilized [65,66], because it can greatly reduce the computational complexity.

Second, the localization problem is generally entangled with the time synchronization problem, if ToA or TDoA are employed. Therefore, the optimization problem is complicated and non-convex. Based on the ToA measurements, the ML estimator is reported to achieves the CRLB at the cost of expensive computation; therefore, a more efficient sub-optimal LS estimator is presented in [1]. In [1], the uncertainties of anchors' clock and location information are also considered. The CRLBs for both the accurate and inaccurate anchor information are derived. In [17], the sequential time-synchronization and localization (STSL) algorithm was proposed, in which an AUV served as the mobile anchor. The

AUV was assumed to be static during a short period of time due to its low speed, which makes time synchronization easier. This method has two problems: first, extra estimation error is introduced by assuming the AUV is static in a short period of time; second, according to the simulation results, it converges slowly.

2.2.4 Continuous Active Sonar

After time synchronization and localization, the WSNs can be used for target detection and localization in the surveillance area. Such targets include icebergs, whales, leaked oil, etc. These targets are silent, and the network needs to work in the proactive mode. To be specific, some nodes will periodically broadcast probe signals, which will hit the targets, get reflected and received by the other nodes. Depending on the target's position and velocity, the received signals will have specific Doppler shift and propagation delay, by measuring which, we can estimate the target's distance and radial velocity.

For such systems, the probe signals should be carefully chosen. Conventionally, short pulse signals with low duty cycles are used as the probe signals. For such systems, the operator only has one detection opportunity for every cycle, which is generally designed to be very long to detect objects far away from the network. The use of short pulses was inevitable in the past because the sonar systems had limited dynamic range, which forced the transmitted signal to have a steady envelop. However, the state-of-the-art sonar systems have much larger dynamic ranges, and the duty cycle is no longer severely limited, which makes it possible to implement the continuous active sonar (CAS).

In CAS, probe signals with very high duty cycle will be used for target detection. Compared with the pulsed active sonar, the CAS has the following advantages.

(1) CAS has larger detection probabilities. For underwater objects, especially large size objects, glint noise is a big problem. Because of glint noise, the strength of the reflected signal varies with time, and is mostly weak. As a result, the pulsed signals have a large miss rate.

(2) CAS suppresses false alarm rate. In shallow waters, there are many unstable reflections. Pulsed active sonar cannot filter these components, while CAS can average them out through time diversity.

(3) CAS can improve tracking performance. Due to the low duty cycle, pulsed active sonar cannot provide continuous information with respect to the target, which leads to target ambiguity.

(4) CAS works at much lower power, which is environmentally friendly. The negative impact of active sonar on underwater animals can be minimized, because the signal strength is at the ambient noise level.

In [67], the authors employed CAS for target localization by jointly estimating target's distance and DoA. To be specific, the localization result is the coordinate that maximizes the likelihood function of the ToA and DoA measurements. In [43], joint estimation of target's velocity and position was considered. In [68], experiment was conducted to show that the CAS can achieve much better performance at lower SNR, compared with the conventional systems.

For CAS, the linear frequency modulated (LFM) signals are preferred, because they achieve great balance between time and frequency domain resolutions, allowing the simultaneous estimation of both target's distance and radial velocity. LFM signals have

time-variant spectrums, and we cannot use the conventional Fourier transform to analyze the spectrum of the received signals. Instead, the Wigner distribution should be computed to accurately estimate the initial frequency and the frequency rate of the received signal. However, this involves very high computational complexity, leading to the difficulty of real-time signal processing. In [69], LFM signals are used for probing, and a band of lag-Doppler filters are used for joint estimation of delay and Doppler shift. The filters are designed based on uniform sampling in velocity and distance. However, it is not self-adaptive. Fortunately, the surge of the Fractional Fourier Transform (FrFT) provides us an alternative [70, 71]. To be specific, the authors showed that the FrFT of a given signal corresponds to a rotation in the Wigner distribution [70]. To reduce the complexity of the FrFT, two fast discrete FrFT algorithms were presented in [71].

When the LFM signal transmitted by a node hits the target, gets reflected and received by another node, the receiver will receive another LFM signal, with different initial frequency and frequency rate. These parameters are dependent on the target's distance and radial velocity. The receiving node will then conduct the FrFT, and we will get the two dimensional spectrum of the received signal. For a LFM signal, we can always find a peak in the spectrum, and its position is dependent on the initial frequency and frequency rate. Therefore, we can estimate the target's distance and radial velocity with respect to the receiving node. With enough receiving nodes, we can then estimate the target's location and velocity.

2.3 Introduction to Massive MIMO

In wireless data transmission, due to the limited energy and bandwidth, efficiency is as important as robustness. During the past decade, we have seen great progress in wireless communication techniques in the 5G cellular systems. Among them, the massive MIMO technique shows great potential in improving spectral and energy efficiency simultaneously. In this part, we will briefly introduce the background, system model, and the pilot contamination issue of massive MIMO systems.

2.3.1 Background

In 2010, Thomas L. Marzetta proposed a new architecture for cellular networks, which is often referred to as massive MIMO or large-scale MIMO [72]. This new framework draws so much attention since being proposed because it casts light on two fundamental problems of wireless communications, namely spectral efficiency and power efficiency. To understand the revolutionary merit of this new technology, we need to briefly review its predecessor, the traditional multi-user MIMO (MU-MIMO). In LTE-A, as many as 8 antennas are deployed at a BS to simultaneously serve two single antenna terminals through SDMA (Space Division Multiple Access), while there are typically tens of users in one cell. Therefore, SDMA needs to coexist with OFDMA (Orthogonal Frequency Division Multiple Access) in the traditional MU-MIMO systems.

Compared with its predecessor, the major upgrade of massive MIMO is the dramatic increase of antenna number at BSs. This change seems trivial but it can actually boost system capacity by orders of magnitude. The secret is that massive MIMO totally discards

OFDMA and is able to serve all users in one cell through SDMA. In other words, every terminal is free to employ all the time-frequency resources for data transmission, instead of sharing them with its peers. Apart from much higher spectral efficiency, the expansion of antenna array at BSs also brings the following advantages. First, resource allocation can be simplified to great extent. Second, uplink signal detection and downlink precoding become much easier because the channel vectors of different users are asymptotically orthogonal. Third, fast fading and random noise can be averaged out through array signal processing. Last but not the least, because of the great power gain of the BS antenna array, cheap power amplifiers working at the milli-Watt level can be employed [73, 74].

The TDD (Time Division Duplex) protocol is widely used in massive MIMO to separate the up-link and down-link data. The communication protocol consists of four phases: 1) up-link transmission of pilot sequences; 2) channel estimation at BSs; 3) up-link data transmission; 4) down-link data transmission. Generally, TDD is favored over FDD (Frequency Division Duplex), because it allows us to only estimate up-link channel and obtain the down-link one through channel reciprocity, supported by practical measurements [75]. It is important to avoid down-link channel estimation, since the communication resources required for that are proportional to the number of antennas at BSs.

Massive MIMO promises many advantages over the conventional MU-MIMO, but to fully exploit these potentials, accurate CSI (Channel State Information) is indispensable. However, channel estimation for massive MIMO is more challenging due to the large antenna array and the aggressive spatial multiplexing. There are many issues to be addressed, and the pilot contamination is perceived as a major one. We will briefly explain this issue in the following section.

2.3.2 System Model and Pilot Contamination

Similar to the traditional multi-user MIMO systems, accurate CSI is indispensable for massive MIMO systems. Generally, orthogonal pilot sequences are assigned to users in the same cell and intra-cell interference can be totally eliminated. However, the limited pilot sequences must be reused in adjacent cells. Therefore, users sharing the same pilot sequence will interfere with each other in the process of channel estimation and this phenomenon is referred to as pilot contamination, which puts a fundamental limit on the capacity of massive MIMO systems [72].

To understand the pilot contamination issue, we need to first introduce the system model. In massive MIMO systems, hundreds of antennas are installed at the BS to serve tens of users. Generally, the antenna array at the BS can be in various forms, e.g., linear, rectangular or even cylindrical. However, to maximize the angular domain resolution, linear arrays are preferred. Suppose M antennas are linearly placed at the BS and the distance between any two adjacent antenna elements is equal to half the carrier wavelength [76]. Given that the number of detectable paths between a user and the BS is B, the channel model will be [76]:

$$\mathbf{h} = \sum_{b=1}^{B} \sqrt{\rho_b}\mathbf{e}[\omega_b]e^{j\phi_b}, \tag{2.9}$$

where ϕ_b and $\mathbf{e}[\omega_b]$ denote the random phase delay and spatial signature of the b-th path, respectively. Using θ_b to denote the angle of arrival of the b-th path, we have $\omega_b = \pi \cos\theta_b$, and $\mathbf{e}[\omega_b]$ is given by [76] as

$$\mathbf{e}[\omega_b] = \frac{1}{\sqrt{M}} \cdot [1, \exp(-j\omega_b), \cdots, \exp(-j(M-1)\omega_b)]^T. \tag{2.10}$$

ρ_b is the slow fading factor of the b-th path, caused by propagation attenuation and shad-

owing, given by

$$\rho_b = \frac{s_b}{d^\gamma}, \tag{2.11}$$

where s_b is a log-normal random variable, i.e., $10\lg s_b \sim \mathcal{N}(0, \sigma^2_{shad})$. γ is the path-loss exponent and d represents the distance between the user and the BS. This model is widely adopted in massive MIMO related literatures [77–80].

Assume that the user number per cell is K and the pilot length is τ, in order to avoid intra-cell interference, users in the same cell should be assigned orthogonal pilot sequences, which demands $\tau \geq K$. Suppose we have L cells in the area of interest, and K orthogonal pilot sequences are fully reused in all cells, the received pilot signal at the l-th BS will be

$$\mathbf{Y}^{(l)} = \mathbf{H}_l^{(l)}\mathbf{P}^T + \sum_{l' \neq l} \mathbf{H}_{l'}^{(l)}\mathbf{P}^T + \mathbf{N}, \tag{2.12}$$

where $\mathbf{P} = [\mathbf{p}_1, \mathbf{p}_2, \cdots, \mathbf{p}_K]$, and $\mathbf{p}_k$ is the k-th pilot sequence. The elements in $\mathbf{N} \in \mathbb{C}^{M\times\tau}$ are independently and identically distributed (i.i.d.) zero-mean complex Gaussian noise, with a variance of σ_n^2. $\mathbf{H}_{l'}^{(l)} \in \mathbb{C}^{M\times K}$ is the channel matrix between the users in cell l' and the BS in cell l. With MF, the channel estimate of the l-th cell will be

$$\hat{\mathbf{H}}_{mf}^{(l)} = \mathbf{Y}^{(l)}\mathbf{P}^*/\tau = \mathbf{H}_l^{(l)} + \sum_{l' \neq l} \mathbf{H}_{l'}^{(l)} + \mathbf{N}\mathbf{P}^*/\tau, \tag{2.13}$$

where we implicitly use the fact that $\mathbf{P}^H\mathbf{P} = \tau \cdot \mathbf{I}_K$, due to the orthogonality of different pilot sequences. For the k-th user in the l-th cell, the MF-based channel estimate will be

$$\hat{\mathbf{h}}_{mf}^{(l,k)} = \mathbf{h}_{l,k}^{(l)} + \sum_{l' \neq l} \mathbf{h}_{l',k}^{(l)} + \mathbf{n}_k, \tag{2.14}$$

where $\mathbf{n}_k = \mathbf{N}\mathbf{p}_k^*/\tau$. As we can observe in (2.14), the MF-based channel estimate consists of three components. The first and last parts are the desired channel information and noise,

respectively, while the middle part contains interference from other cells due to pilot reuse, i.e., pilot contamination. The contaminated channel estimate will then introduces strong inter-cell interference during the data transmission.

In [81], the authors derived a closed-form achievable rate for TDD massive MIMO systems under the impact of pilot contamination. For cell-edge users, this problem is particularly detrimental, because their signal strength is comparable to the peer users in adjacent cells.

2.3.3 Pilot Decontamination Methods

To tackle the pilot contamination issue, many solutions have been proposed [78–80, 82–91]. Generally speaking, pilot decontamination strategies can be divided into four categories [92], and we will summarize them in the following paragraphs.

The first choice is to create more orthogonal pilot sequences. This can be done in time domain by increasing the length of pilot sequences, or in frequency domain by reducing the frequency reuse factor [72]. In [93], the authors employed a pilot length seven times the number of users per cell, so as to guarantee pilot orthogonality among users in adjacent cells. Because adjacent cell users are the major interfering sources, such methods can suppress pilot contamination to the great extent. However, spectral efficiency will decrease due to the increased length of pilots in time or frequency domain. To reduce the overhead, the authors proposed a time-shifted pilot scheme in [84]. In this method, when users in a specific cell are transmitting pilot sequences, all the adjacent cell users are at the phase of downlink data transmission or processing. By doing so, pilot contamination is no longer an issue, but inter-cell interference might get stronger as cell-edge users will experience strong

interferences from the BSs in adjacent cells during the pilot transmission phase. Channel estimation will have to be conducted under a lower SINR (Signal to Interference and Noise Ratio).

The second way of pilot decontamination is to identify the subspace of the desired signals by utilizing the statistics of the CSI and the received signals. For example, eigenvalue decomposition (EVD) is employed for channel estimation in [94], where the authors proved that every channel vector is an eigenvector of the covariance matrix of the received signals when the BS antenna number is sufficiently large. The idea was further developed in [87], where the authors proposed to obtain the subspace of the channel vectors through singular value decomposition (SVD) of the received signal matrix. Pilot contamination can then be eliminated by projecting the received signal onto this subspace. However, the efficacy of these methods is based on the assumption that the desired signals are always stronger than the pilot contamination, which can not be guaranteed for cell-edge users. When the received signals are sparse in space, there is another possible solution for pilot decontamination as proposed in [79] and [95]. In [79], the authors showed that the minimum mean square error (MMSE) estimator can completely eliminate the pilot contamination, given that the angle spreads of the desired and interfering users do not overlap. Therefore, the same pilot sequence should be assigned to those users with minimum overlap in the angular domain. In [95], based on the assumption that the desired signals are generally stronger than the pilot contamination, the authors utilized both angular and power domain discriminations for pilot decontamination.

In the third type of pilot decontamination methods, both data and pilot are employed for channel estimation [86, 91]. Because data is generally longer than the pilot, even when

users are sharing the same pilot sequence, their data are still asymptotically orthogonal. Therefore, the decoded data, in spite of being only partially correct, can be used to suppress pilot contamination and improve channel estimation accuracy.

The last strategy is referred to as pilot contamination precoding (PCP) [89, 90, 96]. Different from the other three methods where different cells work almost independently, PCP is dependent on multi-cell cooperation. The basic idea is to add a precoding and decoding layer among adjacent cells. Pilot contamination can be completely eliminated given that the BS antenna number approaches infinity. The price of the PCP algorithms is the overhead of the CSI exchange among the BSs. It might be a problem for 5G networks where the large user population, high data rate and low latency requirements exist.

2.4 Introduction to Millimeter Wave Communications

2.4.1 Background

The popularity of smart phones have been growing rapidly over the past decade. Currently, our cellular system works on 2 GHz frequency band, which is a very crowded. To be specific, many different communication protocols work on this frequency, including Bluetooth, WiFi, and ZigBee. As a result, researchers propose to move our cellular system to higher frequency band, ranging from 20 to 60 GHz, whose wave length is at the level of several millimeters [97]. As a result, this new technology is referred to as millimeter wave communications [98–100].

Different from most of the new technologies, millimeter wave communication is not trying to improve the utilization of the available bandwidth, but to explore more unoccupied

frequency resources. Besides, when combined with the massive MIMO technology, high spectral efficiency can still be obtained on millimeter wave band [101]. However, millimeter wave signals experience severe attenuations due to the very high frequency. To overcome this issue, massive MIMO is generally viewed as a promising solution. Specifically, the large antenna arrays at BSs can boost the equivalent isotropically radiated power through beamforming. Besides, users can work at the same time-frequency resources through space division multiple access, which improves spectral efficiency. The combination of millimeter wave and massive MIMO shows promising potentials. Nonetheless, accurate CSI is indispensable for this purpose. In fact, the channel estimation in millimeter wave massive MIMO communications is very challenging, which can be attributed to the considerable consumption of the time-frequency and hardware resources. In the following section, we briefly overview the current work in this area.

2.4.2 Channel Estimation for Millimeter Wave Communications

In the conventional fully digital antenna arrays, one RF chain is required for each antenna to control the amplitude and phase of the transmitted signal. In [102], the authors proposed an efficient beam alignment scheme. By employing a hierarchical codebook, the searching space can be narrowed down very fast. In [103], they authors further refined the codebook in [102] by allowing the searching beams to overlap, which further reduced the overhead. However, this kind of approaches demand a huge amount of RF chains. Besides, due to the large physical dimension of the antenna arrays at BSs, vibration and movement of beams caused by wind are inevitable. As a result, the beam alignment should be frequently executed. In [104], the authors jointly estimated the channels of multiple users in the same cell,

and the channel estimation issue was modeled as a tensor decomposition problem. For this purpose, a layered pilot transmission scheme was proposed, in which a much shorter training sequence was required. However, this method only worked in high SNR regime, and thus was not suitable for millimeter wave frequencies. According to the channel measurement results [97, 105], the millimeter wave channels are generally sparse in angle domain, which means the channel estimation can be conducted by estimating the direction and the corresponding gain of each path [103,106–110]. A class of compressed sensing based channel estimation schemes were studied in [103, 107, 110], where the spatial sparsity was exploited. However, as has been pointed out in [103, 107], a communication link between the BS and the mobile user is demanded, which hinders it from practical applications. By noticing that path angles vary much slower than path gains, the authors in [108] proposed a two-stage channel estimation algorithm. The path angles were estimated through the multiple signal classification (MUSIC) method in the first stage, while the gains of individual paths were estimated by the least square method in the second stage. The MUSIC method was also utilized in [109], where a channel subspace matching pursuit (CSMP) algorithm was proposed to reduce the overhead of channel estimation. Also based on the idea of separating the estimation of the direction and gain, the authors in [106] introduced the operation of spatial rotation for channel estimation, which significantly reduced the number of RF chains required in the system while maintained near-optimal system performance. This idea was further developed in [111], where the authors showed that non-orthogonal angle division multiple access is possible for multiple users. Considering the hardware cost and the energy consumption at receivers, low-resolution analog-to-digital converters (ADCs) are preferred in millimeter wave massive MIMO systems. The authors in [112] studied the

channel estimation with few-bits ADCs. They showed that the performance of 4-bit ADCs was comparable to that of infinite-bit ADCs. Noting that millimeter wave channels were clustered in the angle of arrival/departure and delay (AoA-AoD-delay) domain, the authors in [113] proposed the approximate message passing (AMP) with nearest neighbor pattern learning algorithm to exploit the cluster structure, hence improving channel estimation accuracy.

To reduce the channel estimation overhead, a possible choice is channel tracking. The basic idea is that the channel parameters do not vary fast in mmWave channels, and we can use a small number of training symbols to update the CSI. The fundamental reason that makes channel tracking possible is the channel sparsity in space. In the following section, we will analyze the spatial sparsity of the mmWave channels.

2.4.3 The Spatial Sparsity

In this part, we will conduct the discussion based on linear antenna arrays, due to the simplicity. Suppose the user equipment transmits a symbol x to the BS, and M antennas are installed at the BS. Consider the LoS scenario, the received signal at the BS is given by

$$\mathbf{y} = x\sqrt{\rho_s}e^{j\phi}\mathbf{e}[\omega_{\mathrm{s}}] + \mathbf{n}, \tag{2.15}$$

where $\mathbf{e}[\omega_{\mathrm{s}}]$ is the spatial signature of the received signal (given in (2.10)), ϕ is a random phase delay, and $\mathbf{n}$ represents noise component. The *spatial spectrum* of the received signal can be defined as

$$Y(\omega) = \mathbf{e}[\omega]^H\mathbf{y} = x\sqrt{\rho_s}e^{j\phi}\mathbf{e}[\omega]^H\mathbf{e}[\omega_{\mathrm{s}}] + \mathbf{e}[\omega]^H\mathbf{n}. \tag{2.16}$$

From another perspective,

$$Y(\omega) = \mathbf{e}[\omega]^H \mathbf{y} = \frac{1}{\sqrt{M}} \sum_{m=1}^{M} \mathbf{y}[m] e^{jm\omega} = \text{IDTFT}\,[\,\mathbf{y}\,], \tag{2.17}$$

where IDTFT is short for inverse discrete time Fourier transform. From (2.16), we can see that it is important to figure out how the envelope of $\mathbf{e}[\omega]^H \mathbf{e}[\omega_s]$ varies with ω.

Let $f(\Delta\omega) \coloneqq \mathbf{e}[\omega_1]^H \mathbf{e}[\omega_2]\,(\forall\, \omega_1, \omega_2 \in [0, 2\pi))$, where $\Delta\omega = \omega_2 - \omega_1$, and we have

$$f(\Delta\omega) = \frac{\sin \frac{M\Delta\omega}{2}}{M \sin \frac{\Delta\omega}{2}} \cdot e^{-j(M-1)\Delta\omega/2}. \tag{2.18}$$

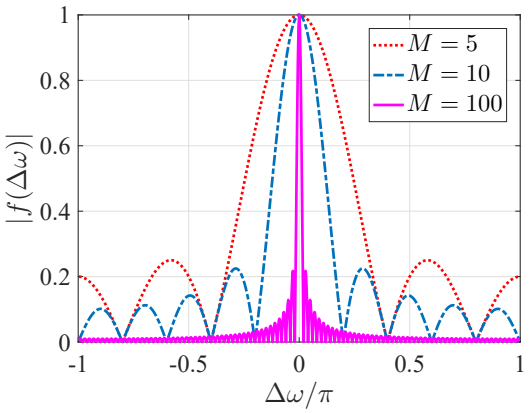

Figure 2.1: The absolute value of $f(\Delta\omega)$ for different M.

Figure 2.1 shows the numerical results of $|f(\Delta\omega)|$ for different M. From the figure, the main lobe of $|f(\Delta\omega)|$ is centered at 0, with a width of $4\pi/M$. For massive MIMO systems, M is generally very large, and most energy concentrates on a small angle spread. Therefore, interference and the desired signals are generally well separated in space (i.e., the *main lobes* of signal and interference do not overlap). In this case, a spatial filter can be constructed to filter out the main lobe of interference while maintain most energy of

the desired signals.

Similar to the time domain signal processing, we can employ IDFT (Inverse Discrete Fourier Transform)[2] instead of IDTFT to analyze the spectrum of a target sequence, which is more suitable for the modern digital signal processors. To be specific, the discrete *spatial spectrum* of the received signal $\mathbf{y}$ is

$$\mathbf{y}_\omega = \mathrm{IDFT}\left[\,\mathbf{y}\,\right] = \mathbf{F}_M \mathbf{y}, \tag{2.19}$$

where $\mathbf{F}_M \coloneqq \left[\,\mathbf{e}\left[\,0\,\right], \mathbf{e}\left[\omega_0\right], \cdots, \mathbf{e}\left[(M-1)\omega_0\right]\,\right]^H$ and $\omega_0 = 2\pi/M$. As a result, $\mathbf{y}_\omega$ is the sampled version of $Y(\omega)$ in (2.17). An arbitrary spatial signature $\mathbf{e}[\omega]\,(\omega \in [0, 2\pi))$ can be decomposed as $\mathbf{e}[\omega] = \sum_{m=0}^{M-1} \alpha_m \mathbf{e}[m\omega_0]$, where α_m and its absolute value are given by

$$\alpha_m = \mathbf{e}[m\omega_0]^H \mathbf{e}[\omega] \text{ and } |\alpha_m| = \frac{1}{M}\left|\frac{\sin\frac{M}{2}(\omega - m\omega_0)}{\sin\frac{1}{2}(\omega - m\omega_0)}\right|. \tag{2.20}$$

There exists an integer $l \in [0, M-1]$, which guarantees $\omega/\omega_0 \in [l,\, l+1)$. Therefore, we can write ω as $\omega = (l+\beta)\omega_0$ $(0 \le \beta < 1)$. Based on these definitions, we present the following theorem.

Theorem 1. *When M is infinitely large, more than 80% of the energy concentrates on $\mathbf{e}[l\omega_0]$ and $\mathbf{e}[(l+1)\omega_0]$. To be specific, $\lim\limits_{M\to\infty} |\alpha_l|^2 + |\alpha_{l+1}|^2 \ge 8/\pi^2$ and the equality holds when $\beta = 0.5$.*

Proof. When $\beta = 0$, we have $\omega = l\omega_0$, leading to $|\alpha_l|^2 + |\alpha_{l+1}|^2 = |f(0)|^2 + |f(\omega_0)|^2 = 1$. When

[2]It should be noted that we can employ the fast Fourier transform (FFT) to reduce computational complexity.

$\beta \neq 0$, the limit of $|\alpha_l|^2 + |\alpha_{l+1}|^2$ can be derived as follows.

$$\begin{aligned}\lim_{M\to\infty} |\alpha_l|^2 + |\alpha_{l+1}|^2 &= \lim_{M\to\infty} |f(\beta\omega_0)|^2 + |f(\omega_0 - \beta\omega_0)|^2 \\ &= \frac{\sin^2 \beta\pi}{\pi^2}\left[\frac{1}{\beta^2} + \frac{1}{(1-\beta)^2}\right].\end{aligned}$$

Define $R(\beta) = \frac{\sin^2 \beta\pi}{\pi^2}\left[\frac{1}{\beta^2} + \frac{1}{(1-\beta)^2}\right] (\beta \in (0,1))$ and the numerical results show that $R(\beta)$ is a convex function. Noticing that $\frac{dR(\beta)}{d\beta}\Big|_{\beta=0.5} = 0$, we can conclude that $R(\beta)$ has a minimum at $\beta = 0.5$, and $R(0.5) = 8/\pi^2$. □

Theorem 1 shows that most energy of the received signal from a specific direction concentrates on the two samples in the main lobe. As a result, if we use $\alpha_l \mathbf{e}[l\omega_0] + \alpha_{l+1}\mathbf{e}[(l+1)\omega_0]$ to approximate $\mathbf{e}[\omega]$, the residual error will be smaller than 20%. Generally, if we take the closest $2R$ components to re-establish $\mathbf{e}[\omega]$, the residual error can be defined as

$$Res[\,R\,] = 1 - \sum_{r=1}^{R} |\alpha_{mod_M(l+1-r)}|^2 + |\alpha_{mod_M(l+r)}|^2, \tag{2.21}$$

where $mod_M(k) = \mathrm{mod}(k, M)$. Then, the residual error is upper bounded by

$$Res[\,R] \leq \frac{\pi^2}{12} + \frac{1}{4R^2} - \sum_{r=1}^{R} \frac{1}{2r^2}, \tag{2.22}$$

which is justified in Appendix D.1.

The above analyses show that the discrete spatial spectrum of the desired signal is *sparse*, and most energy of the received signal concentrates on narrow angle spreads. Due to the spatial sparsity, efficient algorithms can be designed for channel estimation and channel tracking, as we will see in later discussions.

2.5 Summary

In this chapter, we reviewed some existing work in terrestrial and underwater localization techniques, and introduced the fundamentals of massive MIMO and mmWave communications. Specifically, we showed the deficiencies of the conventional RSS-ranging based localization system, the challenges of ToA-based underwater localization, the pilot contamination in massive MIMO systems, and the spatial sparsity in mmWave channels. In the remaining part of this thesis, we will present new algorithms and architectures for more accurate localization and channel estimation in mobile node-aided WSNs.

Chapter 3

Drone-Assisted Zero-Configuration Localization Framework

From the discussions in section 2.1.3, we can see that the positioning framework based on fixed anchors has some deficiencies. Fortunately, the surge of small consumer drones provide us with another possible solution. Recently, drones have been applied in many areas, such as photography, radar imaging [6], telepresence platform [7], and even express delivery [8]. In [9, 10], the energy efficiency and throughput of drone-assisted WSNs are discussed. Drones provide a favorable platform for many applications because they are affordable, agile and versatile. Taking the newest DJI INSPIRE 2 as example, each of the four rotors can provide a thrust of two kilograms, and we can install all kinds of sensors on it conveniently [11].

For localization systems, we can employ a drone as a mobile anchor. The drone hovers over the WSN and serves as virtual anchors. For every broadcast period, the drone broad-

casts its position information, and the target node can measure the RSS value and build a equation with respect to the unknowns. At the target node side, both channel parameters and the nodes' position are viewed as unknowns. Consider 2D localization, after four or more periods, the node will have enough data to localize itself.

Compared with the conventional framework, the drone-assisted one has three major advantages.

a) The density of virtual anchors can be boosted vastly, while the increased cost is negligible, which makes the new framework not only more accurate but also far more stable.

b) The offline configuration such as channel estimation in conventional system is avoided.

c) The central node in conventional system is not required and the communication load among nodes is minimized; therefore, the communication resources such as energy and bandwidth can be saved.

To justify the superiority of this new framework, extensive analysis and simulations will be conducted in this chapter. Besides, it has been implemented on a drone for field experiments, and the results are promising. [1]

[1]The major work in this chapter has been published in [J19]: Z. Gong, C. Li, F. Jiang, R. Su et al., "Design, Analysis, and Field Testing of an Innovative Drone-Assisted Zero-Configuration Localization Framework for Wireless Sensor Networks," *IEEE Trans. Veh. Technol.*, vol. 66, no. 11, pp. 10322-10335, Nov. 2017.

3.1 System Model of the Drone-Assisted Framework

With a drone, the new localization framework is depicted in Figure 3.1. The target node is

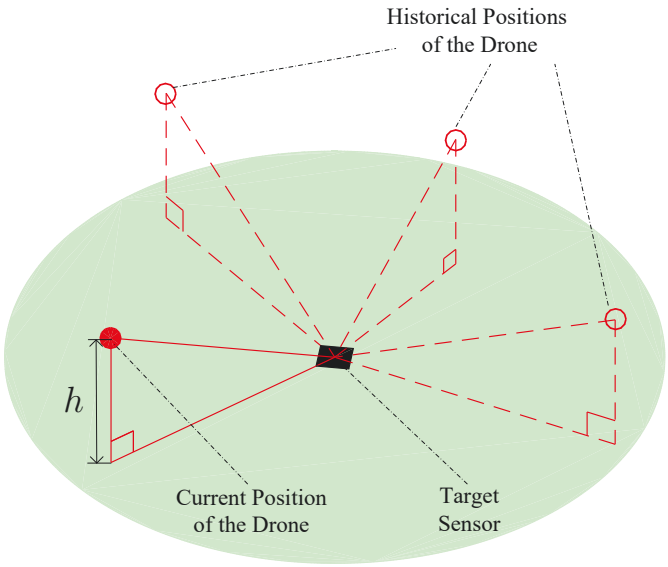

Figure 3.1: Framework of the drone-assisted localization system.

represented by a black square, and the colored disk denotes its communication range. The drone hovers over the target node at the hight of h, and moves from one position to another. The current position of the drone is denoted by a solid disk while its historical positions are denoted by hollow circles. At each position, the drone gets its position information from the onboard GPS chip and broadcasts its 3-dimensional coordinates, serving as one virtual anchor. As it moves around, many virtual anchors can be obtained.

With coordinate and RSS measurement of the i-th virtual anchor, the following equation

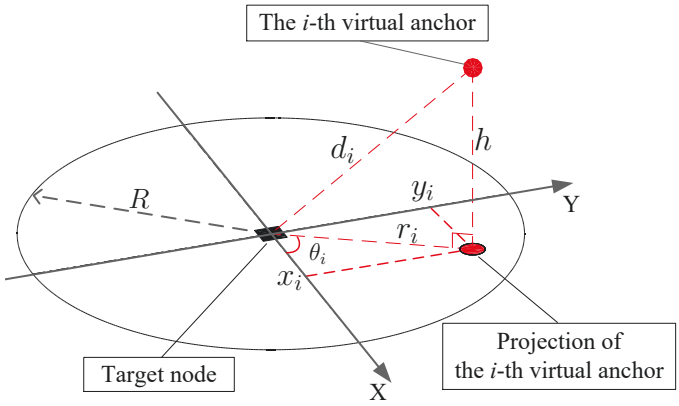

Figure 3.2: Geometrical model.

can be established according to the path-loss propagation model:

$$f_i(x, y, P_0, \beta) = P_0 - \beta \cdot \ln(d_i) = P_i, \tag{3.1}$$

where $d_i^2 = (x - x_i)^2 + (y - y_i)^2 + h^2$. P_i and (x_i, y_i) denote the RSS and 2D position of the drone. The geometrical meanings of these variables are illustrated in Figure 3.2.

As we can see from Equation (3.1), four unknowns are involved, i.e., the two-dimensional coordinate of the target node (x, y) and the channel parameters (P_0, β). Theoretically, with messages from four or more virtual anchors, the target node can localize itself. It is worth noting that this method actually circumvents the process of channel estimation and ranging. Therefore, the defects of the conventional localization framework are eliminated.

Rewriting Equation (3.1) in matrix format, we have

$$\boldsymbol{f}(\mathbf{x}) = \mathbf{P}, \tag{3.2}$$

where $\mathbf{P} = [\, P_1, P_2, \cdots, P_N \,]^T$ denotes the measured RSS vector, $\mathbf{x} = [\, x, y, P_0, \beta \,]^T$ stands for unknown parameters, $\boldsymbol{f}(\mathbf{x}) = [f_1(\mathbf{x}), f_2(\mathbf{x}), \cdots, f_N(\mathbf{x})]^T$, and N is the number of virtual

anchors.

3.2 Newton Iteration Algorithm

We use the Newton iteration method to solve the problem in (3.2). To begin with, the corresponding differential equation of Equation (3.2) is given by

$$\Delta \mathbf{P} = \mathbf{F} \cdot \Delta \mathbf{x}, \tag{3.3}$$

where $\mathbf{F}$ is the gradient of $\boldsymbol{f}(\mathbf{x})$ with respect to $\mathbf{x}$ given by

$$\mathbf{F} = \nabla \boldsymbol{f}(\mathbf{x}) = \begin{bmatrix} \frac{\beta(x_1-x)}{d_1^2} & \frac{\beta(y_1-y)}{d_1^2} & 1 & -\ln(d_1) \\ \frac{\beta(x_2-x)}{d_2^2} & \frac{\beta(y_2-y)}{d_2^2} & 1 & -\ln(d_2) \\ \vdots & \vdots & \vdots & \vdots \\ \frac{\beta(x_N-x)}{d_N^2} & \frac{\beta(y_N-y)}{d_N^2} & 1 & -\ln(d_N) \end{bmatrix}. \tag{3.4}$$

Assume the initial estimation of $\mathbf{x}$ is $\mathbf{x}^{(0)}$, and details of Newton iteration method are shown in Algorithm 1.

Algorithm 1 Newton iteration method for Equation (3.2).

Require:

Measured RSS vector, $\mathbf{P}$;

Drone's positions, (x_i, y_i)'s;

Ensure:

Estimation of $\mathbf{x}$, $\hat{\mathbf{x}}$;

1: The initial value of $\mathbf{x}$ is $\mathbf{x}^{(0)}$;

The initialized iteration counter, $k = 0$;

The maximum iteration number, k_{max};

The iteration threshold $TS = 0.1$, $|\Delta\mathbf{x}| = 2TS$;

2: **while** $|\Delta\mathbf{x}| > TS$ **and** $k < k_{max}$ **do**

3: $\Delta\mathbf{P} = \mathbf{P} - \boldsymbol{f}(\mathbf{x}^{(k)})$;

4: $\mathbf{F} = \nabla \boldsymbol{f}(\mathbf{x})|_{\mathbf{x}=\mathbf{x}^{(k)}}$;

5: $\Delta\mathbf{x} = (\mathbf{F}^T\mathbf{F})^{-1}\mathbf{F}^T\Delta\mathbf{P}$;

6: $\mathbf{x}^{(k+1)} = \mathbf{x}^{(k)} + \Delta\mathbf{x}$;

$k = k + 1$;

7: **end while**

8: $\hat{\mathbf{x}} = \mathbf{x}^{(k)}$

9: **return** $\hat{\mathbf{x}}$;

3.3 Positioning Error Analysis and CRLB

In spite of the advantages of the new framework, it cannot provide absolutely accurate localization results, because errors in RSS measurements are inevitable. Suppose the measurement error of RSS is independently and identically distributed (i.i.d.) [37, 43, 44], and we can denote the measurement errors as a zero-mean Gaussian vector $\boldsymbol{\varepsilon}_{\mathbf{P}}$, which satisfies $E\left\{\boldsymbol{\varepsilon}_{\mathbf{P}}\boldsymbol{\varepsilon}_{\mathbf{P}}^T\right\} = \sigma_n^2\mathbf{I}_N$, and $\mathbf{I}_N$ represents an identity matrix of order N. In the remaining part of this section, the positioning error of the proposed system will be analyzed, and the CRLB will be derived.

3.3.1 Positioning Error Analysis

By taking the first order Taylor expansion, estimation error $\boldsymbol{\varepsilon}_{\mathbf{x}}$ can be approximated as

$$\boldsymbol{\varepsilon}_{\mathbf{x}} = \hat{\mathbf{x}} - \mathbf{x} = \left(\mathbf{F}^T\mathbf{F}\right)^{-1}\mathbf{F}^T\boldsymbol{\varepsilon}_{\mathbf{P}}. \tag{3.5}$$

This approximation is accurate when σ_n^2 is relatively small. The covariance matrix of $\hat{\mathbf{x}}$ can then be derived as

$$\operatorname{cov}\{\hat{\mathbf{x}}, \hat{\mathbf{x}}\} = E\left\{\boldsymbol{\varepsilon}_{\mathbf{x}}\boldsymbol{\varepsilon}_{\mathbf{x}}^T\right\} = \sigma_n^2 \cdot (\mathbf{F}^T\mathbf{F})^{-1}. \tag{3.6}$$

Rewriting $\hat{\mathbf{x}}$ as $\hat{\mathbf{x}} = [\hat{\mathbf{x}}_1^T, \hat{\mathbf{x}}_2^T]^T$, where $\hat{\mathbf{x}}_1 = [\hat{x}, \hat{y}]^T$, and $\hat{\mathbf{x}}_2 = [\hat{P}_0, \hat{\beta}]^T$, it is clear that $\hat{\mathbf{x}}_1$ denotes the estimation of the target's coordinate, while $\hat{\mathbf{x}}_2$ denotes the estimation of channel parameters. In addition, Equation (3.6) can be rewritten as

$$\operatorname{cov}\{\hat{\mathbf{x}}, \hat{\mathbf{x}}\} = \begin{bmatrix} \operatorname{cov}\{\hat{\mathbf{x}}_1, \hat{\mathbf{x}}_1\} & \operatorname{cov}\{\hat{\mathbf{x}}_1, \hat{\mathbf{x}}_2\} \\ \operatorname{cov}\{\hat{\mathbf{x}}_2, \hat{\mathbf{x}}_1\} & \operatorname{cov}\{\hat{\mathbf{x}}_2, \hat{\mathbf{x}}_2\} \end{bmatrix}. \tag{3.7}$$

The variance of the positioning error is given by $\sigma_p^2 = E\{(\hat{x}-x)^2+(\hat{y}-y)^2\} = tr\{\mathrm{cov}\{\hat{\mathbf{x}}_1, \hat{\mathbf{x}}_1\}\}$. Based on Equations (3.6) and (3.7), we can obtain

$$\sigma_p^2 = \sigma_n^2 \cdot \mathrm{tr}\left\{\left[(\mathbf{F}^T\mathbf{F})^{-1}\right]_{2\times 2}\right\}. \tag{3.8}$$

According to Equation (3.4), it is clear that the trace of $\left[(\mathbf{F}^T\mathbf{F})^{-1}\right]_{2\times 2}$ is related to β^2. Besides, it is also determined by the number and geometrical distribution of virtual anchors, quantified as $GDOP$. However, it is difficult for us to fathom how $GDOP$ varies with matrix $\mathbf{F}$ from Equation (3.8). To gain more insights, we can decompose matrix $\mathbf{F}$ as $\mathbf{F} = [\mathbf{F}_1, \mathbf{F}_2]$, where $\mathbf{F}_1$ contains the first two columns of $\mathbf{F}$ and $\mathbf{F}_2$ consists of the remaining parts. Then, the following equation can be obtained

$$\mathbf{F}^T\mathbf{F} = \begin{bmatrix} \mathbf{F}_1^T\mathbf{F}_1 & \mathbf{F}_1^T\mathbf{F}_2 \\ \mathbf{F}_2^T\mathbf{F}_1 & \mathbf{F}_2^T\mathbf{F}_2 \end{bmatrix}. \tag{3.9}$$

According to the *Block Matrix Inversion Theorem* [114] given below

$$\begin{bmatrix} \mathbf{A} & \mathbf{B} \\ \mathbf{B}^T & \mathbf{C} \end{bmatrix}^{-1} = \begin{bmatrix} (\mathbf{A}-\mathbf{B}\mathbf{C}^{-1}\mathbf{B}^T)^{-1} & -(\mathbf{A}-\mathbf{B}\mathbf{C}^{-1}\mathbf{B}^T)^{-1}\mathbf{B}\mathbf{C}^{-1} \\ -\mathbf{C}^{-1}\mathbf{B}^T(\mathbf{A}-\mathbf{B}\mathbf{C}^{-1}\mathbf{B}^T)^{-1} & (\mathbf{C}-\mathbf{B}^T\mathbf{A}^{-1}\mathbf{B})^{-1} \end{bmatrix}, \tag{3.10}$$

$[(\mathbf{F}^T\mathbf{F})^{-1}]_{2\times 2}$ can be rearranged as

$$\left[(\mathbf{F}^T\mathbf{F})^{-1}\right]_{2\times 2} = \left[\mathbf{F}_1^T\mathbf{F}_1 - \mathbf{F}_1^T\mathbf{F}_2\left(\mathbf{F}_2^T\mathbf{F}_2\right)^{-1}\mathbf{F}_2^T\mathbf{F}_1\right]^{-1}. \tag{3.11}$$

From Equation (3.4), we can see that $\mathbf{F}_1$ is proportional to β; therefore, we can ensure that the trace of $\left[(\mathbf{F}^T\mathbf{F})^{-1}\right]_{2\times 2}$ is inversely proportional to β^2. As a result, (3.11) can be rewritten as

$$\mathrm{tr}\left\{\left[(\mathbf{F}^T\mathbf{F})^{-1}\right]_{2\times 2}\right\} = GDOP/\beta^2. \tag{3.12}$$

Substituting (3.12) into (3.8), we have the variance of positioning error in our proposed framework as

$$\sigma_p^2 = GDOP \cdot \sigma_n^2/\beta^2. \tag{3.13}$$

Compared with Equation (2.3), we can see that positioning errors of these two systems are both proportional to their $GDOP$. In our scheme, the $GDOP$ can be much smaller than that of the conventional one because of having a much larger number of virtual anchors by using a drone. We will present some numerical results to support this claim in next section. Furthermore, we have the following inequality proved in [25]:

$$\sigma_n^2/\beta^2 < \exp\left(\frac{\sigma_n^2}{\beta^2 \cdot \ln 10}\right) - 1. \tag{3.14}$$

As a result, even with the same $GDOP$, the variance of the positioning error of the proposed scheme is still smaller than that in the conventional one. It is also worth noting that the positioning error in Equation (2.3) is obtained under the assumption of perfect channel parameters, which means the performance of the conventional system will be worse in practical scenarios.

3.3.2 CRLB Analysis

Assuming RSS observations are independent, their joint PDF conditioned on unknown parameters is given as

$$f_{\mathbf{P}|\mathbf{x}}(\mathbf{P}|\mathbf{x}) = \prod_{i=1}^{N} f_i(P_i|\mathbf{x}), \tag{3.15}$$

where the PDF of the i-th observation is

$$f_i(P_i|\mathbf{x}) = \frac{1}{\sqrt{2\pi\sigma_n^2}} \cdot \exp\left(-\frac{(P_i - \overline{P}_i)^2}{2\sigma_n^2}\right), \tag{3.16}$$

and $\overline{P}_i = E\{P_i\} = P_0 - \beta \cdot \ln d_i$. The logarithm of $f_{\mathbf{P}|\mathbf{x}}(\mathbf{P}|\mathbf{x})$ can be obtained as

$$l_{\mathbf{P}|\mathbf{x}}(\mathbf{P}|\mathbf{x}) = \ln f_{\mathbf{P}|\mathbf{x}}(\mathbf{P}|\mathbf{x}) = \sum_{i=1}^{N} l_i(P_i|\mathbf{x}), \tag{3.17}$$

where

$$l_i(P_i|\mathbf{x}) = \ln f_i(P_i|\mathbf{x}) = -\ln\sqrt{2\pi\sigma_n^2} - \frac{(P_i - \overline{P}_i)^2}{2\sigma_n^2}. \tag{3.18}$$

We then obtain the Fisher information matrix (FIM):

$$\mathbf{F}_{\mathbf{x}} = -E\left\{\nabla_{\mathbf{x}}(\nabla_{\mathbf{x}} l_{\mathbf{P}|\mathbf{x}}(\mathbf{P}|\mathbf{x}))^{\mathrm{T}}\right\} = \begin{bmatrix} f_{1,1} & \cdots & f_{1,4} \\ \vdots & \ddots & \vdots \\ f_{4,1} & \cdots & f_{4,4} \end{bmatrix}. \tag{3.19}$$

By representing $x,\ y,\ P_0,\ \beta$ with $u_1,\ u_2,\ u_3,\ u_4$ respectively, we can explicitly denote $f_{k,l}$ as

$$f_{k,l} = -E\left\{\frac{\partial^2 l_{\mathbf{P}|\mathbf{x}}(\mathbf{P}|\mathbf{x})}{\partial u_k \partial u_l}\right\} = -\sum_{i=1}^{N} E\left\{\frac{\partial^2 l_i(P_i|\mathbf{x})}{\partial u_k \partial u_l}\right\}. \tag{3.20}$$

Through tedious but straight-forward deduction, it can be proven that

$$\mathbf{F}_{\mathbf{x}} = \mathbf{F}^T\mathbf{F}/\sigma_n^2. \tag{3.21}$$

That is to say, with Algorithm 1, we can approximately achieve CRLB and the overall estimation error of the four parameters is minimized. Intuitively, trace of $[(\mathbf{F}_{\mathbf{x}})^{-1}]_{2\times 2}$ can be viewed as a reference of localization accuracy [31]. However, this is only true for unbiased estimators. The Newton iteration algorithm is not unbiased, and the positioning error can be smaller than the trace of $[(\mathbf{F}_{\mathbf{x}})^{-1}]_{2\times 2}$ in some scenarios, as will be shown in simulation results.

3.4 Increase the Quantity of Virtual Anchors

As has been mentioned, the most significant advantage of using a drone is that the number of virtual anchors can be vastly boosted at low cost. Therefore, a fundamental question is how the density of anchors contributes to the performance of the proposed system in terms of estimation error, positioning error, and computational complexity, which will be answered in this section.

3.4.1 Estimation Error Analysis

Suppose the original system has N virtual anchors, and its FIM is given by $\mathbf{F}_{\mathbf{x}}^{(N)} = \mathbf{F}_N^T \mathbf{F}_N / \sigma_n^2$ (obtained from Equation (3.21)). When we add another virtual anchor to the system, matrix $\mathbf{F}_N$ will be extended as $\mathbf{F}_{N+1} = \left[\mathbf{F}_N^T, \mathbf{f}\right]^T$, where $\mathbf{f}$ is given as

$$\mathbf{f} = \left[\frac{\beta(x_{N+1} - x)}{d_{N+1}^2}, \frac{\beta(y_{N+1} - y)}{d_{N+1}^2}, 1, -\ln(d_{N+1})\right]^T. \tag{3.22}$$

(x_{N+1}, y_{N+1}) and d_{N+1} are the 2-dimensional coordinates and distance of the new added virtual anchor. Accordingly, the updated FIM will be

$$\mathbf{F}_{\mathbf{x}}^{(N+1)} = \mathbf{F}_{N+1}^T \mathbf{F}_{N+1} / \sigma_n^2 = \mathbf{F}_{\mathbf{x}}^{(N)} + \mathbf{f}\mathbf{f}^T / \sigma_n^2. \tag{3.23}$$

Here, $\mathbf{f}^T\mathbf{f}$ is positive semidefinite since

$$\mathbf{y}^T \mathbf{f}\mathbf{f}^T \mathbf{y} = |\mathbf{y}^T \mathbf{f}|^2 \geq 0, \ \forall \mathbf{y} \in \mathcal{R}^{4\times 1}. \tag{3.24}$$

According to the matrix theory in [115], the k-th largest eigenvalue o f $\mathbf{F}_{\mathbf{x}}^{(N+1)}$, i.e., $\lambda_k(\mathbf{F}_{\mathbf{x}}^{(N+1)})$, is guaranteed to be no smaller than that of $\mathbf{F}_{\mathbf{x}}^{(N)}$, i.e., $\lambda_k(\mathbf{F}_{\mathbf{x}}^{(N)})$. In other words, we have

$$\lambda_k(\mathbf{F}_{\mathbf{x}}^{(N+1)}) \geq \lambda_k(\mathbf{F}_{\mathbf{x}}^{(N)}) > 0. \tag{3.25}$$

Then, it follows that

$$0 < \lambda_k \left([\mathbf{F}_{\mathbf{x}}^{(N+1)}]^{-1} \right) \leq \lambda_k \left([\mathbf{F}_{\mathbf{x}}^{(N)}]^{-1} \right). \tag{3.26}$$

This inequality indicates that the trace of the FIM's inverse will shrink when we add an extra virtual anchor to the existing network, which ensures that the overall estimation error will decrease. As the overall estimation error is the summation of the positioning error and channel estimation error, we cannot guarantee that the decrease of the overall estimation error indicates the decrease of the positioning error. However, statistically, it is always beneficial to add an extra virtual anchor to the system, as will be shown in the following subsection.

3.4.2 Positioning Error Analysis

In Appendix A.1, the lower bound of $GDOP$ is given as

$$GDOP \geq \frac{4}{\sum_{i=1}^{N} r_i^2 / d_i^4}, \tag{3.27}$$

and the equality holds given:

$$\begin{cases} \mathbf{F}_1^T \mathbf{F}_2 = \mathbf{0} \\ \mathbf{F}_1^T \mathbf{F}_1 = c \cdot \mathbf{I}_2, \end{cases} \tag{3.28}$$

where c is a constant, given as

$$c = \frac{N\beta^2}{2R^2} \cdot \left[\ln \left(\frac{R^2 + h^2}{h^2} \right) - \frac{R^2}{R^2 + h^2} \right]. \tag{3.29}$$

When the number of virtual anchors is relatively large, these two conditions are asymptotically fulfilled, which is illustrated in Appendix A.2. In this case, the limit of $GDOP \cdot N$

can be obtained as

$$\lim_{N\to\infty} N \cdot GDOP = \lim_{N\to\infty} \frac{4N}{\cdot \sum_{i=1}^{N} r_i^2/d_i^4} = \frac{4}{\lim\limits_{N\to\infty} 1/N \cdot \sum_{i=1}^{N} r_i^2/d_i^4}. \tag{3.30}$$

As N grows to infinity, the denominator of Equation (3.30) approaches $E\{r_i^2/d_i^4\}$. As a result, we can rearrange Equation (3.30) and conclude

$$GDOP = \frac{4}{N \cdot E\{r_i^2/d_i^4\}} + o(1/N), \tag{3.31}$$

or equivalently,

$$GDOP \sim \frac{4}{N \cdot E\{r_i^2/d_i^4\}} \ (N \to \infty), \tag{3.32}$$

where $o(1/N)$ indicates a component much smaller than $1/N$. $E\{r_i^2/d_i^4\}$ is determined by h and R, and is discussed in Appendix A.2.

Equation (3.31) explicitly reveals that $GDOP$ is inversely proportional to N when the number of virtual anchors is sufficiently large. That is to say, the positioning accuracy can be vastly improved by incorporating a large number of virtual anchors.

3.4.3 Computational Complexity

Along with the increase of virtual anchors, the computational complexity of the proposed scheme increases. In this subsection, we show that how computational amount grows with N. Algorithm 1 is an iterative process; therefore, we only need to analyze one iteration for the computational complexity. Table 3.1 shows the computational complexity of each step in every iteration. Therefore, the overall computation amount is in the order of $\mathcal{O}(N)$, which is acceptable and comparable to that of the conventional scheme. The first step of the iteration process (step 3) is to compute $\mathbf{\Delta P}$, which takes $2N$ additive, $4N$ multiplicative

and N logarithmic operations. In this process, we compute $1/2 \cdot \ln d^2$ instead of $\ln d$, so as to replace the extraction operation with a multiplicative one. Then, in step 4, it only costs $2N$ multiplications to compose matrix $\mathbf{F}$ in Equation (3.4), if intermediate variables are properly stored. In step 5, the major computation comes from the multiplication of $\mathbf{F}^T$ and $\mathbf{F}$. In spite of the symmetry of $\mathbf{F}^T\mathbf{F}$, $10N$ multiplications and $10N$ additions are still required. Comparatively, the computation amount of its inversion is not very large, only $4^3/2 = 32$ multiplications with Cholesky decomposition [116]. To save computations, the multiplication between $\mathbf{F}^T$ and $\Delta\mathbf{P}$ should be handled first. The multiplications of these three matrixes cost $4N + 16$ multiplications and $4N + 8$ additions. Finally, step 6 contributes another N additive operations.

Table 3.1: Computational Complexity

Step	Multiplications	Additions	Logarithms
3	$2N$	$4N$	N
4	$2N$	0	0
5	$14N$+48	$14N$-2	0
6	0	N	0
Overall	$18N$+48	$19N$-2	N

3.5 Numerical Evaluation

In this sections, comprehensive simulation results will be presented to support the theoretical analysis in previous sections and verify the reliability of the proposed localization framework. To be specific, the simulations will show that the positioning error analysis is very accurate. Besides, we will see that the lower bound of $GDOP$ is very tight and can be achieved when the number of virtual anchors is relatively large.

3.5.1 Positioning Error Approximation

The approximation of positioning error concerning the proposed system is given by (3.13), and the simulation results are shown in Figure 3.3.

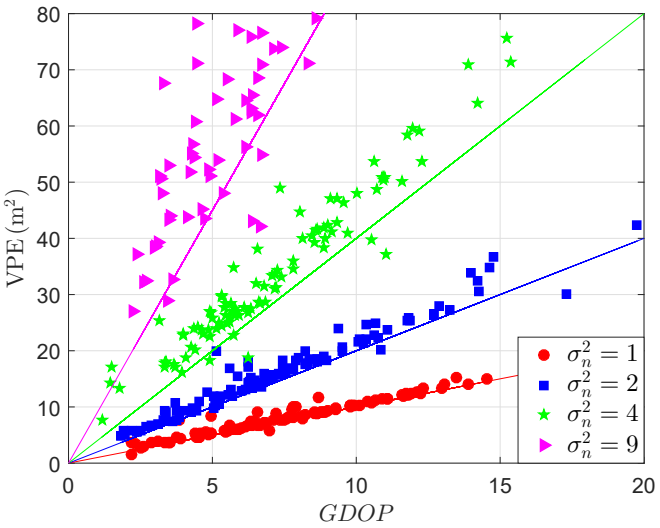

Figure 3.3: The relation between $GDOP$ and positioning error.

The communication radius of nodes and the height of drone are set as 50 meters and

5 meters, respectively. 20 virtual anchors are uniformly distributed in the communication range of the target node. Under different noise levels, the simulation results of the variance of positioning error (VPE) versus $GDOP$ are presented in Figure 3.3, and theoretical results are plotted in solid lines for comparison. Generally, the simulation and theoretical results fit better when σ_n^2 is relatively small. According to the field experiments, the variance of RSS values is between 3 and 4, in which (3.13) gives very accurate approximation of VPE. Also, it should be noted that the simulated error can be smaller than the theoretical results. This is because CRLB is derived for unbiased estimators, while the Newton iteration algorithm is biased. Nevertheless, we can see that the iteration algorithm can very closely approach the CRLB.

3.5.2 The Lower Bound of GDOP

Figure 3.4 shows how the expectation and lower bound of $GDOP$ vary with the number of virtual anchors and the height of the drone. For an arbitrary number of virtual anchors uniformly distributed in the communication range of the target node, the average $GDOP$ can be obtained through simulation. On the other hand, the lower bound of $GDOP$ is given by Equation (3.31) (Theo. I) and Equation (3.27) (Theo. II). As shown in Figure 3.4, both the lower bound and the expectation of $GDOP$ decrease with N. Besides, it is notable that when N is relatively large, for example, $N \geq 80$, a good match of the simulation results and theoretical results is observed. This corroborates our claim that the lower bound of $GDOP$ can be asymptotically achieved when N becomes sufficiently large.

When N is relatively smaller, different columns of matrix $\mathbf{F}$ are nonorthogonal and the left side of Equation (3.27) is strictly larger than the right side. As a result, the gap

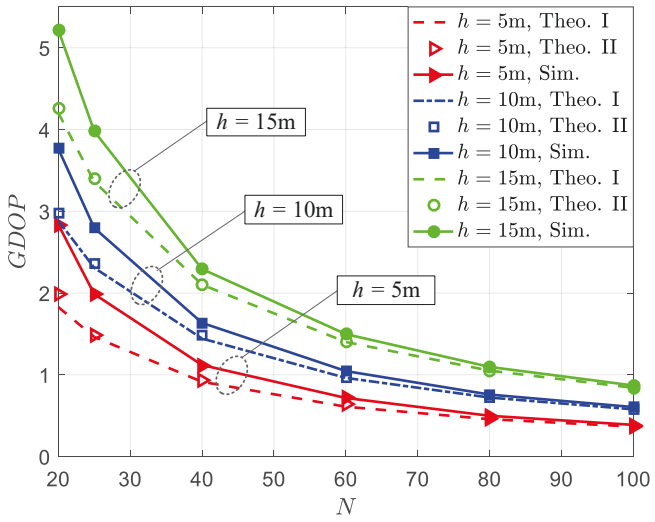

Figure 3.4: The relation between $GDOP$ and N.

between theoretical and simulation results is quite large. Also, we can see that there is small discrepancy between the results of Equation (3.31) (Theo. I) and Equation (3.27) (Theo. II), because generally speaking, $E\{1/w\}$ is unequal to $1/E\{w\}$ for a random variable w. However, when N is large enough, this discrepancy is negligible.

From Figure 3.4, it is also clear that the height of the drone has an impact on $GDOP$. This can be explained by (3.31), where $d_i^2 = r_i^2 + h^2$. As h increases, the denominator will decrease, leading to the increase of $GDOP$ and positioning error. From this respect, lower height is preferred for smaller $GDOP$ and positioning error. However, along with the low height of the drone, several side effects emerge. First, the reflected signals from the ground will have a strong impact on the RSS measurements [117]. Second, the coverage of the drone will be limited in real applications. Last but not least, the airflow stirred up by the drone and reflected from the ground will undermine the stability of the drone,

which introduces interference in RSS measurements. In field experiments, we found that it becomes easier to stabilize the drone at the height of 5 meters or larger, which also provides great coverage.

3.5.3 Variance of GDOP

The increase of the number of virtual anchors not only makes the system more accurate but also more stable. As has been mentioned, $GDOP$ is determined by both the distribution and the number of virtual anchors (or anchors in the conventional system). For an arbitrary N, $GDOP$ is a random variable because of the random distribution of virtual anchors, and the average $GDOP$ is shown to decrease with N in Figure 3.4. Then, the relation between the variance of $GDOP$ and N is presented in Figure 3.5. From Figure 3.5, the variance

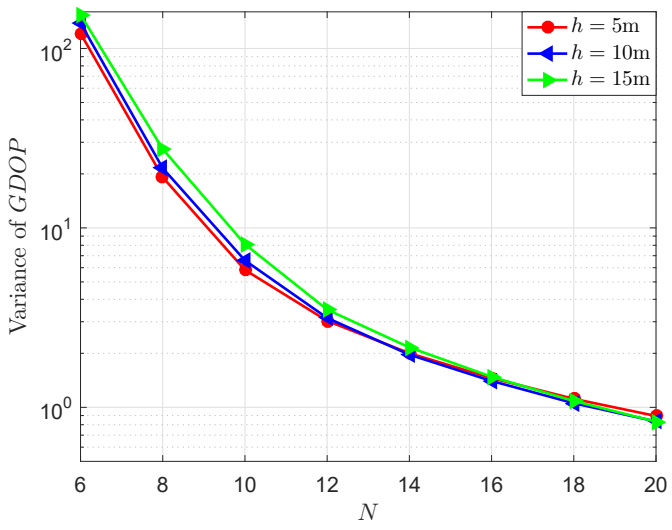

Figure 3.5: The variance of $GDOP$ versus N.

of $GDOP$ is quite large when N is relatively small, which makes the system unstable. However, given that N is large enough (20 or more), we can see in Figure 3.5 that the variance of $GDOP$ is smaller than 1. When we increase N from 6 to 20, the computational amount is only tripled while the variance of $GDOP$ is reduced by two orders of magnitude. Another interesting observation is that the relevance between the variance of $GDOP$ and the height of drone is barely noticeable.

3.6 Field Experiments

To verify the reliability of the proposed system, we implemented it on a DJI Phantom II and conducted field experiments. The field experiments were conducted in a football field

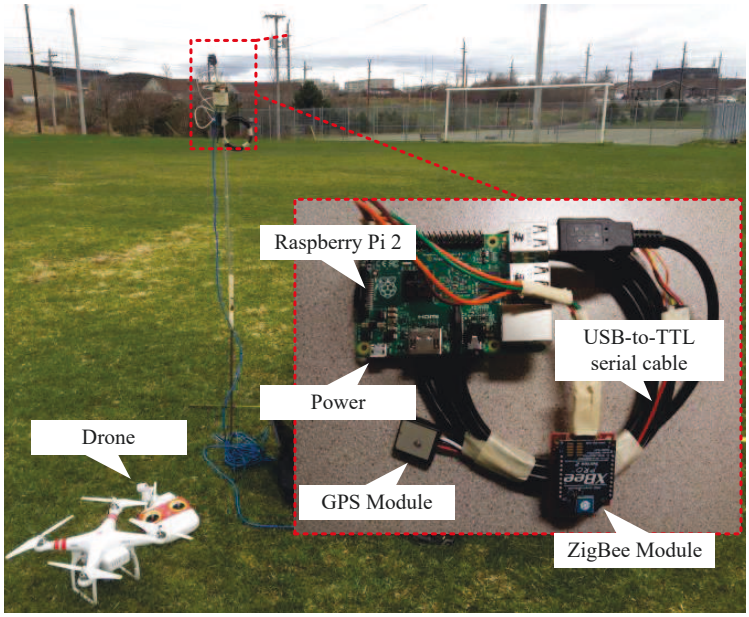

Figure 3.6: Field experiment setup.

in rural area, so as to minimize the RF interferences.

3.6.1 Experimental Setup and Data Collection

In the experiment, the transmitter and receiver are both equipped with ZigBee modules (XBEEPRO2, DIGI). They work in the 2.4 GHz ISM band and the transmit power is 10 mW, being able to cover hundreds of meters in line of sight scenarios. The central control unit is a Raspberry Pi 2 board and we can program it with Java scripts or C language. The transmitter is equipped with a GPS chip (GP-20U7), which sends location information through a serial port to the control unit periodically. Then, the control board will broadcast the location information through the ZigBee module at the frequency of 1 Hz. The receiver receives signals with the ZigBee module and measures the RSS at the same time. For convenience, the receiver is also equipped with a GPS chip, through which the receiver can localize itself and store the location information as reference. Then, the location information and the corresponding RSS are stored as one entry. During the experiment, the receiver is connected to a laptop for initialization and real time monitoring through Ethernet cable.

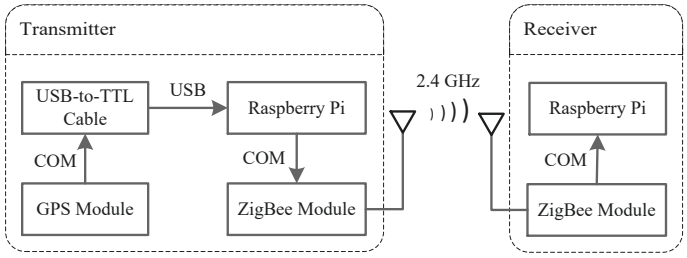

Figure 3.7: System diagram of the receiver and transmitter.

As GPS is reliable on the longitude and latitude measurements while unreliable on the height measurement, due to the poor vertical dilution of precision, we need to collect the height information of the drone in alternative ways (an altimeter, or just a rope). By remotely controlling the drone moves around the target sensor, we collect RSS measurements and coordinates of the drone and record them in the laptop for postprocessing.

3.6.2 Experimental Results

Figure 3.8 shows the top view of the distribution of virtual anchors and the target sensor. The red disk denotes the target node while the asterisks are the projections of virtual an-

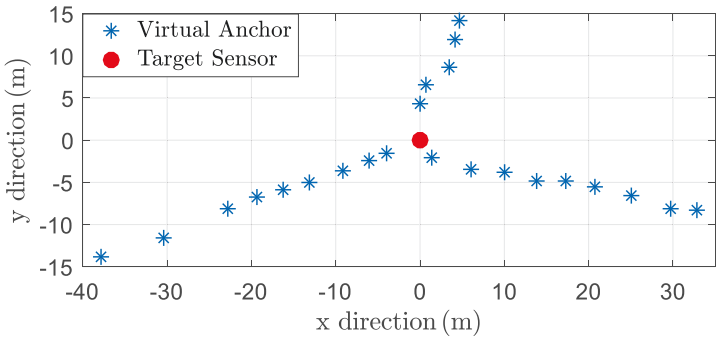

Figure 3.8: Top view of the distribution of virtual anchors.

chors. For convenience, we build a cartesian coordinate system with the origin on the target node. Besides, x axis and y axis are parallel to the longitude and latitude, respectively.

To begin with, we use the collected data to verify the radio propagation model given by Equation (2.1). The results are shown in Figure 3.9, where the solid line denotes the theoretical results and the measured results are represented by solid squares. The

theoretical results are derived by the estimation of channel parameters from Algorithm 1. In this experiments, we have the estimated first meter signal strength and path loss exponent as -14.73 dBm and 2.03, respectively. The variance of the RSS measurements is between 3 and 4. From Figure 3.9, a good match between the measured RSS and the expected RSS generated from the radio propagation model is observed, which indicates that the radio propagation model is suitable for our proposed system.

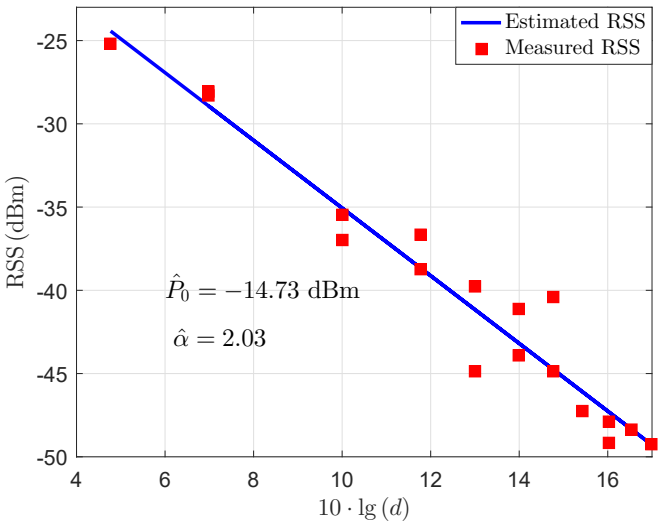

Figure 3.9: The experimental relation between distance and RSS.

Based on the radio propagation model, (3.2) can be established, and then Algorithm 1 can be applied for localization. Figure 3.10 presents the results of the $GDOP$ and positioning error versus the number of virtual anchors. Generally, both $GDOP$ and positioning error decrease with the increase of virtual anchors. We also provide the lower bound of $GDOP$ given by Equation (3.27). It is clear that when N is sufficiently large, the $GDOP$

from our field experiments is quite close to the bound, which is consistent with the previous analysis. Figure 3.10 also reveals that when the number of virtual anchors is greater than 16, the positioning error of the proposed system is less than 3.5 m, which is promising.

The next step is to test our algorithm and theoretical analysis based on the collected data in Figure 3.8. First of all, the four virtual anchors closest to the target node are chosen for localization. Then, the remaining virtual anchors are added one by one. As shown in Figure 3.10, both positioning error and $GDOP$ tend to decrease when the number of virtual anchors increase from 4 to 23. The positive relation between positioning error and $GDOP$ can be clearly observed, in spite of some small discrepancies which will be discussed in next subsection. Also, the lower bound of $GDOP$ given in Equation (3.27) proves to be very

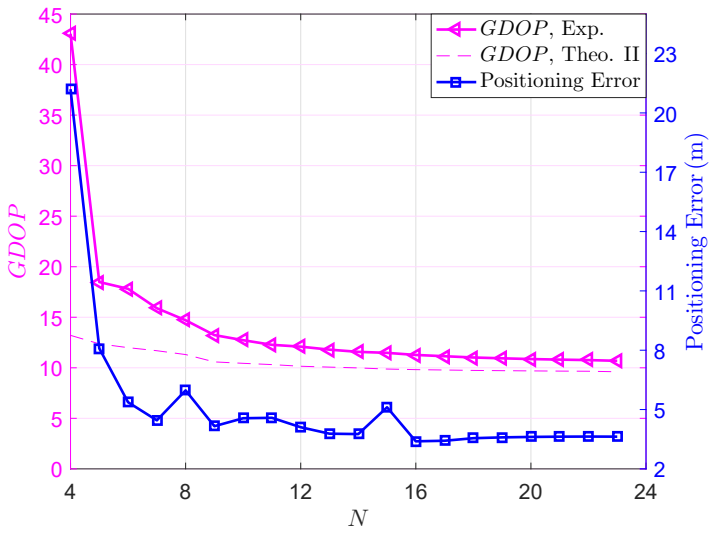

Figure 3.10: Experimental results of positioning error and $GDOP$.

tight when N is relatively large. It should be noted that we will not be able to observe

the reciprocal relationship between $GDOP$ and N, because that is the statistical result of an enormous number of distributions of virtual anchors, while the distribution in our experiment is fixed.

The influence of GPS error on positioning results can be clearly observed in Figure 3.10. $GDOP$ decreases strictly while positioning error shows some small fluctuations. A new added virtual anchor might serve to improve $GDOP$, but its inaccurate position information also induces extra positioning error. Therefore, adding a new virtual anchor does not necessarily improve positioning accuracy. To see this in Figure 3.10, positioning error even increased when we added the 8-th and 10-th virtual anchors to the network. Besides, after N is larger than 16, positioning error stops to change, while $GDOP$ continues to decrease. A possible explanation is that the improvement of $GDOP$ is counteracted by the position error of new added virtual anchors.

Besides, it is also of interest to plan the rout of the drone to provide better $GDOP$ to sensor nodes, because the drone can only stay in the air for a short period (about 25 minutes in our case) due to limited battery capacity. To be specific, we will need to plan such a route for the drone, that can provide decent coverage for all the nodes in the network, given the maximum possible duration of the drone's battery.

3.7 Summary

In this chapter, a drone-assisted localization framework is presented for large-scale WSNs. The drone servers as a mobile anchor and broadcasts its location information periodically. All the nodes can achieve self-localization based on RSS measurements. By viewing the

channel parameters as unknowns, zero-configuration is achieved. The positioning error of the new system is analyzed, and the variance of positioning error is proven to be inversely proportional to the number of virtual anchors statistically. From the simulation results, we can see that the simple Newton iteration algorithm can solve the equations and closely approaches the CRLB. Lastly, field experiments verify the reliability of the proposed system.

Chapter 4

AUV-Aided Joint Localization and Time Synchronization in Underwater Networks

In Chapter 3, we talked about the possibility of employing drones as mobile anchors for localization in terrestrial WSNs. In the following three chapters, we will move to the underwater scenario, and continue our discussions on AUV-aided acoustic sensor networks. To begin with, the AUV-aided joint localization and time synchronization problem will be discussed in this chapter.[1]

As we have mentioned, there are two major challenges for the TDoA- and ToA-based

[1]Related work can be found in [J16]: Z. Gong, C. Li and F. Jiang, "AUV-Aided Joint Localization and Time Synchronization for Underwater Acoustic Sensor Networks," *IEEE Signal Process. Lett.*, vol. 25, no. 4, pp. 477-481, April 2018.

localization systems: (1) the stratification effect; (2) time synchronization is required. To solve the first problem, the average underwater sound speed is considered as an extra unknown. The time synchronization will be conducted simultaneously with the localization process. As a result, there are six unknowns: the three dimensional coordinate of the target, the average underwater sound speed, and the clock bias and skew of the target node's clock. For the conventional architecture based on fixed anchor, this is challenging, because the target node needs at least six anchors in its communication range for simultaneous localization and time synchronization. However, with a mobile anchor, the equivalent number of anchors can be boosted at negligible cost, similar to Chapter 3. In this chapter, we will investigate the AUV-assisted WSNs, in terms of algorithm design and performance analysis.

4.1 System Model

The AUVs generally have onboard navigation systems, such as GPS chips and inertial navigation sensors. An AUV can initialize its position information with the onboard GPS chip before diving. Then, it will dive and navigate itself through predefined trajectories with an inertial sensor. Besides, it can surface periodically to update its position information through GPS, so as to avoid error accumulation in inertial sensors. To achieve 3D localization, the trajectory of the AUV cannot be on a plane. Therefore, we assume that the AUV moves with fixed direction and velocity for $K+1$ time slots, and then it turns to a randomly selected direction, and moves forward at the new direction with fixed velocity for another $K+1$ time slots. During this process, the AUV periodically broadcasts beacon

signals, including its real-time location information and transmitting time of packets. This process will continue until we have N straight lines on AUV's trajectory. Assume that the location information and the transmitting time of the k-th period on the n-th line is $\mathbf{x}_{n,k}$ and $t_{n,k}$, respectively. When this packet is received by a target sensor at time $r_{n,k}$, the measured propagation time will be

$$T_{n,k} = s \cdot r_{n,k} + o - t_{n,k} = \overline{T}_{n,k} + n_{n,k}, \tag{4.1}$$

where s and o denote the clock skew and offset of the clock on target sensor, with respect to the clock on AUV. $\overline{T}_{n,k}$ is the accurate propagation time and $n_{n,k}$ is the overall timing error. Both $r_{n,k}$ and $t_{n,k}$ are contaminated by zero-mean Gaussian noise with an identical variance of σ_t^2. Therefore, the total timing error will be a zero-mean Gaussian variable with a variance of $(s^2+1)\sigma_t^2$. On the other hand, based on the ToA measurement, we have

$$\|\mathbf{x} - \mathbf{x}_{n,k}\| = \overline{T}_{n,k} \cdot c, \tag{4.2}$$

where $\mathbf{x}_{n,k}$ is the three-dimensional coordinate of the AUV at the k-th time slot on the n-th line, c is the average underwater sound speed, and $\|\cdot\|$ indicates the Euclidean norm of an arbitrary vector.

Define a new vector $\boldsymbol{\theta} \triangleq [\mathbf{x}^T, o, c, s]^T$ to contain the unknowns, and reorganize (4.2) as

$$f_{n,k}(\boldsymbol{\theta}) = \|\mathbf{x} - \mathbf{x}_{n,k}\|/c - s \cdot r_{n,k} - o + t_{n,k} = -n_{n,k}, \tag{4.3}$$

in which six unknowns are included. After $K+1$ measurements on each of the N lines, we have $N(K+1)$ nonlinear equations. Generally, these nonlinear equations can be iteratively solved by many algorithms (e.g., Newton iteration method). However, this is a non-convex problem, and the iteration algorithm may stuck at local optimums if we employ random

initializations of the unknowns [17]. To solve this problem, a two-phase algorithm dedicated for (4.3) will be presented in the next section.

4.2 A Two-Phase Algorithm

In the first phase of this algorithm, the relative clock skew is ignored, because it is generally very small. Then, the nonlinear equations can be transformed into linear ones, and LS algorithm is employed to obtain coarse time synchronization and localization results. In the second phase, the coarse estimation is refined by another LS estimator. Compared with the existing algorithms, our proposal achieves the CRLB with much smaller computational complexity. Besides, the proposed method is passive, and thus energy efficient for underwater sensors. To be specific, target sensors are silent and only receive signals from the AUV.

4.2.1 Phase I: Initial Synchronization and Localization Results

In the first phase, we transform the non-linear equations into linear ones, by doing which a coarse estimation of the unknowns can be obtained. Generally, clock skew is less than 200 ppm [118–120], and the corresponding s lies in $[1-2\text{E-}4, 1+2\text{E-}4]$, which is very close to 1. Therefore, we can replace it with $\hat{s}=1$ to roughly estimate the other unknowns. For brevity, define $q_{n,k} \triangleq \hat{s}\cdot r_{n,k} - t_{n,k}$, square both sides of (4.2), and we will have $N(K+1)$ equations of the following form:

$$\|\mathbf{x}-\mathbf{x}_{n,k}\|^2 - q_{n,k}^2 c^2 - o^2 c^2 - 2q_{n,k} o c^2 = e_{n,k}, \tag{4.4}$$

where $e_{n,k}$ is the overall error caused by timing error and the uncertainty in $\hat{s}$, and is given in (4.5) as

$$e_{n,k} = 2c^2(n_{t_{n,k}} - s \cdot n_{r_{n,k}} - (1-s) \cdot r_{n,k})(q_{n,k} + o) + c^2(n_{t_{n,k}} - s \cdot n_{r_{n,k}} - (1-s) \cdot r_{n,k})^2 \quad (4.5)$$

In (4.5), $n_{t_{n,k}}$ and $n_{r_{n,k}}$ are measuring errors of $t_{n,k}$ and $r_{n,k}$, respectively. Then, after subtracting the $(n,0)$-th sub-equation from the (n,k)-th one, we can obtain

$$\begin{aligned}&(\mathbf{x}_{n,0} - \mathbf{x}_{n,k})^T \mathbf{x} + (q_{n,0}^2 - q_{n,k}^2)/2 \cdot c^2 + (q_{n,0} - q_{n,k}) \cdot c^2 o \\ =&(\|\mathbf{x}_{n,0}\|^2 - \|\mathbf{x}_{n,k}\|^2)/2 + (e_{n,k} - e_{n,0})/2 \text{ (for } k \neq 0).\end{aligned}$$

In matrix form, we have

$$\mathbf{H}\mathbf{p} = \mathbf{y} + \mathbf{e}, \quad (4.6)$$

where $\mathbf{e} = [\mathbf{e}_1^T, \mathbf{e}_1^T, \cdots, \mathbf{e}_N^T]^T$ is the error vector and $\mathbf{e}_n = [e_{n,1} - e_{n,0}, \cdots, e_{n,K} - e_{n,0}]^T/2$. The unknown vector $\mathbf{p}$ is given by

$$\mathbf{p} = \left[\mathbf{x}^T, c^2, c^2 o\right]^T. \quad (4.7)$$

Besides, we have $\mathbf{H} = [\mathbf{H}_1^T, \mathbf{H}_2^T, \cdots, \mathbf{H}_N^T]^T$, and $\mathbf{y} = [\mathbf{y}_1^T, \mathbf{y}_2^T, \cdots, \mathbf{y}_N^T]^T$, where $\mathbf{H}_n$ and $\mathbf{y}_n$ are given by

$$\mathbf{H}_n = \begin{bmatrix} (\mathbf{x}_{n,0} - \mathbf{x}_{n,1})^T & (q_{n,0}^2 - q_{n,1}^2)/2 & q_{n,0} - q_{n,1} \\ (\mathbf{x}_{n,0} - \mathbf{x}_{n,2})^T & (q_{n,0}^2 - q_{n,2}^2)/2 & q_{n,0} - q_{n,2} \\ \vdots & \vdots & \vdots \\ (\mathbf{x}_{n,0} - \mathbf{x}_{n,K})^T & (q_{n,0}^2 - q_{n,K}^2)/2 & q_{n,0} - q_{n,K} \end{bmatrix} \quad (4.8)$$

$$\mathbf{y}_n = \left[(\|\mathbf{x}_{n,0}\|^2 - \|\mathbf{x}_{n,1}\|^2), \cdots, (\|\mathbf{x}_{n,0}\|^2 - \|\mathbf{x}_{n,K}\|^2)\right]^T/2.$$

Then, $\mathbf{p}$ can be estimated as

$$\hat{\mathbf{p}} = (\mathbf{H}^T\mathbf{H})^{-1}\mathbf{H}^T\mathbf{y}, \quad (4.9)$$

and we have the positioning result as $\hat{\mathbf{x}} = \hat{\mathbf{p}}[1{:}3]$, where $\hat{\mathbf{p}}[1{:}3]$ is a vector containing the first three elements of $\hat{\mathbf{p}}$. The clock offset and average underwater sound speed are estimated as $\hat{o} = \hat{\mathbf{p}}[5]/\hat{\mathbf{p}}[4]$ and $\hat{c} = \sqrt{\hat{\mathbf{p}}[4]}$, respectively. $\hat{\mathbf{p}}[4]$ and $\hat{\mathbf{p}}[5]$ are the last two elements of $\hat{\mathbf{p}}$. Therefore, a coarse estimation of $\boldsymbol{\theta}$ can be obtained as $\hat{\boldsymbol{\theta}} = [\hat{\mathbf{x}}^T, \hat{o}, \hat{c}, \hat{s}]^T$, where $\hat{s}$ is equal to 1.

To ensure the positioning and timing accuracies, the trajectory of the AUV should be carefully designed to make sure that (4.6) is not ill-conditioned. Because of space limit, we will not discuss this issue here, and the interested readers are referred to [121] and [44].

4.2.2 Phase II: Refined Synchronization and Localization Results

After the coarse estimation in Phase I, $\hat{\boldsymbol{\theta}}$ should be reasonably close to $\boldsymbol{\theta}$, which leads to the following approximation

$$\mathbf{f}(\boldsymbol{\theta}) - \mathbf{f}(\hat{\boldsymbol{\theta}}) \approx \frac{\partial \mathbf{f}}{\partial \boldsymbol{\theta}} \cdot (\boldsymbol{\theta} - \hat{\boldsymbol{\theta}}), \tag{4.10}$$

where

$$\mathbf{f}(\boldsymbol{\theta}) = [\mathbf{f}_1(\boldsymbol{\theta})^T, \mathbf{f}_2(\boldsymbol{\theta})^T, \cdots, \mathbf{f}_N(\boldsymbol{\theta})^T]^T \tag{4.11}$$

and

$$\mathbf{f}_n(\boldsymbol{\theta}) = [f_{n,0}(\boldsymbol{\theta}), f_{n,1}(\boldsymbol{\theta}), \cdots, f_{n,K}(\boldsymbol{\theta})]^T. \tag{4.12}$$

Based on this approximation, $\boldsymbol{\delta}_{\boldsymbol{\theta}} = \boldsymbol{\theta} - \hat{\boldsymbol{\theta}}$ can be estimated to refine the estimate results. As we known, ToA measurement errors are generally very small (at the level of milliseconds [48]), which means we have $\mathbf{f}(\boldsymbol{\theta}) \approx \mathbf{0}_{(K+1)N\times 1}$. Moreover, the partial fraction matrix can be replace by

$$\mathbf{R} = \left.\frac{\partial \mathbf{f}}{\partial \boldsymbol{\theta}}\right|_{\boldsymbol{\theta}=\hat{\boldsymbol{\theta}}}. \tag{4.13}$$

To be specific, $\mathbf{R} = [\mathbf{R}_1^T, \mathbf{R}_2^T, \cdots, \mathbf{R}_N^T]^T$, and $\mathbf{R}_n$ is given as

$$\mathbf{R}_n = \begin{bmatrix} \frac{\hat{\mathbf{x}}^T - \mathbf{x}_{n,0}^T}{\|\hat{\mathbf{x}} - \mathbf{x}_{n,0}\|\hat{c}}, & -1, & \frac{-\|\hat{\mathbf{x}} - \mathbf{x}_{n,0}\|}{\hat{c}^2}, & -r_{n,0} \\ \frac{\hat{\mathbf{x}}^T - \mathbf{x}_{n,1}^T}{\|\hat{\mathbf{x}} - \mathbf{x}_{n,1}\|\hat{c}}, & -1, & \frac{-\|\hat{\mathbf{x}} - \mathbf{x}_{n,1}\|}{\hat{c}^2}, & -r_{n,1} \\ & & \vdots & \\ \frac{\hat{\mathbf{x}}^T - \mathbf{x}_{n,K}^T}{\|\hat{\mathbf{x}} - \mathbf{x}_{n,K}\|\hat{c}}, & -1, & \frac{-\|\hat{\mathbf{x}} - \mathbf{x}_{n,K}\|}{\hat{c}^2}, & -r_{n,K} \end{bmatrix}. \tag{4.14}$$

After the replacement, the approximation in (4.10) can be revised as

$$-\mathbf{f}(\hat{\boldsymbol{\theta}}) \approx \mathbf{R}\boldsymbol{\delta}_{\boldsymbol{\theta}}. \tag{4.15}$$

Then, we can estimate the bias of coarse estimation in Phase I as

$$\hat{\boldsymbol{\delta}_{\boldsymbol{\theta}}} = -(\mathbf{R}^T\mathbf{R})^{-1}\mathbf{R}^T\mathbf{f}(\hat{\boldsymbol{\theta}}), \tag{4.16}$$

and the time synchronization and localization results can be refined as

$$\hat{\boldsymbol{\theta}}_r = \hat{\boldsymbol{\theta}} + \hat{\boldsymbol{\delta}_{\boldsymbol{\theta}}}. \tag{4.17}$$

It should be noted that this process can be repeated to get more accurate results. Besides, we only deal with localization and time synchronization in this paper, and when it comes to tracking, particle filter is a popular tool to further improve accuracy [122–124], which will be part our future work.

4.3 Performance Analysis of the Two-Phase Algorithm

4.3.1 Localization and Time Synchronization Errors

In Equation (4.16), the noise in ToA measurements will cause estimation error, and similar to the works in [25] and [5], the covariance matrix of estimation error can be approximated

by

$$\text{cov}\{\hat{\boldsymbol{\theta}}\} = (s^2+1)\sigma_t^2(\mathbf{R}^T\mathbf{R})^{-1}. \tag{4.18}$$

To further evaluate the performance of the proposed method, the CRLB of ToA based localization and synchronization systems is analyzed below.

In Equation (4.3), we can see that $f_{n,k}(\boldsymbol{\theta})$ follows zero-mean Gaussian distribution, with a variance of $(s^2+1)\sigma_t^2$. We assume all the timing errors are independent and identically distributed, and the joint probability density function of the observations is

$$f_{\mathbf{r},\mathbf{t}}(\mathbf{r},\mathbf{t}|\boldsymbol{\theta}) = (|2\pi\boldsymbol{\Sigma}_{\boldsymbol{t}}|)^{-1/2}\cdot\exp\left\{-\frac{1}{2}\mathbf{f}(\boldsymbol{\theta})^T\boldsymbol{\Sigma}_{\boldsymbol{t}}^{-1}\mathbf{f}(\boldsymbol{\theta})\right\}, \tag{4.19}$$

where $\mathbf{r} = [\mathbf{r}_1^T,\mathbf{r}_2^T,\cdots,\mathbf{r}_N^T]^T$ is the time of receiving vector, and $\mathbf{r}_n = [r_{n,0},r_{n,1},\cdots,r_{n,K}]$; $\mathbf{t} = [\mathbf{t}_1^T,\mathbf{t}_2^T,\cdots,\mathbf{t}_N^T]^T$ is the time of transmission vector, and $\mathbf{t}_n = [t_{n,0},t_{n,1},\cdots,t_{n,K}]^T$. The covariance matrix will be $\boldsymbol{\Sigma} = (s^2+1)\cdot\sigma_t^2\mathbf{I}_{N(K+1)}$, and $|\cdot|$ represents the determinant of an arbitrary square matrix. The natural logarithm of $f_{\mathbf{r},\mathbf{t}}(\mathbf{r},\mathbf{t}|\boldsymbol{\theta})$ is

$$l(\boldsymbol{\theta}) = -\frac{1}{2}\left(\ln|2\pi\boldsymbol{\Sigma}| + \mathbf{f}(\boldsymbol{\theta})^T\boldsymbol{\Sigma}^{-1}\mathbf{f}(\boldsymbol{\theta})\right). \tag{4.20}$$

Define $\mathbf{F}$ as the Fisher information matrix, and the (m,n)-th element of $\mathbf{F}$ will be

$$[\mathbf{F}]_{m,n} = E\left\{\frac{\partial l}{\partial\theta_m}\cdot\frac{\partial l}{\partial\theta_n}\right\}, \tag{4.21}$$

where θ_m and θ_n are the m-th and n-th elements of $\boldsymbol{\theta}$, respectively. For notational succinctness, $\mathbf{f}(\boldsymbol{\theta})$ is replaced by $\mathbf{f}$ in the following derivations.

For $m,n \le 5$, we have

$$[\mathbf{F}]_{m,n} = \frac{1}{(s^2+1)\sigma_t^2}\cdot\frac{\partial\mathbf{f}^T}{\partial\theta_m}\cdot\frac{\partial\mathbf{f}}{\partial\theta_n}. \tag{4.22}$$

For $m \leq 5,\ n = 6$, we have

$$[\mathbf{F}]_{m,6} = -\frac{1}{(s^2+1)\sigma_t^2}\frac{\partial \mathbf{f}^T}{\partial \theta_m} E\left\{\frac{\partial \mathbf{f}^T}{\partial s}\right\}. \tag{4.23}$$

The last case is $m = n = 6$, and we can obtain

$$[\mathbf{F}]_{6,6} = \frac{N^2(K+1)^2 s^2}{(s^2+1)^2} + \frac{1}{(s^2+1)\sigma_t^2} E\left\{\frac{\partial \mathbf{f}^T}{\partial s}\right\} E\left\{\frac{\partial \mathbf{f}}{\partial s}\right\}. \tag{4.24}$$

Define $\mathbf{R}_o$ as

$$\mathbf{R}_o \triangleq \left[\frac{\partial \mathbf{f}}{\partial \mathbf{x}}, \frac{\partial \mathbf{f}}{\partial o}, \frac{\partial \mathbf{f}}{\partial c}, E\left\{\frac{\partial \mathbf{f}}{\partial s}\right\}\right], \tag{4.25}$$

and Fisher information matrix will be

$$\mathbf{F} = \frac{1}{(s^2+1)\sigma_t^2}\left(\mathbf{R}_o^T\mathbf{R}_o + \begin{bmatrix} \mathbf{0}_{5\times 5} & \mathbf{0}_{5\times 1} \\ \mathbf{0}_{1\times 5} & \frac{N^2(K+1)^2 s^2 \sigma_t^2}{s^2+1} \end{bmatrix}\right). \tag{4.26}$$

Given that the estimation results are very close to the actual values, we have $\mathbf{R} \approx \mathbf{R}_o$. Besides, compared with the elements in $\mathbf{R}_o^T\mathbf{R}_o$, the non-zero element at the right bottom of the additional matrix is negligible because σ_t^2 is very small. Thus, we have $\mathrm{cov}\{\hat{\boldsymbol{\theta}}\} \approx \mathbf{F}^{-1}$, and the estimation error of the proposed algorithm is very close to CRLB.

4.3.2 Computational Complexity Analysis

In phase I, the construction of $\mathbf{y}$ requires $3N(K+1)$ multiplications, $3NK+2N$ additions and NK divisions, while the construction of $\mathbf{H}$ requires $6NK+N$ multiplications, $N(K+1)$ additions and NK divisions. In Equation (4.9), we divide the process into three steps: the first part is to compute $\mathbf{H}^T\mathbf{H}$ and its inversion; the second part is to multiply $\mathbf{H}^T$ and $\mathbf{y}$; the last part is the multiplication of the previous two parts. The overall computation complexity will be $20NK+25$ multiplications and $20NK$ additions, plus the 5-dimension

matrix inversion. Similarly, the overall computational complexity of phase II includes $31N(K+1)+36$ multiplications, $33N(K+1)+3$ additions, $3N(K+1)$ divisions and $N(K+1)$ root operations, plus the 6-dimension matrix inversion.

Therefore, the overall computational complexity increases linearly with the number of observations. The algorithm in [1] has a computational complexity of the same order but several times larger, because it contains nine unknowns.

4.4 Numerical Evaluation

In this section, we will conduct Monte Carlo simulation for one hundred thousand times to verify our analysis in previous sections. The average underwater sound speed is uniformly distributed between 1420 and 1560 m/s as in [64]. The broadcast interval is set as 5 seconds, and AUV velocity is chosen between 1.5 m/s to 2.5 m/s. N and K are equal to 4 and 50, respectively. The standard deviation of timing error varies from 0.1 ms to 1.6 ms. For visual convenience, σ_t^2 is transformed to decibel according to $\sigma_t^2/\text{dB} = 10\lg(1000\sigma_t)^2 = 10\lg\sigma_t^2 + 60$, where $\lg(\cdot)$ represents the base-10 logarithm. Clock skew is set as $1 + 1\text{E} - 4$ (or 100 ppm). The normalized mean square error (NMSE) of $\hat{s}$ is defined as

$$\text{NMSE of } \hat{s} = \left(\frac{\hat{s} - s}{s - 1}\right)^2, \tag{4.27}$$

which indicates the relative estimation error with respect to the fractional part of s.

The simulation results are shown in Fig. 4.1, including the estimation error of target sensor's position, clock skew, clock offset, and the average underwater sound speed. "Sim. Res." and "Theo. Res." are short for "Simulation Results" and "Theoretical Results" (in (4.18)). As comparison, the LS algorithm proposed in [1] is also simulated. It should

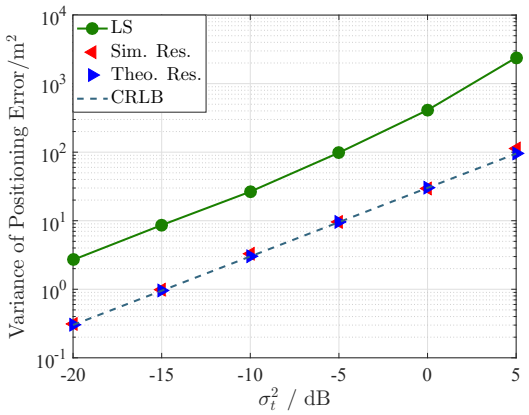

(a) Localization Error

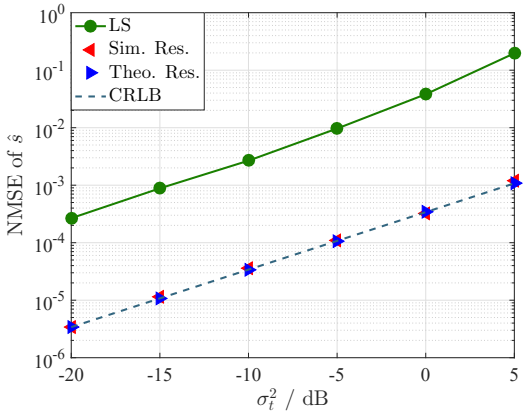

(b) Estimation Error of Clock Skew

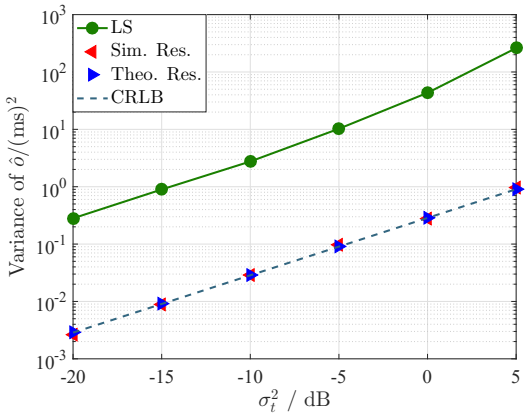

(c) Estimation Error of Clock Offset

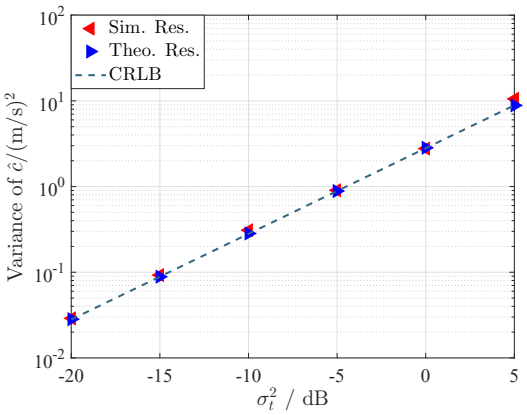

(d) Estimation Error of Underwater Sound Speed

Figure 4.1: Localization and synchronization errors of the presented algorithm and the LS algorithm in [1].

be noted that perfect knowledge of the average sound speed is assumed to be available in [1]. Therefore, only the estimation of our algorithm is presented in Fig. 7(d). As we can see, the proposed method outperforms the LS algorithm in [1]. Besides, the results show that our performance analysis in (4.18) is very accurate in the simulation range of σ_t^2. Moreover, it is clear that our algorithm has a very good approach to CRLB. As we can see, the discrepancy between CRLB and simulation results increases with the growth of σ_t^2, as is suggested by (4.26).

4.5 Summary

In this chapter, a low-complexity two-phase linear algorithm for the AUV-assisted localization and time synchronization system is presented and analyzed. Closed-form error analysis is presented and proves to be accurate through simulation. Besides, the localization and time synchronization errors of this algorithm can approach CRLB, supported by both theoretical and simulation results. Moreover, the computational complexity grows linearly with the number of observations, which is acceptable. Because this is a passive system, i.e., target sensors are silent and only receive signals from the AUV, it is energy efficient and has unlimited capacity.

Chapter 5

Passive AUV-Aided Localization Based on Doppler Shift Measurements

The AUV-aided localization techniques for underwater acoustic devices show promising applications in many scenarios, and most literatures in this area are based on the ToA or the TDoA measurements. However, these measurements are not readily available. To develop a more universally applicable scheme, we will investigate the possibility of employing Doppler shift measurements for underwater localization of acoustic devices in this chapter.[1]

[1]The work in this chapter has been published in [J4]: Z. Gong, C. Li, F. Jiang, and J. Zheng, "AUV-Aided Localization of Underwater Acoustic Devices Based on Doppler Shift Measurements," *IEEE Trans. Wireless Commun.*, vol. 19, no. 4, pp. 2226-2239, April 2020.

5.1 Motivation

Doppler shift is widely used in underwater acoustic sonar to estimate target's radial velocity. However, we will show that the Doppler shift measurements also contain the target's position information, and can be used for localization. Compared with the ToA-based or TDoA-based systems, the Doppler-based system has many advantages. First, localization accuracy can be boosted at very low cost. For example, assume that we need to increase the localization accuracy by one order. For the ToA-based or TDoA-based methods, the AUV needs to broadcast one hundred times faster (or longer). For the Doppler-based method, we just need to sample the sinusoidal wave 4.5 ($\sqrt[3]{100} \approx 4.5$) times longer, as will be shown in the performance evaluation part. Secondly, the TDoA and ToA based methods generally include time synchronization, which increases complexity. Thirdly, the ToA and TDoA measurements are not always available for various underwater localization applications, because our target does not necessarily have onboard communication modules. For example, assume that we want to track some moving objects, such as sharks and whales. We only need to attach a very simple tag that can generate sinusoidal acoustic waves for the Doppler-based localization system. However, for the ToA or TDoA based methods, we will need to install a much more complicated device for bidirectional communications.

In this chapter, we will present a Doppler-based positioning system for the underwater acoustic devices. The AUV moves around in the area of interest and serves as a mobile anchor. This system can works in both active and silent modes. In the active mode, the AUV broadcasts its location information and a sinusoidal wave periodically. The target devices can localize themselves by receiving the signals from the AUV. In the silent mode,

the AUV stays silent and receives signals from the target devices. Based on the received signal, the AUV can estimate the location of the targets.

In most related researches, the Doppler measurements are assumed to be available from the Doppler log files. However, in the presented system, we incorporate the Doppler estimation process into the localization system for two reasons. First, by including the Doppler estimation process, we can boost system performance by improving Doppler estimation accuracy. Second, we can obtain the statistics of the Doppler shift estimates, which allows us to develop more accurate localization algorithms, as we will show in latter discussions. In scenarios where the ToA and TDoA measurements are not available, the proposed method can work as a backup. Besides, even when the ToA or TDoA measurements are available, the proposed algorithm can still be used to improve the system performance through information fusion.

The rest of the chapter is organized as follows. In Section 5.2, the system model is described. In Section 5.3, we briefly introduce the Doppler shift estimation algorithm and conduct comprehensive analysis of the estimation error. In Section 5.4, the intuition and details of the presented algorithm are presented. In Section 5.5, we thoroughly analyze the performance of the proposed system and algorithm, in terms of the CRLB, the localization error, and the computational complexity. In Section 5.6, simulation results are presented and explained in details. The last section briefly summarizes this chapter.

5.2 System Model and Problem Formulation

With the onboard GPS and inertial sensors, the AUV can localize and synchronize itself [125, 126]. It moves around on the predefined trajectories and periodically broadcasts beacon signals[2]. We assume that it moves on an arbitrary direction in constant velocity for several broadcast periods. Then, it alters the direction and repeats this process. This process will be repeated for M times, and the 3-dimensional velocity on the m-th direction is $\mathbf{v}_m = \left[v_x^{(m)}, v_y^{(m)}, v_z^{(m)}\right]^T$. The position of the AUV at the k-th time slot on the m-th direction is $\mathbf{x}_{m,k} = [x_{m,k}, y_{m,k}, z_{m,k}]^T$, and the corresponding Doppler estimate is $f_D^{(m,k)}$. The position of the target device is $\mathbf{x} = [x, y, z]^T$. Then, let $d_{m,k} = \|\mathbf{x} - \mathbf{x}_{m,k}\|$, and we can obtain

$$\frac{(\mathbf{x}^T - \mathbf{x}_{m,k})^T \mathbf{v}_m}{d_{m,k}} \cdot \frac{f_c}{c} = f_D^{(m,k)}, \tag{5.1}$$

where c denotes the underwater sound speed and $d_{m,k} = \|\mathbf{x} - \mathbf{x}_{m,k}\|$. This equation can be rearranged as

$$f_{m,k}(\boldsymbol{\theta}) = \frac{(\mathbf{x}^T - \mathbf{x}_{m,k})^T \mathbf{v}_m f_c}{d_{m,k} c} - f_D^{(m,k)} = 0, \tag{5.2}$$

where $\boldsymbol{\theta} = [x, y, z, c]^T$ contains the 3D coordinate of the target and the *average* underwater sound speed. Let $\mathbf{f}_m(\boldsymbol{\theta}) = [f_{m,1}(\boldsymbol{\theta}), f_{m,2}(\boldsymbol{\theta}), \cdots, f_{m,K}(\boldsymbol{\theta})]^T$ and we have

$$\mathbf{f}(\boldsymbol{\theta}) = [\mathbf{f}_1(\boldsymbol{\theta})^T, \mathbf{f}_2(\boldsymbol{\theta})^T, \cdots, \mathbf{f}_M(\boldsymbol{\theta})^T]^T. \tag{5.3}$$

By solving $\mathbf{f}(\boldsymbol{\theta}) = \mathbf{0}$, we can get the estimate of the target's location. However, this is not a convex problem. If we employ iterative algorithms to solve it, the initial estimate of the unknowns should be carefully chosen to make sure the algorithm converges. To avoid

[2] Although we are presenting the proposed system in the active mode, it can also work passively mode with very little configuration.

the initial estimation process, a low-complexity two-phase algorithm will be presented in latter discussions. Before that, we need to first talk about how to get the Doppler shift measurements.

5.3 Doppler Shift Estimation

In this section, we will employ a widely adopted Doppler estimation algorithm and analyze its estimation error.

5.3.1 Doppler Shift Estimation in Single-Path Scenario

To make the problem mathematically tractable, we will start with the single-path scenario. By removing the multi-path effect, we can better evaluate the impacts of different parameters on system performance. Besides, the theoretical results can still serve as a benchmark. Intuitively, the system performance will degrade at the presence of multi-path effect.

The onboard transmitter of the AUV broadcasts a sinusoidal wave at a frequency of f_c (in Hz). The receiver samples the received signal at f_s (in Hz), and the sampled sequence $\mathbf{s}$ at the target side will be

$$\mathbf{s}[n] = A\sin\left(2\pi(f_c + f_d)/f_s n + \theta\right) + \mathbf{n}_s[n], \tag{5.4}$$

where f_d is the Doppler shift, A is the amplitude of the received signal, and $\mathbf{n}_s$ contains zero-mean Gaussian noise, with a variance of σ^2. Let $\omega = 2\pi(f_c + f_d)/f_s$, and we have

$$\mathbf{s}[n] = A\sin\left(\omega n + \theta\right) + \mathbf{n}_s[n], \tag{5.5}$$

For a sample number of N, we can obtain the discrete spectrum of $\mathbf{s}$ as $\mathbf{s}_\omega = \mathrm{DFT}\{\mathbf{s}\}$. The

k-th element in $\mathbf{s}_\omega$ is

$$\mathbf{s}_\omega[k] = \frac{1}{N}\sum_{n=0}^{N-1}\mathbf{s}[n]e^{-jkn\omega_0}, \tag{5.6}$$

and $\omega_0 = 2\pi/N$. There must exist $l \in \{0, 1, \cdots, N-1\}$ and $\beta \in [0, 1)$ that satisfy $\omega = (l+\beta)\omega_0$. Equation (5.6) can then be rewritten as

$$\begin{aligned}\mathbf{s}_\omega[k] =& \frac{A}{N}\sum_{n=0}^{N-1}\frac{1}{2j}\left(e^{j(\omega n+\theta)} - e^{-j(\omega n+\theta)}\right)e^{-jkn\omega_0} + \mathbf{n}_\omega[k] \\ =& \frac{A}{2N}\left(e^{j\theta_k}\frac{\sin(l+\beta-k)\pi}{\sin(l+\beta-k)\pi/N} - e^{j\tilde{\theta}_k}\frac{\sin(-l-\beta-k)\pi}{\sin(-l-\beta-k)\pi/N}\right) + \mathbf{n}_\omega[k],\end{aligned} \tag{5.7}$$

in which $\tilde{\theta}_k$ and $\tilde{\theta}_k$ are given by

$$\begin{aligned}\theta_k &= \theta - \pi/2 + (N-1)(l+\beta-k)\omega_0/2, \\ \tilde{\theta}_k &= -\theta - \pi/2 + (N-1)(-l-\beta-k)\omega_0/2.\end{aligned} \tag{5.8}$$

The noise $\mathbf{n}_\omega$ is the DFT of $\mathbf{n}_s$, given by

$$\mathbf{n}_\omega[k] = \frac{1}{N}\sum_{n=0}^{N-1}\mathbf{n}_s[n]e^{-jkn\omega_0}. \tag{5.9}$$

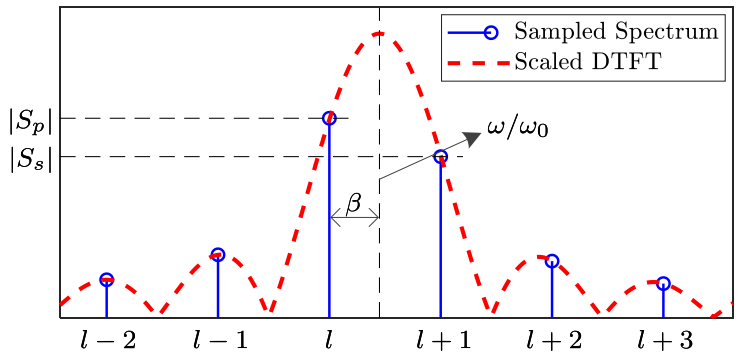

Figure 5.1: The peak location for $0 \le \beta < 0.5$.

When k is close to l, $\mathbf{s}_\omega$ is very close to a scaled sinc function, and there are always two samples in the main lobe, as shown in Figure 5.1. Let S_p and S_s represent the two samples

in the main lobe. When $0 \le \beta < 0.5$, we have $S_p = \mathbf{s}_\omega[l]$, and its amplitude is

$$|S_p| = |\mathbf{s}_\omega[l]| \approx \frac{A\sin(\beta\pi)}{2\beta\pi}. \tag{5.10}$$

$S_s = \mathbf{s}_\omega[l+1]$, and we have

$$|S_s| = |\mathbf{s}_\omega[l+1]| \approx \frac{A\sin(\beta\pi)}{2(1-\beta)\pi}. \tag{5.11}$$

Generally, S_p and S_s have the largest amplitudes in sequence $\mathbf{s}[k]\,(0 \le k \le \lfloor N/2 \rfloor)$. In this case, we can estimate β as

$$\hat{\beta} = \frac{|S_s|}{|S_s| + |S_p|}. \tag{5.12}$$

It should be noted that both S_s and S_p follow Gaussian distribution, and they have the same variance. To analyze the estimation error distribution of (5.12), we rewrite it as

$$\hat{\beta} = \frac{|\bar{S}_s + \mathbf{n}_\omega[l+1]|}{|\bar{S}_p + \mathbf{n}_\omega[l]| + |\bar{S}_s + \mathbf{n}_\omega[l+1]|} = \left(1 + \sqrt{\frac{(R_p+n_3)^2 + (I_p+n_4)^2}{(R_s+n_1)^2 + (I_s+n_2)^2}}\right)^{-1}, \tag{5.13}$$

where $\bar{S}_p$ and $\bar{S}_s$ are expectations of S_p and S_s, respectively. R_s, I_s, R_p and I_p are given by

$$R_s = \Re\{\bar{S}_s\},\ I_s = \Im\{\bar{S}_s\}, R_p = \Re\{\bar{S}_p\},\ I_p = \Im\{\bar{S}_p\}. \tag{5.14}$$

The noise components in (5.13) are defined as follows:

$$n_1 = \Re\{\mathbf{n}_\omega[l+1]\},\ n_2 = \Im\{\mathbf{n}_\omega[l+1]\}, n_3 = \Re\{\mathbf{n}_\omega[l]\},\ n_4 = \Im\{\mathbf{n}_\omega[l]\}. \tag{5.15}$$

n_1, n_2, n_3, n_4 are irrelevant and identically distributed zero-mean Gaussian variables, with a variance of $\frac{\sigma^2}{2N}$. Therefore, we can obtain the approximation of $\hat{\beta}$ through Taylor expansion as

$$\hat{\beta} \approx \frac{|\bar{S}_s|}{|\bar{S}_s| + |\bar{S}_p|} + \frac{R_s|\bar{S}_p|/|\bar{S}_s|}{(|\bar{S}_s| + |\bar{S}_p|)^2} n_1 + \frac{I_s|\bar{S}_p|/|\bar{S}_s|}{(|\bar{S}_s| + |\bar{S}_p|)^2} n_2 - \frac{R_p|\bar{S}_s|/|\bar{S}_p|}{(|\bar{S}_s| + |\bar{S}_p|)^2} n_3 - \frac{I_p/|\bar{S}_p|}{(|\bar{S}_s| + |\bar{S}_p|)^2} n_4. \tag{5.16}$$

In (5.16), we ignore the high-order components, because the absolute values of the noise components are inversely proportional to $\sqrt{N}$, which means they are negligible compared with $\bar{S}_p$ and $\bar{S}_s$. In this case, $\hat{\beta}$ can be approached by Gaussian distribution, and the variance is

$$\mathrm{var}\{\hat{\beta}\} \approx \frac{|\bar{S}_p|^2 + |\bar{S}_s|^2}{(|\bar{S}_s| + |\bar{S}_p|)^4} \cdot \frac{\sigma^2}{2N} \approx \frac{2\sigma^2 r_0(\beta)}{NA^2}, \tag{5.17}$$

where $r_0(\beta)$ is given as

$$r_0(\beta) = \pi^2(2\beta^2 - 2\beta + 1)\beta^2(1-\beta)^2/\sin^2(\beta\pi). \tag{5.18}$$

In (5.17), we implicitly employed the following approximations:

$$|\bar{S}_p| \approx \frac{A\sin(\beta\pi)}{2\beta\pi}, \text{ and } |\bar{S}_s| \approx \frac{A\sin(\beta\pi)}{2(1-\beta)\pi}. \tag{5.19}$$

On the other hand, for $\beta \in [0.5, 1)$, the peak and sub-peak values are given as

$$|S_p| \approx \frac{A\sin(\beta\pi)}{2(1-\beta)\pi} \text{ and } |S_s| \approx \frac{A\sin(\beta\pi)}{2\beta\pi}. \tag{5.20}$$

Then, β can be estimated as

$$\hat{\beta} = \frac{|S_p|}{|S_p| + |S_s|}, \tag{5.21}$$

and we can prove that the variance of $\hat{\beta}$ is identical to the results in (5.17).

5.3.2 Improve Doppler Shift Estimation Accuracy

When β is very close to 0 or 1, the algorithm described in the previous section is not reliable. To be specific, there is a high probability that the sub-peak cannot be correctly identified, because it is very weak. This scenario is illustrated in Figure 5.2. Originally,

the peak sample and the sub-peak sample are indexed by $l_p = l + 1$ and l, respectively. However, β is very close to one, and the sub-peak is very weak, comparable to the other samples outside the main lobe. At the presence of noise, l cannot be accurately identified. In this case, the following method can be employed to improve estimation accuracy.

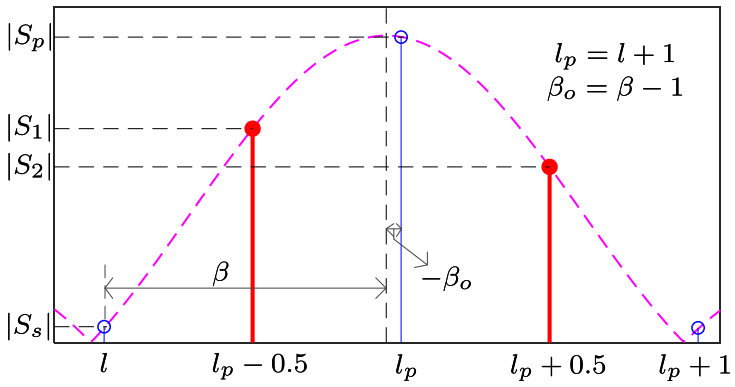

Figure 5.2: The refinement of Doppler shift estimation.

Let l_p be the index of the peak value in the spectrum, and there must exist $\beta_o \in [-0.5, 0.5)$ that satisfies $\omega = (l_p + \beta_o)\omega_0$. We have $l_p + \beta_o = l + \beta$, or $\beta_o = \beta - \lfloor \beta \rceil$ equivalently. As shown in Figure 5.2, we take another two samples equally spaced around the peak sample, (i.e., S_1 and S_2). They are given as

$$\begin{aligned} S_1 &= \frac{1}{N} \sum_{n=0}^{N-1} \mathbf{s}[n] e^{-j(l_p - 0.5)n\omega_0}, \\ S_2 &= \frac{1}{N} \sum_{n=0}^{N-1} \mathbf{s}[n] e^{-j(l_p + 0.5)n\omega_0}, \end{aligned} \tag{5.22}$$

and their absolute values can be approximated by

$$|S_1| \approx \frac{A\cos(\beta_o \pi)}{2(0.5 - \beta_o)\pi} \text{ and } |S_2| \approx \frac{A\cos(\beta_o \pi)}{2(0.5 + \beta_o)\pi}. \tag{5.23}$$

Then, we can obtain the estimate of β_o as

$$\hat{\beta}_o = \frac{(|S_2| - |S_1|)/2}{|S_2| + |S_1|}. \tag{5.24}$$

By employing the Taylor expansion and keep the first order components, we have the approximation as follows

$$\hat{\beta}_o \approx \beta_o + \frac{R_2|\bar{S}_1|/|\bar{S}_2|}{(|\bar{S}_1| + |\bar{S}_2|)^2} n_1 + \frac{I_2|\bar{S}_1|/|\bar{S}_2|}{(|\bar{S}_1| + |\bar{S}_2|)^2} n_2 - \frac{R_1|\bar{S}_2|/|\bar{S}_1|}{(|\bar{S}_1| + |\bar{S}_2|)^2} n_3 - \frac{I_1|\bar{S}_2|/|\bar{S}_1|}{(|\bar{S}_1| + |\bar{S}_2|)^2} n_4. \tag{5.25}$$

$\bar{S}_1$ and $\bar{S}_1$ are the expectations of S_1 snd S_2, respectively. R_1, I_1, R_2 and I_2 are defined as

$$\begin{aligned} R_1 = \Re\{\bar{S}_1\},\ I_1 = \Im\{\bar{S}_1\}, \\ R_2 = \Re\{\bar{S}_2\},\ I_2 = \Im\{\bar{S}_2\}. \end{aligned} \tag{5.26}$$

Based on (5.25), we can decide that the estimation error can be well approximated by zero-mean Gaussian distribution. Similar to the analysis in previous section, we can obtain the variance of $\hat{\beta}_o$ as

$$\mathrm{var}\{\hat{\beta}_o\} = \frac{2\pi^2\sigma^2}{NA^2}(0.5 - \beta_o)^2(0.5 + \beta_o)^2 \cdot \left((0.5 - \beta_o)^2 + (0.5 + \beta_o)^2\right). \tag{5.27}$$

The estimate of β will be

$$\hat{\beta} = \hat{\beta}_o - \lfloor \hat{\beta}_o \rfloor, \tag{5.28}$$

and the variance of $\hat{\beta}$ is

$$\mathrm{var}\{\hat{\beta}\} = \mathrm{var}\{\hat{\beta}_o\} = \frac{2\sigma^2 r_1(\beta)}{NA^2}, \tag{5.29}$$

where $r_1(\beta)$ is given in (5.30).

$$r_1(\beta) = \begin{cases} \pi^2(0.5 - \beta)^2(0.5 + \beta)^2[(0.5 - \beta)^2 + (0.5 + \beta)^2]/\cos^2(\beta\pi), & \beta \in [0, 0.5) \\ \pi^2(0.5 - \beta)^2(1.5 - \beta)^2[(0.5 - \beta)^2 + (1.5 - \beta)^2]/\cos^2(\beta\pi), & \beta \in [0.5, 1). \end{cases} \tag{5.30}$$

As we can see in Figure 5.3, when $\beta \in (0.25, 0.75)$, $r_0(\beta) < r_1(\beta)$. This means we should use (5.12) or (5.21) to estimate β. On the other hand, when $\beta \in [0, 0.25) \cup (0.75, 1)$, we have $r_0(\beta) > r_1(\beta)$. That is to say, (5.24) and (5.28) provide better estimate in this case. As a result, after the estimation in the previous section, we need to decide if we should refine the results based on the method presented in this section. To be specific, when $\hat{\beta} \in [0, 0.25) \cup (0.75, 1)$, we should re-estimate β based on (5.24) and (5.28).

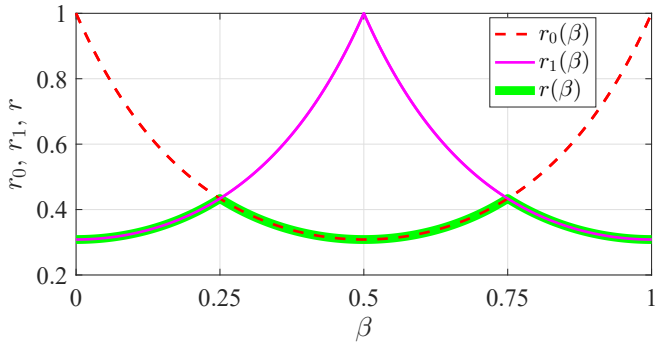

Figure 5.3: The numerical result of $r_0(\beta)$, $r_1(\beta)$ and $r(\beta)$, with respect to β.

Finally, we have the variance of $\hat{\beta}$ as

$$\text{var}\{\hat{\beta}\} = \frac{2\sigma^2}{NA^2} r(\beta), \tag{5.31}$$

where $r(\beta)$ is defined as

$$r(\beta) = \begin{cases} r_1(\beta) & \beta \in [0, 0.25) \cup [0.75, 1) \\ r_0(\beta) & \beta \in [0.25, 0.75). \end{cases} \tag{5.32}$$

With $\hat{\beta}$, we have the estimate of f_d as

$$\hat{f}_d = f_s(l + \hat{\beta})/N - f_c, \tag{5.33}$$

and the variance is

$$\mathrm{var}\{\hat{f}_d\} \approx \frac{f_s^2}{N^2} \cdot \mathrm{var}\{\hat{\beta}\} \approx \frac{2\sigma^2 f_s^2}{N^3 A^2} r(\beta), \tag{5.34}$$

as is verified by the simulation results in Figure 5.4.

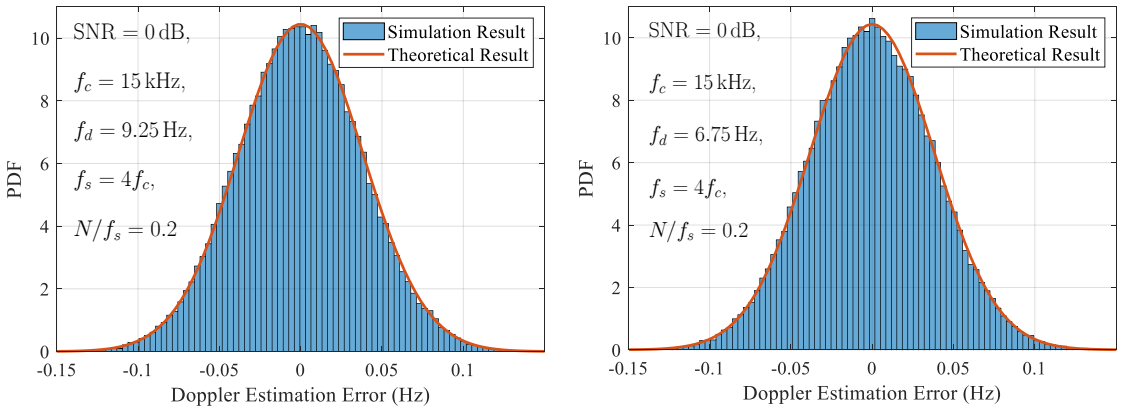

(a) $\beta = 0.85$. (b) $\beta = 0.35$.

Figure 5.4: The numerical and theoretical Doppler estimation error.

Besides, the amplitude can be estimated by the least square (LS) method. For $\hat{\beta} \in [0, 0.5)$, the LS estimate of A is

$$\hat{A} = \frac{2\pi(1-\hat{\beta})\hat{\beta}}{\sin(\hat{\beta}\pi)} \cdot \frac{(1-\hat{\beta})|S_p| + \hat{\beta}|S_s|}{(1-\hat{\beta})^2 + \hat{\beta}^2}. \tag{5.35}$$

For $\hat{\beta} \in [0.5, 1)$, we have the estimate of A as

$$\hat{A} = \frac{2\pi(1-\hat{\beta})\hat{\beta}}{\sin(\hat{\beta}\pi)} \cdot \frac{(1-\hat{\beta})|S_s| + \hat{\beta}|S_p|}{(1-\hat{\beta})^2 + \hat{\beta}^2}. \tag{5.36}$$

$\hat{A}$ can be used for SNR estimation, which is essential for the localization algorithm in the following section. To be specific, different Doppler shift measurements have different

accuracy due to different SNRs, and they should be assigned with different weights during the localization.

As we know, underwater acoustic signals generally experience severe multi-path effect. As the AUV transmits a sinusoidal wave, the target will receive a series of sinusoidal waves of different frequencies. However, in all these paths, only the line-of-sight (LoS) one provides information about the location of the target.

$$r(t) = \sum_{l=0}^{L-1} A_l \sin\left(2\pi\left(f_c + f_d^{(l)}\right)t + \theta_l\right) + n(t), \tag{5.37}$$

where $f_d^{(l)}$ is the Doppler shift of the l-th path and L is total path number. Generally, the LoS path is much stronger than the other paths, and it is the major contributor of the Doppler shift [55, 58, 127–129]. As a result, the LoS path signal is desired, while the other paths can be modeled as additive Gaussian noise, which increases the noise level [58]. It is expected that the system performance will degrade at the presence of multi-path effect, but the theoretical results in this section can still serve as a benchmark.

5.4 Doppler-Based Localization

As has been discussed in [5] and [66], by employing the AUVs for underwater localization, better performance can be achieved at lower cost. In this section, we present a low-complexity AUV-aided localization system based on Doppler shift measurements.

5.4.1 A Linear Localization Algorithm

The localization algorithm has two phases. In the first phase, the coarse result is obtained by extracting linear constraints on the unknowns. By doing this, we can obtain the

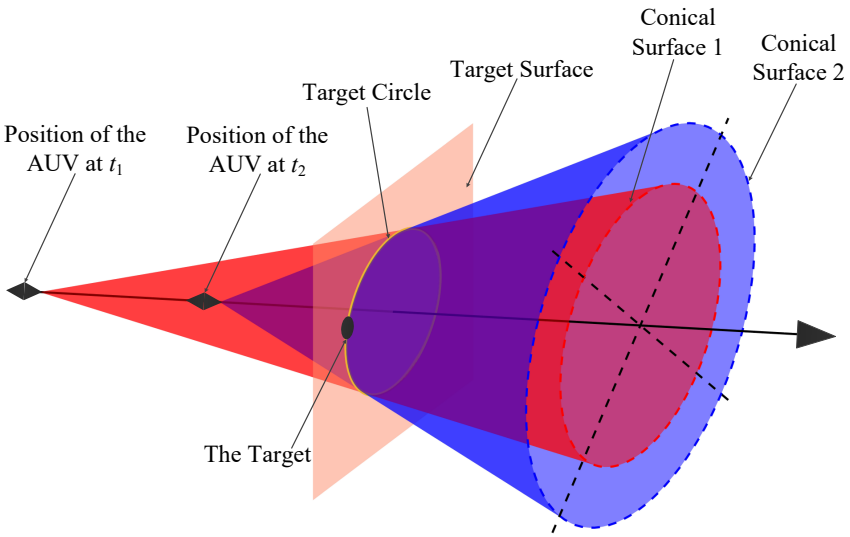

Figure 5.5: Geometrical intuition of the low-complexity algorithm.

localization result with linear algorithms, but we are not fully utilizing the information. Therefore, we add a second phase, during which the localization result will be refined.

5.4.1.1 Phase I: Coarse Localization

As we have discussed, we want to extract linear constraints on the target's location from the nonlinear equations. The intuition is presented in Figure 5.5. As we can see, the AUV moves on a straight line at a constant velocity. At t_1, it broadcasts the beacon signal, and the target can decide that it is on a conical surface by estimating the Doppler shift. At t_2, a second conical surface can be identified. The target must lie on the intersection of these two conical surfaces, which is a circle, and that circle must lie on a specific surface. As long as we can find that surface, we can establish a linear equation with respect to the target's location. When the AUV moves in different directions, we can obtain a series of

linear equations, by solving which the target's position can be estimated. We will unveil the mathematical details of this process in the following discussions.

Assume that the AUV is moving on the m-th direction at a constant speed $\mathbf{v}_m$. We have two Doppler shift measurements $f_D^{(m,i)}$ and $f_D^{(m,j)}$, at the i-th and the j-th broadcast periods, respectively. Given that the positions of the AUV at these two periods are $\mathbf{x}_{m,i}$ and $\mathbf{x}_{m,j}$, the following equations can then be constructed

$$(\mathbf{x}^T - \mathbf{x}_{m,i}^T)\mathbf{v}_m = c_{m,i}d_{m,i}, \tag{5.38a}$$

$$(\mathbf{x}^T - \mathbf{x}_{m,j}^T)\mathbf{v}_m = c_{m,j}d_{m,j}, \tag{5.38b}$$

where $c_{m,i} = cf_D^{(m,i)}/f_c$ and $c_{m,j} = cf_D^{(m,j)}/f_c$. For (5.38a), we square both sides, and multiply them with $c_{m,j}^2$; for (5.38b), we square both sides and multiply them with $c_{m,i}^2$. We can then obtain

$$c_{m,j}^2(\mathbf{x}^T\mathbf{v}_m - \mathbf{x}_{m,i}^T\mathbf{v}_m)^2 = c_{m,i}^2c_{m,j}^2\|\mathbf{x} - \mathbf{x}_{m,i}\|^2, \tag{5.39a}$$

$$c_{m,i}^2(\mathbf{x}^T\mathbf{v}_m - \mathbf{x}_{m,j}^T\mathbf{v}_m)^2 = c_{m,i}^2c_{m,j}^2\|\mathbf{x} - \mathbf{x}_{m,j}\|^2. \tag{5.39b}$$

Subtract (5.39b) from (5.39a), leading to

$$\begin{aligned} &c_{m,j}^2(\mathbf{x}^T\mathbf{v}_m - \mathbf{x}_{m,i}^T\mathbf{v}_m)^2 - c_{m,i}^2(\mathbf{x}^T\mathbf{v}_m - \mathbf{x}_{m,j}^T\mathbf{v}_m)^2 \\ =&c_{m,i}^2c_{m,j}^2(2\Delta T_{m,i,j}\mathbf{x}^T\mathbf{v}_m + \|\mathbf{x}_{m,i}\|^2 - \|\mathbf{x}_{m,j}\|^2), \end{aligned} \tag{5.40}$$

where $\Delta T_{m,i,j}$ denotes the time lapse between the i-th and j-th time slots, and it satisfies $\mathbf{x}_{m,j} - \mathbf{x}_{m,i} = \Delta T_{m,i,j}\mathbf{v}_m$. Define $\omega_m = \mathbf{x}^T\mathbf{v}_m$, and we have

$$\begin{aligned} &c_{m,j}^2(\omega_m - \mathbf{x}_{m,i}\mathbf{v}_m)^2 - c_{m,i}^2(\omega_m - \mathbf{x}_{m,j}\mathbf{v}_m)^2 \\ =&c_{m,i}^2c_{m,j}^2(2\Delta T_{m,i,j}\omega_m + \|\mathbf{x}_{m,i}\|^2 - \|\mathbf{x}_{m,j}\|^2). \end{aligned} \tag{5.41}$$

Equation (5.41) can be reorganized as

$$a_m\omega_m^2 + b_m\omega_m + c_m = 0, \tag{5.42}$$

where

$$\begin{aligned} a_m =& (c_{m,j}^2 - c_{m,i}^2), \\ b_m =& 2\left(-c_{m,j}^2\mathbf{x}_{m,i}^T\mathbf{v}_m + c_{m,i}^2\mathbf{x}_{m,j}^T\mathbf{v}_m - c_{m,i}^2c_{m,j}^2\Delta T_{m,i,j}\right), \\ c_m =& c_{m,j}^2(\mathbf{x}_{m,i}^T\mathbf{v}_m)^2 - c_{m,i}^2(\mathbf{x}_{m,j}^T\mathbf{v}_m)^2 + \Delta T_{m,i,j}c_{m,i}^2c_{m,j}^2(\mathbf{x}_{m,i} + \mathbf{x}_{m,j})^T\mathbf{v}_m. \end{aligned} \tag{5.43}$$

By solving (5.42), we will obtain two roots as

$$\hat{\omega}_m = \frac{-b_m \pm \sqrt{b_m^2 - 4a_mc_m}}{2a_m}. \tag{5.44}$$

These two roots represent two parallel surfaces, and the target can only lie on one of them. In Figure 5.6, we show these two surfaces in top view. As we can see, the intersection of two conical surfaces lies on the true target surface. However, if we extend the second conical surface to the opposite direction, it will have another intersection with the first conical surface, and that gives us the fake target surface. Mathematically, the fake solution originates from the squaring operations in (5.39a) and (5.39b). To identify the true target surface, we notice that ω_m must satisfy the following inequality:

$$(\omega_m - \mathbf{x}_{m,k}^T\mathbf{v}_m)f_D^{(m,k)} = (\omega_m - \mathbf{x}_{m,k}^T\mathbf{v}_m)^2 f_c/d_{m,k}/c > 0, \tag{5.45}$$

where we implicitly replace $f_D^{(m,k)}$ with the left hand side of (5.1).

Note that we can use different combinations of $i, j \in \{1, 2, \cdots, K\}$ to estimate ω_m and average out noise. Assume we have obtained the valid solution as $\hat{\omega}_m$, and the target surface will be determined by

$$\mathbf{v}_m^T\mathbf{x} = \hat{\omega}_m. \tag{5.46}$$

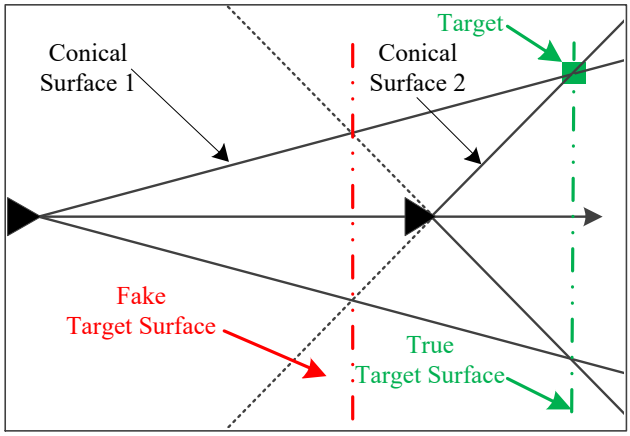

Figure 5.6: The fake target surface and the true target surface.

This process will be repeated on M directions, and the following linear equation can be obtained:

$$\mathbf{V}\mathbf{x} = \boldsymbol{\omega}, \tag{5.47}$$

where $\boldsymbol{\omega} = [\hat{\omega}_1, \hat{\omega}_2, \cdots, \hat{\omega}_M]^T$ and $\mathbf{V} = [\mathbf{v}_1, \mathbf{v}_2, \cdots, \mathbf{v}_M]^T$. We can then employ the least square estimator to obtain the coarse estimate of the target's location, given by

$$\hat{\mathbf{x}}_c = \left(\mathbf{V}^T\mathbf{V}\right)^{-1}\mathbf{V}^T\boldsymbol{\omega}. \tag{5.48}$$

As we can see, the complexity of this algorithm grows linearly with the number of Doppler measurements. Besides, it should be noted that c is assumed to be known in this algorithm. Generally, it is not far away from 1500 m/s, and we can employ this value for the coarse estimation.

5.4.1.2 Phase II: Refinement of the Result

In *Phase I*, we are only partially using the information provided by the Doppler measurements. For example, in Figure 5.5, the Doppler estimates tell us that the target lies on a specific circle, but we are extending the searching area to a surface, which leads to information loss. As a result, we should find a way to further extract the available information and try to improve localization accuracy.

After Phase I, the coarse estimate of $\boldsymbol{\theta}$ is obtained as $\hat{\boldsymbol{\theta}}_c = [\hat{\mathbf{x}}_c^T, \hat{c}_c]^T$, where $\hat{c} = 1500\,\mathrm{m/s}$. Let $\Delta\boldsymbol{\theta}$ be the estimation error, i.e., $\hat{\boldsymbol{\theta}}_c = \boldsymbol{\theta} + \Delta\boldsymbol{\theta}$, and $\Delta\boldsymbol{\theta}$ can be approximated by the first order Taylor expansion as

$$\mathbf{f}(\hat{\boldsymbol{\theta}}_c) - \mathbf{f}(\boldsymbol{\theta}) \approx \mathbf{H}\Delta\boldsymbol{\theta}. \tag{5.49}$$

$\mathbf{H}$ is the Jacobian matrix given by

$$\mathbf{H} = \frac{\partial \mathbf{f}(\boldsymbol{\theta})}{\partial \boldsymbol{\theta}} = [\mathbf{H}_1^T, \mathbf{H}_2^T, \cdots, \mathbf{H}_M^T]^T, \tag{5.50}$$

where $\mathbf{H}_m$ is

$$\mathbf{H}_m = \begin{bmatrix} \frac{\partial f_{m,1}(\boldsymbol{\theta})}{\partial x} & \frac{\partial f_{m,1}(\boldsymbol{\theta})}{\partial y} & \frac{\partial f_{m,1}(\boldsymbol{\theta})}{\partial z} & \frac{\partial f_{m,1}(\boldsymbol{\theta})}{\partial c} \\ \frac{\partial f_{m,2}(\boldsymbol{\theta})}{\partial x} & \frac{\partial f_{m,2}(\boldsymbol{\theta})}{\partial y} & \frac{\partial f_{m,2}(\boldsymbol{\theta})}{\partial z} & \frac{\partial f_{m,2}(\boldsymbol{\theta})}{\partial c} \\ \vdots & \vdots & \vdots & \vdots \\ \frac{\partial f_{m,K}(\boldsymbol{\theta})}{\partial x} & \frac{\partial f_{m,K}(\boldsymbol{\theta})}{\partial y} & \frac{\partial f_{m,K}(\boldsymbol{\theta})}{\partial z} & \frac{\partial f_{m,K}(\boldsymbol{\theta})}{\partial c} \end{bmatrix}. \tag{5.51}$$

The partial derivatives in (5.51) are given by

$$\begin{aligned}
\frac{\partial f_{m,k}(\boldsymbol{\theta})}{\partial x} &= \frac{f_c}{c} \cdot \left[\frac{v_x^{(m)}}{d_{m,k}} - \frac{(\mathbf{x} - \mathbf{x}_{m,k})^T \mathbf{v}_m (x - x_{m,k})}{d_{m,k}^3} \right] \\
\frac{\partial f_{m,k}(\boldsymbol{\theta})}{\partial y} &= \frac{f_c}{c} \cdot \left[\frac{v_y^{(m)}}{d_{m,k}} - \frac{(\mathbf{x} - \mathbf{x}_{m,k})^T \mathbf{v}_m (y - y_{m,k})}{d_{m,k}^3} \right] \\
\frac{\partial f_{m,k}(\boldsymbol{\theta})}{\partial z} &= \frac{f_c}{c} \cdot \left[\frac{v_z^{(m)}}{d_{m,k}} - \frac{(\mathbf{x} - \mathbf{x}_{m,k})^T \mathbf{v}_m (z - z_{m,k})}{d_{m,k}^3} \right] \\
\frac{\partial f_{m,k}(\boldsymbol{\theta})}{\partial c} &= -\frac{f_c}{c^2} \cdot \frac{(\mathbf{x} - \mathbf{x}_{m,k})^T \mathbf{v}_m}{d_{m,k}}.
\end{aligned} \tag{5.52}$$

$\Delta\boldsymbol{\theta}$ can then be estimated with the weighted least square algorithm. However, $\mathbf{H}$ is unavailable in practical scenarios, because $\boldsymbol{\theta}$ is unknown. As a result, we need to use $\mathbf{H}_c = \frac{\partial \mathbf{f}(\boldsymbol{\theta})}{\partial \boldsymbol{\theta}} \big|_{\boldsymbol{\theta}=\hat{\boldsymbol{\theta}}_c}$ instead, and the final result will be

$$\Delta\hat{\boldsymbol{\theta}} \approx (\mathbf{H}_c^T \mathbf{W} \mathbf{H}_c)^{-1} \mathbf{H}_c^T \mathbf{W} \mathbf{f}(\hat{\boldsymbol{\theta}}_c), \tag{5.53}$$

where $\mathbf{W}$ is the weight matrix. Define $w_{m,k}$ as

$$w_{m,k} = A_{m,k}^2 / r(\beta_{m,k}) \propto \frac{1}{var\left\{ f_D^{(m,k)} \right\}}, \tag{5.54}$$

where $A_{m,k}$ is unavailable and we need to estimate it through (5.35) or (5.36). The weight matrix is given by

$$\mathbf{W} = \text{diag}\{[\mathbf{w}_1^T, \mathbf{w}_2^T, \cdots, \mathbf{w}_M^T]\}, \tag{5.55}$$

where $\mathbf{w}_m = [w_{m,1}, w_{m,2}, \cdots, w_{m,K}]^T$.

Then, the coarse estimate $\hat{\boldsymbol{\theta}}_c$ can be refined as

$$\hat{\boldsymbol{\theta}} = \hat{\boldsymbol{\theta}}_c - \Delta\hat{\boldsymbol{\theta}}. \tag{5.56}$$

The refined estimate of $\mathbf{x}$ and c will be $\hat{\mathbf{x}} = \hat{\boldsymbol{\theta}}[1:3]$ and $\hat{c} = \hat{\boldsymbol{\theta}}[4]$, respectively. It should be noted that this process can be iterated to further improve the estimation accuracy.

Based on our simulations, one or two iterations should be enough to provide very accurate localization results.

5.4.2 Time Synchronization Based on Localization Results

After localization, passive time synchronization can be easily achieved. To be specific, the AUV can broadcast signals with time stamps, while the acoustic sensors will receive the signal and synchronize their local clocks.

The time stamp of the m,k-th packet is $t_{m,k}$, and it is received by the target node at local time $r_{m,k}$.

$$\|\mathbf{x}-\mathbf{x}_{m,k}\| = c\cdot(s\cdot r_{m,k}+o-t_{m,k}) \tag{5.57}$$

Then, we can construct the following equation:

$$\hat{\mathbf{d}} = \hat{c}\cdot(s\cdot\mathbf{r}+o\cdot\mathbf{1}_{MK}-\mathbf{t}), \tag{5.58}$$

where $\hat{\mathbf{d}} = [\hat{\mathbf{d}}_1^T,\hat{\mathbf{d}}_2^T,\cdots,\hat{\mathbf{d}}_M^T]^T$, $\hat{\mathbf{d}}_m = [\hat{d}_{m,1},\hat{d}_{m,2},\cdots,\hat{d}_{m,K}]^T$. $\hat{\mathbf{r}} = [\hat{\mathbf{r}}_1^T,\hat{\mathbf{r}}_2^T,\cdots,\hat{\mathbf{r}}_M^T]^T$, $\hat{\mathbf{r}}_m = [\hat{r}_{m,1},\hat{r}_{m,2},\cdots,\hat{r}_{m,K}]^T$. $\hat{\mathbf{t}} = [\hat{\mathbf{t}}_1^T,\hat{\mathbf{t}}_2^T,\cdots,\hat{\mathbf{t}}_M^T]^T$, $\hat{\mathbf{t}}_m = [\hat{t}_{m,1},\hat{t}_{m,2},\cdots,\hat{t}_{m,K}]^T$.

With MK observations, s and o can be estimated with least square method. To be specific, (5.58) can be reorganized as

$$\mathbf{t}_t = \mathbf{T}\boldsymbol{\alpha} \tag{5.59}$$

where $\mathbf{t}_t = \hat{\mathbf{d}}/\hat{c}+\mathbf{t}$, $\mathbf{T} = [\mathbf{r},\mathbf{1}_{MK}]$, and $\boldsymbol{\alpha} = [s,o]^T$. Then, s and o can be estimated as

$$\hat{\boldsymbol{\alpha}} = (\mathbf{T}^T\mathbf{T})^{-1}\mathbf{T}^T\mathbf{t}_t. \tag{5.60}$$

5.5 Performance Analysis

5.5.1 Positioning Error of the System

Due to the estimation error in Doppler shifts, the localization error is inevitable. Suppose $\mathbf{f}_D$ contains the Doppler shift estimates and is given by $\mathbf{f}_D = \left[\mathbf{f}_{D,1}^T, \mathbf{f}_{D,2}^T, \cdots, \mathbf{f}_{D,M}^T\right]^T$, where $\mathbf{f}_{D,m}$ is given by $\mathbf{f}_{D,m} = \left[f_D^{(m,1)}, f_D^{(m,2)}, \cdots, f_D^{(m,K)}\right]^T$. Let $\boldsymbol{\mu} = E\{\mathbf{f}_D|\mathbf{x}, c\}$ denote the accurate Doppler shifts, and the Doppler estimation error vector will be $\mathbf{e_f} = \mathbf{f}_D - \boldsymbol{\mu}$, which leads to estimation error in $\hat{\boldsymbol{\theta}}$. If we take the first order Taylor expansion, we have $\mathbf{e_f} \approx \mathbf{H}\mathbf{e}_{\boldsymbol{\theta}}$, where $\mathbf{e}_{\boldsymbol{\theta}} = \hat{\boldsymbol{\theta}} - \boldsymbol{\theta}$ is the estimation error. Equivalently, we have

$$\mathbf{e}_{\boldsymbol{\theta}} = \left(\mathbf{H}^T\mathbf{W}\mathbf{H}\right)^{-1}\mathbf{H}^T\mathbf{W}\mathbf{e_f}. \tag{5.61}$$

The covariance matrix of $\hat{\boldsymbol{\theta}}$ is given by

$$\mathbf{R}_{\hat{\boldsymbol{\theta}}} = E\left\{\mathbf{e}_{\boldsymbol{\theta}}\mathbf{e}_{\boldsymbol{\theta}}{}^T\right\} = (\mathbf{H}^T\mathbf{W}\mathbf{H})^{-1}\mathbf{H}^T\mathbf{W}E\left\{\mathbf{e_f}\mathbf{e_f}{}^T\right\}\mathbf{W}\mathbf{H}(\mathbf{H}^T\mathbf{W}\mathbf{H})^{-1} \approx (\mathbf{H}^T\boldsymbol{\Sigma}\mathbf{H})^{-1}. \tag{5.62}$$

where $\boldsymbol{\Sigma} = E\{(\mathbf{f}_D - \boldsymbol{\mu})(\mathbf{f}_D - \boldsymbol{\mu})^T|\mathbf{x}, c\}$ gives the covariance matrix of $\mathbf{f}_D$. Generally, the estimation error of different Doppler shifts is independent, and $\boldsymbol{\Sigma}$ is a diagonal matrix. In the last step of (5.62), we implicitly employ the approximation $\mathbf{W} \approx N^3/(2\sigma^2 f_s^2) \cdot \boldsymbol{\Sigma}^{-1}$.

The estimation error of $\mathbf{x}$ is

$$\mathbf{e_x} = \hat{\mathbf{x}} - \mathbf{x}. \tag{5.63}$$

The estimation error of c is

$$e_c = \hat{c} - c = \mathbf{e}_{\boldsymbol{\theta}}[4]. \tag{5.64}$$

From another perspective, $\mathbf{R}_{\hat{\boldsymbol{\theta}}}$ can also be written as

$$\mathbf{R}_{\hat{\boldsymbol{\theta}}} = E\left\{\mathbf{e}_{\boldsymbol{\theta}}\mathbf{e}_{\boldsymbol{\theta}}{}^{T}\right\} = \begin{bmatrix} \mathbf{R}_{\hat{\mathbf{x}}} & \mathbf{R}_{\hat{\mathbf{x}},\hat{c}} \\ \mathbf{R}_{\hat{\mathbf{x}},\hat{c}}^{T} & R_{\hat{c}} \end{bmatrix}. \tag{5.65}$$

$\mathbf{R}_{\hat{\mathbf{x}}}$ is the covariance matrix of $\hat{\mathbf{x}}$, $R_{\hat{c}}$ is the variance of $\hat{c}$, and $\mathbf{R}_{\hat{\mathbf{x}},\hat{c}} = E\{(\hat{\mathbf{x}} - \mathbf{x})(\hat{c} - c)\}$. The mean squared positioning error is

$$MSE\{\hat{\mathbf{x}}\} = \mathrm{tr}\{\mathbf{R}_{\hat{\mathbf{x}}}\}. \tag{5.66}$$

5.5.2 CRLB of the Doppler-based Localization System

As we have demonstrated in Section 5.3, the Doppler estimation error can be well approximated by zero-mean Gaussian distribution, and the variance is given by (5.34). In this section, we will derive the FIM, which can be used to quantify the amount of target's location information that can be extracted from the Doppler shift estimates.

To start with, the probability density function of $\mathbf{f}_D$ is given by

$$p(\mathbf{f}_D|\mathbf{x}, c) = (2\pi)^{-NK/2} \cdot |\boldsymbol{\Sigma}|^{-1/2} \cdot \exp\left(-\frac{1}{2}(\mathbf{f}_D - \boldsymbol{\mu})^T \boldsymbol{\Sigma}^{-1}(\mathbf{f}_D - \boldsymbol{\mu})\right), \tag{5.67}$$

while its logarithm (i.e., $l(\mathbf{f}_D|\mathbf{x}, c) = \ln p(\mathbf{f}_D|\mathbf{x}, c)$) is given by

$$l(\mathbf{f}_D|\boldsymbol{\theta}) = \frac{-NK}{2}\ln 2\pi - \frac{1}{2}\ln|\boldsymbol{\Sigma}| - \frac{1}{2}(\mathbf{f}_D - \boldsymbol{\mu})^T \boldsymbol{\Sigma}^{-1}(\mathbf{f}_D - \boldsymbol{\mu}). \tag{5.68}$$

Based on our analysis in Appendix B.2, the FIM $\mathbf{F}$ is given as

$$\mathbf{F} = \frac{\partial \boldsymbol{\mu}^T}{\partial \boldsymbol{\theta}} \boldsymbol{\Sigma}^{-1} \frac{\partial \boldsymbol{\mu}}{\partial \boldsymbol{\theta}} + \frac{1}{2}\left\{\frac{\partial \boldsymbol{\sigma}^T}{\partial \boldsymbol{\theta}} \boldsymbol{\Sigma}^{-2} \frac{\partial \boldsymbol{\sigma}}{\partial \boldsymbol{\theta}}\right\}, \tag{5.69}$$

where we have $\boldsymbol{\sigma} = \mathrm{diag}\{\boldsymbol{\Sigma}\}$. In Appendix B.3, we have justified the following equations:

$$\frac{\partial \boldsymbol{\mu}}{\partial \boldsymbol{\theta}} = \mathbf{H}, \text{ and } \frac{\partial \boldsymbol{\sigma}}{\partial \boldsymbol{\theta}} = \mathbf{P}\mathbf{H}, \tag{5.70}$$

where $\mathbf{P} = \text{diag}([\mathbf{p}_1^T, \mathbf{p}_2^T, \cdots, \mathbf{p}_M^T])$, and the k-th element of $\mathbf{p}_m$ is given as

$$\mathbf{p}_m[k] = \frac{2f_s\sigma^2}{N^2 A_{m,k}^2} \cdot \frac{dr}{d\beta_{m,k}}. \tag{5.71}$$

Then, the FIM can be reorganized as

$$\mathbf{F} = \mathbf{H}^T\boldsymbol{\Sigma}^{-1}\mathbf{H} + \frac{1}{2}\left\{\mathbf{H}^T\mathbf{P}\boldsymbol{\Sigma}^{-2}\mathbf{P}\mathbf{H}\right\} = \mathbf{H}^T\left(\boldsymbol{\Sigma}^{-1} + \frac{1}{2}\mathbf{P}\boldsymbol{\Sigma}^{-2}\mathbf{P}\right)\mathbf{H}. \tag{5.72}$$

The l-th diagonal element in $\boldsymbol{\Sigma}^{-1}$ is

$$\boldsymbol{\Sigma}^{-1}[l,l] = \frac{N^3 A_{m,k}^2}{2f_s^2\sigma^2 r(\beta_{m,k})} = \frac{NT_c^2 A_{m,k}^2}{2\sigma^2 r(\beta_{m,k})}, \tag{5.73}$$

where $T_c = N/f_s$ is the total sampling time. The l-th diagonal element in $\frac{1}{2}\mathbf{P}\boldsymbol{\Sigma}^{-2}\mathbf{P}$ is

$$\left(\frac{1}{2}\mathbf{P}\boldsymbol{\Sigma}^{-2}\mathbf{P}\right)[l,l] = \left(\frac{2f_s^2\sigma^2}{N^3 A_{m,k}^2} \cdot r(\beta_{m,k})\right)^{-2}\left(\frac{2f_s\sigma^2}{N^2 A_{m,k}^2} \cdot \frac{dr}{d\beta_{m,k}}\right)^2 = \frac{T_c^2(dr/d\beta_{m,k})^2}{2r^2(\beta_{m,k})}. \tag{5.74}$$

As we can see, the l-th diagonal element in $\boldsymbol{\Sigma}^{-1}$ is proportional to N, while the corresponding value in $\frac{1}{2}\mathbf{P}\boldsymbol{\Sigma}^{-2}\mathbf{P}$ is a constant. Generally, N is very large, which renders the second part negligible. When N is infinitely large, we have the limit of $\mathbf{F}/N$ as

$$\lim_{N\to\infty} \mathbf{F}/N = \mathbf{H}^T\boldsymbol{\Sigma}_N^{-1}\mathbf{H}, \tag{5.75}$$

where $\boldsymbol{\Sigma}_N = N\boldsymbol{\Sigma}$. Or equivalently, the asymptotic FIM is

$$\mathbf{F} \sim \mathbf{H}^T\boldsymbol{\Sigma}^{-1}\mathbf{H}. \tag{5.76}$$

This result is identical to the inverse of $\mathbf{R}_{\hat{\boldsymbol{\theta}}}$ in (5.62), which means the two-phase algorithm can asymptotically achieve the CRLB. Although the result in (5.62) is only approximation by taking the first order Taylor expansion, it is actually very accurate, as will be shown in simulations.

5.5.3 Computational Complexity

The localization algorithm contains three steps. The first step is to estimate Doppler shifts. The Doppler estimation algorithm involves the FFT, and the complexity is at the order of $\mathcal{O}\{N \log_2 N\}$. For MK measurements, the overall complexity is $MK\mathcal{O}\{N \log_2 N\}$. The second step is the coarse localization. In (5.44), the computation complexity of calculating ω_m's is at the order of $\mathcal{O}\{MK\}$. In (5.48), the complexity of $\mathbf{V}^T\mathbf{V}$ is at the order of $\mathcal{O}\{M\}$, while that of matrix inversion is $\mathcal{O}\{M^3\}$. In *Phase II*, the complexity of calculating the individual components is at the order of $\mathcal{O}\{MK\}$. To compute (5.54), the complexity is also at the level of $\mathcal{O}\{MK\}$. Generally, M and K are much smaller than N. As a result, the major computational complexity lies in the Doppler estimation, and thus, is at the order of $\mathcal{O}\{MKN \log_2 N\}$. To modern central processors, this complexity is acceptable even when N is very large. Besides, if we have some statistical information about the Doppler shifts, we do not need to compute the whole spectrum, and the FFT can be avoided. To be specific, we only need to analyze the spectrum for a specific frequency range, and the complexity can be reduced to the order of $\mathcal{O}\{MKN\}$.

5.6 Numerical Evaluations

In this section, we will conduct simulations to verify the analytical results in previous sections. To be specific, we will show that the approximated 3D positioning error is accurate and the asymptotical CRLB can be closely approached. Besides, we will show how different parameters contribute to the overall performance.

5.6.1 The Impact of Iteration Number and SNR

As we have briefly mentioned in Section 5.4.1, if we repeat the refinement process in *Phase II*, the localization accuracy can be improved. Simulations are conducted and the results are presented in Figure 5.7. f_c is set as 15 kHz, the sampling time is fixed as 0.1 s, and sampling frequency is 60 kHz. When the iteration number (N_{iter}) equals zeros, there is a discernable gap between the CRLB and the MSE of the presented algorithm, especially in low SNR regime. However, by adding one iteration, the localization accuracy can be substantially improved. By increasing the iteration number to 2 or 3, the localization error will decrease continuously, but the performance gain is negligible. Besides, we notice that as SNR increases, localization error decreases constantly, because Doppler shift can be more accurately estimated. As a matter of fact, the variance of 3D localization error is inversely proportional to the SNR, as we can observe in (5.62).

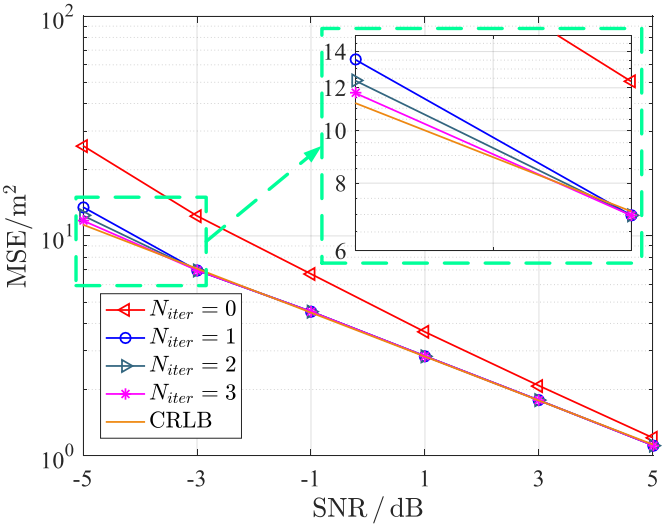

Figure 5.7: The impact of iteration number and SNR on localization accuracy.

5.6.2 The Impact of N and SNR

Intuitively, as we increase N or SNR, the accuracy of Doppler estimation will be improved. As a result, localization accuracy should be improved. In this section, we will evaluate the system performance for different N and SNR values. The sampling frequency is fixed. Therefore, the increase of N is equivalent to the increase of sampling time. Based on our theoretical analysis, the variance of positioning results is inversely proportional to N^3. The simulation results are presented in Figure 5.8. Every time we double the number of

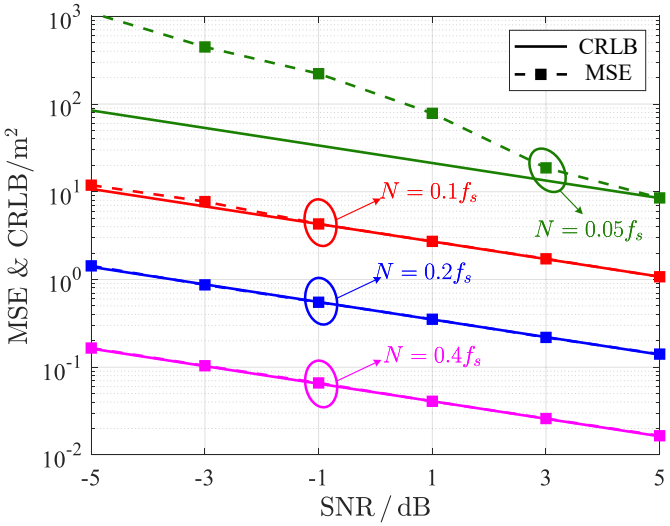

Figure 5.8: The impact of N on localization accuracy.

samples, the MSE of localization result will be reduced by a factor of 8, which is consistent with our analysis. Besides, we notice that for $N = 0.05f_s$, the proposed algorithm has a significant performance gap compared to CRLB. This is because our analysis is based on first order Taylor expansion, which is only accurate for small Doppler shift estimation

error. However, when N is not large enough, Doppler estimation error will be significant and the result in (5.66) is no longer accurate.

5.6.3 The impact of M and K

When we increase M and K, the localization error is expected to decrease. In this section, we conduct simulations for different combinations of M and K. The results are shown in Figure 5.9. As we can see, M is increased from 2 to 4, and then to 6, while K varies in

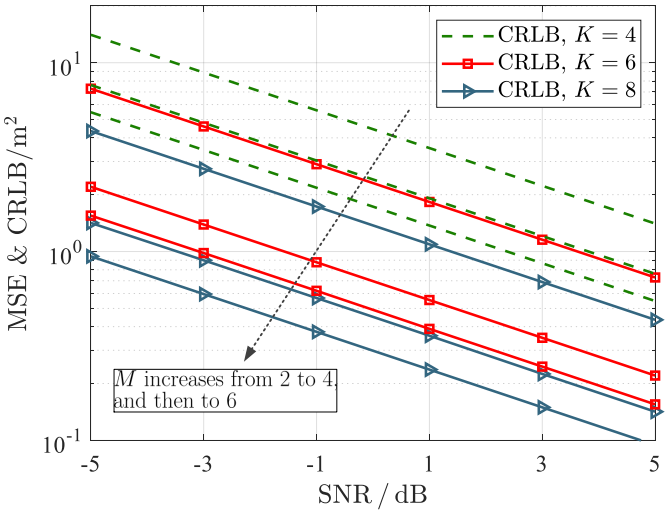

Figure 5.9: The impact of M and K on localization accuracy.

$\{4, 6, 8\}$. Generally, by increasing M and K, more measurements can be obtained, and better localization accuracy can be achieved. However, the impact of M and K is more complicated than that of N. As has been pointed out by many researchers, the trajectory of the AUV has a significant impact on the localization accuracy. Therefore, depending on the trajectory of the AUV, the increase of M and K may show significant or negligible

influence on performance.

5.7 Summary

In this chapter, we thoroughly investigated the possibility of employing Doppler shifts for underwater localization. A low complexity algorithm for Doppler estimation was presented, and the estimation error can be well approximated by zero-mean Gaussian distribution. Based on the Doppler estimates, a two-phase linear algorithm was employed to extract high-accuracy position information of the target devices. Both the closed-form localization error and the CRLB were provided. They proved to be consistent for reasonably small Doppler estimation error. Besides, extensive simulations were conducted to verify the theoretical results. Overall, we can see that the Doppler-based underwater localization system has great advantages over the ToA- or TDoA-based ones in some aspects, and it can also work complementarily with the conventional systems.

Chapter 6

Proactive Underwater Target Detection and Tracking Based on LFM Signals

In Chapter 4, an AUV is employed to locate a target equipped with a hydrophone. In Chapter 5, this requirement is relaxed, and the target only needs an acoustic device being able to generate sinusoidal waves at a fixed frequency. However, what if the target is totally silent and cannot transmit or receive any acoustic signals? This kind of examples include icebergs, whales, leaked oil, etc. For these scenarios, one AUV will not be enough and multiple anchors are required. In previous sections, we have talked about the localization and time synchronization in larger-scale underwater acoustic sensor networks. The localized and synchronized nodes can then server as anchors for proactive underwater target detection and tracking, which will be investigated in this chapter. Although the system

model will be presented based on fixed anchors, the algorithms can be easily modified to work with mobile ones. [1]

6.1 Introduction

In Section 2.2.4, we already briefly introduced the CAS based on LFM signals. Such a system contains a huge number of location-aware nodes, serving as anchors. A small number of them are transmitting signals while all the others are listening. A major challenge in implementation is the computational complexity. Although the fast DFrFT algorithms proposed in [71] have already reduced the computational complexity to great extent, we still need to process very large two dimensional spectrum. If there are multiple objects, it will become highly complicated. To solve this problem, we propose a machine learning-based approach to first roughly estimate the position of the peak, and then conduct over-sampling on the small area around the peak. This is possible depending on the following observation: if a target exists, we will be able to find an "X" pattern on the spectrum, and the cross point is dependent on the target's location and velocity. If multiple targets exist, there will be multiple "X" patterns. As we know, there are many machine-learning architectures, and the Convolutional Neural Networks (CNNs) are specifically designed for pattern recognition. We will thus design our system based on a CNN. The major advantage of this approach is that it allows us to compute the discrete spectrum with much larger sampling interval. With the under-sampled spectrum, although we won't be able to accurately estimate the

[1] The presented work has been published in [J1]: Z. Gong, C. Li and F. Jiang, "A Machine Learning-based Approach for Auto-Detection and Localization of Targets in Underwater Acoustic Array Networks," *IEEE Trans. Veh. Technol.*, accepted, to appear in 2020.

position of the peak, the "X" patterns can still be reserved, which allows us to perform coarse estimation. The computational complexity can thus be significantly reduced.

In this chapter, we will present an innovative underwater localization architecture based on CNN and FrFT. The system is composed of three parts: the FrFT-based spectrum analysis, the CNN-based auto-detection of the "X" patterns, and the joint estimation of target's location and velocity. The topics are summarized as follows.

1) We will see that the MLE of the initial frequency and frequency rate can be obtained by identifying the peak of the FrFT of a LFM signal contaminated by white Gaussian noise. The parameters are designed carefully for efficient signal processing.

2) A CNN architecture will be presented for automatic detection of the targets and rough position of the peak in the two dimensional spectrum.

3) A low-complexity algorithm will be designed for joint estimation of target's location and velocity based on the FrFT of the received signals.

4) Extensive simulations will be conducted and the results show that the presented framework has great potential in achieving accurate object detection and tracking.

The rest of this paper is organized as follows. In Section 6.2, the system model is presented in details, and the discrete FrFT (DFrFT) algorithm and some important properties will also be unveiled. In Section 6.3, a low-complexity algorithm for joint estimation of target's location and velocity is proposed. In Section 6.4, the CNN-based auto-detection system is introduced, including the system architecture, data preparation, and training details. The simulation results are presented in Section 6.5, and the last section summarizes this chapter.

6.2 System Model and The DFrFT Algorithm

6.2.1 System Model

We will start with a simple 2D model with only two nodes: node 0 is transmitting a probe signal periodically, while node 1 is listening. When a target enters the surveillance area, the signal transmitted by node 0 will be reflected by the target and received by node 1, as illustrated in Figure 6.1.

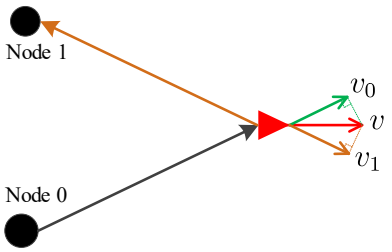

Figure 6.1: System model illustration.

Suppose node 0 and node 1 are located at $\mathbf{x}_0 = [x_0, y_0]^T$ and $\mathbf{x}_1 = [x_1, y_1]^T$. The target moves at a constant speed of $\mathbf{v} = [v_x, v_y]^T$. Node 0 transmits a LFM signal from $t = 0$ to $t = T$, given by

$$s(t) = Ae^{j(2\pi f_0 t + k\pi t^2)}, \ t \in [0, \ T], \tag{6.1}$$

where f_0 is the initial frequency and k is the frequency rate.

The received signal at node 1 will be

$$r(t) = P_0 s(\rho(t - \tau)), \tag{6.2}$$

which is another LFM signal. P_0 is the propagation loss and $P_0 A$ is the amplitude of the

received signal. τ is the delay of the received signal, and it is proportional to the sum of the distances between nodes and the target, at the time the signal first reached the target. ρ is the time scaling factor (Doppler rate), given by

$$\rho = \frac{c - v_0}{c + v_1}, \tag{6.3}$$

where v_0 and v_1 are the radial speeds of the target with respect to node 0 and 1. c is the average underwater sound speed. If the target is moving away from the node, the velocity is positive. Otherwise, it will be negative. Suppose the target's position is $\mathbf{x} = [x, y]^T$ at $t = 0$, and we have

$$\begin{aligned} v &= \|\mathbf{v}\|, \\ v_0 &= \frac{(\mathbf{x} - \mathbf{x}_0)^T \mathbf{v}}{\|\mathbf{x} - \mathbf{x}_0\|}, \\ v_1 &= \frac{(\mathbf{x} - \mathbf{x}_1)^T \mathbf{v}}{\|\mathbf{x} - \mathbf{x}_1\|}. \end{aligned} \tag{6.4}$$

The signal will first reach the target roughly at $t = \tau_0 = \|\mathbf{x} - \mathbf{x}_0\| / (c - v_0)^2$, when the target is located at $\mathbf{x}_{\tau_0} = \mathbf{x} + \mathbf{v}\tau_0$. As a result, we have

$$\|\mathbf{x}_0 - \mathbf{x}_{\tau_0}\| + \|\mathbf{x}_1 - \mathbf{x}_{\tau_0}\| = c\tau. \tag{6.5}$$

Assume the maximum scanning distance is d_{max}, and the maximum delay will be $\tau_{max} = 2d_{max}/c$. After frequency mixing at the receiver, the received signal will go through a low-pass filter, and the baseband signal will be

$$\begin{aligned} r(t) =& A_0 e^{j[2\pi f_0(1-\rho)t + k\pi(1-\rho^2)t^2 + 2k\pi\rho^2\tau t + \theta]} \\ =& A_0 e^{j(2\pi \tilde{f}_0 t + \pi \tilde{k} t^2 + \theta)}, \end{aligned} \tag{6.6}$$

[2]Here we are assuming that the v_0 is constant from $t = 0$ to $t = \tau_0$.

where A_0 is the amplitude of the signal after filtering. $\tilde{f}_0$ and $\tilde{k}$ are given as

$$\tilde{f}_0 = f_0(1-\rho) + k\rho^2\tau \text{ and } \tilde{k} = k(1-\rho^2), \tag{6.7}$$

for $t \in [\tau_{max}, T]$. θ is the phase delay and it is of no significant for the localization purpose.

Apparently, this is a new LFM signal, whose initial frequency and frequency rate are given as $\tilde{f}_0$ and $\tilde{k}$ in (6.7). By estimating $\tilde{f}_0$ and $\tilde{k}$, we can compute the values of ρ and τ, which are directly dependent on the Doppler shift and delay. For a large-scale underwater sensor network, by incorporating the information from multiple nodes, we can estimate the target's location and velocity.

The major challenge here is the accurate estimation of the parameters of the LFM signals received at listening nodes. In the past two decades, the Fractional Fourier Transform (FrFT) has been developed as a powerful tool for underwater acoustic sonar signal processing. In [70], the authors unveiled the strong connection between the FrFT and the Wigner distribution. In [71], a fast discrete FrFT algorithm was proposed, and the complexity was almost identical to the conventional FFT. In the following sections, we will briefly introduce the FrFT-based joint estimation of delay and radial velocity.

6.2.2 FrFT-Based Parameter Estimation for LFM Signals

For an arbitrary LFM signal with amplitude A, initial frequency f_0 and frequency rate k, assume additive white Gaussian noise is presented, the received signal will be

$$r(t) = Ae^{j(2\pi f_0 t + k\pi t^2)} + n(t), \ t \in [0, T]. \tag{6.8}$$

The maximum likelihood estimate should be

$$[\hat{f}_0, \hat{k}, \hat{A}] = \arg\min_{\bar{f}_0, \bar{k}, \bar{A}} \int_{t=0}^{T} \left| r(t) - \bar{A}e^{j(2\pi \bar{f}_0 t + \bar{k}\pi t^2)} \right|^2 dt. \tag{6.9}$$

Because we are only interested in f_0 and k, (6.9) is equivalent to

$$[\hat{f}_0, \hat{k}] = \arg\max_{\bar{f}_0, \bar{k}} \left| \int_{t=0}^{T} r(t) \exp\left(-j2\pi \bar{f}_0 t - \bar{k}\pi t^2\right) dt \right|, \tag{6.10}$$

as has been shown in Appendix C.1. Conventionally, this can be achieved by taking the Wigner distribution of $r(t)$, because Wigner distribution approximately gives the energy distribution of the received signal in time-frequency domain. After getting the Wigner distribution, a two-dimensional search can be conducted to find the peak, and the corresponding horizontal and vertical coordinates are dependent on f_0 and k. However, this process involves high computational complexity.

Another choice will be the FrFT, which is a powerful tool for LFM signal processing. The a-th order FrFT of $r(t)$ is given as

$$R_a(u) = \int_{-\infty}^{\infty} K_a(u,t) r(t) dt. \tag{6.11}$$

$K_a(u,t)$ is the kernel function given as

$$K_a(u,t) = \sqrt{1 - j\cot\phi}\, e^{j\pi(u^2 \cot\phi - 2\csc\phi ut + t^2 \cot\phi)}, \tag{6.12}$$

where $\phi = a\pi/2$. For $a = 0$ or $a = \pm 2$, the kernel approaches $K_0(u,t) = \delta(u-t)$ and $K_{\pm 2}(u,t) = \delta(u+t)$, respectively. $a = 1$ gives us the conventional Fourier transform. The FrFT has two important characteristics:

$$R_a(u) = R_{a+4}(u) \text{ and } R_a(u) = R_{a+2}(-u). \tag{6.13}$$

Therefore, we only need to conduct the FrFT for $a \in [-1, 1]$. As we can see, the FrFT tries to decompose the received signal into a series of LFM signals, and we will obtain a two dimensional spectrum. In the spectrum, assume we have found the peak at $[\hat{a}, \hat{u}]$:

$$[\hat{a}, \hat{u}] = \arg\max_{a,u} |R_a(u)|. \tag{6.14}$$

Obviously, the absolute value of $R_a(u)$ will be maximized for

$$f_0 = u \csc\phi \text{ and } k = -\cot\phi. \tag{6.15}$$

Therefore, the initial frequency and frequency rate can be estimated as

$$\hat{f}_0 = \hat{u} \csc\hat{\phi} \text{ and } \hat{k} = -\cot\hat{\phi}, \tag{6.16}$$

where $\hat{\phi} = \hat{a}\pi/2$.

The direct computation of the FrFT introduces high complexity. In [71], two fast discrete algorithms were proposed, and we will customize one of them for our use in the underwater localization systems. Particular, we will explore efficient methods to narrow down the search area for lower computational complexity.

6.2.3 Discrete Implementation of the FrFT

Consider a signal $x(t)$ confined to $t \in [0, T]$, given by

$$x(t) = Ae^{j\left(2\pi f_0 t + \pi k t^2\right)}, \qquad t \in [0, T]. \tag{6.17}$$

Suppose k is positive, the instantaneous frequency of $x(t)$ is $f_0 + kt$, which ranges from f_0 to $f_0 + kT$. The FrFT of $x(t)$ is

$$X_a(u) = \int_{-\infty}^{\infty} K_a(u,t)x(t)dt. \tag{6.18}$$

To simplify the notation, we can rewrite $K_a(u,t)$ as

$$K_a(u,t) = A_a \exp\left[j\pi\left(\alpha u^2 - 2\beta ut + \alpha t^2\right)\right], \tag{6.19}$$

where $\alpha = \cot\phi$, $\beta = \csc\phi$, and A_a is given as

$$A_a \equiv \frac{\exp\left(j\pi \operatorname{sgn}(\sin\phi)/4 + j\phi/2\right)}{|\sin\phi|^{1/2}}. \tag{6.20}$$

(6.18) can be rewritten as

$$\begin{aligned} X_a(u) =& A_a e^{j\pi\alpha u^2} \int_0^T e^{-j2\pi\beta ut} e^{j\pi\alpha t^2} x(t)dt, \\ =& A_a e^{j\pi(\alpha-\beta)u^2} \int_0^T e^{j\pi\beta(u-t)^2} e^{j\pi(\alpha-\beta)t^2} x(t)dt. \end{aligned}$$

By defining $\eta = \alpha - \beta = -\tan(\phi/2)$, we can rewrite $X_a(u)$ as

$$X_a(u) = A_a e^{j\pi\eta u^2} \int_0^T e^{j\pi\beta(u-t)^2} e^{j\pi\eta t^2} x(t)dt. \tag{6.21}$$

If we further define $g(t) = e^{j\pi\eta t^2} x(t)$, $h(t) = e^{j\pi\beta t^2}$, and $\tilde{x}_a(t) = A_a g(t) * h(t)$ ($*$ denotes linear convolution), an immediate observation here is

$$\arg\max_{u,a} |X_a(u)| = \arg\max_{u,a} |\tilde{x}_a(u)|. \tag{6.22}$$

The spectrum of $h(t)$ is $H(f)$, given by

$$H(f) = \frac{1}{\sqrt{\beta}} e^{j\pi/4} \exp(-j\pi f^2/\beta). \tag{6.23}$$

In this case, one might be attempted to directly sample $g(t)$, $h(t)$, and $\tilde{x}_a(t)$, and then use the FFT to implement the convolution. However, we cannot do that for now because $h(t)$ is not bandlimited, and we will take the following approach.

Suppose the Fourier transforms of $g(t)$ and $\tilde{x}_a(u)$ are $G(f)$ and $\tilde{X}_a(f)$, respectively. We apparently have

$$\tilde{X}_a(f) = A_a G(f) H(f). \tag{6.24}$$

We can see that $G(f)$ is bandlimited to $[f_0, f_0 + kT]$. Therefore, if we define $\tilde{H}(f)$ as

$$\tilde{H}(f) = \begin{cases} H(f), & |f| < f_0 + kT, \\ 0, & \text{otherwise}, \end{cases} \tag{6.25}$$

we have

$$\tilde{X}_a(u) = A_a G(f)\tilde{H}(f). \tag{6.26}$$

Suppose $\tilde{h}(t)$ is the inverse Fourier transform of $\tilde{H}(f)$, we have

$$\tilde{x}_a(u) = A_a \tilde{h}(u) * g(u). \tag{6.27}$$

Because $\tilde{x}_a(u)$, $g(t)$, and $\tilde{h}(t)$ are all bandlimited to $[f_0, f_0 + kT]$, we can now sample them to get the discrete version of (6.27) as

$$\tilde{x}_a(mT_s) = A_a T_s \sum_{n=-N_a/2}^{N_a/2-1} \tilde{h}((m-n)T_s)x(nT_s), \tag{6.28}$$

where N_a is the total number of samples.

An example of the implementation of this algorithm is shown in Figure 6.2. The initial frequency is 120 Hz, and the frequency rate is 4.2, with a sampling rate of 400 Hz. Suppose the signal lasts for 4 seconds, the amplitude of $\tilde{x}_a(u)$ is given in Figure 6.2. The peak is roughly located at $a = -0.149$ and $u = -27.795$.

For this fast FrFT algorithm, N_a should be very carefully chosen. For $x(t)$, with a sampling rate of $f_s = 1/T_s$, we have totally $f_s T$ samples. Generally, we have $N_a \gg N$ to avoid the the *alising*. As a result, we need to conduct over-sampling on $\tilde{H}(f)$ and $G(f)$ when we are using the FFT algorithm to implement the convolution. There are two different ways to do that. The first choice is to conduct zero-padding on $g(t)$ and $\tilde{h}(t)$ after sampling. The other option is to directly conduct interpolations on the discrete spectrums of $g(t)$ and $\tilde{h}(t)$. Then interpolations are equivalent to over-sampling.

For $a = 1$, the FrFT is equivalent to the conventional DFT. For the given LFM, the frequency lies between f_0 to $f_0 + kT$. If $a = -1$, the spectrum lies between $-f_0$ and $-f_0 - kT$.

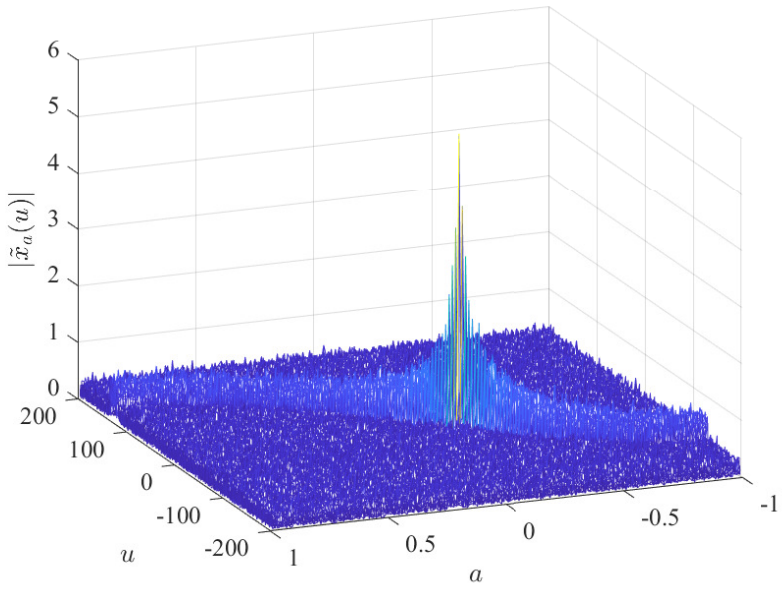

Figure 6.2: An example of the DFrFT.

As a result, to avoid aliasing, we must have

$$N_a T_s \geq 2(f_0 + kT). \tag{6.29}$$

Or equivalently, N_a should be chosen as

$$N_a \geq 2(f_0 + kT) f_s. \tag{6.30}$$

For example, as we can see in Figure 6.2, for $a = 1$ the frequency varies from 120 to 136 Hz; for $a = -1$, the frequency lies between -136 to -120 Hz. The minimum N_a is dependent on the initial frequency, frequency rate, broadcast period, and sampling frequency. For a given system, we can choose N_a based on system parameters.

6.3 Position and Velocity Estimation of the Targets

Suppose $M+1$ nodes are distributed in the area of interest, indexed from 0 to M. Node 0 is periodically broadcasting a LFM signal, while the other nodes are all listening. Assume the target moves at a constant speed $\mathbf{v} = [v_x, v_y]^T$. The radial velocity with respect to the m-th node will be

$$v_m = \frac{(\mathbf{x} - \mathbf{x}_m)^T \mathbf{v}}{\|\mathbf{x} - \mathbf{x}_m\|}, \tag{6.31}$$

where $\mathbf{x}_m$ and $\mathbf{x}$ are the positions of the m-th node and the target at $t = 0$. Based on $\hat{\tau}_m$ and $\hat{\rho}_m$, we can build equations accordingly to estimate the target's location and velocity.

6.3.1 Coarse Localization

Suppose the reflected signal is received at the m-th node, with the initial frequency f_m and frequency rate k_m, given as

$$\begin{aligned} f_m &= f_0(1-\rho_m) + k\rho_m^2\tau_m \\ k_m &= k(1-\rho_m^2). \end{aligned} \tag{6.32}$$

Suppose f_m and k_m are estimated as $\hat{f}_m$ and $\hat{k}_m$ based on the DFrFT algorithm. The estimates of τ_m and ρ_m can be computed as

$$\begin{aligned} \hat{\rho}_m &= \sqrt{1 - \hat{k}_m/k}, \\ \hat{\tau}_m &= \frac{\hat{f}_m - f_0(1-\hat{\rho}_m)}{k\hat{\rho}_m^2}. \end{aligned} \tag{6.33}$$

Based on $\hat{\tau}_m$ and $\hat{\rho}_m$, we can obtain two equations

$$\begin{aligned} \hat{\tau}_m &= \|\mathbf{x}_{\tau_0} - \mathbf{x}_m\|/c + \|\mathbf{x}_{\tau_0} - \mathbf{x}_0\|/c, \\ \hat{\rho}_m &= \frac{c - v_0}{c + v_m}, \end{aligned} \tag{6.34}$$

where ρ_m is the doppler scaling factor and $\mathbf{x}_{\tau_0}$ is the target's location at $t = \tau_0$. With M listening nodes, $2M$ equations will be available, and five unknowns are involved: two dimensional coordinate and velocity, and the average underwater sound speed. Define $f_m(\mathbf{x}_{\tau_0}, c)$ as

$$f_m(\mathbf{x}_{\tau_0}, c) = \|\mathbf{x}_{\tau_0} - \mathbf{x}_m\| + \|\mathbf{x}_{\tau_0} - \mathbf{x}_0\| - c\hat{\tau}_m, \tag{6.35}$$

and the least square estimator is

$$[\hat{\mathbf{x}}_{\tau_0}, \hat{c}] = \arg\min_{\mathbf{x}_{\tau_0}, c} \sum_{m=1}^{M} |f_m(\mathbf{x}_{\tau_0}, c)|^2. \tag{6.36}$$

The objective function is not convex, and we need to conduct coarse estimation first to get an approximation of the optimal solution , before the iterative algorithms can be employed to refine the result.

The first step is to rewrite (6.35) as

$$\|\mathbf{x}_{\tau_0} - \mathbf{x}_m\| = -\|\mathbf{x}_{\tau_0} - \mathbf{x}_0\| + c\hat{\tau}_m. \tag{6.37}$$

By squaring both sides, we have

$$\|\mathbf{x}_{\tau_0}\|^2 + \|\mathbf{x}_m\|^2 - 2\mathbf{x}_m^T\mathbf{x}_{\tau_0} = d_0^2 - 2c\hat{\tau}_m d_0 + c^2\hat{\tau}_m^2, \tag{6.38}$$

where $d_0 = \|\mathbf{x}_{\tau_0} - \mathbf{x}_0\|$. Then we minus the m-th equation from the first one and we will obtain

$$\|\mathbf{x}_m\|^2 - \|\mathbf{x}_1\|^2 + 2\mathbf{x}_1^T\mathbf{x}_{\tau_0} - 2\mathbf{x}_m^T\mathbf{x}_{\tau_0} = 2(\hat{\tau}_1 - \hat{\tau}_m)cd_0 + (\hat{\tau}_m^2 - \hat{\tau}_1^2)c^2. \tag{6.39}$$

In this case, we can define $\boldsymbol{\phi} = [\mathbf{x}_{\tau_0}^T, cd_0, c^2]^T$ and (6.39) can be transformed into a linear equation of $\boldsymbol{\phi}$:

$$\mathbf{A}\boldsymbol{\phi} = \mathbf{b}, \tag{6.40}$$

where $\mathbf{A}$ and $\mathbf{b}$ are given as

$$\mathbf{A} = \begin{bmatrix} 2(\mathbf{x}_1 - \mathbf{x}_2)^T & 2(\hat{\tau}_2 - \hat{\tau}_1) & \hat{\tau}_1^2 - \hat{\tau}_2^2 \\ 2(\mathbf{x}_1 - \mathbf{x}_3)^T & 2(\hat{\tau}_3 - \hat{\tau}_1) & \hat{\tau}_1^2 - \hat{\tau}_3^2 \\ \vdots & \vdots & \vdots \\ 2(\mathbf{x}_1 - \mathbf{x}_M)^T & 2(\hat{\tau}_M - \hat{\tau}_1) & \hat{\tau}_1^2 - \hat{\tau}_M^2 \end{bmatrix},$$
$$\mathbf{b} = \begin{bmatrix} \|\mathbf{x}_1\|^2 - \|\mathbf{x}_2\|^2 \\ \|\mathbf{x}_1\|^2 - \|\mathbf{x}_3\|^2 \\ \vdots \\ \|\mathbf{x}_1\|^2 - \|\mathbf{x}_M\|^2 \end{bmatrix}. \tag{6.41}$$

The least square estimate of $\boldsymbol{\phi}$ can be obtained as

$$\hat{\boldsymbol{\phi}} = \left(\mathbf{A}^T\mathbf{A}\right)^{-1}\mathbf{A}^T\mathbf{b}. \tag{6.42}$$

The coarse estimate of target's position can be obtained as $\hat{\mathbf{x}}_{\tau_0,c} = \hat{\boldsymbol{\phi}}[1:2]$, while the average underwater sound speed can be estimated as $\hat{c}_c = \sqrt{\hat{\boldsymbol{\phi}}[3]}$. These results are just coarse estimates, but they should be reasonably close to the true value. Thus, we can now use them as the initial estimate and use iterative algorithms to refine the result.

6.3.2 Refined Location and Velocity Estimation

Define $\boldsymbol{\theta} = [\mathbf{x}_{\tau_0}^T, c]^T$, and the least square estimate of $\boldsymbol{\theta}$ is

$$\hat{\boldsymbol{\theta}} = \arg\min_{\boldsymbol{\theta}} \sum_{m=1}^{M} |f_m(\boldsymbol{\theta})|^2. \tag{6.43}$$

To iteratively improve the estimation accuracy, we can construct $\hat{\boldsymbol{\theta}}_0 = [\hat{\mathbf{x}}_{\tau_0,c}^T, \hat{c}_c]^T$, which should be very close to $\boldsymbol{\theta}$ and can serve as the initial estimate.

Define $\mathbf{f}(\boldsymbol{\theta}) = [f_1(\boldsymbol{\theta}), f_2(\boldsymbol{\theta}), \cdots, f_M(\boldsymbol{\theta})]^T$, and the Jacobian matrix is given by

$$\mathbf{F} = \frac{\partial \mathbf{f}}{\partial \boldsymbol{\theta}} = \begin{bmatrix} \frac{\mathbf{x}_{\tau_0}-\mathbf{x}_1}{\|\mathbf{x}_{\tau_0}-\mathbf{x}_1\|} + \frac{\mathbf{x}_{\tau_0}-\mathbf{x}_0}{\|\mathbf{x}_{\tau_0}-\mathbf{x}_0\|} & -\hat{\tau}_1 \\ \frac{\mathbf{x}_{\tau_0}-\mathbf{x}_2}{\|\mathbf{x}_{\tau_0}-\mathbf{x}_2\|} + \frac{\mathbf{x}_{\tau_0}-\mathbf{x}_0}{\|\mathbf{x}_{\tau_0}-\mathbf{x}_0\|} & -\hat{\tau}_2 \\ \vdots & \vdots \\ \frac{\mathbf{x}_{\tau_0}-\mathbf{x}_M}{\|\mathbf{x}_{\tau_0}-\mathbf{x}_M\|} + \frac{\mathbf{x}_{\tau_0}-\mathbf{x}_0}{\|\mathbf{x}_{\tau_0}-\mathbf{x}_0\|} & -\hat{\tau}_M \end{bmatrix}. \tag{6.44}$$

Suppose $\boldsymbol{\theta}$ is estimated as $\hat{\boldsymbol{\theta}}_k$ in the k-th iteration, we can update the estimate in the $(k+1)$-th iteration as

$$\hat{\boldsymbol{\theta}}_{k+1} = \hat{\boldsymbol{\theta}}_k - (\mathbf{F}_k^T \mathbf{F}_k)^{-1} \mathbf{F}_k \mathbf{f}(\hat{\boldsymbol{\theta}}_k), \tag{6.45}$$

where $\mathbf{F}_k$ is the Jacobian matrix evaluated at $\boldsymbol{\theta} = \hat{\boldsymbol{\theta}}_k$.

Generally, one or two iterations should lead to the convergence, which has very low computational complexity. Suppose the refined localization result is $\hat{\mathbf{x}}_{\tau_0}$ and the average underwater sound speed is estimated as $\hat{c}$. The next step is to estimate the target's velocity.

From the second part of (6.34), we have

$$c - \frac{\mathbf{x}^T - \mathbf{x}_0^T}{\|\mathbf{x} - \mathbf{x}_m\|}\mathbf{v} = \rho_m c + \rho_m \frac{\mathbf{x}^T - \mathbf{x}_m^T}{\|\mathbf{x}^T - \mathbf{x}_m^T\|}\mathbf{v}. \tag{6.46}$$

Because we are assuming that the target's radial velocity is constant during the sampling time, we can replace $\mathbf{x}$ with $\mathbf{x}_{\tau_0}$ in (6.46). The incurred error will be negligible. To be specific, we can obtain the following approximation

$$\left(\frac{\rho_m(\hat{\mathbf{x}}_{\tau_0} - \mathbf{x}_m)}{\|\hat{\mathbf{x}}_{\tau_0} - \mathbf{x}_m\|} + \frac{(\hat{\mathbf{x}}_{\tau_0} - \mathbf{x}_0)}{\|\hat{\mathbf{x}}_{\tau_0} - \mathbf{x}_0\|} \right)^T \mathbf{v} \approx (1 - \hat{\rho}_m)\hat{c}, \tag{6.47}$$

which is a linear function of the target's velocity. There are M equations like this and they can be easily solved with the least square method.

6.4 CNN-Based Target Detection

6.4.1 Motivation

For the discussed underwater localization system, the proactive node is periodically broadcasting the LFM signals, with a period of T, of several seconds. To achieve real-time scanning, the computation load must be handled very fast. However, the computation cost of Figure 6.2 is still very challenging. Another problem is that the accurate localization of the peak in the spectrum is highly dependent on the sampling interval. With smaller interval, higher accuracy can be obtained, but the over-sampling leads to very high computational cost.

Apart from the computational cost, how to identify the existence of targets is also a huge problem. An intuitive idea is to set up a threshold and claim the existence of targets whenever there are samples larger than the threshold. However, the spectrum is not sparse, and we can see quite a few side peaks comparable to the highest peak, even when we only have one target in the surveillance area. Also, if multiple objects exist, the situation will become more complicated.

These two problems can be simultaneously solved by the incorporating a CNN in the system. As we know, CNN is becoming very popular these years because of its ability of pattern recognition. We will thus employ this tool to first search for the desired pattern in the obtained map and try to identify the positions of the peaks. Then, around each peak,

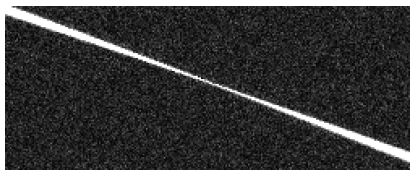

Figure 6.3: Top view of Figure 6.2 around the peak.

over-sampling can be conducted to refine the result.

Practically, we cut a small portion of the map in Figure 6.2, and normalize all the values to [0, 255]. We can draw the top view of that partial map in gray scale, as shown in Figure 6.3. An interesting observation is that we can always find an "X" pattern around the peak value. The position, angle, and width of the pattern varies with the parameters, including initial frequency, frequency rate, signal duration, sampling frequency, and so on. Even when we sample the spectrum at a much lower rate, this pattern can still be reserved. As a result, an intuitive idea is to search this pattern in a under-sampled spectrum, and then conduct fine search around the target area to improve the accuracy. By doing this, high accuracy can be obtained without very high complexity.

The fundamental reason for the performance improvement is that the "X" pattern can be very well preserved even when we conduct under-sampling on the 2D spectrum. Then, the powerful CNN allows us to find the rough location of the peak based on the low-resolution 2D spectrum.

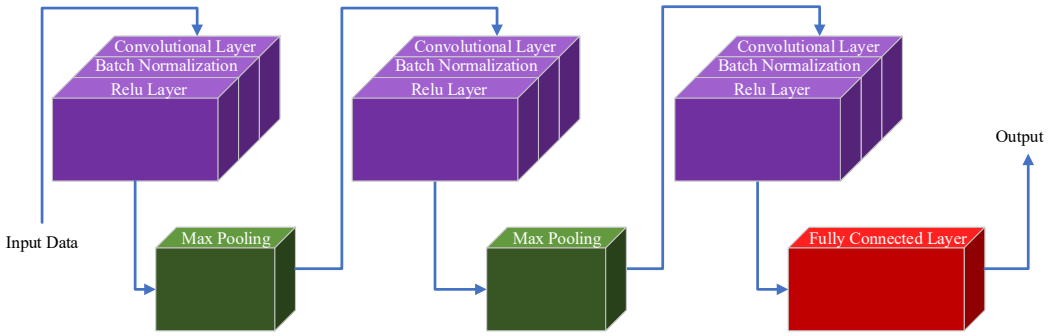

Figure 6.4: The structure of the CNN.

6.4.2 Structure of the Convolutional Neural Network

The structure of the employed CNN is shown in Figure 6.4. The input is the 99×99 figures obtained from the spectrum, while the output is "Negative" or "Positive", depending on whether the targets are identified or not in the figures. There are totally six layers: three convolutional layers, two max pooling layers, and one full connected layer. Each pixel stores a number varying from 0 to 255. A figure will first be fed into a convolutional layer, with eight filters of size 3×3. The convolutional layer will be followed by a batch normalization layer and an Relu layer. A max pooling layer is added to eliminate the redundancy.

The second convolutional layer has 16 filters of size 3×3, while the third convolutional layer has 32 filters of the same size. The increase of the filters can help to extract the high-level structures. Lastly, we have a fully connected layer with ten outputs, followed by the soft-max layer and the classification layer.

Because the input has a dimension of 99×99, while the original spectrum is very large, we need to first conduct under-sampling on the 2D spectrum. The default sampling interval is 100, if not specified. Then we can get a much smaller map, and a carpet search will

be conducted with the trained CNN. The under-sampled map will be divided into tens of blocks, which will be fed into the CNN sequentially. This structure will apparently allow us to detect multiple objects.

One input figure contains around ten thousand pixels, which is quite large. However, due to the sparse structure of the CNN, only a very small number of parameters are required for training. To be specific, for each convolutional layer, one filter has only $3 \times 3 = 9$ parameters. With the 56 filters, only hundreds of parameters are needed for the whole network. Therefore, we can see that the number of parameters is not dependent on the input size, which means the training complexity grows linearly with the input size. After three convolutional layers, the output is then fed into a fully connected layer, but the size is small and the complexity is low. These advantages all come from the fact that the CNN can extract the sparse features from the pictures.

6.4.3 Data Preparation and Training

Apparently, the major challenge is how to generate and label the training datasets. In our case, simulations are conducted in Matlab to generate maps, and these maps are divided into small blocks. Codes are written to automatically label the generated blocks for training purposes.

In our case there are only two labels: "Negative" means no target detected, while "Positive" indicates detected pattern. Examples are given below in Figure 6.5.

In Figure 6.5 (a), we have a positive case, where the "X" pattern can be clearly observed. White noise presents out of that pattern and the noise is weaker than the signal components. In (b), we have a negative case. Part of the tail of a pattern is captured, and we can infer

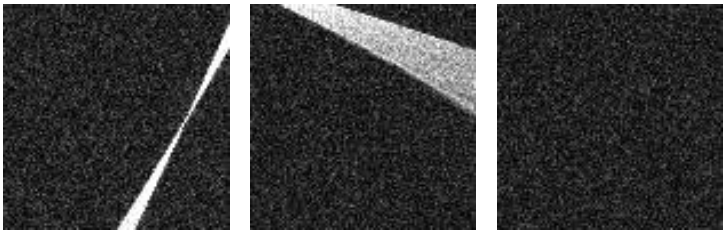

Figure 6.5: Examples of the positive and negative cases.

that we should be able to find the pattern by shifting the window to the top-left. In (c) we have another negative case, and the map contains pure noise.

Simulations for different distance-velocity combinations are conducted. For each combination, the DFrFT was utilized to compute the two dimensional spectrum. Then, the program will automatically divide the spectrum into small blocks of 99×99, and each piece will be stored as a png file. Those figures with the "X" patterns will be stored in the "Positive" folder, while the others will be stored in the "Negative" folder. For the positive cases, data augmentation will be conducted to enlarge the dataset.

Based on the collected data, we conduct data augmentation. The basic idea is to shift, rotate, and scale the figures of the positive cases, and obtain variations of the original data. This will help to improve the robustness of the CNN, by training it to recognize the shifted, rotated and scaled patterns. In practical measurements, the position, width, and angle of the "X" pattern is dependent on many parameters, including sampling rate, sampling time, and also the under-sampling process. For different parameters, the "X" patterns may look quite different for the same LFM signal. Therefore, the data augmentation is an important step to improve the robustness of the CNN.

6.5 Simulations

In this section, comprehensive simulations will be conducted to verify the theoretical results presented in the previous sections. The initial frequency of the probe signal is chosen as 1 kHz, and the frequency rate is 50 Hz/s. The scanning period is eight seconds, and the maximum scanning distance is three kilometers. As a result, for each period, we will conduct FrFT on the received signals in the last four seconds to avoid ambiguity. The average underwater sound speed is 1500 m/s. After frequency mixing of the received signal and the local probe signal, we will get the signal in (6.7). This signal will then be sampled at the frequency of $f_s = 400$ Hz. N_a is thus chosen as $N_a = f_s^2$, and we will need to expand the sampled sequence length from $N = 4f_s$ by $f_s/4$ times through zero-padding. That is to say, the original sequence has a length of $N = 1600$, and we will need to add $N_a - N = 9N$ zeros at the end of the sequence. The fast DFrFT algorithm can then be employed to obtain the spectrum of the signal.

The sampling frequency is 5 kHz, and the sampling period is four seconds. There are nine anchors distributed on the sea floor, one of which is actively broadcasting the probe signal while the others are silent. Without loss of generality, we build a two dimensional coordinate centered at the proactive node, and the silent nodes are located at: $[-1000, -1000]^T$; $[-1000, 1000]^T$; $[1000, -1000]^T$; $[1000, 1000]^T$; $[-2000, -2000]^T$; $[-2000, 2000]^T$; $[2000, -2000]^T$; $[2000, 2000]^T$. Suppose the target is located at $[0, 1500]^T$ at $t = 0$, and it is moving at a velocity of $[2, 1]^T$ m/s.

6.5.1 CNN-Based Target Detection

For the CNN-based target detection, we conduct the training with 500 and 750 training samples. The trained network is then used for target detection for 300 samples. The results can be found in Table 6.1. "True Positive" means that the target exists, and is

Table 6.1: Validation Statistics

	500 Training Samples		750 Training Samples	
	Positive	Negative	Positive	Negative
True	99.27%	97.27%	99.67%	99%
False	2.73%	0.73%	1%	0.33%
Error Rate	1.73%		0.67%	

successfully detected by the network; "True Negative" means that the target does not exist, and is correctly reported as "Negative"; "False Positive" means the target does not exist, but reported as "Positive"; "False Negative" means a "Positive" case is reported to be "Negative". By increasing the training sample number from 500 to 750, the overall error rate will decrease from 1.73 % to 0.67 %. For practical applications, this error rate is totally acceptable. Because the network keeps scanning in a period of T seconds, the probability that a target is not detected in two consecutive periods is negligible.

6.5.2 Joint Localization and Speed Estimation

For the joint estimation of target's location and speed, the accuracy is dependent on various parameters. In this part, we will evaluate how SNR, node number, and iteration number contribute to the system performance.

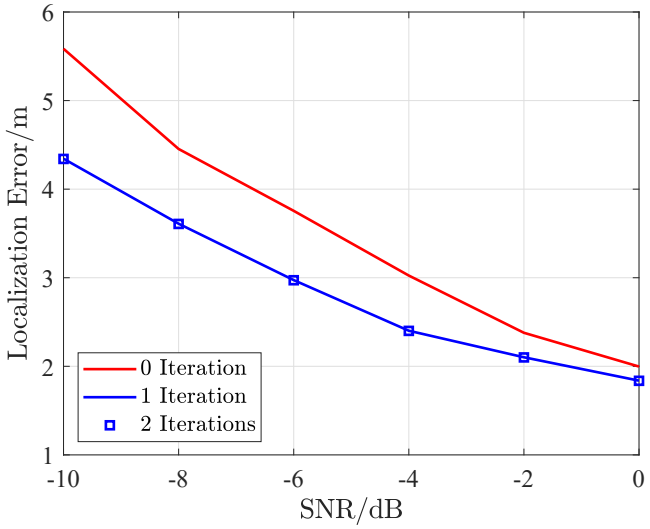

Figure 6.6: Localization error for different iteration numbers.

In Figure 6.6, the impact of SNR and M on localization accuracy is evaluated. The SNR varies from -10 to 0 dB. As we increase the SNR, the localization error will gradually decrease. For 0 iteration, namely the result in (6.42), we can see that the average localization error is at the level of 2 to 6 meters. If we add one iteration, the accuracy will be improved by around one meter at -10 dB. However, for high SNR, the improvement will gradually become negligible. If we further increase the iteration number to 2, we can see that the results are almost identical for those of one iteration. As a result, we can conclude

that one iteration is totally enough.

In Figure 6.7, simulations are conducted for $M \in \{6, 7, 8\}$. Every time we add one extra node, the average localization error will decrease by around one meter. This is a well known effect, because the increase of anchor number leads to the decreased GDOP (Geographical Dilution of Precision), which is proportional to the variance of localization error. For

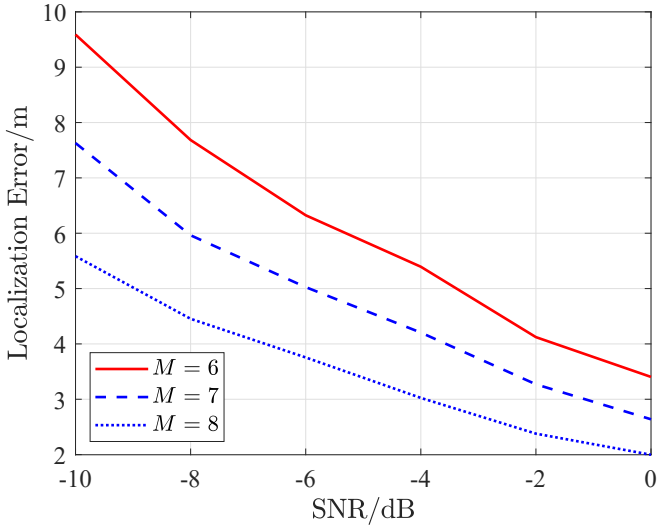

Figure 6.7: Localization error for different M.

very large underwater sensor networks, M is generally very large, which leads to high positioning accuracy. Practically, the distribution of the nodes also contributes to the localization accuracy, and thus should be carefully manipulated.

Based on the localization result, we can now estimate the target's velocity. This can be easily done through (6.47). Simulations are conducted for different anchor numbers, and the results are presented in Figure 6.8. Because (6.47) is an approximation, we can

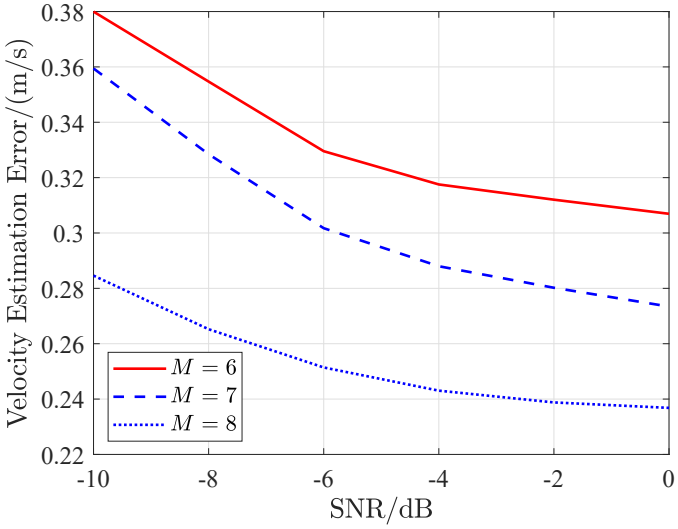

Figure 6.8: Velocity estimation error for different M.

expect the result to level off, as observed in Figure 6.8. Similar to the localization error, we can see that the increase of anchor number leads to improved performance. The velocity estimation error is at the level of 0.2 to 0.3 m/s, which renders a ten percent relative error.

6.6 Summary

In this chapter, a proactive positioning system based on CNN and DFrFT is presented for underwater localization of silent objects. The active nodes periodically broadcast LFM signals, and the silent nodes can estimate target's position and velocity based on the reflections. The DFrFT is employed to obtain the spectrum of the reflected signals, and the CNN is the utilized to search for target. With the rough location of the peak provided by the CNN, over-sampling can be conducted to improve the accuracy. Based on the location of the peaks in the spectrum, a low-complexity algorithm is presented for the

joint estimation of the target's location and velocity. The simulation results show that the localization error is at the level of 2 to 6 meters, while the velocity estimation error is about ten percent.

Chapter 7

Pilot Decontamination in Non-cooperative Massive MIMO Cellular Networks Based on Spatial Filter

In the previous chapters, the possibility of employing mobile nodes for localization in WSNs has been discussed. For such applications, fast communications between the mobile anchors and the BSs is critical. For the terrestrial scenario, the 5G cellular network plays a very important role, and the massive MIMO technique is crucial for 5G. However, to employ massive MIMO for high-speed data transmission from drones to BSs, the pilot contamination issue must be resolved, as we have discussed in Chapter 2. In this chapter,

a pilot decontamination method based on spatial filter will be presented.[1]

7.1 Motivation

The massive MIMO technology has been a very hot research topic in recent years for its great potential to improve the spectral and energy efficiencies [72]. As one of the most important enabling techniques for the 5G cellular networks, it aims to serve tens of single-antenna users with hundreds of antennas at the BS. The increase in antenna numbers at the BSs brings many advantages. First, energy efficiency can be improved because energy can be concentrated on the target users through beamforming [94]. Besides, spatial division multiple access (SDMA) can be employed over the orthogonal frequency division multiple access (OFDMA), which allows the same time-frequency resources be reused by all users in the same cell, hence, leading to much higher spectral efficiency. In spite of the tradeoff between the energy efficiency and the spectral efficiency [130], massive MIMO will boost both of them in a reasonably wide signal to noise ratio (SNR) range. Moreover, low-complexity algorithms (e.g., matched filter) can be employed for precoding and decoding in massive MIMO systems [131, 132] because channel vectors of different users are asymptotically orthogonal when the BS antenna number is sufficiently large. Although the large antenna arrays at the BSs will lead to high computational complexity, iterative algorithms can be adopted to maintain it on an acceptable level [133–136]. It is well known that one of the major goals of 5G is to reduce service delay, including both

[1]The presented work has been published in [J11]: Z. Gong, C. Li and F. Jiang, "Pilot Decontamination in Noncooperative Massive MIMO Cellular Networks Based on Spatial Filter," *IEEE Trans. Wireless Commun.*, vol. 18, no. 2, pp. 1419-1433, Feb. 2019.

propagation delay and processing delay [137]. Last but not the least, because of the great power gain of the BS antenna array, cheap power amplifiers working at the milli-Watt level can be employed [73,74]. Despite the advantages discussed above, practical massive MIMO applications still face many challenges, of which the pilot contamination is perceived as a major one.

Most pilot decontamination research assumes that the desired signals are stronger than the pilot contamination. However, it is very difficult to guarantee this condition for cell-edge users in practical scenarios. Based on the channel model in (2.9), the received signal strength decreases fast with distance, which leads to the following observations.

(a). First, the most significant pilot contamination must come from the adjacent cells. Considering typical hexagonal cell arrangement, for the k-th user in the l-th cell, there are only six neighbor cells and every cell only contains one interfering user. Therefore, pilot contamination for a specific target user is sparse, compared with the huge number of antennas at the BS.

(b). For users close to the BS, pilot contamination is not a big issue because their signals will be much stronger than the interference. However, cell-edge users are vulnerable to pilot contamination, because their signals may be overwhelmed by interfering users.

Motivated by these observations, a pilot decontamination method will be presented in the next section, aiming to improve the achieved SINR of cell-edge users [138]. As we know, there are generally four phases in massive MIMO communication protocols: *pilot transmission*, *processing*, *uplink data transmission*, and *downlink data transmission*. When

a cell is in the *pilot transmission* phase, the BS will receive signals from both the desired and interfering users. By employing the FFT algorithm, the BS can obtain the energy distribution of the received signal in space. Then, during the *processing* phase, users in the target cell will stay silent. The BS can monitor signals from interfering users in adjacent cells and analyze their energy distribution in space. By comparing these two distributions, the BS can identify the DoA of pilot contamination and construct the corresponding subspace. Finally, the channel estimate from the MF will be projected onto its complementary subspace to eliminate the pilot contamination and improve channel estimation accuracy. The fundamental idea behind this new method is that wireless channels are sparse in the space domain, i.e., most energy of the desired signals concentrates on a small number of paths (or directions, equivalently) [78, 79, 139–143]. This is especially true for massive MIMO systems, because compared with the huge antenna quantity at the BS, the number of significant paths is much smaller. In [79] and [78], the authors even assume that the DOA spread of every terminal is limited to a narrow angle. Moreover, the propagation model of millimeter wave, being viewed as the perfect match for massive MIMO [144], tends to be LoS or near-LoS [97], which means the wireless channel for millimeter wave will be even sparser.

7.2 Spatial Filter Based Channel Estimation

From previous discussions, pilot contamination mainly comes from adjacent cells, and the received signal is generally sparse in space. Besides, cell-edge users are most vulnerable to pilot contamination, because their signals are not necessarily stronger than the interference.

Motivated by these observations, we will talk about how to identify and eliminate pilot contamination in space.

The first step is to divide all cells into three groups, G_1, G_2 and G_3, and make sure that adjacent cells belong to different groups, as shown in Figure 7.1 (a). Then, we slightly modify the widely employed TDD communication protocol by shifting the processing phase of different groups, as illustrated in Figure 7.1 (b). The same pilot sequences are shared by all cells.

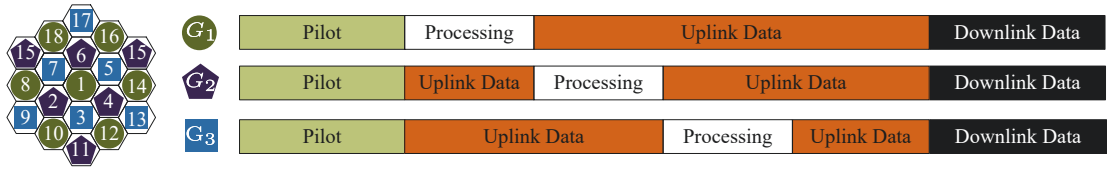

(a) Group distribution (b) Shifted TDD protocol

Figure 7.1: The geometrical distribution of cells and groups, and the shifted pilot schedule.

As shown in Figure 7.1 (b), all cells are synchronized. In the first phase, users in all cells transmit pilots to their base stations. Then, cells in different groups perform the uplink data detection and pilot signal processing in a shifted fashion. After all groups have finished receiving uplink data, they transmit downlink data at the same time. In the conventional researches, the processing phase is generally employed for channel estimation [144–147]. However, in the presented method, the BS has two tasks during the processing phase. The first task is to perform lease square channel estimation, while the second one is to receive signals from users in other cells. These signals can provide statistical information about the inter-cell interference from adjacent cells, and help to mitigate pilot contamination in

future processing.

It should be noted that when the BSs in one group are in the processing phase, the BSs belong to the other two groups are receiving uplink data. We assume that the processing phase lasts for one symbol duration, which is the minimum length required. As a matter of fact, the length of the processing phase has two-fold impacts on system performance. On one hand, longer processing phase leads to larger overhead, thus reducing the spectral efficiency. On the other hand, longer processing phase allows the BS to obtain more statistical information about pilot contamination, thus helping to improve the channel estimation accuracy and boost spectral efficiency. However, the optimal choice of processing phase length is a complicated problem, and is out of the scope of this chapter. Therefore, we assume the processing phase lasts for one symbol duration, which helps to keep the analysis simple and the overhead low. If we assume that the BS has very strong computational capacity, which renders the processing time negligible, we can still insert an idle phase of one symbol duration, so that the BS can collect the statistical information of inter-cell interference. Although with this small increased cost, the presented method shows much improved performance than the existing ones, as will be shown in simulations and performance analysis.

Another issue worth noting is that the decoding of uplink data will be delayed. In the presented protocol, after pilot transmission, the BS cannot obtain uncontaminated channel estimates, and thus uplink data decoding cannot be performed. As a result, the BS will have to buffer the received uplink signal, until the decontaminated channel estimate becomes available. This is generally not a big problem, and it exists in many protocols. For example, in [88], the authors proposed to obtain the CSI through eigenvalue decomposition of the

received uplink signal matrix, which means uplink data cannot be detected immediately upon receiving. Another example is the data-aided channel estimator [91], in which the authors proposed to employ both uplink data and pilot for channel estimation. As a result, the uplink data detection will be delayed.

Without loss of generality, we assume the l-th cell is the target cell, and it belongs to G_1. Then, by employing the MF channel estimator, we can obtain the channel estimate of the k-th user in the l-th cell as

$$\hat{\mathbf{h}}_{mf}^{(l,k)} = \mathbf{Y}^{(l)}\mathbf{p}_k^*/\tau = \mathbf{h}_{l,k}^{(l)} + \sum_{c_{l'}\notin G_1} \mathbf{h}_{l',k}^{(l)} + \sum_{c_{l'}\in G_1, l'\neq l} \mathbf{h}_{l',k}^{(l)} + \mathbf{n}_k, \tag{7.1}$$

where c_l denotes the l-th cell, and $\mathbf{n}_k = \mathbf{N}\mathbf{p}_k^*/\tau$. $\mathbf{h}_{l',k}^{(l)}$ represents the channel vector from the k-th user in the l'-th cell to the l-th BS. In (7.1), the first and last parts are the desired CSI and white noise, respectively. The second part contains pilot contamination from the k-th users in G_2 and G_3. It should be noted that only six of them are located in adjacent cells for a typical hexagonal cell structure, which means there are at most six strong pilot contamination components. The third part contains pilot contamination from users in G_1, which are all weak because they are at least three cell radius away from c_l. Overall, there are potentially seven strong components in $\hat{\mathbf{h}}_{mf}^{(l,k)}$, and it is very sparse compared with the number of BS antennas.

During the *processing phase* of cells in G_1, all users in c_l are silent (as we have mentioned previously, we assume $c_l \in G_1$ without loss of generality), and the BS can receive signals from users in active cells ($c_{l'} \in G_2 \cup G_3$ or $c_{l'} \notin G_1$) as

$$\mathbf{y}_{proc}^{(l)} = \sum_{c_{l'}\notin G_1} \mathbf{h}_{l',k}^{(l)} s_{l',k} + \sum_{k'\neq k} \sum_{c_{l'}\notin G_1} \mathbf{h}_{l',k'}^{(l)} s_{l',k'} + \mathbf{n}_{proc}, \tag{7.2}$$

where $s_{l',k}$ is the transmitted symbol of the k-th user in the l'-th cell during the *processing phase* of cells in G_1. In (7.2), the first part denotes signals from the k-th users in cells belong to G_2 and G_3, and contains at most six strong components. The second part denotes general inter-cell interference from active cells, which does not exist in (7.1), because none of these interfering users in this part is using the k-th pilot sequence.

Based on the above discussion, we can see that $\hat{\mathbf{h}}_{mf}^{(l,k)}$ is sparse in space, and the major components include both the desired signals and the pilot contamination. On the other hand, $\mathbf{y}_{proc}^{(l)}$ is composed of pilot contamination and general inter-cell interference. The spatial spectrums of these two vectors will overlap on those spatial signatures dominated by pilot contamination, as shown in Figure 7.2. As a result, an intuitive idea is to eliminate

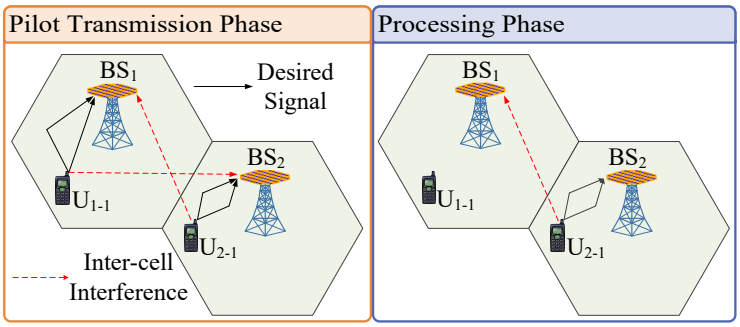

Figure 7.2: Illustration of pilot contamination.

pilot contamination by identifying their spatial signatures and constructing the complementary subspace. To achieve this goal, the first step is to identify the major spatial signatures in $\hat{\mathbf{h}}_{mf}^{(l,k)}$, where the pilot contamination from adjacent cells must exist. By doing this, we only need to focus on a small number of spatial signatures when we try to identify pilot contamination in future steps, which will cut down the complexity and processing time.

In this chapter, we will develop this idea based on linear antenna arrays. However, it should be noted that this method can also be applied to antenna arrays of nonlinear forms, such as planar and lens antenna arrays. The only difference is that we need to calculate the spatial spectrums of different antenna arrays in different ways.

7.2.1 Identification of the Spatial Signatures of the Desired Signals and Pilot Contamination

As we have discussed, the third part in (7.1) is negligible. Besides, the maximum number of strong components in the second part is six. Without loss of generality, we assume that the indexes of these six adjacent cells are $l_1, l_2, \cdots, l_6$, and (7.1) can be reorganized as

$$\hat{\mathbf{h}}_{mf}^{(l,k)} = \sum_{b=1}^{B} a_b^{(l,k)} \cdot \mathbf{e}[\omega_b^{(l,k)}] + \sum_{i=1}^{6} \sum_{b=1}^{B} a_b^{(l_i,k)} \cdot \mathbf{e}[\omega_b^{(l_i,k)}] + \sum_{l' \notin \{l, \{l_i\}_{i=1}^{6}\}} \sum_{b=1}^{B} a_b^{(l,k)} \cdot \mathbf{e}[\omega_b^{(l,k)}] + \mathbf{n}_k, \quad (7.3)$$

where $a_b^{(l,k)} = \sqrt{\rho_b^{(k,l)}} e^{j\phi_b^{(k,l)}}$ denotes the coefficient of the b-th path from the k-th user in the l-th cell. $\rho_b^{(k,l)}$ and $e^{j\phi_b^{(k,l)}}$ are the path-loss coefficient and random phase, respectively.

To identify the spatial signatures of the desired signals and the pilot contamination, we need to analyze the spatial spectrum of $\hat{\mathbf{h}}_{mf}^{(l,k)}$ through IDFT as $\hat{\mathbf{h}}_{\omega}^{(l,k)} = \mathbf{F}_M \hat{\mathbf{h}}_{mf}^{(l,k)}$, which indicates the energy distribution of $\hat{\mathbf{h}}_{mf}^{(l,k)}$ on different directions and the m-th component of $\hat{\mathbf{h}}_{mf}^{(l,k)}$ is given by

$$\begin{aligned} \hat{\mathbf{h}}_{\omega}^{(l,k)}[m] = &\sum_{b=1}^{B} a_b^{(l,k)} \cdot f\left(\omega_b^{(l,k)} - m\omega_0\right) + \sum_{i=1}^{6} \sum_{b=1}^{B} a_b^{(l_i,k)} \cdot f\left(\omega_b^{(l_i,k)} - m\omega_0\right) + \\ &\sum_{l' \notin \{l, \{l_i\}_{i=1}^{6}\}} \sum_{b=1}^{B} a_b^{(l',k)} \cdot f\left(\omega_b^{(l',k)} - m\omega_0\right) + \mathbf{n}_k[m]. \end{aligned} \quad (7.4)$$

For $l' \notin \{l, \{l_i\}_{i=1}^{6}\}$, $a_b^{(l',k)}$ is negligible because users in these cells are at least three cell-radius away from the target BS. According to the *Central Limit Theorem*, the third

part in (7.4) can be viewed as Gaussian noise [2]. Therefore, we define $\tilde{\mathbf{n}}_k[m]$ to replace the last two parts:

$$\tilde{\mathbf{n}}_k[m] = \sum_{l' \notin \{l_i\}_{i=1}^{6}} \sum_{b=1}^{B} a_b^{(l',k)} \cdot f\left(\omega_b^{(l',k)} - m\omega_0\right) + \mathbf{n}_k[m]. \tag{7.5}$$

As we have mentioned, most of the received energy concentrates on a few directions; therefore, the received signal will be much stronger than noise on those directions. Motivated by this observation, we define the following metric to identify the spatial signatures of the desired signals or pilot contamination:

$$\lambda_m^{(l,k)} = \left|\hat{\mathbf{h}}_\omega^{(l,k)}[m]\right|^2. \tag{7.6}$$

In this equation, $\lambda_m^{(l,k)}$ indicates the received energy of the l-th BS on the m-th spatial signature (or direction). When $\hat{\mathbf{h}}_\omega^{(l,k)}$ does not have a strong component on $m\omega_0$ or the signal is substantially weaker than the noise, $\lambda_m^{(l,k)}$ is generally small and follows the exponential distribution. On the other hand, $\lambda_m^{(l,k)}$ will be much larger if $\hat{\mathbf{h}}_\omega^{(l,k)}$ has a strong component on $m\omega_0$, and the probability density function (PDF) of $\lambda_m^{(l,k)}$ is very close to normal distribution. The empirical distribution of $\lambda_m^{(l,k)}$ is shown in Figure 7.3.

In Figure 7.3, $H_0 = 1$ means that neither the desired signal nor the pilot contamination exists on $m\omega_0$, while $H_1 = 1$ represents the opposite situation. Given that $H_0 = 1$ on $m\omega_0$, the value of $\lambda_m^{(l,k)}$ is very small. On the contrary, when $H_1 = 1$, the received signal strength on $m\omega_0$ will be much larger. As a result, we can set a threshold to identify these strong components and their spatial signatures. Here, we just assume that the threshold has been

[2] If we consider interference from cells within a distance of eight cell diameters, there will be 192 interfering users, and every user has up to B detectable paths. That is to say, the third part is a composition of around $200B$ components, which is quite a huge number. Therefore, it can be accurately modeled by Gaussian distribution.

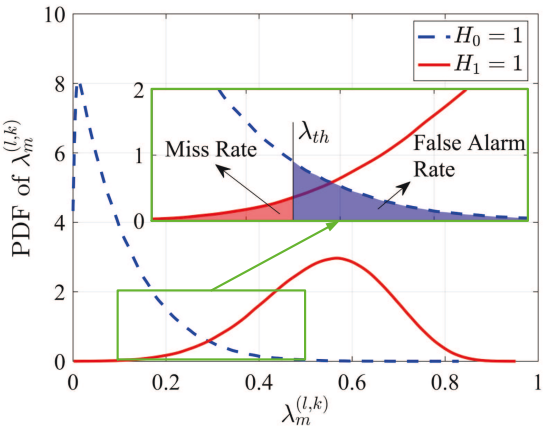

Figure 7.3: Probability density function of $\lambda_m^{(l,k)}$ for SNR=10 dB on $m\omega_0$.

obtained as λ_{th}, and further details on threshold selection will be discussed in the next section. Then, the subspace of the desired signals or pilot contamination of the k-th user in the l-th cell can be represented by the following matrix:

$$\mathbf{U}_{S,P}^{(l,k)} = [\,\mathbf{e}[m_1\omega_0]\,, \mathbf{e}[m_2\omega_0]\,, \cdots, \mathbf{e}[m_Q\omega_0]\,]\,, \tag{7.7}$$

where m_q satisfies $\lambda_{m_q}^{(l,k)} > \lambda_{th}$.

7.2.2 Selection of λ_{th}

Define $\mathbf{h}_{S,P}^{(l,k)}[m]$ as follows

$$\mathbf{h}_{S,P}^{(l,k)}[m] = \sum_{b=1}^{B} a_b^{(l,k)} \cdot f(\omega_b^{(l,k)} - m\omega_0) + \sum_{i=1}^{6}\sum_{b=1}^{B} a_b^{(l_i,k)} \cdot f(\omega_b^{(l_i,k)} - m\omega_0), \tag{7.8}$$

which represents the desired signal (or pilot contamination) on $m\omega_0$. Then, combining (7.4), (7.5), and (7.8), (7.6) can be reorganized as

$$\lambda_m^{(l,k)} = \left|\mathbf{h}_{S,P}^{(l,k)}[m] + \tilde{\mathbf{n}}_k[m]\right|^2. \tag{7.9}$$

Let $f_0(\lambda_m^{(l,k)})$ and $f_1(\lambda_m^{(l,k)})$ denote the PDFs of $\lambda_m^{(l,k)}$ in $H_0 = 1$ and $H_1 = 1$ scenarios. When $H_0 = 1$, noise dominates in $\lambda_m^{(l,k)}$, and $f_0(\lambda_m^{(l,k)})$ can be approximated as exponential distribution, which is given by

$$f_0\left(\lambda_m^{(l,k)}\right) = \frac{1}{\sigma_o^2} \cdot \exp\left(-\lambda_m^{(l,k)}/\sigma_o^2\right), \tag{7.10}$$

where $\sigma_o^2 = E\left\{|\tilde{\mathbf{n}}_k[m]|^2\right\}$. On the other hand, when $H_1 = 1$, the desired signal (or pilot contamination) is much stronger than the noise. By ignoring the second order noise components, $f_1(\lambda_m^{(l,k)})$ is very close to the normal distribution, which is given by

$$f_1\left(\lambda_m^{(l,k)}\right) = \frac{1}{\sqrt{4\pi\left|\mathbf{h}_{S,P}^{(l,k)}[m]\right|^2\sigma_o^2}} \cdot \exp\left(-\frac{\left(\lambda_m^{(l,k)} - \left|\mathbf{h}_{S,P}^{(l,k)}[m]\right|^2 - \sigma_o^2\right)^2}{4\left|\mathbf{h}_{S,P}^{(l,k)}[m]\right|^2\sigma_o^2}\right). \tag{7.11}$$

The detailed discussions can be found in Appendix D.2.

Based on signal detection theory, the false alarm rate and the miss rate can be defined as:

$$\begin{aligned} R_{FA} &= \Pr\left(\lambda_m^{(l,k)} > \lambda_{th} | H_0 = 1\right), \\ R_M &= \Pr\left(\lambda_m^{(l,k)} \leq \lambda_{th} | H_1 = 1\right), \end{aligned} \tag{7.12}$$

and they are demonstrated in Figure 7.3. To minimize the sum of false alarm and miss rates, λ_{th} should satisfy $f_0(\lambda_{th}) = f_1(\lambda_{th})$. As a result, we have

$$\lambda_{th} = \left[-\sqrt{2SNR_o \cdot (4SNR_o + 2 - \ln(4\pi SNR_o))} + 3SNR_o + 1\right] \cdot \sigma_o^2, \tag{7.13}$$

where SNR_o indicates the ratio of signal (or pilot contamination) strength to σ_o^2, given by

$$SNR_o = \left|\mathbf{h}_{S,P}^{(l,k)}[m]\right|^2/\sigma_o^2. \tag{7.14}$$

The miss rate (R_M) and the false alarm rate (R_{FA}) are exclusively dependent on SNR_o, as shown in the following equations

$$R_M = 0.5 \cdot \mathrm{erfc}\left(-\sqrt{SNR_o} + \sqrt{2SNR_o + 1 - 0.5 \cdot \ln\left(4\pi SNR_o\right)}\right) \tag{7.15a}$$

$$R_{FA} = \exp\left(-3SNR_o - 1 + \sqrt{2SNR_o \cdot \left(4SNR_o + 2 - \ln\left(4\pi SNR_o\right)\right)}\right), \tag{7.15b}$$

where $\mathrm{erfc}(\cdot)$ denotes the complementary error function. The proof can be found in Appendix D.2. Besides, we can prove that both R_M and R_{FA} decrease as SNR_o grows.

In practical scenarios, both SNR_o and σ_o are unknown. Therefore, we need to estimate them from the MF channel estimate, i.e., $\hat{\mathbf{h}}_{mf}^{(l,k)}$. As we have mentioned, the desired signals and the pilot contamination only exist on a small fraction of the components in $\hat{\mathbf{h}}_{\omega}^{(l,k)}$. As a result, we can sort the components in $\hat{\mathbf{h}}_{\omega}^{(l,k)}$ based on their strength, and choose the weakest ones of them to estimate σ_o^2. On the other hand, the strongest ones can be employed to estimate signal (or pilot contamination) strength. Then, SNR_o can be estimated as the ratio of signal strength to σ_o^2.

7.2.3 The Isolation of Pilot Contamination in $\mathbf{y}_{proc}$

During the *processing* phase, the received signal is given by (7.2), which is composed of signals from all cells in G_2 and G_3. However, only six of them are adjacent to the target BS and generate strong interferences. Therefore, we can rewrite (7.2) as (7.16),

$$\mathbf{y}_{proc}^{(l)} = \sum_{i=1}^{6} \mathbf{h}_{l_i,k}^{(l)} s_{l_i,k} + \sum_{k' \neq k} \sum_{i=1}^{6} \mathbf{h}_{l_i,k'}^{(l)} s_{l_i,k'} + \sum_{c_{l'} \notin \left\{G_1 \cup \{l_i\}_{i=1}^{6}\right\}} \sum_{k'} \mathbf{h}_{l',k'}^{(l)} s_{l',k'} + \mathbf{n}_{proc}, \tag{7.16}$$

and the spatial spectrum of $\mathbf{y}_{proc}^{(l)}$ can be obtained through IDFT as $\mathbf{y}_{\omega}^{(l)} = \mathbf{F}_M \mathbf{y}_{proc}^{(l)}$. The m-th element will be

$$\mathbf{y}_{\omega}^{(l)}[m] = \sum_{i=1}^{6} \sum_{b=1}^{B} a_b^{(l_i,k)} \cdot f\left(\omega_b^{(l_i,k)} - m\omega_0\right) s_{l_i,k} + \tilde{\mathbf{n}}_{proc}[m], \tag{7.17}$$

where $\tilde{\mathbf{n}}_{proc}$ indicates the IDFT of the last three parts in (7.16) combined. Due to the large number of users, $\tilde{\mathbf{n}}_{proc}$ can be treated as the Gaussian noise.

The strong components in $\mathbf{y}_{\omega}^{(l)}$ fall in two categories: pilot contamination and general inter-cell interferences. It should be noted that both these two categories come from adjacent cell users that are located close to the edge of c_l. Our major objective is to identify the spatial signatures of the pilot contamination through the following metric:

$$\phi_m^{(l,k)} = \frac{|\mathbf{y}_{\omega}^{(l)}[m]|^2}{|\hat{\mathbf{h}}_{\omega}^{(l,k)}[m]|^2}, \tag{7.18}$$

where $\mathbf{y}_{\omega}^{(l)}[m]$ is given by (7.17). It should be noted that we only need to compute $\phi_m^{(l,k)}$ for $m = m_q\,(q = 1, 2, \cdots, Q)$, because spatial signatures of the pilot contamination of the k-th user in the l-th cell must be among the columns of $\mathbf{U}_{S,P}^{(l,k)}$.

Depending on whether the desired signal or pilot contamination exists on $m\omega_0$, the conditional PDFs of $\phi_m^{(l,k)}$ can be represented as $f_{ds}(\phi_m^{(l,k)})$ or $f_{pc}(\phi_m^{(l,k)})$, respectively. The closed-form representations of these two functions will be discussed in the next section. Then, we can identify the pilot contamination components through the maximum likelihood estimator. As a result, the subspace of pilot contamination for the k-th user in the l-th cell can be represented by

$$\mathbf{U}_P^{(l,k)} = \left[\, \mathbf{e}\left[m_1'\omega_0\right], \mathbf{e}\left[m_2'\omega_0\right], \cdots, \mathbf{e}\left[m_P'\omega_0\right] \right], \tag{7.19}$$

where m_p' satisfies $\lambda_{m_p'}^{(l,k)} > \lambda_{th}$ and $f_{pc}\left(\phi_{m_p'}^{(l,k)}\right) > f_{ds}\left(\phi_{m_p'}^{(l,k)}\right)$. The last step is to project

the MF-based channel estimate onto the null space of $\mathbf{U}_P^{(l,k)}$ to eliminate strong pilot contamination as

$$\hat{\mathbf{h}}_{sf}^{(l,k)} = \left(\mathbf{I} - \mathbf{U}_P^{(l,k)}\mathbf{U}_P^{(l,k)^H}\right)\hat{\mathbf{h}}_{mf}^{(l,k)}, \tag{7.20}$$

where $\hat{\mathbf{h}}_{sf}^{(l,k)}$ is the new channel estimate of the k-th user in c_l based on *spatial filter*. The presented algorithm is briefly summarized in Algorithm 2.

Algorithm 2 Channel estimate for the k-th user in the l-th cell based on spatial filter.

Require:

Received pilot, $\mathbf{Y}^{(l)}$;

Received signal on processing phase, $\mathbf{y}_{proc}^{(l)}$;

The k-th pilot sequence, $\mathbf{p}_k$.

Ensure:

Channel estimate

1: Obtain MF channel estimate through (7.1), i.e., $\hat{\mathbf{h}}_{mf}^{(l,k)}$;

2: Compute the spectrum of $\hat{\mathbf{h}}_{mf}^{(l,k)}$ through IDFT as $\hat{\mathbf{h}}_{\omega}^{(l,k)} = \mathbf{F}_M\hat{\mathbf{h}}_{mf}^{(l,k)}$;

3: Find threshold (λ_{th}) through (7.13);

4: Construct $\mathbf{U}_{S,P}^{(l,k)}$ through (7.7);

5: Compute the spectrum of $\mathbf{y}_{proc}^{(l)}$ through IDFT as $\mathbf{y}_{\omega}^{(l)} = \mathbf{F}_M\mathbf{y}_{proc}^{(l)}$;

6: Construct the subspace of pilot contamination (i.e., $\mathbf{U}_P^{(l,k)}$) through (7.19);

7: Pilot contamination elimination by subspace projection
$\hat{\mathbf{h}}_{sf}^{(l,k)} = (\mathbf{I} - \mathbf{U}_P^{(l,k)}\mathbf{U}_P^{(l,k)^H})\hat{\mathbf{h}}_{mf}^{(l,k)}$;

8: **return** $\hat{\mathbf{h}}_{sf}^{(l,k)}$;

7.2.4 Conditional PDF of $\phi_m^{(l,k)}$

As we have mentioned, $\phi_m^{(l,k)}$ tends to be smaller when pilot contamination exists on $m\omega_0$. On the other hand, $\phi_m^{(l,k)}$ will be larger when the desired signals come from $m\omega_0$. Therefore, $\phi_m^{(l,k)}$ follows different distributions in these two scenarios. To employ the maximum likelihood estimator, we need to first analyze the statistical properties of $\phi_m^{(l,k)}$ in different situations.

We will first analyze the distribution of $\phi_m^{(l,k)}$ when pilot contamination exists on $m\omega_0$. Without loss of generality, we assume that the pilot contamination on $m\omega_0$ comes from the b-th path of the k-th user in the l_i-th cell. In other words, $\omega_b^{(l_i,k)}$ is close to $m\omega_0$, and there will be strong pilot contamination components in both $\mathbf{y}_\omega^{(l)}[m]$ and $\hat{\mathbf{h}}_\omega^{(l,k)}[m]$, presented as

$$\begin{cases} \hat{\mathbf{h}}_\omega^{(l,k)}[m] = a_b^{(l_i,k)} \cdot f\left(\omega_b^{(l_i,k)} - m\omega_0\right) + \tilde{\mathbf{n}}_k[m] \\ \mathbf{y}_\omega^{(l)}[m] = a_b^{(l_i,k)} \cdot f\left(\omega_b^{(l_i,k)} - m\omega_0\right) s_{l_i,k} + \tilde{\mathbf{n}}_{proc}[m], \end{cases} \tag{7.21}$$

where $\tilde{\mathbf{n}}_{proc} \sim N(\mathbf{0}, \sigma_{proc}^2 \cdot \mathbf{I}_M)$. In this case, we have

$$\phi_m^{(l,k)} = \frac{\left|r_{pc} s_{l_i,k} + \tilde{\mathbf{n}}_{proc}[m]\right|^2}{\left|r_{pc} + \tilde{\mathbf{n}}_k[m]\right|^2}, \tag{7.22}$$

where $r_{pc} = a_b^{(l_i,k)} \cdot f\left(\omega_b^{(l_i,k)} - m\omega_0\right)$. $\tilde{\mathbf{n}}_k[m]$ is much weaker than r_{pc}, and by ignoring $\tilde{\mathbf{n}}_k[m]$, we can approximate (7.22) as

$$\phi_m^{(l,k)} 2|r_{pc}|^2/\sigma_{proc}^2 = \left|\frac{\Re\{r_{pc}\} + \Re\left\{\tilde{\mathbf{n}}_{proc}[m] s_{l_i,k}^*\right\}}{\sigma_{proc}/\sqrt{2}}\right|^2 + \left|\frac{\Im\{r_{pc}\} + \Im\left\{\tilde{\mathbf{n}}_{proc}[m] s_{l_i,k}^*\right\}}{\sigma_{proc}/\sqrt{2}}\right|^2. \tag{7.23}$$

Noticing that the right hand side of (7.23) follows the noncentral chi-square distribution, we can obtain the approximate PDF of $\phi_m^{(l,k)}$ as

$$f_{pc}(\phi_m^{(l,k)}) = \frac{|r_{pc}|^2}{\sigma_{proc}^2} \exp\left(-\frac{|r_{pc}|^2}{\sigma_{proc}^2}\left(\phi_m^{(l,k)} + 1\right)\right) \cdot I_0\left(\frac{2|r_{pc}|^2}{\sigma_{proc}^2}\sqrt{\phi_m^{(l,k)}}\right), \tag{7.24}$$

where $I_0(\cdot)$ denotes the modified Bessel function of the first kind given by

$$I_v(y) = (y/2)^v \sum_{j=0}^{\infty} \frac{(y^2/4)^j}{j!\Gamma(v+j+1)}. \tag{7.25}$$

This result is justified in Appendix D.4.

On the other hand, when a specific path of the desired signals is close to $m\omega_0$, there will be strong signal component in $\hat{\mathbf{h}}_{\omega}^{(l,k)}[m]$. Without loss of generality, assume that the index of that path is b and we have the following approximation:

$$\begin{cases} \hat{\mathbf{h}}_{\omega}^{(l,k)}[m] = a_b^{(l,k)} \cdot f(\omega_b^{(l,k)} - m\omega_0) + \tilde{\mathbf{n}}_k[m] \\ \mathbf{y}_{\omega}^{(l)}[m] = \tilde{\mathbf{n}}_{proc}[m]. \end{cases} \tag{7.26}$$

In this case,

$$\phi_m^{(l,k)} = \frac{|\tilde{\mathbf{n}}_{proc}[m]|^2}{|r_{ds} + \tilde{\mathbf{n}}_k[m]|^2} \approx \frac{|\tilde{\mathbf{n}}_{proc}[m]|^2}{|r_{ds}|^2}, \tag{7.27}$$

where $r_{ds} = a_b^{(l,k)} \cdot f\left(\omega_b^{(l,k)} - m\omega_0\right)$. $\tilde{\mathbf{n}}_k[m]$ can be neglected because it is much weaker than r_{ds}. Therefore, the PDF of $\phi_m^{(l,k)}$ can be approximated by the exponential distribution, given by

$$f_{ds}(\phi_m^{(l,k)}) = \frac{|r_{ds}|^2}{\sigma_{proc}^2} \exp\left(-\frac{|r_{ds}|^2}{\sigma_{proc}^2} \cdot \phi_m^{(l,k)}\right). \tag{7.28}$$

In practical scenarios, $|r_{pc}|^2$ and $|r_{ds}|^2$ can be approximated by $|\hat{\mathbf{h}}_{\omega}^{(l,k)}[m]|^2$, because they are much stronger than $\tilde{\mathbf{n}}_k[m]$. Besides, $|\tilde{\mathbf{n}}_{proc}[m]|^2$ can be estimated from those components in $\mathbf{y}_{\omega}^{(l)}$, where neither the desired signal nor the pilot contamination exists.

When the number of users increases in adjacent cells, the spatial spectrum in the second phase is almost white. Intuitively, it seems impossible to estimate the DoA of the pilot contamination, because they are overwhelmed by general inter-cell interference. However, the spectrums in the pilot transmission phase and processing phase are highly correlated on

those directions, where pilot contamination exists. On the other hand, if the desired signals exist, the received signal strength in these two phases will be independent. Therefore, we can still extract some information. As a matter of fact, even when the number of users is very large, the results in (7.24) and (7.28) are still valid.

7.2.5 The Probability that the Main Lobes of the Desired Signal and Pilot Contamination Overlap

In previous discussion, we assume that the main lobes of the desired signals and the pilot contamination from adjacent cells do not overlap. As a matter of fact, it is possible for them to overlap in space, and we will analyze the probability in this section. To simplify notations, we define the following symbols:

$$\begin{aligned} DS_m &= \begin{cases} 1, & \exists b : \left|\omega_b^{(l,k)} - m\omega_0\right| < \omega_0, \\ 0, & \text{otherwise;} \end{cases} \\ PC_m &= \begin{cases} 1, & \exists b, i : \left|\omega_b^{(l_i,k)} - m\omega_0\right| < \omega_0. \\ 0, & \text{otherwise.} \end{cases} \end{aligned} \tag{7.29}$$

Given that a strong component of the desired signals exists on $m\omega_0$, the probability that a strong pilot contamination component coexists is $Pr(PC_m = 1|DS_m = 1)$. On the other hand, given that a strong component of pilot contamination exists on $m\omega_0$, the probability that a strong desired signal coexists is $Pr(DS_m = 1|PC_m = 1)$. Then, we have the following theorem.

Theorem 2. *When the number of BS antennas is very large, both* $Pr(PC_m = 1|DS_m = 1)$ *and* $Pr(DS_m = 1|PC_m = 1)$ *are inversely proportional to the BS antenna number. To be*

specific, we have

$$\begin{aligned} Pr(PC_m = 1|DS_m = 1) &= 12B/M + o(1/M), \\ Pr(DS_m = 1|PC_m = 1) &= 2B/M + o(1/M), \end{aligned} \tag{7.30}$$

where $o(1/M)$ *indicates a component much smaller than* $1/M$*.*

The proof of Theorem 2 can be found in Appendix D.3. For massive MIMO systems, M is generally very large, and it is safe for us to assume that the desired signals do not overlap with the pilot contamination in space.

7.2.6 Computational Complexity

Due to the large number of antennas at the BSs, it is important to maintain the computational complexity of the channel estimators at an acceptable level. The proposed channel estimation algorithm contains three parts: the MF channel estimation, pilot contamination identification and SF channel estimation. The complexity of the MF channel estimator is $\mathcal{O}\{M\tau^2\}$. The second part contains two steps: the first step is to identify the spatial signatures of both the desired signals and the pilot contamination from the MF-based channel estimate, while the second step is to pick out the pilot contamination from the components identified in step one. For every user, the complexity of spatial spectrum analysis is $\mathcal{O}\{M \log_2 M\}$ through FFT. Considering K users per cell and the spatial spectrum analysis of $\mathbf{y}_{proc}^{(l)}$, the overall complexity of the second part is $\mathcal{O}\{(K+1)M \log_2 M\}$. In the third part, we can reorganize (7.20) as

$$\hat{\mathbf{h}}_{sf}^{(l,k)} = \hat{\mathbf{h}}_{mf}^{(l,k)} - \mathbf{U}_P^{(l,k)} \left(\mathbf{U}_P^{(l,k)^H} \hat{\mathbf{h}}_{mf}^{(l,k)} \right). \tag{7.31}$$

The complexity of $\mathbf{U}_P^{(l,k)^H}\hat{\mathbf{h}}_{mf}^{(l,k)}$ is $\mathcal{O}\{MP\}$, where P is the number of detected pilot contamination components in space. Considering K users per cell, the complexity of the third part will be $\mathcal{O}\{KMP\}$.

Generally, we have $\log_2 M < \tau = K$, while P should be smaller than 10. Therefore, the overall complexity of these three parts combined will be $\mathcal{O}\{MK^2\}$, almost identical to that of the MF estimator.

7.3 Performance Evaluation

In this section, simulations will be conducted to evaluate the performance of the presented algorithm, in terms of normalized channel estimation error, achieved SINR and achievable rate. Results will be compared with other existing methods. Besides, simulations will be conducted in different communication scenarios, where the intensity of pilot contamination varies.

7.3.1 Performance Comparison Under Different SNRs

To start with, we will first investigate the impact of SNR. The presented method will be compared with the MF [72], SVD [87], and data-aided schemes [91]. The channel model in (2.9) will be employed with $B = 3$. The simulation parameters are almost identical to those employed in [72], as shown in Table 7.1. Same to [72], we consider interference from all cells whose distance to the target cell is less than eight cell-diameters. Therefore, there are totally 199 cells in the simulations. We assume a coherence time of 0.5 millisecond, which is equivalent to the length of seven OFDM symbols in LTE systems, while the frequency

Table 7.1: Simulation Parameters

Path Loss Exponent	3.8
Cell Radius	500 m
Cell-Hole Radius	50 m
User Number / Cell	10
Antenna Number / BS	400
Pilot Length (τ)	10
Frequency Smooth Interval	14 Carriers
Coherence Time	0.5 ms
Standard Deviation of Shadowing	8 dB
Modulation	QPSK

smooth interval is equal to 14 sub-carriers. Therefore, the channel remains stationary over 98 time-frequency resource blocks. The simulation results are presented in Figure 7.4 and 7.5.

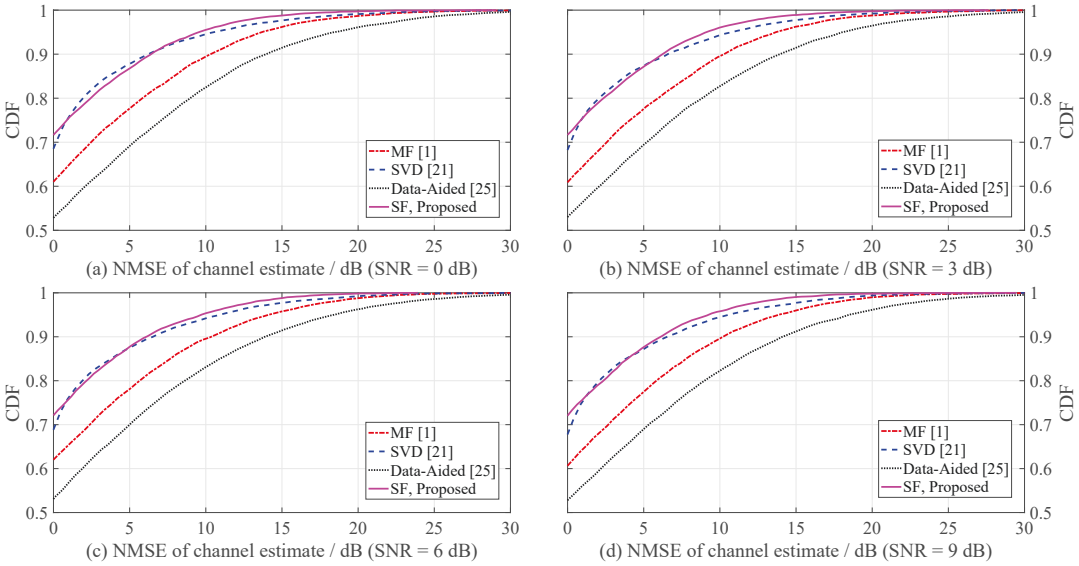

Figure 7.4: The normalized channel estimation error of different channel estimators.

In Figure 7.4, we present the CDF of the normalized channel estimation error of users in the target cell. From the figure, for all the estimators, there always exists a small proportion of users experiencing "bad" channels, and these users are most probably located far away from their BSs (or equivalent, close to cell edges). Due to the long distance between the user and the BS, the desired signal will be weaker, and the pilot contamination will be relatively stronger. By employing the proposed method, as shown in Figure 7.4, the proportion of users experiencing "bad" link conditions will be much reduced.

For the normalized channel estimation error in Figure 7.4, the data-aided channel es-

timator shows the worst performance. By utilizing both the pilot and data for channel estimation, the data-aided channel estimator can suppress the pilot contamination to some extent, and eliminate the intra-cell interference by using the zero-forcing algorithm. However, the general inter-cell interference will be inevitable, because user data from adjacent cells are not orthogonal with that of the desired users, and the target BS does not have the uplink CSI from adjacent cells. Moreover, the general inter-cell interference will be stronger than the pilot contamination. For example, the maximum number of strong pilot contamination sources is six, while all the users in adjacent cells contribute to the general inter-cell interference, which is much larger. The SVD-based and the proposed estimators have similar performance in terms of the NMSE of the channel estimate. However, for cell-edge users, the presented channel estimator demonstrates slight advantage over the SVD-based estimator. For example, 95 percent of the users will experience an NMSE less than 9.5 dB when the proposed estimator is employed, whereas the value for the SVD-based estimator will be 10.5 dB. In general, both the presented channel estimator and the SVD-based one have a significant performance gain over the MF-based channel estimator. For example, only around 5% of the users will experience an NMSE larger than 10 dB for the first two algorithms, whereas this number is doubled for the MF-based channel estimator.

From Figure 7.4, we also notice that the performance of channel estimators under different SNRs is very consistent. This is not surprising because the large antenna arrays at the BSs can provide significant gains and boost actual SNR. Therefore, system performance will be mainly affected by the pilot contamination because noise is negligible. Similar results can be observed in Figure 7.5 for the achieved SINR performance.

In Figure 7.5, we employ the zero-forcing estimator for data detection and compare the

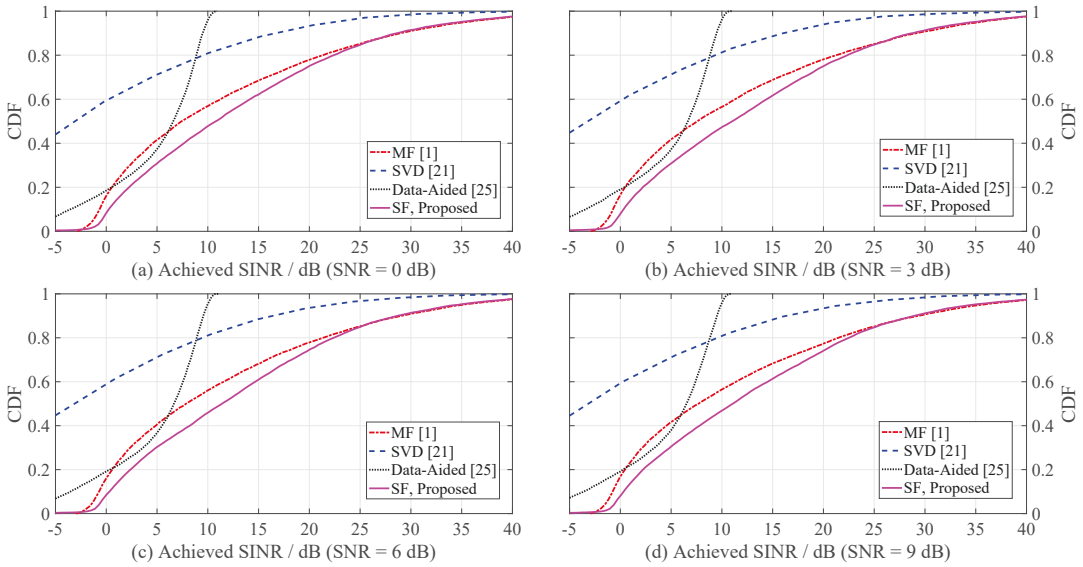

Figure 7.5: The achieved SINR comparison of different channel estimators.

achieved SINRs of different channel estimators. Due to the asymptotical orthogonality of different users' channel vectors, the zero-forcing estimator is asymptotically optimal [72]. It is clear that the proposed method outperforms the existing ones. For example, for an SNR of 0 dB, only 7% of the users will experience an SINR less than 0 dB. However, this number will be more than doubled for other three algorithms. These users are experiencing low SINR because they are located at cell edges, and as a result, suffer from attenuated signal strength and strong pilot contamination. As observed from the figure, the SVD-based channel estimator has the worst performance, which seems to be contradictory to the results in Figure 7.4. As a matter of fact, the SVD-based algorithm assumes that the desired signals are always stronger than the pilot contamination. However, it is not always the case for cell edge users. Therefore, the CSI for some users may be completely lost and

these users will experience very low SINR. However, the NMSE of their channel estimation results may not be necessarily large, which we will demonstrate through a simple example.

Assume that we are trying to estimate a specific channel vector $\mathbf{h}$, while the pilot contamination is presented as $\mathbf{h}_{pc}$. Besides, the pilot contamination is much stronger than, but orthogonal to the desired signal, i.e., $\|\mathbf{h}_{pc}\|^2 > \|\mathbf{h}\|^2$ and $\|\mathbf{h}_{pc}^H \mathbf{h}\| = 0$. When we ignore the noise, the original MF-based channel estimator will give $\hat{\mathbf{h}}_{mf} = \mathbf{h}_{pc} + \mathbf{h}$. On the other hand, for the SVD-based estimator, the channel estimate will be $\hat{\mathbf{h}}_{svd} = \mathbf{h}_{pc}$. The normalized channel estimation error of these two estimators are given by $NMSE_{svd} = |\hat{\mathbf{h}}_{svd} - \mathbf{h}|^2/|\mathbf{h}|^2 = 1+|\mathbf{h}_{pc}|^2/|\mathbf{h}|^2$ and $NMSE_{mf} = |\mathbf{h}_{pc}|^2/|\mathbf{h}|^2$, respectively. However, if we compare the achieved SINR, we have $SINR_{mf} = |\mathbf{h}|^2/|\mathbf{h}_{pc}|^2$ and $SINR_{svd} = 0$, respectively. As we can see, the SVD-based and MF-based channel estimators have comparable performance in terms of the normalized channel estimation error. Intuitively, they should have similar performance in the achieved SINR. However, the gap in the achieved SINR (expressed in dB) between these two estimators will be infinitely large, because the SVD-based channel estimator lost all the channel state information. From this example, we can see that a smaller channel estimation error does not always lead to a larger achieved SINR (or achievable rate, equivalently). This helps to explain why the SVD-based estimator behaves differently for the achieved SINR and the NMSE.

By removing the assumption that the desired signals are always stronger than the pilot contamination, the presented algorithm becomes more applicable to practical use. A noticeable gain is achieved because it can effectively identify the spatial signatures of the pilot contamination and then eliminate them. When the pilot contamination becomes stronger, our proposed algorithm has a better chance to find it. That is, the two PDFs of

$\phi_m^{(l,k)}$ (i.e., $f_{pc}(\phi_{m'_p}^{(l,k)})$ and $f_{ds}(\phi_{m'_p}^{(l,k)})$) can be better separated when the pilot contamination is strong on $m\omega_0$.

7.3.2 Impact of K, M and B on the Proposed Method

As we have explained, spatial sparsity is very important to the proposed method. Intuitively, as the number of users per cell and the number of paths per user increase, the proposed method will see performance degradation. Besides, if the antenna number at the BS decreases, it will impose challenges for the proposed method to effectively identify the pilot contamination, which also leads to performance degradation. In this section, we investigate how these three factors influence the presented method. As shown in the previous subsection, the SNR is not a major impact factor in massive MIMO systems. Therefore, a constant SNR of 0 dB will be considered here. Having shown that the MF-based channel estimator has comparable performance to the presented one, while the performance of the other two existing methods is much inferior in sparse channels, we will only compare the proposed method with the MF-based one.

First, we conduct simulations for $M \in \{100, 200, 400\}$, while $K = 20$ is fixed. Intuitively, when the number of BS antennas increases, the presented method should have better performance, because it is more capable of detecting the pilot contamination. From Figure 7.6 (a), we can see that the results are consistent with our intuitions. Besides, we also see that the MF-based estimator will have better performance for a larger M. As the number of antennas decreases, the performance gap between the presented and the MF-based estimators will become smaller. When $M = 100$, superior performance of the presented method will no longer exist. It is because the pilot contamination will become too crowded

to be detected by the proposed method.

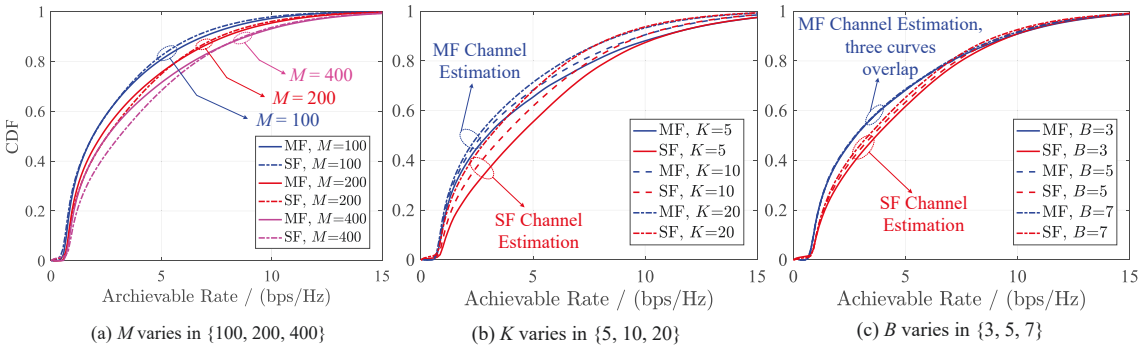

(a) M varies in {100, 200, 400} (b) K varies in {5, 10, 20} (c) B varies in {3, 5, 7}

Figure 7.6: The achievable rate for different M, K and B.

For a fixed $M = 400$, we present the performance of different estimators for $K \in \{5, 10, 20\}$, as shown in Figure 7.6 (b). When the number of users per cell increases, pilot contamination will become more intensive, and the achievable rates of both methods will decrease. However, the presented method still have a perceivable gain over the MF-based method.

In Figure 7.6 (c), the path number per user varies from 3 to 5 and then to 7, while M and K are fixed to 400 and 10, respectively. The three curves of the MF-based estimator are almost overlapped, because the strength of the desired signals and the pilot contamination increases at the same time, leading to almost constant achieved SINR for different B values. However, for the proposed method, the increased number of paths per user will make it more difficult to isolate the pilot contamination from the desired signals. Therefore, we can see the performance of the proposed method will degrade for larger B. Nevertheless, the proposed method still outperforms the MF-based estimator.

From Figure 7.6, it is clear that the proposed method is more sensitive to the change of the BS antenna number and the user number per cell. The number of paths per user also has some impact, but slightly less significant. Overall, the proposed method always outperforms the conventional MF-based estimator for a reasonably large M to K ratio.

7.4 Summary

In this chapter, we presented an innovative channel estimation scheme for massive MIMO systems. The key idea is to identify the spatial signatures of the pilot contamination from adjacent cells and eliminate them by constructing a spatial filter. The stronger the pilot contamination is, the better chance we have to identify it. Such estimation method is especially helpful to cell-edge users, because their signals can be overwhelmed by pilot contamination from adjacent cells. Compared with the existing pilot decontamination methods, the proposed scheme has two major advantages: 1) no *a priori* statistical information is required; and 2) no need for the assumption that the desired signals are always stronger than the pilot contamination to perform effective estimation. As a matter of fact, the probability that the second condition cannot be fulfilled for cell-edge users is too large to be ignored. This algorithm is evaluated through simulations in the normalized channel estimation error, the achieved SINR and the achievable rate. Both simulation results and theoretical analysis show that the proposed spatial filter-based approach provides a promising technique to battle the pilot contamination problem in future 5G massive MIMO systems.

Chapter 8

Channel Tracking for Millimeter Wave Communications

In the previous chapter, we introduced the massive MIMO and the pilot contamination issue. Another very important enabling technology of 5G is the millimeter wave communications. As we know, the current cellular spectrum is becoming more and more crowded. To explore more available bandwidth, researchers have been talking about the possibility of moving the cellular system to millimeter wave frequency band, from 30 to 300 GHz, which is less occupied. However, the high carrier frequency brings some problems, one of them is the huge attenuation. To solve this problem, large antenna arrays should be installed on base stations. Then, the BS can generate a narrow beam directly pointing to the user. To achieve this goal, the CSI is indispensable. Intuitively, the BS needs to know the direction of the user, before a proper beam can be generated. [1]

[1]The work presented in this chapter has been published in [J5]: Zijun Gong, Fan Jiang, and Cheng Li, "Angle Domain Channel Tracking with Large Antenna Array for High Mobility V2I Millimeter Wave

8.1 Introduction

As has been mentioned, the antenna array form is very important for mmWave communication systems, and the linear or planar arrays are the most common choices. In recent years, lens antenna array provides another solution [148–152]. In [148], the authors conducted experimental measurements with a prototype system, and the measurements demonstrated the utility of this new array form. In [149], the authors derived the array response of lens antenna arrays. They also showed that compared to the conventional unitary planar arrays in millimeter wave communications, the new system based on lens achieved similar spectral efficiency with significantly reduced signal processing complexity and much less RF chains. Generally, lens antenna arrays have the following advantages. First of all, beamforming can be performed with only a few antennas, which means less RF chains are required. Second, due to the small number of active antennas, the computational complexity of beamforming is reduced to great extent, leading to small delay. These properties are important in many real-time and high-rate applications, for example, the modern vehicular applications. A few literatures have talked about the channel estimation for millimeter wave massive MIMO systems with lens arrays. For instance, in [153], an adaptive selecting network was constructed for antenna selection. Based on the antenna selection, the authors formulated the channel estimation issue as a sparse signal recovery problem, and a support detection (SD)-based channel estimation scheme was proposed. The authors showed that the proposed algorithm worked great even in low SNR regime. However, the proposed framework cannot be easily extended to broadband frequency selective channels [150]. By

Communications," *IEEE J. Sel. Topics Signal Process.*, vol. 13, no. 5, pp. 1077-1089, Sept. 2019.

employing the energy focusing property of the lens arrays, jointly with the spatial sparsity, the authors in [150] transformed the millimeter wave massive MIMO channel estimation into reduced-size MIMO channel estimation.

In millimeter wave communications, channel estimation consumes many resources, in terms of time, bandwidth, and hardware. This is especially true for high mobility user equipment. Because the channel is varying fast, and the CSI should be updated frequently. However, the good news is that the millimeter wave channels are generally sparse in space and channel states at consecutive time slots are highly correlated in angle domain. Therefore, it is possible to track the channel state with less resources, instead of re-estimating it for every time slot. For millimeter wave communications, the antenna array form is important, and a lens antenna array will be employed in later discussions, because it has much lower complexity and it allows the BS to use only a few RF (Radio Frequency) chains for beamforming. Based on the lens antenna array and the spatial sparsity of the millimeter wave channels, a data-aided channel tracking scheme will be presented for drone-to-BS communications. The basic idea is to employ the channel estimate from the previous time slot for the data detection at the current one. After data detection, the detected data sequence can be used for channel update, and this process iterates. By doing this, the overhead of channel estimation can be reduced to great extent. Due to the high correlation of channels between adjacent time slots, the channel variation is negligible. Therefore, as long as the inducted channel estimation error is within the data detection capacity (efficient data detection schemes discussed in [133, 134, 154, 155]), the data symbols can be successfully recovered.

The presented method has the following major advantages. First, there is no overhead

for channel tracking, and the block length can be adaptively changed to cope with fast movement and narrow beams. Even for low-speed situations, the presented method still outperforms the existing ones in terms of achievable rate, because the training overhead is eliminated. Secondly, it can work in very low SNR regime, because the data sequences can be much longer than pilot sequences, which helps to suppress noise. Thirdly, even if the moving direction and speed of the user change fast, this algorithm still works great and no calibration is required. As comparison, the channel tracking scheme proposed in [151] requires periodical calibration.

8.2 System Model

For millimeter wave communications, large antenna arrays are always indispensable, and many different array forms have been proposed and investigated. Among them, the discrete lens antenna arrays (DLAs) are very popular, because they require very few RF chains and allow easy antenna selection. To be specific, for signals coming from an arbitrary direction, most of the energy concentrates on two or three antennas, which means we can transmit and receive signals on only a small number of antennas with negligible performance loss. Therefore, we will introduce the system model based on the DLAs.

8.2.1 Channel Model

Assume that every BS has M antenna elements, and serves up to K users simultaneously. The channel vector of the k-th user is given as

$$\mathbf{h}_k = \beta_k^{(0)} \mathbf{a}\left(\phi_k^{(0)}\right) + \sum_{l=1}^{L} \beta_k^{(l)} \mathbf{a}\left(\phi_k^{(l)}\right), \tag{8.1}$$

where $\phi_k^{(l)}$ is the DoA of the l-th path from the k-th user, while $\beta_k^{(l)}$ is the complex channel gain. Without loss of generality, let $\beta_k^{(0)}\mathbf{a}(\phi_k^{(0)})$ denote the LoS component. In [149], the authors proved that the array response can be approximated by a scaled sinc function. To be specific, for signal coming from ϕ, $\mathbf{a}(\phi)$ is the array response, and the m-th element is given as

$$\mathbf{a}(\phi)[m] = \text{sinc}\left(m - D\left(1+\cos\phi\right)\right)\left(0 \le m \le M-1\right)^2, \tag{8.2}$$

where M denotes antenna number at the BS. D is the normalized dimension of the lens, and it should satisfy $M = 1 + \lfloor 2D \rfloor$. To simplify the mathematical notation, let $\alpha = D(1+\cos\phi)$, and (8.2) can be rewritten as

$$\mathbf{a}(\phi)[m] = \text{sinc}\left(m - \alpha\right). \tag{8.3}$$

It should be noted that α has a one-to-one relationship with the DoA of the received signal. Based on (8.3), it is clear that the received energy will be distributed on all M antennas for signals coming from a specific direction. However, only a small number of them are very strong, while the others are much weaker. As has been discussed in [151, 156, 157], more than 80% of the received energy concentrates on the two antennas in the main lobe of the sinc function. As a matter of fact, if we only collect energy from Q antennas with strongest channel gains, the energy loss will be a function of α, and the worst case scenario will be discussed in latter part of this section.

[2]Throughout this paper, sinc$(\cdot)$ denotes the normalized sinc function, and is give as $\text{sinc}(x) = \frac{\sin(\pi x)}{\pi x}$

8.2.2 Channel Estimation

For initial channel estimation, we employ the method from [150]. Due to the limited number of RF chains, every user will be served by V antennas, and the total number of RF chains will be KV. Besides, users served by the same BS will be assigned orthogonal pilot sequences. For every time slot, we can only estimate the channel gains of KV antenna elements at the BS. As a result, the pilot sequence will be repeatedly transmitted for $\lceil M/(KV) \rceil$ time slots. By stacking all the received signals, the BS has

$$\mathbf{Y}_p = \sum_{k=1}^{K} \mathbf{h}_k \mathbf{p}_k^T + \mathbf{N}, \tag{8.4}$$

where $\mathbf{p}_k$ denotes the pilot sequence of the k-th user and $\mathbf{N}$ is additive complex Gaussian noise. The elements in $\mathbf{N}$ are i.i.d. zero-mean circularly symmetric complex Gaussian random variables. The least square estimate of $\mathbf{h}_k$ will be

$$\hat{\mathbf{h}}_k = \mathbf{Y}_p \mathbf{p}_k^* / |\mathbf{p}_k|^2 = \mathbf{h}_k + \mathbf{n}_k, \tag{8.5}$$

where $\mathbf{n}_k = \mathbf{N}\mathbf{p}_k^* / |\mathbf{p}_k|^2$. By doing this, the initial estimate of the CSI can be obtained.

As we can see, if we conduct channel estimation for every data block independently, it will consume many resources. To reduce the overhead, channel tracking scheme should be carefully designed.

8.2.3 Truncated Channel Vector

Suppose every user is served by up to V active antennas. Intuitively, we should choose the V antennas with the strongest channel gains. By doing this, we will lose some energy for both the uplink and the downlink, but the performance degradation is negligible. In this

section, we introduce the concept of truncated channel vector, and analyze the concomitant energy loss. Without loss of generality, we take the uplink as example, and the analysis for downlink is very similar.

For notational simplicity, we will ignore the user index k and focus on the single-user scenario in this section. Assume the channel vector is $\mathbf{h}$, and the transmitted data sequence is $\mathbf{x} \in \mathbb{C}^N$, where N denotes the sequence length. If all antennas are active, the received signal at the BS will be $\mathbf{Y} \in \mathbb{C}^{M \times N}$:

$$\mathbf{Y} = \mathbf{h}\mathbf{x}^T + \mathbf{N}. \tag{8.6}$$

On the other hand, if we only use V consecutive antennas with strongest channel gains for data detection, the received signal will be $\mathbf{Y}_t \in \mathbb{C}^{V \times N}$:

$$\mathbf{Y}_t = \mathbf{h}_t\mathbf{x}^T + \mathbf{N}_t, \tag{8.7}$$

where $\mathbf{h}_t = \mathbf{h}[v_0 : v_0 + V - 1]$ is the truncated channel vector, and the active antennas are indexed from v_0 to $v_0 + V - 1$. $\mathbf{N}_t \in \mathbb{C}^{V \times N}$ denotes additive Gaussian noise on the active antennas.

Intuitively, if we only collect energy from V antennas with the strongest channel gains, a small portion of the energy will be lost. However, this is not a big issue, as has been discussed in many papers [151, 156, 157]. In [156] and [157], it has been proven that more than 80% energy of a sinc function concentrates on the two samples in the main lobe. As a result, we can use a very small number of antennas for beamforming, and the performance degradation is negligible. As a matter of fact, the received energy for most antennas is at noise level, and they will not contribute to system performance in low SNR regime [157].

To investigate how energy loss varies with the number of RF chains, we define $R(\alpha - \lfloor\alpha\rfloor, V)$ to represent the energy loss ratio, which is dependent on V and the fractional part of α. In V2I millimeter wave communications, if we only consider the predominant LoS signal, we approximately have $\mathbf{h}[m] = \beta\text{sinc}(m - \alpha)$. By sorting the elements of $\mathbf{h}$ based on their amplitudes in the descending order, a new vector can be obtained as $\mathbf{h}_s$ ($|\mathbf{h}_s[m]| \geq |\mathbf{h}_s[m+1]|$). Given that we only employ the V antennas with the strongest channel gains for uplink data detection, the energy loss ratio is given by

$$R(\alpha - \lfloor\alpha\rfloor, V) = 1 - \frac{\sum_{v=0}^{V-1} |\mathbf{h}_s[v]|^2}{\sum_{m=0}^{M} |\mathbf{h}_s[m]|^2}. \tag{8.8}$$

The numerical results are presented in Figure 8.1. It should be noted that the energy loss ratio is not dependent on the total antenna number based on (8.2). When we increase antenna number and maintain the RF chain number, the energy loss will increase, but energy loss ratio stays the same because the energy loss is normalized by total energy.

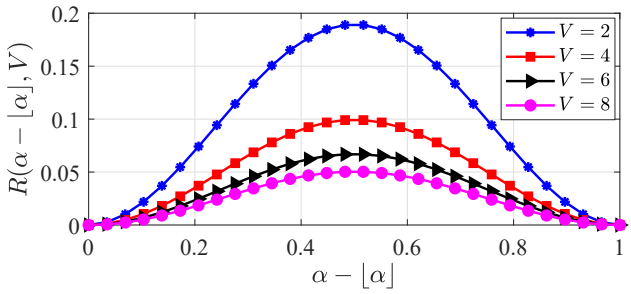

Figure 8.1: Energy loss caused by channel truncation.

As we can see in Figure 8.1, by using two antennas for beamforming, the energy loss ratio is less than 20%. When we increase the active antenna number to four, the worst case energy loss ratio will be reduced to 10 percent. However, if we keep increasing active

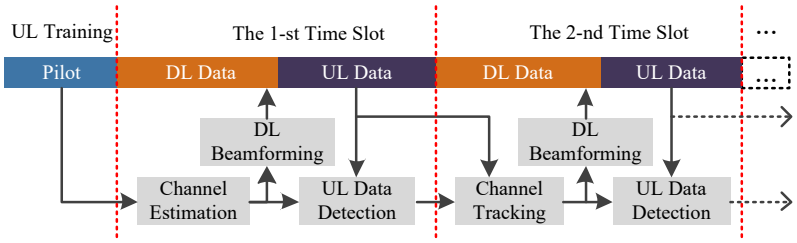

Figure 8.2: The data flow of the proposed channel tracking scheme.

antenna number, the improvement will be negligible.

From Figure 8.1, it is clear that lens antenna arrays with truncated channel vectors provide a very promising solution for millimeter wave communications. However, similar to other millimeter wave communication systems, the overhead of channel estimation is significant. As a result, we will present a low-complexity data-aided channel tracking scheme for the system discussed in the following section.

8.3 Data-Aided Channel Tracking

In this section, we will talk about the channel tracking method by only considering the single-user scenario for the following reasons. First, by isolating inter-user interference, we can better analyze the impacts of different parameters on channel tracking accuracy. Secondly, millimeter wave communication systems are generally assumed to work in low SNR regime, which means that noise is much stronger than inter-user interference, as we will see in the simulation results. Moreover, the large antenna arrays provide very good angular resolution. As long as the main lobes of two users' signals do not overlap, the interference will be negligible. When two users' signals do overlap in space, the BS can

still isolate them by allocating orthogonal time-frequency resources to them, which is a very mature technique in LTE. As a result, we will focus on the single-user scenario for theoretical analysis, while the multi-user scenario will be numerically evaluated in the simulation results.

The TDD communication protocol is shown in Figure 8.2. Due to channel reciprocity, only uplink channel is estimated, and the channel estimate will be used for uplink data detection and downlink beamforming. At the very beginning, to setup the communication link, the mobile user transmits an uplink training sequence to the BS. In the following communications, there are three phases in every block: processing, downlink data transmission and uplink data detection. During the processing phase of the first block, the BS can estimate the channel state information (signal strength, direction, and phase) based on the received pilot signals. The channel state information will be used for downlink data transmission and uplink data detection. At the end of the first block, the BS employs the decoded data to update channel estimate, which is referred to as channel tracking. The channel tracking result will be used for downlink data transmission and uplink data detection at the second block. This process iterates, and as long as the channel tracking is executed frequently (or fast, equivalently) enough, the mobile user will not need to transmit training sequence for channel estimation in the following communications. By doing this, the overhead can be significantly reduced.

The system diagram is depicted in Figure 8.3. Assume that the truncated channel vector of the n-th block has been estimated as $\hat{\mathbf{h}}_t^{(n)}$, and the active antennas are indexed from $v_0^{(n)}$ to $v_0^{(n)}+V-1$. At the $(n+1)$-th block, the received uplink signal is $\mathbf{Y}_{ul}^{(n+1)} \in \mathbb{C}^{V\times N}$, where N is the number of symbols transmitted on uplink during one block.

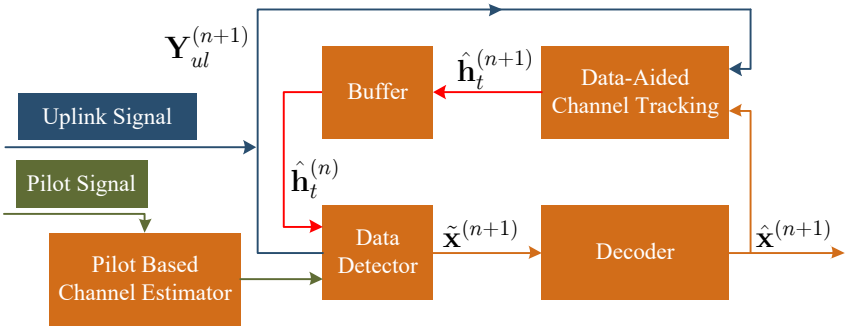

Figure 8.3: System diagram.

As we can see in Figure 8.3, the data detector will use the truncated channel estimate at the n-th block for data detection of the $(n+1)$-th block. In the data detector, symbols are detected independently. Due to the inaccurate channel state information and noise, the detected data sequence (i.e., $\tilde{\mathbf{x}}^{(n+1)}$) may have some errors. However, most errors will be corrected by the decoder through powerful channel coding schemes. As a result, $\hat{\mathbf{x}}^{(n+1)}$ should be fairly accurate, and it can be used for channel tracking. The updated truncated channel estimate of the $(n+1)$-th block can then be obtained through data-aided channel tracking, and buffered for data detection of the next time slot. This process will iterate, and as long as the channel state information is updated fast enough, channel estimation based on pilot will be unnecessary in following communications. In the remaining part of this section, we will mathematically formulate the problem.

The received uplink signal at the $(n+1)$-th block is

$$\mathbf{Y}_{ul}^{(n+1)} = \mathbf{h}_d^{(n+1)} \left(\mathbf{x}^{(n+1)}\right)^T + \mathbf{N}_{ul}^{(n+1)}, \tag{8.9}$$

where we have $\mathbf{h}_d^{(n+1)} = \mathbf{h}^{(n+1)}\left[v_0^{(n)} : v_0^{(n)} + V - 1\right]$, and $v_0^{(n)}$ represents the index of the first active antenna at the n-th block. The elements in $\mathbf{N}_{ul}^{(n+1)}$ are i.i.d. zero-mean circularly

symmetric complex Gaussian random variables, with a variance of σ^2. Suppose we already have the truncated channel estimate of the n-th block, given as

$$\hat{\mathbf{h}}_t^{(n)} = \hat{\mathbf{h}}^{(n)}\left[v_0^{(n)} : v_0^{(n)} + V - 1\right], \tag{8.10}$$

and our target is to track the channel state at the $(n+1)$-th block.

The multi-path effect is not severe in millimeter wave channels, which leads to much longer coherence time. As a result, we can safely assume that the channel vectors at two consecutive blocks are very close. As a result, we have $\hat{\mathbf{h}}^{(n)} \approx \mathbf{h}^{(n+1)}$, which means

$$\hat{\mathbf{h}}_t^{(n)} \approx \mathbf{h}_d^{(n+1)}. \tag{8.11}$$

By employing the matched filter for data detection based on $\hat{\mathbf{h}}_t^{(n)}$, the result is given as

$$\tilde{\mathbf{x}}^{(n+1)} = \left(\mathbf{Y}_{ul}^{(n+1)}\right)^T \left(\hat{\mathbf{h}}_t^{(n)}\right)^* / \|\hat{\mathbf{h}}_t^{(n)}\|^2. \tag{8.12}$$

$\tilde{\mathbf{x}}^{(n+1)}$ is subject to detection error, caused by both noise and inaccurate CSI. However, with powerful channel coding algorithms, most errors can be corrected, and we can obtain a much more accurate estimate of the data sequence, i.e., $\hat{\mathbf{x}}^{(n+1)}$. This result can then be used to estimate $\mathbf{h}_d^{(n+1)}$:

$$\hat{\mathbf{h}}_d^{(n+1)} = \mathbf{Y}_{ul}^{(n+1)}(\hat{\mathbf{x}}^{(n+1)})^* / \|\hat{\mathbf{x}}^{(n+1)}\|^2. \tag{8.13}$$

The last step of the channel tracking scheme is *transition*. In lens antenna arrays, by activating specific antennas, a beam pointing to the corresponding direction can be generated. If we are not able to activate the 'right' antennas, the user equipment can only receive very weak signals. The user mobility makes this even more challenging, because we

need to adaptively change the active antennas to track the user and guarantee reliable communications. Although the channel variation of adjacent blocks is very small, this change will increment and become very large for a long period of time. If the channel tracking algorithm fails to adjust the direction of the mainlobe, the BS will see a huge loss of energy. The purpose of the *transition* process is to adaptively change active antennas to guarantee good performance, and it is illustrated in Figure 8.4, where $V = 3$. The horizontal axis indicates the index of antennas while the vertical axis represents the normalized channel gains of different antennas. $\alpha^{(n)} = D\left(1 + \cos\phi^{(n)}\right)$, and $\phi^{(n)}$ is the DoA of the LoS path at the n-th block.

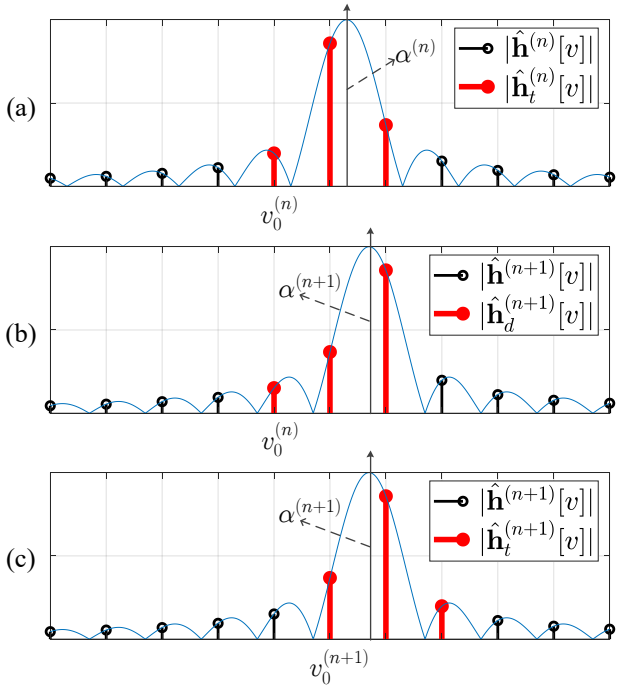

Figure 8.4: The transition process from the n-th block to the $(n+1)$-th block.

As we can see in Figure 8.4 (a), there are three antennas activated at the n-th block, and their indexes are $v_0^{(n)}$, $v_0^{(n)}+1$, and $v_0^{(n)}+2$. The $(v_0^{(n)}+1)$-th antenna has the strongest channel gain. At the $(n+1)$-th block, these three antennas are used to receive uplink signal and data detection is conducted, as shown in Figure 8.4 (b). We can then employ the detected uplink data for the data-aided channel tracking, and $\hat{\mathbf{h}}_d^{(n+1)}$ can be obtained. Due to the relative movement between the mobile user and the BS, the $\left(v_0^{(n)}+2\right)$-th antenna has the strongest channel gain at this moment, and we should re-select the active antennas. To achieve this goal, we will recover the whole channel vector, and select the three consecutive antennas with strongest channel gains. As we can see in Figure 8.4 (c), after the antenna selection, the active antennas are indexed from $v_0^{(n+1)} = v_0^{(n)} + 1$. By introducing the transition phase, the active antennas are periodically adjusted to steer the beam and make sure the mobile user is properly covered.

Generally, to complete the *transition* from the n-th to the $(n+1)$-th block, we need to reconstruct the whole channel vector, i.e., $\hat{\mathbf{h}}^{(n+1)}$. Equivalently, we need to estimate the $\alpha^{(n+1)}$ and $\beta^{(n+1)}$ based on $\hat{\mathbf{h}}_d^{(n+1)}$. In the following sections, we will first try to formulate the problem mathematically, and then present a low-complexity algorithm.

8.3.1 Maximum Likelihood Estimate

As we know, the maximum likelihood estimator is asymptotically consistent and efficient [158]. Therefore, we will formulate the estimation problem and estimate the parameters with maximum likelihood estimator.

Assume that the estimation error of $\hat{\mathbf{h}}_d^{(n+1)}$ follows zero-mean Gaussian distribution.

To be specific, we have

$$E\left\{\left(\hat{\mathbf{h}}_d^{(n+1)}-\mathbf{h}_d^{(n+1)}\right)\left(\hat{\mathbf{h}}_d^{(n+1)}-\mathbf{h}_d^{(n+1)}\right)^H\right\}=\sigma_d^2\mathbf{I}_V, \tag{8.14}$$

where σ_d^2 is the variance of $\hat{\mathbf{h}}_d^{(n+1)}[v]$. The justification of (8.14) and the expression of σ_d^2 will be presented in later discussions. As we have mentioned, the LoS path is predominant in millimeter wave communications, given that it exists. Besides, for reasonable SNRs, the noise is generally stronger than non-line-of-sight (NLoS) paths. As a result, by ignoring the NLoS paths, $\mathbf{h}_d^{(n+1)}$ is approximately a function of $\alpha^{(n+1)}$ and $\beta^{(n+1)}$:

$$\mathbf{h}_d^{(n+1)}[v]\approx\beta^{(n+1)}\,\mathrm{sinc}\left(v_0^{(n)}+v-\alpha^{(n+1)}\right). \tag{8.15}$$

Based on (8.14), we have the likelihood density function of $\hat{\mathbf{h}}_d^{(n+1)}$ as

$$\begin{aligned}&f\left(\hat{\mathbf{h}}_d^{(n+1)}|\alpha^{(n+1)},\beta^{(n+1)}\right)\\ =&\frac{1}{(\pi\sigma_d^2)^V}\exp\left\{-\|\hat{\mathbf{h}}_d^{(n+1)}-\mathbf{h}_d^{(n+1)}\|^2/\sigma_d^2\right\}.\end{aligned} \tag{8.16}$$

The maximum likelihood estimate of $\alpha^{(n+1)}$ and $\beta^{(n+1)}$ can then be given as

$$\begin{aligned}[\hat{\alpha}_{ml}^{(n+1)},\hat{\beta}_{ml}^{(n+1)}]&=\underset{\alpha^{(n+1)},\beta^{(n+1)}}{\arg\max}\ f(\hat{\mathbf{h}}_d^{(n+1)}|\alpha^{(n+1)},\beta^{(n+1)})\\ &=\underset{\alpha^{(n+1)},\beta^{(n+1)}}{\arg\min}\ \|\hat{\mathbf{h}}_d^{(n+1)}-\mathbf{h}_d^{(n+1)}\|^2.\end{aligned} \tag{8.17}$$

It is difficult to obtain the closed-form expression of the optimal solution, but we can generally employ iterative algorithms to obtain a close approximation, as will be discussed in the following section.

8.3.2 Low Complexity LS Estimate

In this section, we will present a least square (LS) solution for the channel tracking problem in (8.17). To simplify the mathematical representations, we define $\mathbf{h}_r$, $\mathbf{h}_i$, $\hat{\mathbf{h}}_r$, $\hat{\mathbf{h}}_i$, β_r, β_i,

$\hat{\beta}_r$ and $\hat{\beta}_i$ as follows

$$\begin{aligned}
\mathbf{h}_r &= \Re\{\mathbf{h}_d^{(n+1)}\},\ \mathbf{h}_i = \Im\{\mathbf{h}_d^{(n+1)}\},\\
\hat{\mathbf{h}}_r &= \Re\{\hat{\mathbf{h}}_d^{(n+1)}\},\ \hat{\mathbf{h}}_i = \Im\{\hat{\mathbf{h}}_d^{(n+1)}\},\\
\beta_r &= \Re\{\beta^{(n+1)}\},\ \beta_i = \Im\{\beta^{(n+1)}\},\\
\hat{\beta}_r &= \Re\{\hat{\beta}^{(n+1)}\},\ \hat{\beta}_i = \Im\{\hat{\beta}^{(n+1)}\}.
\end{aligned} \tag{8.18}$$

Let $\boldsymbol{\theta} = [\alpha^{(n+1)}, \beta_r, \beta_i]^T$, and we have the MLE of $\boldsymbol{\theta}$ as

$$\begin{aligned}
\hat{\boldsymbol{\theta}}_{ml} &= \arg\min_{\boldsymbol{\theta}} \|\hat{\mathbf{h}}_r - \mathbf{h}_r\|^2 + \|\hat{\mathbf{h}}_i - \mathbf{h}_i\|^2\\
&= \arg\min_{\boldsymbol{\theta}} \|\hat{\mathbf{h}}_s - \mathbf{h}_s\|^2,
\end{aligned} \tag{8.19}$$

where $\hat{\mathbf{h}}_s$ and $\mathbf{h}_s$ are defined as

$$\hat{\mathbf{h}}_s = [\hat{\mathbf{h}}_r^T, \hat{\mathbf{h}}_i^T]^T,\ \mathbf{h}_s = [\mathbf{h}_r^T, \mathbf{h}_i^T]^T. \tag{8.20}$$

Note that (8.19) is equivalent to (8.17).

Generally, (8.19) can be solved by the Newton's method. Assume that we have obtained the estimate of $\boldsymbol{\theta}$ in the j-th iteration as $\hat{\boldsymbol{\theta}}^{(j)}$, and the $(j+1)$-th iteration can be performed as

$$\hat{\boldsymbol{\theta}}^{(j+1)} = \left(\mathbf{S}^H\mathbf{S}\right)^{-1}\mathbf{S}^H\left(\hat{\mathbf{h}}_s - \mathbf{s}(\hat{\boldsymbol{\theta}}^{(j)})\right) + \hat{\boldsymbol{\theta}}^{(j)}, \tag{8.21}$$

where $\mathbf{s}(\boldsymbol{\theta}) = [\mathbf{s}_r^T, \mathbf{s}_i^T]^T$ is given as

$$\begin{aligned}
\mathbf{s}_r(\boldsymbol{\theta})[v] &= \beta_r \operatorname{sinc}\left(v_0^{(n)} + v - \alpha^{(n+1)}\right),\\
\mathbf{s}_i(\boldsymbol{\theta})[v] &= \beta_i \operatorname{sinc}\left(v_0^{(n)} + v - \alpha^{(n+1)}\right),
\end{aligned} \tag{8.22}$$

and $\mathbf{S} \in \mathbb{R}^{2V\times 3}$ is the Jacobi matrix at $\boldsymbol{\theta} = \hat{\boldsymbol{\theta}}^{(j)}$:

$$\mathbf{S} = \left[\frac{\partial \mathbf{h}_r^T}{\partial \boldsymbol{\theta}}, \frac{\partial \mathbf{h}_i^T}{\partial \boldsymbol{\theta}}\right]^T\Bigg|_{\boldsymbol{\theta}=\hat{\boldsymbol{\theta}}^{(j)}}. \tag{8.23}$$

For this iterative algorithm, the initial estimate should be carefully chosen to guarantee fast convergence. As we have mentioned, the channel does not vary much between two adjacent time slots, i.e., $\alpha^{(n)} \approx \alpha^{(n+1)}$ and $\beta^{(n)} \approx \beta^{(n+1)}$. As a result, we can use the estimated channel parameters of the n-th time slot as the initial estimate of the channel parameters at the $(n+1)$-th block, i.e., $\hat{\boldsymbol{\theta}}^{(0)} = [\hat{\alpha}^{(n)}, \Re\{\hat{\beta}^{(n)}\}, \Im\{\hat{\beta}^{(n)}\}]$.

After several iterations, the result should converge to the solution of (8.17). Let the final estimate of $\boldsymbol{\theta}$ be $\hat{\boldsymbol{\theta}} = [\hat{\alpha}^{(n+1)}, \hat{\beta}_r, \hat{\beta}_i]$, and we have the MLE of $\beta^{(n+1)}$ as $\hat{\beta}^{(n+1)} = \hat{\beta}_r + i\hat{\beta}_i$. Based on $\hat{\alpha}^{(n+1)}$ and $\hat{\beta}^{(n+1)}$, the complete channel vector can then be reconstructed as

$$\hat{\mathbf{h}}^{(n+1)}[m] = \hat{\beta}^{(n+1)} \mathrm{sinc}\left(m - \hat{\alpha}^{(n+1)}\right). \tag{8.24}$$

With the updated channel estimate, we should re-select antennas with the strongest channel gains, and construct the truncated channel estimate, which is given as

$$\hat{\mathbf{h}}_t^{(n+1)} = \hat{\mathbf{h}}^{(n+1)}\left[v_0^{(n+1)} : v_0^{(n+1)} + V - 1\right]. \tag{8.25}$$

The active antennas are indexed from $v_0^{(n+1)}$ to $v_0^{(n+1)} + V - 1$. When V is odd, we have

$$v_0^{(n+1)} = m_p^{(n+1)} - (V-1)/2, \tag{8.26}$$

where $m_p^{(n+1)}$ is given by

$$m_p^{(n+1)} = \arg\max_m \left|\hat{\mathbf{h}}^{(n+1)}[m]\right|. \tag{8.27}$$

When V is even, $v_0^{(n+1)}$ should be chosen as

$$v_0^{(n+1)} = \begin{cases} m_p^{(n+1)} - (V/2-1), & m_p^{(n+1)} \le \hat{\alpha}^{(n+1)} \\ m_p^{(n+1)} - V/2, & m_p^{(n+1)} > \hat{\alpha}^{(n+1)}. \end{cases} \tag{8.28}$$

The presented data-aided channel tracking algorithm is briefly summarized in Algorithm 3.

Algorithm 3 Data-aided channel tracking algorithm.

Require:

Truncated channel estimate at the n-th block, $\hat{\mathbf{h}}_t^{(n)}$;

Received signal at the $(n+1)$-th block, $\mathbf{Y}_{ul}^{(n+1)}$;

Ensure:

Truncated channel estimate at the $(n+1)$-th block

1: Data detection of the $(n+1)$-th block through (8.26);

2: Data-aided channel tracking through (8.13), $\hat{\mathbf{h}}_d^{(n+1)}$;

3: The estimate of $\alpha^{(n+1)}$ and $\beta^{(n+1)}$ through the Newton iteration algorithm in (8.21);

4: Construct $\hat{\mathbf{h}}^{(n+1)}$ through (8.24);

5: Find $v_0^{(n+1)}$ through (8.26) and (8.28), and update $\hat{\mathbf{h}}_t^{(n+1)}$ through (8.25);

6: **return** $\hat{\mathbf{h}}_t^{(n+1)}$;

8.3.3 Multi-User Scenario

In previous discussions, we presented the data-aided channel tracking scheme in the single user case. In this section, we will talk about how to apply it to multi-user scenario. Without loss of generality, we assume the BS serves two users with six RF chains simultaneously. The first step is initial channel estimation. Each user is assigned a pilot sequence and two pilot sequences are orthogonal. The initial channel estimate can be obtained through the method in [150]. Then, if these two users are well separated, i.e., the main lobes of their signals do not overlap in space, three RF chains will be used to serve each user. After initial channel estimation, the BS will keep the communications with user one with the first three RF chains, and follow the TDD communication protocol in Figure 8.2. The

second user will be served by the other RF chains. Theoretically, joint precoding and decoding should be conducted at the BS to eliminate the interference between two users. However, when they are well separated, the inter-user interference is very weak and can be ignored. As a result, data-aided channel tracking will be conducted at the BS for both users independently. That is to say, data detection and channel tracking for user one will be conducted only based on signals received from the first three RF chains. When users cannot be separated in space, they will be assigned with different time-frequency resources, and they can then work with their RF chains independently. In later simulations, results are presented for scenarios where users are well separated.

8.4 Performance Analysis

8.4.1 The Data-Aided Channel Tracking Error

As we have mentioned, the channel tracking result in (8.13) is subject to noise and data detection error. To be specific, the data-aided channel estimate of the $(n+1)$-th block is given by

$$\begin{aligned}\hat{\mathbf{h}}_d^{(n+1)} =& \mathbf{Y}_{ul}^{(n+1)} \left(\hat{\mathbf{x}}^{(n+1)}\right)^* / \|\hat{\mathbf{x}}^{(n+1)}\|^2 \\ =& \left(\mathbf{h}_d^{(n+1)} \left(\mathbf{x}^{(n+1)}\right)^T + \mathbf{N}_{ul}^{(n+1)}\right) \frac{\left(\hat{\mathbf{x}}^{(n+1)}\right)^*}{\|\hat{\mathbf{x}}^{(n+1)}\|^2}.\end{aligned} \tag{8.29}$$

In (8.29), $\hat{\mathbf{x}}^{(n+1)}$ is the detected data of the $(n+1)$-th block, and the error pattern is $\mathbf{e}^{(n+1)} = \hat{\mathbf{x}}^{(n+1)} - \mathbf{x}^{(n+1)}$. Thanks to the powerful forward error correction coding, we can safely assume that $\|\mathbf{e}^{(n+1)}\| \ll \|\mathbf{x}^{(n+1)}\|$. Therefore, we can take the first-order Taylor expansion, and (8.29) can be approximated by

$$\hat{\mathbf{h}}_d^{(n+1)} \approx \mathbf{h}_d^{(n+1)} + \mathbf{h}_d^{(n+1)} \frac{\mathbf{e}^H \mathbf{x}^{(n+1)}}{\|\mathbf{x}^{(n+1)}\|^2} + \mathbf{n}_{ul}^{(n+1)}, \tag{8.30}$$

where $\mathbf{n}_{ul}^{(n+1)} = \mathbf{N}_{ul}^{(n+1)} \left(\hat{\mathbf{x}}^{(n+1)}\right)^* \|\hat{\mathbf{x}}^{(n+1)}\|^2$. In (8.30), the estimation error originates from both data detection error and noise. However, we will see that noise dominates in estimation error.

For the v-th element in $\hat{\mathbf{h}}_d^{(n+1)}$, we have

$$\hat{\mathbf{h}}_d^{(n+1)}[v] \approx \mathbf{h}_d^{(n+1)}[v] + \mathbf{h}_d^{(n+1)}[v] \frac{\mathbf{e}^H \mathbf{x}^{(n+1)}}{\|\mathbf{x}^{(n+1)}\|^2} + n_v, \tag{8.31}$$

where $n_v = \mathbf{n}_{ul}^{(n+1)}[v]$. On the right hand side of (8.31), the first part is the desired information, while the second and third parts are channel estimation error caused by date detection error and noise, respectively. We can compute and compare their strength.

To start with, we can prove that when N is very large, the limit of $\|\mathbf{e}^H \mathbf{x}^{(n+1)}\|^2 / \|\mathbf{x}^{(n+1)}\|^4$ is given as p_e^2, i.e.,

$$\lim_{N\to\infty} \frac{\|\mathbf{e}^H \mathbf{x}^{(n+1)}\|^2}{\|\mathbf{x}^{(n+1)}\|^4} = p_e^2. \tag{8.32}$$

As a result, the strength of estimation error caused by symbol detection error is

$$\sigma_e^2 \sim |\mathbf{h}_d^{(n+1)}[v]|^2 p_e^2. \tag{8.33}$$

On the other hand, the strength of noise-incurred channel estimation error is

$$\begin{aligned} \sigma_n^2 =& E\left\{ \frac{\|\mathbf{N}_{ul}^{(n+1)}[v,:](\hat{\mathbf{x}}^{(n+1)})^*\|^2}{\|\hat{\mathbf{x}}^{(n+1)}\|^4} \right\} \\ =& E\left\{ \frac{\|\hat{\mathbf{x}}^{(n+1)}\|^2 \sigma^2}{\|\hat{\mathbf{x}}^{(n+1)}\|^4} \right\} = E\left\{ \frac{\sigma^2}{\|\hat{\mathbf{x}}^{(n+1)}\|^2} \right\}. \end{aligned} \tag{8.34}$$

We can prove that the asymptotic limit of $1/\|\hat{\mathbf{x}}^{(n+1)}\|^2$ is $1/N$. To be specific, we have

$$E\left\{ \frac{1}{\|\hat{\mathbf{x}}^{(n+1)}\|^2} \right\} = \frac{1}{N} + \mathcal{O}\{1/N^2\}. \tag{8.35}$$

As a result, the asymptotic limit of σ_n^2 is

$$\sigma_n^2 \sim \sigma^2/N, \tag{8.36}$$

noticing that σ^2 is the strength of uplink noise. The ratio of σ_n^2 to σ_e^2 is

$$\frac{\sigma_n^2}{\sigma_e^2} \approx \frac{1}{Np_e^2 SNR_v}, \tag{8.37}$$

where $SNR_v = |\mathbf{h}_d^{(n+1)}[v]|^2/\sigma^2$ is the uplink SNR on the v-th active antenna at the $(n+1)$-th data block. To guarantee system performance, we generally have SNR_v around several dB, N varies from one hundred to one thousand, while p_e is less than 10^{-3}. As we can see, for reasonable SNR and p_e ranges, we have $\sigma_n^2 \gg \sigma_e^2$, which means that noise dominates in data-aided channel tracking error. Therefore, (8.30) can be approximated by

$$\hat{\mathbf{h}}_d^{(n+1)} \approx \mathbf{h}_d^{(n+1)} + \mathbf{n}_{ul}^{(n+1)}, \tag{8.38}$$

and the covariance matrix of $\mathbf{n}_{ul}^{(n+1)}$ is $\sigma_n^2 \mathbf{I}_V$. Note that we have $\sigma_d^2 \approx \sigma_n^2$ from (8.14) and (8.38).

8.4.2 Error Analysis of the Transition Process

In the *transition* process, due to the tracking error in $\hat{\mathbf{h}}_d^{(n+1)}$, $\hat{\alpha}^{(n+1)}$ and $\hat{\beta}^{(n+1)}$ will also have errors, which further propagate to $\hat{\mathbf{h}}_t^{(n+1)}$. In this section, we will analyze the error propagation in this process.

Considering the scenarios in which the LoS path predominates, $\mathbf{h}_d^{(n+1)}$ is approximately a function of $\boldsymbol{\theta}$. The noise in (8.38) will cause estimation error in $\boldsymbol{\theta}$, and this noise is generally much weaker than $\mathbf{h}_d^{(n+1)}$ when N is very large. Stack the real and imaginary

parts of $\mathbf{n}_{ul}^{(n+1)}$ as

$$\mathbf{n}_s = \left[\Re\{\mathbf{n}_{ul}^{(n+1)}\}^T, \Im\{\mathbf{n}_{ul}^{(n+1)}\}^T\right]^T, \tag{8.39}$$

and we can then employ the first order Taylor expansion to approximately describe the relation of estimation error and observation noise as

$$\mathbf{n}_s \approx \hat{\mathbf{h}}_s - \mathbf{h}_s \approx \mathbf{H}\mathbf{e}_{\boldsymbol{\theta}}, \tag{8.40}$$

where $\mathbf{e}_{\boldsymbol{\theta}}$ is the estimation error of $\boldsymbol{\theta}$, and $\mathbf{H}$ is the Jacobian matrix given by

$$\mathbf{H} = \left[\frac{\partial \mathbf{h}_r^T}{\partial \boldsymbol{\theta}}, \frac{\partial \mathbf{h}_i^T}{\partial \boldsymbol{\theta}}\right]^T. \tag{8.41}$$

Equivalently, we have

$$\mathbf{e}_{\boldsymbol{\theta}} \approx \left(\mathbf{H}^T\mathbf{H}\right)^{-1}\mathbf{H}^T\mathbf{n}_s, \tag{8.42}$$

and the covariance matrix of $\mathbf{e}_{\boldsymbol{\theta}}$ will be

$$\mathbf{R}_{\boldsymbol{\theta}} \approx \frac{\sigma_n^2}{2}\left(\mathbf{H}^T\mathbf{H}\right)^{-1}. \tag{8.43}$$

As we can see, the estimation error of $\boldsymbol{\theta}$ is also inversely proportional to N and is very small. Therefore, when we use $\hat{\alpha}^{(n+1)}$ and $\hat{\beta}^{(n+1)}$ for channel update, the induced error can be closely approximated by the first order Taylor expansion as

$$\mathbf{e}_{\mathbf{h}_t} \approx \left[\frac{\partial \Re\{\mathbf{h}_t^{(n+1)}\}}{\partial \boldsymbol{\theta}} + i\frac{\partial \Im\{\mathbf{h}_t^{(n+1)}\}}{\partial \boldsymbol{\theta}}\right]\mathbf{e}_{\boldsymbol{\theta}}, \tag{8.44}$$

where $\mathbf{e}_{\mathbf{h}_t}$ is the estimation error in $\hat{\mathbf{h}}_t^{(n+1)}$. The MSE of the truncated channel update will be

$$\|\mathbf{e}_{\mathbf{h}_t}\|^2 \approx \mathrm{tr}\left\{\frac{\partial \Re\{\mathbf{h}_t^{(n+1)}\}^T}{\partial \boldsymbol{\theta}}\mathbf{R}_{\boldsymbol{\theta}}^{-1}\frac{\partial \Re\{\mathbf{h}_t^{(n+1)}\}}{\partial \boldsymbol{\theta}}\right\} + \mathrm{tr}\left\{\frac{\partial \Im\{\mathbf{h}_t^{(n+1)}\}^T}{\partial \boldsymbol{\theta}}\mathbf{R}_{\boldsymbol{\theta}}^{-1}\frac{\partial \Im\{\mathbf{h}_t^{(n+1)}\}}{\partial \boldsymbol{\theta}}\right\}. \tag{8.45}$$

Normalize it by the channel strength, and we have the NMSE of truncated channel update as

$$\|\mathbf{e}_{\mathbf{h}_t}\|^2/\|\mathbf{h}_t^{(n+1)}\|^2 \approx \|\mathbf{e}_{\mathbf{h}_t}\|^2/|\beta^{(n+1)}|^2. \tag{8.46}$$

It should be noticed that the NMSE of truncated channel estimation is inversely proportional to the sequence length, which means we can improve channel tracking accuracy by using longer data sequences.

8.4.3 CRLB of Channel Estimation Error

In this section, we will discuss the CRLB of the estimation error in the *transition* prcess. To be specific, from the PDF of $\hat{\mathbf{h}}_d^{(n+1)}$, we can derive the Fisher information matrix to quantify the amount of information that can be extracted. To simplify the notations, we ignore the block index for now. To be specific, we use α, β, $\hat{\mathbf{h}}_d$, $\mathbf{h}_d$, $\mathbf{h}_t$ and v_0 to represent $\alpha^{(n+1)}$, $\beta^{(n+1)}$, $\hat{\mathbf{h}}_d^{(n+1)}$, $\mathbf{h}_d^{(n+1)}$, $\mathbf{h}_t^{(n+1)}$ and $v_0^{(n)}$, respectively.

The probability density function of $\hat{\mathbf{h}}_d$ is

$$f(\hat{\mathbf{h}}_d|\alpha,\beta) = \frac{1}{(\pi\sigma_d^2)^V}\exp\left\{-\frac{1}{\sigma_d^2}\left(\|\hat{\mathbf{h}}_d - \mathbf{h}_d\|^2\right)\right\}, \tag{8.47}$$

while the likelihood function is

$$l(\hat{\mathbf{h}}_d|\alpha,\beta) = \ln(f) = -V\ln(\pi\sigma_d^2) - \|\hat{\mathbf{h}}_d - \mathbf{h}_d\|^2/\sigma_d^2. \tag{8.48}$$

The partial derives of l with respect to α, β_r and β_i are given as

$$\begin{aligned}
\frac{\partial l}{\partial \alpha} &= \frac{2}{\sigma_d^2}\left[(\hat{\mathbf{h}}_r - \mathbf{h}_r)^T\frac{\partial \mathbf{h}_r}{\partial \alpha} + (\hat{\mathbf{h}}_i - \mathbf{h}_i)^T\frac{\partial \mathbf{h}_i}{\partial \alpha}\right],\\
\frac{\partial l}{\partial \beta_r} &= \frac{2}{\sigma_d^2}(\hat{\mathbf{h}}_r - \mathbf{h}_r)^T\frac{\partial \mathbf{h}_r}{\partial \beta_r},\\
\frac{\partial l}{\partial \beta_i} &= \frac{2}{\sigma_d^2}(\hat{\mathbf{h}}_i - \mathbf{h}_i)^T\frac{\partial \mathbf{h}_i}{\partial \beta_i},
\end{aligned} \tag{8.49}$$

where we implicitly use the fact that $\|\hat{\mathbf{h}}_d - \mathbf{h}_d\|^2 = \|\hat{\mathbf{h}}_r - \mathbf{h}_r\|^2 + \|\hat{\mathbf{h}}_i - \mathbf{h}_i\|^2$. The Fisher information matrix is given as

$$\mathbf{F} = E\left\{\begin{bmatrix} \left(\frac{\partial l}{\partial \alpha}\right)^2 & \frac{\partial l}{\partial \alpha}\frac{\partial l}{\partial \beta_r} & \frac{\partial l}{\partial \alpha}\frac{\partial l}{\partial \beta_i} \\ \frac{\partial l}{\partial \beta_r}\frac{\partial l}{\partial \alpha} & \left(\frac{\partial l}{\partial \beta_r}\right)^2 & \frac{\partial l}{\partial \beta_r}\frac{\partial l}{\partial \beta_i} \\ \frac{\partial l}{\partial \beta_i}\frac{\partial l}{\partial \alpha} & \frac{\partial l}{\partial \beta_i}\frac{\partial l}{\partial \beta_r} & \left(\frac{\partial l}{\partial \beta_i}\right)^2 \end{bmatrix}\right\}, \tag{8.50}$$

and the expectations of the quadratic terms are given by

$$\begin{aligned} E\left\{\left(\frac{\partial l}{\partial \alpha}\right)^2\right\} &= \frac{2}{\sigma_d^2}\left(\left|\frac{\partial \mathbf{h}_r}{\partial \alpha}\right|^2 + \left|\frac{\partial \mathbf{h}_i}{\partial \alpha}\right|^2\right), \\ E\left\{\left(\frac{\partial l}{\partial \beta_r}\right)^2\right\} &= \frac{2}{\sigma_d^2}\left(\left|\frac{\partial \mathbf{h}_r}{\partial \beta_r}\right|^2\right), \\ E\left\{\left(\frac{\partial l}{\partial \beta_i}\right)^2\right\} &= \frac{2}{\sigma_d^2}\left(\left|\frac{\partial \mathbf{h}_i}{\partial \beta_i}\right|^2\right), \\ E\left\{\frac{\partial l}{\partial \alpha}\frac{\partial l}{\partial \beta_r}\right\} &= \frac{2}{\sigma_d^2}\left(\frac{\partial \mathbf{h}_r^T}{\partial \alpha}\frac{\partial \mathbf{h}_r}{\partial \beta_r}\right), \\ E\left\{\frac{\partial l}{\partial \alpha}\frac{\partial l}{\partial \beta_i}\right\} &= \frac{2}{\sigma_d^2}\left(\frac{\partial \mathbf{h}_i^T}{\partial \alpha}\frac{\partial \mathbf{h}_i}{\partial \beta_i}\right), \\ E\left\{\frac{\partial l}{\partial \beta_r}\frac{\partial l}{\partial \beta_i}\right\} &= \frac{2}{\sigma_d^2}\left(\frac{\partial \mathbf{h}_r^T}{\partial \beta_r}\frac{\partial \mathbf{h}_r}{\partial \beta_i}\right). \end{aligned} \tag{8.51}$$

Through tedious but straight forward derivations, the Fisher information matrix can be rewritten as

$$\mathbf{F} = \frac{2}{\sigma_d^2}\left(\frac{\partial \mathbf{h}_r^T}{\partial \boldsymbol{\theta}}\frac{\partial \mathbf{h}_r}{\partial \boldsymbol{\theta}} + \frac{\partial \mathbf{h}_i^T}{\partial \boldsymbol{\theta}}\frac{\partial \mathbf{h}_i}{\partial \boldsymbol{\theta}}\right) = \frac{2}{\sigma_d^2}\mathbf{H}^T\mathbf{H}. \tag{8.52}$$

The Jacobian Matrixes are

$$\begin{aligned} \frac{\partial \mathbf{h}_r}{\partial \boldsymbol{\theta}} &= \left[\frac{\partial \mathbf{h}_r}{\partial \alpha}, \frac{\partial \mathbf{h}_r}{\partial \beta_r}, \frac{\partial \mathbf{h}_r}{\beta_i}\right], \\ \frac{\partial \mathbf{h}_i}{\partial \boldsymbol{\theta}} &= \left[\frac{\partial \mathbf{h}_i}{\partial \alpha}, \frac{\partial \mathbf{h}_i}{\partial \beta_i}, \frac{\partial \mathbf{h}_i}{\beta_i}\right], \end{aligned} \tag{8.53}$$

and the partial derives are given by

$$\begin{aligned}
\frac{\partial \mathbf{h}_r[v]}{\partial \alpha} &= \frac{\beta_r \left(\mathrm{sinc}(v + v_0^{(n)} - \alpha) - \cos(v + v_0^{(n)} - \alpha)\pi\right)}{v + v_0^{(n)} - \alpha}, \\
\frac{\partial \mathbf{h}_i[v]}{\partial \alpha} &= \frac{\beta_i \left(\mathrm{sinc}(v + v_0^{(n)} - \alpha) - \cos(v + v_0^{(n)} - \alpha)\pi\right)}{v + v_0^{(n)} - \alpha}, \\
\frac{\partial \mathbf{h}_r[v]}{\partial \beta_r} &= \frac{\partial \mathbf{h}_i[v]}{\partial \beta_i} = \mathrm{sinc}(v + v_0^{(n)} - \alpha), \\
\frac{\partial \mathbf{h}_r[v]}{\partial \beta_i} &= \frac{\partial \mathbf{h}_i[v]}{\partial \beta_r} = 0.
\end{aligned} \tag{8.54}$$

Considering that $\sigma_d^2 \approx \sigma_n^2$, the Fisher information matrix should be very close to the inversion of $\mathbf{R}_{\boldsymbol{\theta}}$ in (8.43). That is to say, the estimation errors of α and β are very close to the CRLBs. Specifically, the CRLBs of estimation errors of α and β are given as

$$\begin{aligned}
|\Delta\alpha|^2 &\geq \mathbf{F}^{-1}[1,1] \propto \sigma_d^2, \\
|\Delta\beta|^2 &\geq \mathbf{F}^{-1}[2,2] + \mathbf{F}^{-1}[3,3] \propto \sigma_d^2.
\end{aligned} \tag{8.55}$$

As we can see, the lower bounds of estimation errors of α and β are both proportional to σ_d^2. As a result, they are inversely proportional to N, which means longer data sequence helps to reduce channel tracking error.

Due to the dominance of the LoS path, the truncated channel vector is approximately related to α and β as

$$\mathbf{h}_t[v] \approx \beta\,\mathrm{sinc}(v + v_0 - \alpha) \tag{8.56}$$

and estimation errors in $\hat{\beta}$ and $\hat{\alpha}$ lead to estimation error of $\hat{\mathbf{h}}_t$. The first order estimation error can be approximated by

$$\Delta\mathbf{h}_t \approx \left[\frac{\partial \Re\{\mathbf{h}_t\}}{\partial \boldsymbol{\theta}} + i\frac{\partial \Im\{\mathbf{h}_t\}}{\partial \boldsymbol{\theta}}\right]\Delta\boldsymbol{\theta}. \tag{8.57}$$

The lower bound of the estimation error of $\hat{\mathbf{h}}_t$ can be approximated by

$$|\Delta \mathbf{h}_t|^2 \geq \mathrm{tr}\left\{ \frac{\partial \Re\{\mathbf{h}_t\}}{\boldsymbol{\theta}}^T \mathbf{F}^{-1} \frac{\partial \Re\{\mathbf{h}_t\}}{\boldsymbol{\theta}} \right\} + \mathrm{tr}\left\{ \frac{\partial \Im\{\mathbf{h}_t\}}{\boldsymbol{\theta}}^T \mathbf{F}^{-1} \frac{\partial \Im\{\mathbf{h}_t\}}{\boldsymbol{\theta}} \right\}. \tag{8.58}$$

Similar to (8.55), we can see that estimation error of $\mathbf{h}_t$ is inversely proportional to N, and longer sequences help to reduce estimation error.

8.4.4 Computational Complexity

The channel tracking scheme presented in this paper involves two steps. The first one is to use the currently detected data for channel estimation given by (8.13), whose complexity is at the order of $\mathcal{O}(NV)$. The second step is the transition process and the complexity is at the order of $\mathcal{O}(V)$, which is negligible. As a result, we can see the overall complexity mainly comes from the data-aided channel estimation, and it grows linearly with the data block length and the number of RF chains per user.

At first sight, the iteration process may introduce huge delay. However, we believe this is not a huge problem for the following reasons. First, the algorithm will converge very fast because of the accurate initial estimate. Generally, two or three iterations are more than enough for reasonable SNR range. Secondly, when the channel is not varying fast, we do not need to conduct channel tracking for every block. Thirdly, we can further reduce the delay by using part of the uplink data for channel tracking, instead of the whole sequence. There is a trade-off between complexity and channel tracking accuracy. Last but not the least, the channel tracking process can be conducted simultaneously with downlink data transmission. Based on these discussions, we can cut off the delay by reducing channel tracking frequency, reducing data sequence length used for channel tracking, and employing

a pipeline architecture.

8.5 Numerical Evaluations

For the presented system, there are several parameters of great importance, including the data block length, number of RF chains per user, SNR, antenna number at the BS, etc. In this section, we will conduct simulations to evaluate the impacts of these parameters on system performance. The vehicle is moving at 360 km per hour, which is the typical speed for the Chinese high-speed railway system. We assume that block length is one thousand symbols and the rate is 10^6 symbols per second. That is to say, every data block has a duration of 1 ms. The default modulation scheme is QPSK, if not specified. The length of pilots is 10 symbols for initial channel estimation. Due to the existence of the LoS path, the path loss exponent is chosen as 2. Also, we conduct simulations for the multi-user scenario, and compare the presented method with that of [151] in terms of normalized channel estimation error.

8.5.1 Channel Tracking of High-Mobility Vehicle

In this first part, we will apply the presented method to the high-speed railway systems and conduct simulations. The number of antennas at the BS is 128, and $V = 3$. The train moves at 360 km per hour for 200 data blocks. The results are show in Figure 8.5 for SNR $= 5$ dB. In Figure 8.5, we have the NMSE of truncated channel estimate, MSE of the estimates of α and β. As we can see, for the simulated 200 blocks, the NMSE of the presented algorithm is very close to the CRLB. As we have mentioned, both data-detection error

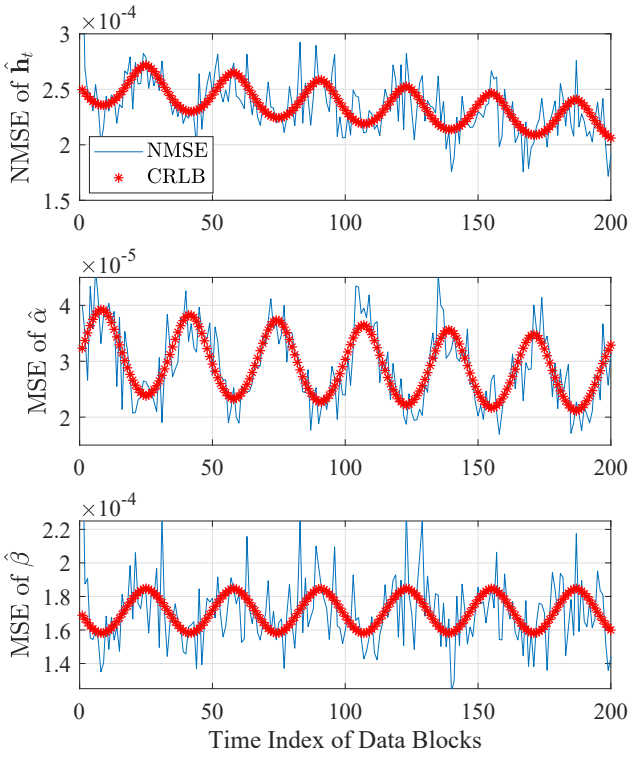

Figure 8.5: Channel tracking error.

and noise contribute to channel estimation error, while the CRLB is derived by ignoring the data-detection error. That is to see, the impact of data detection error is negligible on channel estimation accuracy, as we have proven.

In Figure 8.5, we have two important observations: first, the channel tracking error oscillates; second, the overall channel tracking error decreases from a long-term perspective. As we have mentioned previously, by using limited RF chains and truncated channel vectors, there will be energy loss, and the energy loss ratio is related to the fractional part of α. In Figure 8.5, the user's movement leads to periodical variation of the fractional part of α, and thus causes periodically changing SNR. Then, the channel tracking accuracy will vary accordingly, and we can observe the fast fluctuation. The long-term decrease of estimation error can be explained by the fact that the user is moving towards the base station in our simulation setup, which leads to increased SNR. The long-term decrease of channel estimation error is subtle, because the total distance travelled by the vehicle is only 20 meters for 200 blocks, which does not cause significant change of signal strength.

8.5.2 How to Choose V

In the presented system, the number of active antennas should be carefully chosen. On one hand, V cannot be too large because the RF chains are expensive. On the other hand, V should at least be equal to three, so that the transition process can be completed. As has been proven in [156] and [157], more then 80% of the energy concentrates on two antennas in the main lobe of a sinc function. That is to say, three active antennas should be enough to achieve comparable performance with respect to that with M active antennas.

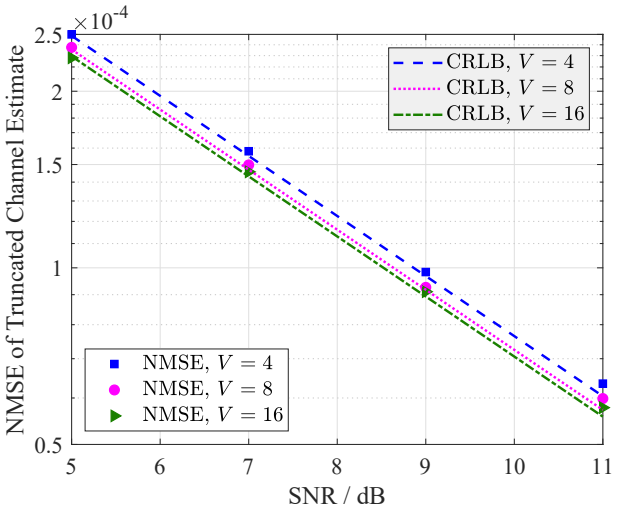

Figure 8.6: Impact of V on channel tracking error.

In Figure 8.6, we have the channel tracking results at the 20-th block, in terms of the normalized channel estimation error. V varies in $\{4, 8, 16\}$, and the performance improvement is negligible every time we double V. Also, it should be noted that the presented algorithm can closely approach the CRLB.

8.5.3 The Trade-off of the Block Length

There is a trade-off concerning the block length of the presented channel tracking scheme. On one hand, longer block means longer data sequence, which helps to improve channel tracking accuracy by suppressing noise. On the other hand, we are using the CSI of the previous block for the data detection of the current block, by assuming that the channel is almost constant for consecutive blocks. As a result, longer blocks may lead to channel variation and data detection errors, which will propagate and deteriorate system perfor-

mance. In Figure 8.7, we have the simulation results for $N \in \{200, 400, 800, 1600\}$. As we

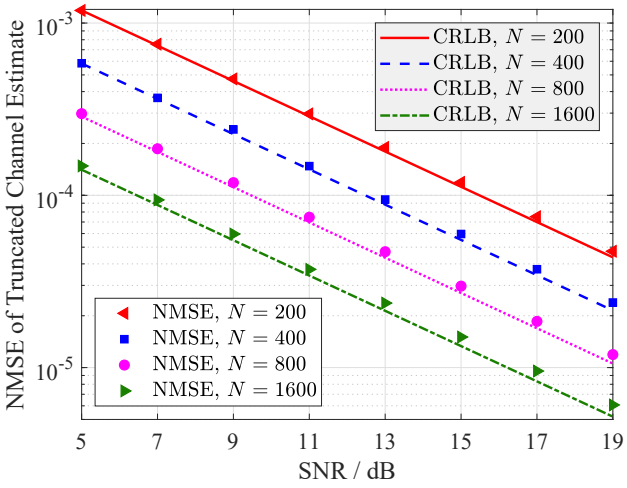

Figure 8.7: Impact of block length on channel tracking error.

can see, for the simulated values of N, every time we double the data sequence length, the NMSE of channel estimation will be reduced by a factor of two, which is consistent with the previous theoretical analysis.

8.5.4 Impact of Antenna Number

The number of antennas at the BS definitely has an important impact on the presented system, both positively and negatively. On one hand, more antennas help to concentrate energy better and thus improve energy efficiency. On the other hand, larger antenna arrays lead to narrower main lobes and faster channel variations. Intuitively, when the beam is narrower, channel tracking will be more challenging, because the user can easily move out of the beam and lose communication with the BS.

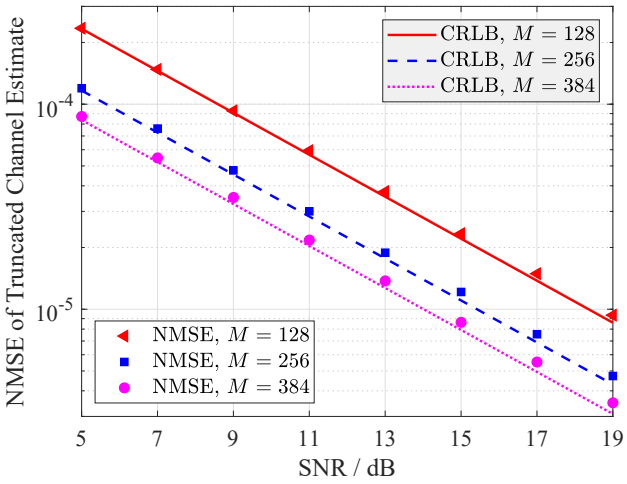

Figure 8.8: Impact of antenna number on truncated channel estimation error.

As we can see in Figure 8.8, as we double or triple the number of antennas at the BS, the NMSE of truncated channel estimate decreases proportionally, noticing that the number of RF chains is constant in this process.

8.5.5 Channel Tracking of Multiple Users

In this section, we consider multiple users served by the same BS. To be specific, the BS will serve four well separated users with the same time-frequency resource. The users are distributed in a line along a road, and the minimum distance between any two users is large enough to guarantee that they will be served by different active antennas. Users are assigned with orthogonal pilot sequences, and each pilot sequence has ten QPSK symbols. Based on pilots, initial channel estimation can be conducted for users. In the following communications, V RF chains will be used to serve one user, every user will experience interference from the others, and data-aided channel tracking will be conducted for all

users independently. That is to say, data detection and channel tracking for an arbitrary user will be conducted only based on signals received from the corresponding RF chains. The results are presented in Figure 8.9.

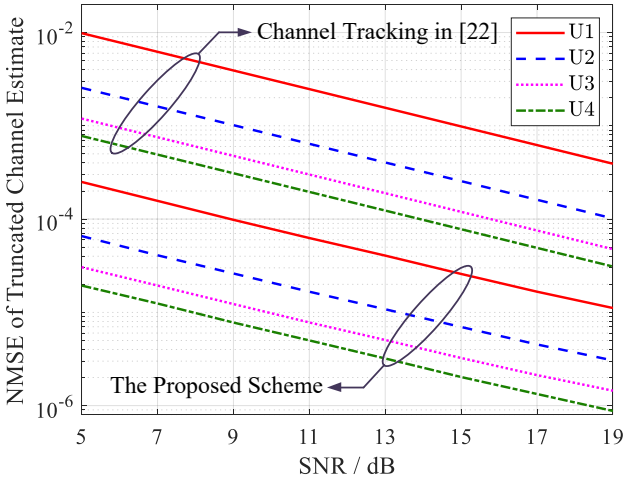

Figure 8.9: Truncated channel estimation for multiple users served by the same BS.

In Figure 8.9, we also have the results from [151], and the pilot length is 100 symbols. As we can see, the channel estimation errors of different users decrease monotonically with the increase of SNR. Different users have different channel tracking errors, because their distances to the BS are different, leading to different signal strength. Also, the presented scheme outperforms that from [151] by more than one order of magnitude in terms of channel estimation error. This can be explained by two reasons. First, the data sequence is ten times longer than the pilot sequence, which means the noise will be suppressed by ten times. Second, the correlations of different antenna gains in the truncated channel vector are considered in the presented method, while [151] does not. Basically, the

presented approach exploits the fact that the channel response can be approximated by a sinc function, and thus can further suppress noise. Moreover, it should be noted that the overhead of the presented scheme is almost zero, because no training sequence is required except for the initial channel estimation.

When it comes to achievable rate, it is true that smaller channel estimation error does not necessarily lead to larger achievable rate. However, our case is quite special. There are two parameters contributing to the achievable rate: the achieved SINR and the overhead. Assume the overall block length is N, out of which N_p is used for channel tracking. Therefore, the achievable rate is

$$AR = \frac{N - N_p}{N} \log_2(1 + SINR). \tag{8.59}$$

For the presented scheme, $N_p = 0$, which means no overhead. As to SINR, because the presented method shows smaller channel tracking error, it will have better SINR. As a result, the presented scheme will outperform that in [151] in terms of achievable rate.

8.6 Summary

In this chapter, a data-aided channel tracking scheme for TDD millimeter wave communications is presented. Due to the channel reciprocity, the uplink channel tracking results can be used for down-link beamforming. The fundamental idea is that millimeter wave channels are sparse, and the LoS component dominates, leading to high correlation between channels in adjacent time slots. From the angle domain perspective, the DoA of the desired signal does not vary much between two consecutive data blocks. As a result, we can employ the channel estimate from the previous time slot for the data detection of the current one.

Then, the detected data sequence can be used to update the channel estimate. Due to the iterative process, one might be concerned with the error propagation issue. However, we proved that for reasonable SNR range, the channel estimation error is dominated by noise, and the data detection error from the previous data block has a negligible impact on the channel estimation of the current block. As a result, the error propagation issue can be ignored. Through both theoretical analysis and numerical simulations, we show that channel tracking is possible without consuming any time-frequency resource in millimeter wave communications, as long as the LoS path dominates.

Chapter 9

Conclusions and Future Work

This dissertation has presented the modeling, algorithm design and performance analysis on mobile node-aided localization and communications in large-scale WSNs. Simulations and experiments are conducted to verify the theoretical results.

9.1 Summary of Contributions

The main contributions of this research are summarized as follows:

- **The Drone-Assisted Zero-Configuration Localization System**

  A new localization framework has been proposed to replace the conventional architecture based on fixed anchors. A drone serves as a mobile anchor for localization in large-scale WSNs. The channel parameters are viewed as extra unknowns, and the Newton's method is employed to jointly estimate the location of sensors and the channel parameters. Therefore, no off-line training is required. It has also been shown that the variance of positioning error will decreases linearly with the number of

measurements. Extensive analysis and numerical evaluations are conducted to show that the proposed system is not only more accurate, but also more stable.

- **ToA-based Joint Localization and Time Synchronization**

  A two-phase low complexity linear algorithm has been proposed for the joint localization and time synchronization for large scale underwater acoustic sensor networks. An AUV is employed as a mobile anchor to broadcast beacon signals, and all the sensors are silent. This system has been shown to provide better coverage and imposes very low communication burden for the network. The closed-form positioning and time synchronization errors are derived and prove to be almost identical to the CRLBs. The theoretical analysis is supported by the simulation results.

- **Doppler-based Underwater Localization**

  A Doppler-based underwater localization system has been proposed and comprehensively analyzed. Compared with ToA or TDoA based system, this new system does not demand communication capability from the target. The target only needs to transmit a sinusoidal wave at a constant frequency, and the AUV can localize the target in its communication range. A low-complexity Doppler estimation algorithm has been presented and the closed-form estimation error is given. Based on the Doppler estimates, the Newton's method is employed for localization. The variance of positioning error is inversely proportional to the cube of sampled sequence length, which means we can easily improve system performance by prolonging the sampling time.

- **Machine Learning-Assisted Target Detection**

A machine learning-assisted proactive target detection and tracking system based on underwater acoustic networks has been proposed. The active nodes periodically broadcast LFM signals, which will hit the target, get reflected and received by the other nodes. Based on the received signals, the FrFT can be used to get the 2D spectrum. The CNN is employed to automatically scan the spectrum and detect the existence of targets. If targets are detected, over-sampling will be conducted on the spectrum to get more accurate estimate of target's distance and radial velocity. Such an architecture has been shown to significantly reduce the computational complexity and achieve real-time scanning of the surveillance area.

- **Pilot Decontamination based on the Spatial Filter**

  A pilot decontamination method has been proposed for massive MIMO systems. The key idea is to identify the spatial signatures of the pilot contamination from adjacent cells and eliminate them by constructing a spatial filter. The stronger the pilot contamination is, the better chance we have to identify it. Such estimation method is especially helpful to cell-edge users, because their signals can be overwhelmed by pilot contamination from adjacent cells. Compared with the existing pilot decontamination methods, the proposed scheme has two major advantages: 1) no *a priori* statistical information is required; and 2) no need for the assumption that the desired signals are always stronger than the pilot contamination to perform effective estimation.

- **Data-Aided Channel Tracking**

  A data-aided channel tracking scheme for TDD mmWave communications has been presented. Due to the channel reciprocity, the up-link channel tracking results can

be used for down-link beamforming. The fundamental idea is that millimeter wave channels are sparse, and the LoS component dominates, leading to high correlation between channels in adjacent time slots. As a result, we can employ the channel estimate from the previous time slot for the data detection of the current slot. Then, the detected data sequence can be used to update the channel estimate. Due to the iterative process, one might be concerned with the error propagation issue. However, we proved that for reasonable SNR range, the channel estimation error is dominated by noise, and the data detection error from the previous data block has a negligible impact on the channel estimation of the current block. As a result, the error propagation issue can be ignored.

9.2 Further Work

In the thesis, various application scenarios are modeled and analyzed for mobile node assisted large-scale WSNs. As future work, the following problems should be investigated.

Firstly, the trajectory of mobile nodes should be carefully designed. As we have mentioned, the geometrical distribution of nodes in a network has significant impact on positioning accuracy. Therefore, if a random trajectory is chosen, some nodes may have very poor localization accuracy, while the others may experience small positioning error. Therefore, the trajectory should be designed to minimize the maximum GDOP in the network. Also, we also need to consider the limited battery life and the maximum acceleration of the mobile nodes during the design process.

Secondly, the data-association problem should be considered in Chapter 6. To be

specific, suppose two objects are located in the surveillance area. Every listening node will see two bright "X" patterns on their spectrum. At the server sides, after receiving the data from the listening nodes, the sever needs to figure out what pattern corresponds to which target. This is the data-association issue in space domain, and similar problem should be solved in the time domain. An effective solution will help to address the simultaneous localization of the multiple targets problems in the network.

Thirdly, the Doppler effect is assumed to be compensated on the RF chain in Chapter 8. However, this can be quite challenging, and demands complicated hardware design. A better solution is to eliminate the Doppler shift on the baseband signal. To achieve this goal, an accurate channel model is required for the RF band, but is still absent. Besides, the near-field effect should be considered for large antenna arrays, because the array dimension is no longer negligible.

Bibliography

[1] J. Zheng and Y. C. Wu. Joint time synchronization and localization of an unknown node in wireless sensor networks. *IEEE Transactions on Signal Processing*, 58(3):1309–1320, March 2010.

[2] M. Conti, J. Willemsen, and B. Crispo. Providing source location privacy in wireless sensor networks: A survey. *IEEE Communications Surveys Tutorials*, 15(3):1238–1280, Third Quarter 2013.

[3] O. Demigha, W. K. Hidouci, and T. Ahmed. On energy efficiency in collaborative target tracking in wireless sensor network: A review. *IEEE Communications Surveys Tutorials*, 15(3):1210–1222, Third Quarter 2013.

[4] M. T. Isik and O. B. Akan. A three dimensional localization algorithm for underwater acoustic sensor networks. *IEEE Transactions on Wireless Communications*, 8(9):4457–4463, Sept. 2009.

[5] Z. Gong, C. Li, F. Jiang, R. Su, R. Venkatesan, C. Meng, S. Han, Y. Zhang, S. Liu, and K. Hao. Design, analysis, and field testing of an innovative drone-assisted zero-configuration localization framework for wireless sensor networks. *IEEE Transactions on Vehicular Technology*, 66(11):10322–10335, Nov. 2017.

[6] C. J. Li and H. Ling. High-resolution, downward-looking radar imaging using a small consumer drone. In *Proceedings of the 2016 IEEE International Symposium on Antennas and Propagation (APSURSI)*, pages 2037–2038, Fajardo, Puerto Rico, June 2016.

[7] I. H. Bae. Avatar drone: drone as telepresence platform with 3D mobility. In *Proceedings of the IEEE 13th International Conference on Ubiquitous Robots and Ambient Intelligence (URAI)*, pages 452–453, Xi'an, Shaanxi, China, August 2016.

[8] J. O'Malley. Keeping drones at bay [drones control and automation]. *Engineering Technology*, 11(6):32–35, July 2016.

[9] Z. M. Fadlullah, D. Takaishi, H. Nishiyama, N. Kato, and R. Miura. A dynamic trajectory control algorithm for improving the communication throughput and delay in UAV-aided networks. *IEEE Network*, 30(1):100–105, January 2016.

[10] A. E. A. A. Abdulla, Z. M. Fadlullah, H. Nishiyama, N. Kato, F. Ono, and R. Miura. Toward fair maximization of energy efficiency in multiple UAS-aided networks: A game-theoretic methodology. *IEEE Transactions on Wireless Communications*, 14(1):305–316, January 2015.

[11] `https://store.dji.com/product/inspire-2?from=store_index_banner#/?_k=0sjuvb`.

[12] M. Erol, L. F. M. Vieira, and M. Gerla. AUV-aided localization for underwater sensor networks. In *International Conference on Wireless Algorithms, Systems and Applications (WASA 2007)*, pages 44–54, Chicago, Illinois, USA, Aug 2007.

[13] D. Mirza and C. Schurgers. Collaborative localization for fleets of underwater drifters. In *OCEANS 2007*, pages 1–6, Vancouver, BC, Canada, Sept. 2007.

[14] M. Waldmeyer, H. Tan, and W. K. G. Seah. Multi-stage AUV-aided localization for underwater wireless sensor networks. In *2011 IEEE Workshops of International Conference on Advanced Information Networking and Applications*, pages 908–913, March 2011.

[15] R. Zandi, M. Kamarei, and H. Amiri. Underwater acoustic sensor network localization using four directional beams. In *2013 21st Iranian Conference on Electrical Engineering (ICEE)*, pages 1–6, Mashhad, Iran, May 2013.

[16] H. Maqsood, N. Javaid, A. Yahya, B. Ali, Z. A. Khan, and U. Qasim. MobiL-AUV: AUV-aided localization scheme for underwater wireless sensor networks. In *2016 10th International Conference on Innovative Mobile and Internet Services in Ubiquitous Computing (IMIS)*, pages 170–175, July 2016.

[17] R. Diamant and L. Lampe. Underwater localization with time-synchronization and propagation speed uncertainties. *IEEE Transactions on Mobile Computing*, 12(7):1257–1269, July 2013.

[18] D. M. Crimmins, C. T. Patty, M. A. Beliard, J. Baker, J. C. Jalbert, R. J. Komerska, S. G. Chappell, and D. R. Blidberg. Long-endurance test results of the solar-powered AUV system. In *OCEANS 2006*, pages 1–5, Boston, MA, USA, Sept. 2006.

[19] B. Ferreira, M. Pinto, A. Matos, and N. Cruz. Modeling and motion analysis of the mares autonomous underwater vehicle. In *OCEANS 2009*, pages 1–10, Oct 2009.

[20] H. Chen, Q. Shi, R. Tan, H. V. Poor, and K. Sezaki. Mobile element assisted cooperative localization for wireless sensor networks with obstacles. *IEEE Transactions on Wireless Communications*, 9(3):956–963, March 2010.

[21] A. Conti, M. Guerra, D. Dardari, N. Decarli, and M. Z. Win. Network experimen-

tation for cooperative localization. *IEEE Journal on Selected Areas in Communications*, 30(2):467–475, February 2012.

[22] X. Wang, H. Zhou, S. Mao, S. Pandey, P. Agrawal, and D. M. Bevly. Mobility improves LMI-based cooperative indoor localization. In *Proceedings of the 2015 IEEE Wireless Communications and Networking Conference (WCNC)*, pages 2215–2220, New Orleans, LA, USA, March 2015.

[23] A. Coluccia and F. Ricciato. On ml estimation for automatic rss-based indoor localization. In *Wireless Pervasive Computing (ISWPC), 2010 5th IEEE International Symposium on*, pages 495–502, May 2010.

[24] A. Coluccia. Reduced-bias ML-based estimators with low complexity for self-calibrating rss ranging. *IEEE Transactions on Wireless Communications*, 12(3):1220–1230, March 2013.

[25] S. Han, Z. Gong, W. Meng, C. Li, D. Zhang, and W. Tang. Automatic precision control positioning for wireless sensor network. *IEEE Sensors Journal*, 16(7):2140–2150, April 2016.

[26] S. H. Fang, C. H. Wang, T. Y. Huang, C. H. Yang, and Y. S. Chen. An enhanced zigbee indoor positioning system with an ensemble approach. *IEEE Communications Letters*, 16(4):564–567, April 2012.

[27] H. Ren and M. Q. H. Meng. Power adaptive localization algorithm for wireless sensor networks using particle filter. *IEEE Transactions on Vehicular Technology*, 58(5):2498–2508, Jun 2009.

[28] K. W. Cheung, H. C. So, W. K. Ma, and Y. T. Chan. Least squares algorithms for time-of-arrival-based mobile location. *IEEE Transactions on Signal Processing*,

52(4):1121–1130, April 2004.

[29] W. Meng, D. Zhang, Y. Wang, and C. Li. An extended centroid localization algorithm based on error correction in wsn. In *2014 IEEE Global Communications Conference*, pages 442–447, Dec 2014.

[30] E. Kim and K. Kim. Distance estimation with weighted least squares for mobile beacon-based localization in wireless sensor networks. *IEEE Signal Processing Letters*, 17(6):559–562, June 2010.

[31] Y. Shen and M. Z. Win. Fundamental limits of wideband localization—part I: A general framework. *IEEE Transactions on Information Theory*, 56(10):4956–4980, Oct 2010.

[32] Y. Shen, H. Wymeersch, and M. Z. Win. Fundamental limits of wideband localization—part II: Cooperative networks. *IEEE Transactions on Information Theory*, 56(10):4981–5000, Oct 2010.

[33] Y. Shen and M. Z. Win. On the accuracy of localization systems using wideband antenna arrays. *IEEE Transactions on Communications*, 58(1):270–280, January 2010.

[34] D. Oh and J. H. Lee. Low-complexity range-azimuth fmcw radar sensor using joint angle and delay estimation without svd and evd. *IEEE Sensors Journal*, 15(9):4799–4811, Sept 2015.

[35] M. R. Ataei, T. Kunz, and A. H. Banihashemi. Localization and location verification in non-homogeneous one-dimensional wireless ad-hoc networks. *IEEE Journal on Selected Areas in Communications*, 33(7):1304–1316, July 2015.

[36] Slobodan N Simic and Shankar Sastry. Distributed localization in wireless ad hoc

networks. Technical report, Technical Report UCB/ERL, 2002.

[37] G. Giorgetti, S. K. S. Gupta, and G. Manes. Understanding the limits of rf-based collaborative localization. *IEEE/ACM Transactions on Networking*, 19(6):1638–1651, Dec 2011.

[38] X. Wang, L. Gao, and S. Mao. CSI phase fingerprinting for indoor localization with a deep learning approach. *IEEE Internet of Things Journal*, 3(6):1113–1123, December 2016.

[39] X. Wang, L. Gao, S. Mao, and S. Pandey. CSI-based fingerprinting for indoor localization: A deep learning approach. *IEEE Transactions on Vehicular Technology*, 66(1):763–776, January 2017.

[40] X. Wang, L. Gao, and S. Mao. BiLoc: Bi-Modal deep learning for indoor localization with commodity 5 GHz WiFi. *IEEE Access*, 5:4209–4220, March 2017.

[41] Shuai Han, Zijun Gong, Weixiao Meng, and Cheng Li. An indoor radio propagation model considering angles for wlan infrastructures. *Wireless Communications and Mobile Computing*, 15(16):2038–2048, 2015.

[42] S. Y. Seidel and T. S. Rappaport. 914 mhz path loss prediction models for indoor wireless communications in multifloored buildings. *IEEE Transactions on Antennas and Propagation*, 40(2):207–217, Feb 1992.

[43] Kexin Zhao, Junli Liang, Johan Karlsson, and Jian Li. Enhanced multistatic active sonar signal processing. *The Journal of the Acoustical Society of America*, 134(1):300–311, 2013.

[44] N. Patwari, A. O. Hero, M. Perkins, N. S. Correal, and R. J. O'Dea. Relative location estimation in wireless sensor networks. *IEEE Transactions on Signal Processing*,

51(8):2137–2148, Aug 2003.

[45] C. Li, R. Venkatesan, and T. Bian. A refined localization method for underwater tetherless sensor networks. In *2010 IEEE Wireless Communication and Networking Conference*, pages 1–6, April 2010.

[46] B. Zhou, Q. Chen, and P. Xiao. The error propagation analysis of the received signal strength-based simultaneous localization and tracking in wireless sensor networks. *IEEE Transactions on Information Theory*, 63(6):3983–4007, June 2017.

[47] G. Han, J. Jiang, L. Shu, Y. Xu, and F. Wang. Localization algorithms of underwater wireless sensor networks: a survey. *Sensors (Basel)*, 12(2):2026–2061, 2012.

[48] Q. Liang, B. Zhang, C. Zhao, and Y. Pi. TDoA for passive localization: Underwater versus terrestrial environment. *IEEE Transactions on Parallel and Distributed Systems*, 24(10):2100–2108, Oct. 2013.

[49] J. Liu, Z. Wang, J. H. Cui, S. Zhou, and B. Yang. A joint time synchronization and localization design for mobile underwater sensor networks. *IEEE Transactions on Mobile Computing*, 15(3):530–543, March 2016.

[50] D. Park, K. Kwak, W. K. Chung, and J. Kim. Development of underwater short-range sensor using electromagnetic wave attenuation. *IEEE Journal of Oceanic Engineering*, 41(2):318–325, April 2016.

[51] P. A. M. de Theije and J. . Sindt. Single-ping target speed and course estimation using a bistatic sonar. *IEEE Journal of Oceanic Engineering*, 31(1):236–243, Jan. 2006.

[52] R. Diamant, L. M. Wolff, and L. Lampe. Location tracking of ocean-current-related underwater drifting nodes using Doppler shift measurements. *IEEE Journal of*

Oceanic Engineering, 40(4):887–902, Oct. 2015.

[53] D. J. Peters. A Bayesian method for localization by multistatic active sonar. *IEEE Journal of Oceanic Engineering*, 42(1):135–142, January 2017.

[54] Patrick Carroll, Katherine Domrese, Hao Zhou, Shengli Zhou, and Peter Willett. Doppler-aided localization of mobile nodes in an underwater distributed antenna system. *Physical Communication*, 18:49–59, 2016.

[55] R. Spindel, R. Porter, W. Marquet, and J. Durham. A high-resolution pulse-doppler underwater acoustic navigation system. *IEEE Journal of Oceanic Engineering*, 1(1):6–13, Sept. 1976.

[56] C. R. Berger, S. Zhou, J. C. Preisig, and P. Willett. Sparse channel estimation for multicarrier underwater acoustic communication: From subspace methods to compressed sensing. In *OCEANS 2009-EUROPE*, pages 1–8, Bremen, Germany, May 2009.

[57] Y. Zhao, H. Yu, G. Wei, F. Ji, and F. Chen. Parameter estimation of wideband underwater acoustic multipath channels based on Fractional Fourier Transform. *IEEE Transactions on Signal Processing*, 64(20):5396–5408, Oct. 2016.

[58] B. Li, S. Zhou, M. Stojanovic, L. Freitag, and P. Willett. Multicarrier communication over underwater acoustic channels with nonuniform doppler shifts. *IEEE Journal of Oceanic Engineering*, 33(2):198–209, April 2008.

[59] T. Xu, Z. Tang, G. Leus, and U. Mitra. Multi-rate block transmission over wideband multi-scale multi-lag channels. *IEEE Transactions on Signal Processing*, 61(4):964–979, Feb. 2013.

[60] M. Stojanovic and J. Preisig. Underwater acoustic communication channels: Prop-

agation models and statistical characterization. *IEEE Communications Magazine*, 47(1):84–89, January 2009.

[61] Y. Zhang, Y. Huang, L. Wan, S. Zhou, X. Shen, and H. Wang. Adaptive OFDMA with partial CSI for downlink underwater acoustic communications. *Journal of Communications and Networks*, 18(3):387–396, June 2016.

[62] R. Diamant, H. Tan, and L. Lampe. LOS and NLOS classification for underwater acoustic localization. *IEEE Transactions on Mobile Computing*, 13(2):311–323, 2014.

[63] C. R. Berger, S. Zhou, P. Willett, and L. Liu. Stratification effect compensation for improved underwater acoustic ranging. *IEEE Transactions on Signal Processing*, 56(8):3779–3783, Aug. 2008.

[64] W.S. Burdic. *Underwater Acoustic System Analysis*. Peninsula Publ., 2002.

[65] Jun Zheng, Kenneth W.K. Lui, and H.C. So. Accurate three-step algorithm for joint source position and propagation speed estimation. *Signal Processing*, 87(12):3096–3100, 2007.

[66] Z. Gong, C. Li, and F. Jiang. AUV-aided joint localization and time synchronization for underwater acoustic sensor networks. *IEEE Signal Processing Letters*, 25(4):477–481, April 2018.

[67] J. Liang, L. Xu, J. Li, and P. Stoica. On designing the transmission and reception of multistatic continuous active sonar systems. *IEEE Transactions on Aerospace and Electronic Systems*, 50(1):285–299, Jan. 2014.

[68] Robbert van Vossen, S. Peter Beerens, and Ernest van der Spek. Anti-submarine warfare with continuously active sonar. *Sea Technology*, 52(11):33–35, 2011.

[69] Nicolas F. Josso, Cornel Ioana, Jérôme I. Mars, and Cédric Gervaise. Source motion detection, estimation, and compensation for underwater acoustics inversion by wideband ambiguity lag-doppler filtering. *The Journal of the Acoustical Society of America*, 128(6):3416–3425, 2010.

[70] L. B. Almeida. The fractional Fourier transform and time-frequency representations. *IEEE Transactions on Signal Processing*, 42(11):3084–3091, Nov. 1994.

[71] H. M. Ozaktas, O. Arikan, M. A. Kutay, and G. Bozdagt. Digital computation of the fractional Fourier transform. *IEEE Transactions on Signal Processing*, 44(9):2141–2150, Sep. 1996.

[72] T. Marzetta. Noncooperative cellular wireless with unlimited numbers of base station antennas. *IEEE Transactions on Wireless Communications*, 9(11):3590–3600, Nov. 2010.

[73] E. Larsson, O. Edfors, F. Tufvesson, and T. Marzetta. Massive MIMO for next generation wireless systems. *IEEE Communications Magazine*, 52(2):186–195, Feb. 2014.

[74] M. Di Renzo, H. Haas, A. Ghrayeb, S. Sugiura, and L. Hanzo. Spatial modulation for generalized MIMO: Challenges, opportunities, and implementation. *Proceedings of the IEEE*, 102(1):56–103, Jan. 2014.

[75] Clayton Shepard, Hang Yu, Narendra Anand, Erran Li, Thomas Marzetta, Richard Yang, and Lin Zhong. Argos: Practical many-antenna base stations. In *Proceedings of the 18th Annual International Conference on Mobile Computing and Networking*, Mobicom '12, pages 53–64, New York, NY, USA, 2012. ACM.

[76] David Tse and Pramod Viswanath. *Fundamentals of wireless communication*. New

York: Cambridge University Press, 2005.

[77] J. Zhang, B. Zhang, S. Chen, X. Mu, M. El-Hajjar, and L. Hanzo. Pilot contamination elimination for large-scale multiple-antenna aided OFDM systems. *IEEE Journal of Selected Topics in Signal Processing*, 8(5):759–772, Oct. 2014.

[78] C. Wen, S. Jin, K. Wong, J. Chen, and P. Ting. Channel estimation for massive MIMO using Gaussian-mixture Bayesian learning. *IEEE Transactions on Wireless Communications*, 14(3):1356–1368, March 2015.

[79] H. Yin, D. Gesbert, M. Filippou, and Y. Liu. A coordinated approach to channel estimation in large-scale multiple-antenna systems. *IEEE Journal on Selected Areas in Communications*, 31(2):264–273, Feb. 2013.

[80] H. Yin, L. Cottatellucci, D. Gesbert, R. Müller, and G. He. Pilot decontamination using combined angular and amplitude based projections in massive MIMO systems. In *2015 IEEE 16th International Workshop on Signal Processing Advances in Wireless Communications (SPAWC)*, pages 216–220, Stockholm, Sweden, June 2015.

[81] M. Alkhaled, E. Alsusa, and D. K. C. So. On the performance of TDD massive MIMO systems with pilot contamination. In *2017 IEEE 85th Vehicular Technology Conference (VTC Spring)*, pages 1–6, Sydney, Australia, June 2017.

[82] J. Jose, A. Ashikhmin, T. Marzetta, and S. Vishwanath. Pilot contamination problem in multi-cell TDD systems. In *IEEE International Symposium on Information Theory (ISIT) 2009*, pages 2184–2188, Seoul, South Korea, June 2009.

[83] H. Yin, D. Gesbert, M. Filippou, and Y. Liu. Decontaminating pilots in massive MIMO systems. In *2013 IEEE International Conference on Communications (ICC)*,

pages 3170–3175, Budapest, Hungary, June 2013.

[84] F. Fernandes, A. Ashikhmin, and T. Marzetta. Inter-cell interference in noncooperative TDD large scale antenna systems. *IEEE Journal on Selected Areas in Communications*, 31(2):192–201, Feb. 2013.

[85] K. Appaiah, A. Ashikhmin, and T. Marzetta. Pilot contamination reduction in multi-user TDD systems. In *2010 IEEE International Conference on Communications (ICC)*, pages 1–5, Cape Town, South Africa, May 2010.

[86] D. Hu, L. He, and X. Wang. Semi-blind pilot decontamination for massive MIMO systems. *IEEE Transactions on Wireless Communications*, 15(1):525–536, Jan. 2016.

[87] R. Müller, L. Cottatellucci, and M. Vehkapera. Blind pilot decontamination. *IEEE Journal of Selected Topics in Signal Processing*, 8(5):773–786, Oct. 2014.

[88] H. Ngo and E. Larsson. EVD-based channel estimation in multicell multiuser MIMO systems with very large antenna arrays. In *2012 IEEE International Conference on Acoustics, Speech and Signal Processing (ICASSP)*, pages 3249–3252, Kyoto, Japan, March 2012.

[89] A. Ashikhmin and T. Marzetta. Pilot contamination precoding in multi-cell large scale antenna systems. In *2012 IEEE International Symposium on Information Theory Proceedings (ISIT)*, pages 1137–1141, Cambridge, MA, USA, July 2012.

[90] J. Jose, A. Ashikhmin, T. Marzetta, and S. Vishwanath. Pilot contamination and precoding in multi-cell TDD systems. *IEEE Transactions on Wireless Communications*, 10(8):2640–2651, Aug. 2011.

[91] J. Ma and L. Ping. Data-aided channel estimation in large antenna systems. *IEEE*

Transactions on Signal Processing, 62(12):3111–3124, June 2014.

[92] Z. Gong, C. Li, and F. Jiang. Pilot contamination mitigation strategies in massive MIMO systems. *IET Communications*, 11(16):2403–2409, Nov. 2017.

[93] X. Vu, T. Vu, and T. Quek. Successive pilot contamination elimination in multi-antenna multicell networks. *IEEE Wireless Communications Letters*, 3(6):617–620, Dec. 2014.

[94] Hien Ngo, Erik Larsson, and Thomas Marzetta. Energy and spectral efficiency of very large multiuser MIMO systems. *IEEE Transactions on Communications*, 61(4):1436–1449, Feb. 2013.

[95] H. Yin, L. Cottatellucci, D. Gesbert, R. Müller, and G. He. Robust pilot decontamination based on joint angle and power domain discrimination. *IEEE Transactions on Signal Processing*, 64(11):2990–3003, June 2016.

[96] L. Li, A. Ashikhmin, and T. Marzetta. Pilot contamination precoding for interference reduction in large scale antenna systems. In *2013 51st Annual Allerton Conference on Communication, Control, and Computing (Allerton)*, pages 226–232, Monticello, IL, USA, Oct. 2013.

[97] T. Rappaport, S. Sun, and R. Mayzus *et al.* Millimeter wave mobile communications for 5G cellular: It will work! *IEEE Access*, 1:335–349, May 2013.

[98] R. C. Daniels, J. N. Murdock, T. S. Rappaport, and R. W. Heath. 60 GHz wireless: Up close and personal. *IEEE Microwave Magazine*, 11(7):44–50, Dec. 2010.

[99] M. Xiao, S. Mumtaz, Y. Huang, L. Dai, Y. Li, M. Matthaiou, G. K. Karagiannidis, E. Björnson, K. Yang, C. I, and A. Ghosh. Millimeter wave communications for future mobile networks. *IEEE Journal on Selected Areas in Communications*,

35(9):1909–1935, Sep. 2017.

[100] A. L. Swindlehurst, E. Ayanoglu, P. Heydari, and F. Capolino. Millimeter-wave massive MIMO: the next wireless revolution? *IEEE Communications Magazine*, 52(9):56–62, Sep. 2014.

[101] L. You, X. Gao, G. Y. Li, X. Xia, and N. Ma. BDMA for millimeter-wave/Terahertz massive MIMO transmission with per-beam synchronization. *IEEE Journal on Selected Areas in Communications*, 35(7):1550–1563, July 2017.

[102] S. Hur, T. Kim, D. J. Love, J. V. Krogmeier, T. A. Thomas, and A. Ghosh. Millimeter wave beamforming for wireless backhaul and access in small cell networks. *IEEE Transactions on Communications*, 61(10):4391–4403, Oct. 2013.

[103] M. Kokshoorn, H. Chen, P. Wang, Y. Li, and B. Vucetic. Millimeter wave MIMO channel estimation using overlapped beam patterns and rate adaptation. *IEEE Transactions on Signal Processing*, 65(3):601–616, Feb. 2017.

[104] Z. Zhou, J. Fang, L. Yang, H. Li, Z. Chen, and S. Li. Channel estimation for millimeter-wave multiuser MIMO systems via PARAFAC decomposition. *IEEE Transactions on Wireless Communications*, 15(11):7501–7516, Nov. 2016.

[105] T. S. Rappaport, G. R. MacCartney, M. K. Samimi, and S. Sun. Wideband millimeter-wave propagation measurements and channel models for future wireless communication system design. *IEEE Transactions on Communications*, 63(9):3029–3056, Sept. 2015.

[106] J. Zhao, F. Gao, W. Jia, S. Zhang, S. Jin, and H. Lin. Angle domain hybrid precoding and channel tracking for millimeter wave massive mimo systems. *IEEE Transactions on Wireless Communications*, 16(10):6868–6880, Oct 2017.

[107] A. Alkhateeb, J. Mo, N. Gonzalez-Prelcic, and R. W. Heath. MIMO precoding and combining solutions for millimeter-wave systems. *IEEE Communications Magazine*, 52(12):122–131, Dec. 2014.

[108] Z. Guo, X. Wang, and W. Heng. Millimeter-wave channel estimation based on 2-D beamspace MUSIC method. *IEEE Transactions on Wireless Communications*, 16(8):5384–5394, Aug. 2017.

[109] C. Tsai, Y. Liu, and A. Wu. Efficient compressive channel estimation for millimeter-wave large-scale antenna systems. *IEEE Transactions on Signal Processing*, 66(9):2414–2428, May 2018.

[110] J. Rodríguez-Fernández, N. González-Prelcic, K. Venugopal, and R. W. Heath. Frequency-domain compressive channel estimation for frequency-selective hybrid millimeter wave mimo systems. *IEEE Transactions on Wireless Communications*, 17(5):2946–2960, May 2018.

[111] H. Lin, F. Gao, S. Jin, and G. Y. Li. A new view of multi-user hybrid massive MIMO: Non-orthogonal angle division multiple access. *IEEE Journal on Selected Areas in Communications*, 35(10):2268–2280, Oct. 2017.

[112] J. Mo, P. Schniter, and R. W. Heath. Channel estimation in broadband millimeter wave MIMO systems with few-bit ADCs. *IEEE Transactions on Signal Processing*, 66(5):1141–1154, March 2018.

[113] X. Lin, S. Wu, C. Jiang, L. Kuang, J. Yan, and L. Hanzo. Estimation of broadband multiuser millimeter wave massive MIMO-OFDM channels by exploiting their sparse structure. *IEEE Transactions on Wireless Communications*, 17(6):3959–3973, June 2018.

[114] Sung Eun Jo, Sang Woo Kim, and Tae Joon Park. Equally constrained affine projection algorithm. In *Proceedings of the 38th Asilomar Conference on Signals, Systems and Computers*, volume 1, pages 955–959, Pacific Grove, California, USA, Nov. 2004.

[115] R.A. Horn and C.R. Johnson. *Matrix Analysis*. Cambridge University Press, 1990.

[116] Aravindh Krishnamoorthy and Deepak Menon. Matrix inversion using cholesky decomposition. *arXiv preprint arXiv:1111.4144*, Nov 2011.

[117] F. T. Dagefu and K. Sarabandi. Analysis and modeling of near-ground wave propagation in the presence of building walls. *IEEE Transactions on Antennas and Propagation*, 59(6):2368–2378, June 2011.

[118] M. Aoki, E. Oki, and R. Rojas-Cessa. Measurement scheme for one-way delay variation with detection and removal of clock skew. *ETRI Journal*, 32(6):854–862, Dec. 2010.

[119] M. Cristea and B. Groza. Fingerprinting smartphones remotely via icmp timestamps. *IEEE Communications Letters*, 17(6):1081–1083, June 2013.

[120] S. Jana and S. K. Kasera. On fast and accurate detection of unauthorized wireless access points using clock skews. *IEEE Transactions on Mobile Computing*, 9(3):449–462, March 2010.

[121] M. A. Spirito. On the accuracy of cellular mobile station location estimation. *IEEE Transactions on Vehicular Technology*, 50(3):674–685, May 2001.

[122] P. Closas and M. F. Bugallo. Improving accuracy by iterated multiple particle filtering. *IEEE Signal Processing Letters*, 19(8):531–534, Aug. 2012.

[123] P. M. Djurić, J. H. Kotecha, Jianqui Zhang, Yufei Huang, T. Ghirmai, M. F. Bugallo,

and J. Miguez. Particle filtering. *IEEE Signal Processing Magazine*, 20(5):19–38, Sep. 2003.

[124] P. M. Djurić, M. Vemula, and M. F. Bugallo. Target tracking by particle filtering in binary sensor networks. *IEEE Transactions on Signal Processing*, 56(6):2229–2238, June 2008.

[125] G. T. Donovan. Position error correction for an autonomous underwater vehicle inertial navigation system (INS) using a particle filter. *IEEE Journal of Oceanic Engineering*, 37(3):431–445, July 2012.

[126] C. M. Lee, S. W. Hong P. M. Lee, S. M. Kim, and W. Seong. Underwater navigation system based on an inertial sensor and a Doppler velocity log using indirect feedback Kalman filter. *Journal of Ocean Engineering and Technology*, 6(6), Jan. 2004.

[127] R. Porter, R. Spindel, and R. Jaffee. CW beacon system for hydrophone motion determination. *The Journal of the Acoustical Society of America*, 53(6):1691–1699, 1973.

[128] S. F. Mason, C. R. Berger, S. Zhou, and P. Willett. Detection, synchronization, and Doppler scale estimation with multicarrier waveforms in underwater acoustic communication. *IEEE Journal on Selected Areas in Communications*, 26(9):1638–1649, Dec. 2008.

[129] F. Qu, Z. Wang, L. Yang, and Z. Wu. A journey toward modeling and resolving doppler in underwater acoustic communications. *IEEE Communications Magazine*, 54(2):49–55, Feb. 2016.

[130] J. Tang, D. K. C. So, E. Alsusa, K. A. Hamdi, and A. Shojaeifard. On the energy efficiency-spectral efficiency tradeoff in MIMO-OFDMA broadcast channels. *IEEE*

Transactions on Vehicular Technology, 65(7):5185–5199, July 2016.

[131] H. Yang and T. Marzetta. Performance of conjugate and zero-forcing beamforming in large-scale antenna systems. *IEEE Journal on Selected Areas in Communications*, 31(2):172–179, Feb. 2013.

[132] J. Hoydis, S. ten Brink, and M. Debbah. Massive MIMO in the UL/DL of cellular networks: How many antennas do we need? *IEEE Journal on Selected Areas in Communications*, 31(2):160–171, Feb. 2013.

[133] F. Jiang, C. Li, Z. Gong, and R. Su. Stair matrix and its applications to massive MIMO uplink data detection. *IEEE Transactions on Communications*, 66(6):2437–2455, June 2018.

[134] F. Jiang, C. Li, and Z. Gong. Low complexity and fast processing algorithms for V2I massive MIMO uplink detection. *IEEE Transactions on Vehicular Technology*, 67(6):5054–5068, June 2018.

[135] F. Jiang, C. Li, and Z. Gong. Block Gauss-Seidel method based detection in vehicle-to-infrastructure massive MIMO uplink. In *2017 IEEE GLOBECOM*, pages 1–5, Signapore, Dec. 2017.

[136] F. Jiang, C. Li, and Z. Gong. A low complexity soft-output data detection scheme based on Jacobi method for massive MIMO uplink transmission. In *2017 IEEE International Conference on Communications (ICC)*, pages 1–5, Paris, France, May 2017.

[137] T. G. Rodrigues, K. Suto, H. Nishiyama, and N. Kato. Hybrid method for minimizing service delay in edge cloud computing through VM migration and transmission power control. *IEEE Transactions on Computers*, 66(5):810–819, May 2017.

[138] Z. Gong, C. Li, and F. Jiang. Pilot decontamination for cell-edge users in multi-cell massive mimo based on spatial filter. In *2018 IEEE International Conference on Communications (ICC)*, pages 1–6, Kansas City, MO, USA, May 2018.

[139] M. Masood, L. Afify, and T. Al-Naffouri. Efficient coordinated recovery of sparse channels in massive MIMO. *IEEE Transactions on Signal Processing*, 63(1):104–118, Jan. 2015.

[140] F. Wan, W. Zhu, and M. Swamy. Semiblind sparse channel estimation for MIMO-OFDM systems. *IEEE Transactions on Vehicular Technology*, 60(6):2569–2582, July 2011.

[141] M. Ozdemir and H. Arslan. Toward real-time adaptive low-rank LMMSE channel estimation of MIMO-OFDM systems. *IEEE Transactions on Wireless Communications*, 5(10):2675–2678, Oct. 2006.

[142] Y. Barbotin, A. Hormati, S. Rangan, and M. Vetterli. Estimation of sparse MIMO channels with common support. *IEEE Transactions on Communications*, 60(12), Dec. 2012.

[143] S. Haghighatshoar and G. Caire. Massive MIMO pilot decontamination and channel interpolation via wideband sparse channel estimation. *IEEE Transactions on Wireless Communications*, 16(12):8316–8332, Dec. 2017.

[144] L. Lu, G. Y. Li, A. L. Swindlehurst, A. Ashikhmin, and R. Zhang. An overview of massive MIMO: Benefits and challenges. *IEEE Journal of Selected Topics in Signal Processing*, 8(5):742–758, Oct. 2014.

[145] K. Zheng, L. Zhao, J. Mei, B. Shao, W. Xiang, and L. Hanzo. Survey of large-scale MIMO systems. *IEEE Communications Surveys Tutorials*, 17(3):1738–1760,

thirdquarter 2015.

[146] O. Elijah, C. Y. Leow, T. A. Rahman, S. Nunoo, and S. Z. Iliya. A comprehensive survey of pilot contamination in massive MIMO-5G system. *IEEE Communications Surveys Tutorials*, 18(2):905–923, Secondquarter 2016.

[147] A. Ashikhmin and T. Marzetta. Pilot contamination precoding in multi-cell large scale antenna systems. In *2012 IEEE International Symposium on Information Theory Proceedings*, pages 1137–1141, Cambridge, MA, USA, 2012.

[148] J. Brady, N. Behdad, and A. M. Sayeed. Beamspace mimo for millimeter-wave communications: System architecture, modeling, analysis, and measurements. *IEEE Transactions on Antennas and Propagation*, 61(7):3814–3827, July 2013.

[149] Y. Zeng and R. Zhang. Millimeter wave MIMO with lens antenna array: A new path division multiplexing paradigm. *IEEE Transactions on Communications*, 64(4):1557–1571, April 2016.

[150] L. Yang, Y. Zeng, and R. Zhang. Channel estimation for millimeter-wave MIMO communications with lens antenna arrays. *IEEE Transactions on Vehicular Technology*, 67(4):3239–3251, April 2018.

[151] X. Gao, L. Dai, Y. Zhang, T. Xie, X. Dai, and Z. Wang. Fast channel tracking for terahertz beamspace massive MIMO systems. *IEEE Transactions on Vehicular Technology*, 66(7):5689–5696, July 2017.

[152] R. W. Heath, N. González-Prelcic, S. Rangan, W. Roh, and A. M. Sayeed. An overview of signal processing techniques for millimeter wave MIMO systems. *IEEE Journal of Selected Topics in Signal Processing*, 10(3):436–453, April 2016.

[153] X. Gao, L. Dai, S. Han, C. I, and X. Wang. Reliable beamspace channel estima-

tion for millimeter-wave massive MIMO systems with lens antenna array. *IEEE Transactions on Wireless Communications*, 16(9):6010–6021, Sep. 2017.

[154] F. Jiang, Y. Zhang, and C. Li. A new SQRD-based soft interference cancelation scheme in multi-user MIMO SC-FDMA system. *IEEE Communications Letters*, 21(4):821–824, April 2017.

[155] J. Zhao, F. Gao, Q. Wu, S. Jin, Y. Wu, and W. Jia. Beam tracking for UAV mounted SatCom on-the-move with massive antenna array. *IEEE Journal on Selected Areas in Communications*, 36(2):363–375, Feb. 2018.

[156] Z. Gong, C. Li, and F. Jiang. Pilot decontamination in noncooperative massive mimo cellular networks based on spatial filtering. *IEEE Transactions on Wireless Communications*, 18(2):1419–1433, 2019.

[157] Z. Gong, C. Li, and F. Jiang. Channel estimation for sparse massive MIMO channels in low SNR regime. *IEEE Transactions on Cognitive Communications and Networking*, 4(4):883–893, Dec. 2018.

[158] Steven M. Kay. *Fundamentals of Statistical Signal Processing: Estimation Theory*. Prentice-Hall, Inc., Upper Saddle River, NJ, USA, 1993.

Appendix A

Appendix for Drone-Assisted Localization Framework

A.1 Proof of the Lower Bound of GDOP

In this appendix, we will try to find the lower bound of $GDOP$ given by Equation (3.27), and show that this bound can be achieved under the conditions of Equation (3.28). To begin with, we need to develop the following lemma.

Lemma 1: *Given a symmetric and positive definite matrix* $\mathbf{A} \in \mathcal{R}^{M\times M}$*, we have the following inequality:*

$$\mathrm{tr}\{\mathbf{A}^{-1}\} \geq \frac{M^2}{\mathrm{tr}\{\mathbf{A}\}}. \tag{A.1}$$

The equality holds when $\mathbf{A} = \lambda \cdot \mathbf{I}_M$*, where* λ *is a positive real number.*

Proof. Assuming the M eigenvalues of $\mathbf{A}$ are λ_m's ($m = 1, 2, \cdots, M$), $1/\lambda_m$'s will be the eigenvalues of $\mathbf{A}^{-1}$. Therefore, traces of $\mathbf{A}$ and $\mathbf{A}^{-1}$ are $\sum_{m=1}^{M} \lambda_m$ and $\sum_{m=1}^{M} 1/\lambda_m$, respec-

tively. Because $\mathbf{A}$ is positive definite, its M eigenvalues are all positive. According to the well known *Inequality of Arithmetic and Geometric Means*, we have

$$\sum_{m=1}^{M} 1/\lambda_m \geq \frac{M}{\left(\prod_{m=1}^{M} \lambda_m\right)^{1/M}} \geq \frac{M^2}{\sum_{m=1}^{M} \lambda_m}, \tag{A.2}$$

where the equalities hold if and only if $\lambda_m = \lambda$ for any m. Through eigenvalue decomposition, $\mathbf{A}$ can be decomposed as $\mathbf{A} = \mathbf{W}\mathbf{\Lambda}\mathbf{W}^{\mathbf{T}}$, where $\mathbf{W}$ is an orthogonal matrix and $\mathbf{\Lambda} = \text{diag}\{[\lambda_{\mathbf{1}}, \lambda_{\mathbf{2}}, \cdots, \lambda_{\mathbf{M}}]\}$. When $\lambda_m = \lambda$ for any m, we have $\mathbf{A} = \mathbf{W}\mathbf{\Lambda}\mathbf{W}^{\mathbf{T}} = \lambda\mathbf{W}\mathbf{W}^{\mathbf{T}} = \lambda \cdot \mathbf{I}_{\mathbf{M}}$. On the other hand, given $\mathbf{A} = \lambda \cdot \mathbf{I}_M$, we have $\lambda_m = \lambda(\forall\ 1 \leq m \leq M)$. □

Then, we can try to find the lower bound of the trace of $[(\mathbf{F}^T\mathbf{F})^{-1}]_{2\times 2}$. Through SVD, we can obtain

$$\mathbf{F}_2 = \mathbf{U}\mathbf{\Sigma}\mathbf{V}, \tag{A.3}$$

where $\mathbf{U}$ and $\mathbf{V}$ are two orthogonal matrixes. $\mathbf{\Sigma}$ has the form of

$$\mathbf{\Sigma} = \begin{bmatrix} \mathbf{\Lambda} \\ \\ \mathbf{0} \end{bmatrix}, \tag{A.4}$$

where $\mathbf{0} \in \mathcal{R}^{N-2\times 2}$ is a zero matrix and $\mathbf{\Lambda}$ is a diagonal matrix. The right side of Equation (3.11) can be reorganized as

$$\begin{aligned} &\mathbf{F}_1^T \left(\mathbf{I}_N - \mathbf{F_2}(\mathbf{F}_2^T\mathbf{F}_2)^{-1}\mathbf{F}_2^T\right)\mathbf{F}_1 \\ =&\mathbf{F}_1^T \left(\mathbf{I}_N - \mathbf{U}\mathbf{\Sigma}(\mathbf{\Sigma}^T\mathbf{\Sigma})^{-1}\mathbf{\Sigma}^{\mathrm{T}}\mathbf{U}^T\right)\mathbf{F}_1 \\ =&\mathbf{F}_1^T\mathbf{U}\left(\mathbf{I}_N - \mathbf{\Sigma}(\mathbf{\Sigma}^T\mathbf{\Sigma})^{-1}\mathbf{\Sigma}^T\right)\mathbf{U}^T\mathbf{F}_1. \end{aligned} \tag{A.5}$$

Then, $\mathbf{I}_N - \mathbf{\Sigma}(\mathbf{\Sigma}^T\mathbf{\Sigma})^{-1}\mathbf{\Sigma}^T$ can be further simplified to the following form

$$\begin{bmatrix} \mathbf{0}_2 & \mathbf{0}_{2\times N-2} \\ \\ \mathbf{0}_{N-2\times 2} & \mathbf{I}_{N-2} \end{bmatrix}. \tag{A.6}$$

Define $\mathbf{U} = [\mathbf{U}_L,\ \mathbf{U}_R]$, in which $\mathbf{U}_L$ is the left two columns of $\mathbf{U}$ while $\mathbf{U}_R$ consists of the right side $N-2$ columns. Continue with Equation (A.5),

$$\begin{aligned}
&\mathbf{F}_1^T\mathbf{U}\left(\mathbf{I}_N - \mathbf{\Sigma}(\mathbf{\Sigma}^T\mathbf{\Sigma})^{-1}\mathbf{\Sigma}^T\right)\mathbf{U}^T\mathbf{F}_1 \\
=&\mathbf{F}_1^T\left[\mathbf{U}_L,\ \mathbf{U}_R\right]\begin{bmatrix} \mathbf{0}_2 & \mathbf{0}_{2\times N-2} \\ \mathbf{0}_{N-2\times 2} & \mathbf{I}_{N-2} \end{bmatrix}\begin{bmatrix} \mathbf{U}_L^T \\ \mathbf{U}_R^T \end{bmatrix}\mathbf{F}_1 \\
=&\mathbf{F}_1^T\mathbf{U}_R\mathbf{U}_R^T\mathbf{F}_1.
\end{aligned} \tag{A.7}$$

As a result, the trace of $\mathbf{F}_1^T\left(\mathbf{I}_N - \mathbf{F_2}(\mathbf{F}_2^T\mathbf{F}_2)^{-1}\mathbf{F}_2^T\right)\mathbf{F}_1$ is

$$\mathrm{tr}\left\{\mathbf{F}_1^T\left(\mathbf{I}_N - \mathbf{F_2}(\mathbf{F}_2^T\mathbf{F}_2)^{-1}\mathbf{F}_2^T\right)\mathbf{F}_1\right\} = \left(\left\|\mathbf{F}_1^T\mathbf{U}_R\right\|_2\right)^2. \tag{A.8}$$

On the other hand,

$$\mathbf{F}_1^T\mathbf{F}_1 = \mathbf{F}_1^T\mathbf{U}\mathbf{U}^T\mathbf{F}_1 = \mathbf{F}_1^T\left[\mathbf{U}_L,\ \mathbf{U}_R\right]\begin{bmatrix} \mathbf{U}_L^T \\ \mathbf{U}_R^T \end{bmatrix}\mathbf{F}_1 = \mathbf{F}_1^T\mathbf{U}_L\mathbf{U}_L^T\mathbf{F}_1 + \mathbf{F}_1^T\mathbf{U}_R\mathbf{U}_R^T\mathbf{F}_1, \tag{A.9}$$

and the trace of $\mathbf{F}_1^T\mathbf{F}_1$ will be

$$\begin{aligned}
\mathrm{tr}\left\{\mathbf{F}_1^T\mathbf{F}_1\right\} &= \mathrm{tr}\left\{\mathbf{F}_1^T\mathbf{U}_L\mathbf{U}_L^T\mathbf{F}_1\right\} + \mathrm{tr}\left\{\mathbf{F}_1^T\mathbf{U}_R\mathbf{U}_R^T\mathbf{F}_1\right\} \\
&= \left\|\mathbf{F}_1^T\mathbf{U}_R\right\|_F^2 + \left\|\mathbf{F}_1^T\mathbf{U}_L\right\|_F^2.
\end{aligned} \tag{A.10}$$

Therefore, we have the following inequality

$$\mathrm{tr}\left\{\mathbf{F}_1^T\left(\mathbf{I}_N - \mathbf{F_2}(\mathbf{F}_2^T\mathbf{F}_2)^{-1}\mathbf{F}_2^T\right)\mathbf{F}_1\right\} \le \mathrm{tr}\left\{\mathbf{F}_1^T\mathbf{F}_1\right\}, \tag{A.11}$$

and the equality holds when $\mathbf{F}_1^T\mathbf{U}_L = \mathbf{0}$, or $\mathbf{F}_1^T\mathbf{F}_2 = \mathbf{0}$, because $\mathrm{Span}\{\mathbf{F}_2\} = \mathrm{Span}\{\mathbf{U}_L\}$.

Based on the previous discussions, the lower bound of the trace of $[(\mathbf{F}^T\mathbf{F})^{-1}]_{2\times 2}$ can

be given as

$$\operatorname{tr}\left\{\left[\left(\mathbf{F}^T\mathbf{F}\right)^{-1}\right]_{2\times 2}\right\} \tag{A.12a}$$

$$=\operatorname{tr}\left\{\left[\mathbf{F}_1^T\mathbf{F}_1-\mathbf{F}_1^T\mathbf{F}_2\left(\mathbf{F}_2^T\mathbf{F}_2\right)^{-1}\mathbf{F}_2^T\mathbf{F}_1\right]^{-1}\right\} \tag{A.12b}$$

$$\geq\frac{4}{\operatorname{tr}\left\{\mathbf{F}_1^T\left(\mathbf{I}_N-\mathbf{F_2}(\mathbf{F}_2^{\mathrm{T}}\mathbf{F}_2)^{-1}\mathbf{F}_2^T\right)\mathbf{F}_1\right\}} \tag{A.12c}$$

$$\geq\frac{4}{\operatorname{tr}\left\{\mathbf{F}_1^T\mathbf{F}_1\right\}} \tag{A.12d}$$

$$=\frac{4}{\beta^2\cdot\sum_{i=1}^{N}r_i^2/d_i^4}. \tag{A.12e}$$

Based on Equation (A.11), the equality in step (A.12d) holds if $\mathbf{F}_1^T\mathbf{F}_2=\mathbf{0}$. Meantime, according to Lemma 1, the equality in step (A.12c) holds given $\mathbf{F}_1^T\mathbf{F}_1=c\cdot\mathbf{I}_2$.

A.2 Proof of the Asymptotic Orthogonality between Different Columns of F

In this part, we assume that the projections of virtual anchors are uniformly distributed in the communication range of the target node. Based on this assumption, we will try to prove the asymptotic orthogonality between different columns of $\mathbf{F}$ mentioned in end of Section 3.4-B. For convenience, set the origin on target node's location and establish a reference frame, with the x axis and y axis pointing to the Ease and the North, respectively. Then, we can obtain the PDF of virtual anchors' coordinates as

$$f_{X_i,Y_i}(x_i,y_i)=\frac{1}{\pi R^2}, \tag{A.13}$$

where (x_i, y_i) is the coordinate of the i-th anchor's projection, as shown in Figure 3.2. Transform the Cartesian coordinates into polar coordinates:

$$\begin{cases} x_i = r_i \cdot \cos\theta_i \\ y_i = r_i \cdot \sin\theta_i, \end{cases} \tag{A.14}$$

where r_i and θ_i are the distance and azimuth of the i-th anchor's projection, with respect to the target node. As a result, it can be easily proved that the θ_i follows uniform distribution in $[0, \pi]$, while the PDF of r_i is

$$f_{R_i}(r_i) = \frac{2r_i}{R^2}. \tag{A.15}$$

The expectation of r_i^2/d_i^4 is

$$E\left\{r_i^2/d_i^4\right\} = \int_0^R \frac{r_i^2}{(r_i^2+h^2)^2} \cdot \frac{2r_i}{R^2} \mathrm{d}r_i = \frac{1}{R^2} \cdot \left[\ln\left(\frac{R^2+h^2}{h^2}\right) - \frac{R^2}{R^2+h^2}\right]. \tag{A.16}$$

Define $\mathbf{F} \triangleq [\mathbf{f}_1, \mathbf{f}_2, \mathbf{f}_3, \mathbf{f}_4]$, where $\mathbf{f}_i$ is the i-th column of $\mathbf{F}$. Then, we can obtain

$$\lim_{N\to\infty} \frac{\mathbf{f}_1^T \mathbf{f}_2}{N} = \beta^2 \cdot \underbrace{\lim_{N\to\infty} \frac{1}{N} \sum_{i=1}^{N} \sin\theta_i \cos\theta_i \cdot r_i^2/d_i^4}_{A}. \tag{A.17}$$

Because all the virtual anchors are independently and identically distributed, the limit of A is actually the expectation of $\sin\theta_i \cos\theta_i \cdot r_i^2/d_i^4$ for arbitrary integer $i \in [1, N]$, which leads to

$$\lim_{N\to\infty} \frac{\mathbf{f}_1^T \mathbf{f}_2}{N} = \beta^2 \cdot E\{\sin\theta_i \cos\theta_i \cdot r_i^2/d_i^4\} = \beta^2 \cdot E\{\sin\theta_i \cos\theta_i\} \cdot E\{r_i^2/d_i^4\} = 0. \tag{A.18}$$

Besides, the expectation of the norm of $\mathbf{f}_1/\sqrt{N}$ is

$$\lim_{N\to\infty} \frac{\|\mathbf{f}_1\|^2}{N} = \lim_{N\to\infty} \beta^2 \cdot \frac{1}{N} \sum_{i=1}^{N} \cos\theta_i{}^2 \cdot r_i^2/d_i^4 = \beta^2 \cdot E\{\cos\theta_i{}^2 \cdot r_i^2/d_i^4\} = \beta^2/2 \cdot E\left\{r_i^2/d_i^4\right\}. \tag{A.19}$$

Similarly, we have

$$\lim_{N\to\infty} \frac{\|\mathbf{f}_2\|^2}{N} = \lim_{N\to\infty} \frac{\|\mathbf{f}_1\|^2}{N}, \tag{A.20}$$

and thus, we can conclude that

$$\lim_{N\to\infty} \frac{\mathbf{F}_1^T\mathbf{F}_1}{N} = \frac{c}{N}\cdot\mathbf{I}_2. \tag{A.21}$$

Similar to the above discussions, we can prove that $\mathbf{F}_1$ and $\mathbf{F}_2$ are asymptotically orthogonal. To be specific,

$$\lim_{N\to\infty} \frac{\mathbf{F}_1^T\mathbf{F}_2}{N} = \mathbf{0}. \tag{A.22}$$

As a result, the conditions in Equation (3.28) are asymptotically fulfilled.

Appendix B

Appendix for the Doppler-Based Localization Framework

B.1 Statistics of $\mathbf{n}_\omega$

The covariance matrix of $\mathbf{n}_\omega$ is $E\{\mathbf{n}_\omega \mathbf{n}_\omega^H\} = \sigma^2/N \cdot \mathbf{I}_N$. The real part of $\mathbf{n}_\omega[k]$ is

$$\Re\{\mathbf{n}_\omega[k]\} = \frac{1}{N} \sum_{n=0}^{N-1} \mathbf{n}_s[n] \cos(kn\omega_0), \tag{B.1}$$

while the imaginary part is

$$\Im\{\mathbf{n}_\omega[k]\} = \frac{1}{N} \sum_{n=0}^{N-1} \mathbf{n}_s[n] \sin(kn\omega_0). \tag{B.2}$$

We can prove that they are uncorrelated:

$$\begin{aligned} E\{\Re\{\mathbf{n}_\omega[k]\}\Im\{\mathbf{n}_\omega[k]\}\} =& E\left\{\frac{1}{N^2}\sum_{n_1=0}^{N-1}\sum_{n_2=0}^{N-1}\mathbf{n}_s[n_1]\mathbf{n}_s[n_2]\cos(kn_1\omega_0)\sin(kn_2\omega_0)\right\} \\ =& \frac{1}{N^2}\sum_{n_1=0}^{N-1}\sum_{n_2=0}^{N-1}E\{\mathbf{n}_s[n_1]\mathbf{n}_s[n_2]\}\cos(kn_1\omega_0)\sin(kn_2\omega_0) \\ =& \frac{1}{N^2}\sum_{n=0}^{N-1}\sigma^2\cos(kn\omega_0)\sin(kn\omega_0) \\ =& 0. \end{aligned} \tag{B.3}$$

Similarly, for any two elements in $\mathbf{n}_\omega$ (e.g., $\mathbf{n}_\omega[k]$ and $\mathbf{n}_\omega[k']$, $k \neq k'$), we can prove that

$$E\{\Re\{\mathbf{n}_\omega[k']\}\Im\{\mathbf{n}_\omega[k]\}\} = E\{\Re\{\mathbf{n}_\omega[k']\}\Re\{\mathbf{n}_\omega[k]\}\} = E\{\Im\{\mathbf{n}_\omega[k']\}\Im\{\mathbf{n}_\omega[k]\}\} = 0. \tag{B.4}$$

B.2 Proof of CRLB in (5.69)

Define θ_p as the p-th element in $\boldsymbol{\theta}$, i.e., $\theta_p = \boldsymbol{\theta}[p]$. The partial derivative of $l(\mathbf{f}_D|\mathbf{x}, c)$, with respect to θ_p is given in (B.5). As we can see, $\frac{\partial l}{\partial \theta_p}$ contains three components, $B_{p,1}$, $B_{p,2}$, and $B_{p,3}$.

$$\begin{aligned} \frac{\partial l}{\partial \theta_p} =& -\frac{1}{2}\left(\frac{\partial \boldsymbol{\mu}^T}{\partial \theta_p}\boldsymbol{\Sigma}^{-1}(\boldsymbol{\mu}-\mathbf{f}_D) + (\boldsymbol{\mu}-\mathbf{f}_D)^T\left(\frac{\partial \boldsymbol{\Sigma}^{-1}}{\partial \theta_p}(\boldsymbol{\mu}-\mathbf{f}_D) + \boldsymbol{\Sigma}^{-1}\frac{\partial \boldsymbol{\mu}}{\partial \theta_p}\right) + \frac{\partial \ln|\boldsymbol{\Sigma}|}{\partial \theta_p}\right) \\ =& \underbrace{-\frac{\partial \boldsymbol{\mu}^T}{\partial \theta_p}\boldsymbol{\Sigma}^{-1}(\boldsymbol{\mu}-\mathbf{f}_D)}_{B_{p,1}} \underbrace{-\frac{1}{2}(\boldsymbol{\mu}-\mathbf{f}_D)^T\frac{\partial \boldsymbol{\Sigma}^{-1}}{\partial \theta_p}(\boldsymbol{\mu}-\mathbf{f}_D)}_{B_{p,2}} \underbrace{-\frac{1}{2}\frac{\partial \ln|\boldsymbol{\Sigma}|}{\partial \theta_p}}_{B_{p,3}} \end{aligned} \tag{B.5}$$

The (p,q)-th element in $\mathbf{F}$ is

$$\mathbf{F}[p,q] = E\left\{\frac{\partial l}{\partial \theta_p}\cdot\frac{\partial l}{\partial \theta_q}\right\} = \frac{1}{4}E\left\{\sum_{i=1}^{3}\sum_{j=1}^{3}B_{p,i}B_{q,j}\right\}. \tag{B.6}$$

We have

$$
\begin{aligned}
E\{B_{p,1}B_{q,1}\} &= 4\frac{\partial \boldsymbol{\mu}^T}{\partial \theta_p}\boldsymbol{\Sigma}^{-1}\frac{\partial \boldsymbol{\mu}}{\partial \theta_q} \\
E\{B_{p,1}B_{q,2}\} &= E\{B_{p,1}B_{q,3}\} = 0 \\
E\{B_{p,2}B_{q,3}\} &= B_{p,3}E\{B_{q,2}\} = -\operatorname{tr}\left\{\boldsymbol{\Sigma}^{-1}\frac{\partial \boldsymbol{\Sigma}}{\partial \theta_p}\right\}\operatorname{tr}\left\{\boldsymbol{\Sigma}^{-1}\frac{\partial \boldsymbol{\Sigma}}{\partial \theta_q}\right\} \\
E\{B_{p,3}B_{q,3}\} &= B_{p,3}B_{q,3} = \operatorname{tr}\left\{\boldsymbol{\Sigma}^{-1}\frac{\partial \boldsymbol{\Sigma}}{\partial \theta_p}\right\}\operatorname{tr}\left\{\boldsymbol{\Sigma}^{-1}\frac{\partial \boldsymbol{\Sigma}}{\partial \theta_q}\right\},
\end{aligned}
\tag{B.7}
$$

and $E\{B_{p,2}B_{q,2}\}$ is derived in (B.8).

$$
\begin{aligned}
E\{B_{p,2}B_{q,2}\} &= E\left\{(\boldsymbol{\mu}-\mathbf{f}_D)^T\frac{\partial \boldsymbol{\Sigma}^{-1}}{\partial \theta_p}(\boldsymbol{\mu}-\mathbf{f}_D)(\boldsymbol{\mu}-\mathbf{f}_D)^T\frac{\partial \boldsymbol{\Sigma}^{-1}}{\partial \theta_q}(\boldsymbol{\mu}-\mathbf{f}_D)\right\} \\
&= E\left\{\operatorname{diag}\left\{\boldsymbol{\Sigma}^{-2}\frac{\partial \boldsymbol{\Sigma}}{\partial \theta_p}\right\}(\boldsymbol{\mu}-\mathbf{f}_D)\circ(\boldsymbol{\mu}-\mathbf{f}_D)(\boldsymbol{\mu}-\mathbf{f}_D)\circ(\boldsymbol{\mu}-\mathbf{f}_D)\operatorname{diag}\left\{\boldsymbol{\Sigma}^{-2}\frac{\partial \boldsymbol{\Sigma}}{\partial \theta_q}\right\}\right\} \\
&= \operatorname{diag}\left\{\boldsymbol{\Sigma}^{-2}\frac{\partial \boldsymbol{\Sigma}}{\partial \theta_p}\right\}E\left\{(\boldsymbol{\mu}-\mathbf{f}_D)\circ(\boldsymbol{\mu}-\mathbf{f}_D)(\boldsymbol{\mu}-\mathbf{f}_D)\circ(\boldsymbol{\mu}-\mathbf{f}_D)\right\}\operatorname{diag}\left\{\boldsymbol{\Sigma}^{-2}\frac{\partial \boldsymbol{\Sigma}}{\partial \theta_q}\right\} \\
&= \operatorname{diag}\left\{\boldsymbol{\Sigma}^{-2}\frac{\partial \boldsymbol{\Sigma}}{\partial \theta_p}\right\}(\boldsymbol{\sigma}\boldsymbol{\sigma}^T+2\boldsymbol{\Sigma}^2)\operatorname{diag}\left\{\boldsymbol{\Sigma}^{-2}\frac{\partial \boldsymbol{\Sigma}}{\partial \theta_q}\right\} \\
&= \operatorname{diag}\left\{\boldsymbol{\Sigma}^{-2}\frac{\partial \boldsymbol{\Sigma}}{\partial \theta_p}\right\}\boldsymbol{\sigma}\boldsymbol{\sigma}^T\operatorname{diag}\left\{\boldsymbol{\Sigma}^{-2}\frac{\partial \boldsymbol{\Sigma}}{\partial \theta_q}\right\}+2\operatorname{diag}\left\{\boldsymbol{\Sigma}^{-2}\frac{\partial \boldsymbol{\Sigma}}{\partial \theta_p}\right\}\boldsymbol{\Sigma}^2\operatorname{diag}\left\{\boldsymbol{\Sigma}^{-2}\frac{\partial \boldsymbol{\Sigma}}{\partial \theta_q}\right\} \\
&= \operatorname{tr}\left\{\boldsymbol{\Sigma}^{-1}\frac{\partial \boldsymbol{\Sigma}}{\partial \theta_p}\right\}\operatorname{tr}\left\{\boldsymbol{\Sigma}^{-1}\frac{\partial \boldsymbol{\Sigma}}{\partial \theta_q}\right\}+2\operatorname{tr}\left\{\frac{\partial \boldsymbol{\Sigma}}{\partial \theta_p}\boldsymbol{\Sigma}^{-2}\frac{\partial \boldsymbol{\Sigma}}{\partial \theta_q}\right\} \\
&= \operatorname{tr}\left\{\boldsymbol{\Sigma}^{-1}\frac{\partial \boldsymbol{\Sigma}}{\partial \theta_p}\right\}\operatorname{tr}\left\{\boldsymbol{\Sigma}^{-1}\frac{\partial \boldsymbol{\Sigma}}{\partial \theta_q}\right\}+2\left\{\frac{\partial \boldsymbol{\sigma}^T}{\partial \theta_p}\boldsymbol{\Sigma}^{-2}\frac{\partial \boldsymbol{\sigma}}{\partial \theta_q}\right\}
\end{aligned}
\tag{B.8}
$$

Therefore, $\mathbf{F}[p,q]$ is given by

$$
\mathbf{F}[p,q] = \frac{\partial \boldsymbol{\mu}^T}{\partial \theta_p}\boldsymbol{\Sigma}^{-1}\frac{\partial \boldsymbol{\mu}}{\partial \theta_q}+\frac{1}{2}\left\{\frac{\partial \boldsymbol{\sigma}^T}{\partial \theta_p}\boldsymbol{\Sigma}^{-2}\frac{\partial \boldsymbol{\sigma}}{\partial \theta_q}\right\}, \tag{B.9}
$$

where we implicitly use the fact that $\frac{\partial \boldsymbol{\Sigma}^{-1}}{\partial \theta_p} = -\boldsymbol{\Sigma}^{-2}\frac{\partial \boldsymbol{\Sigma}}{\partial \theta_p}$, and $B_{p,3} = \operatorname{tr}\left\{\boldsymbol{\Sigma}^{-1}\frac{\partial \boldsymbol{\Sigma}}{\partial \theta_p}\right\}$. (B.9) can then be reorganized as (5.69).

B.3 Proof of (5.70)

Let $\boldsymbol{\mu}_m = [\mu_{m,1}, \mu_{m,2}, \cdots, \mu_{m,K}]^T$, and we have $\boldsymbol{\mu} = [\boldsymbol{\mu}_1^T, \boldsymbol{\mu}_2^T, \cdots, \boldsymbol{\mu}_M^T]^T$, where $\mu_{m,k}$ is given as

$$\mu_{m,k} = E\{f_D^{(m,k)} | \mathbf{x}, c\} = \frac{(\mathbf{x} - \mathbf{x}_{m,k})^T \mathbf{v}_m}{d_{m,k}} \cdot \frac{f_c}{c}. \tag{B.10}$$

As a result, we have

$$\frac{\partial \boldsymbol{\mu}}{\partial \boldsymbol{\theta}} = \mathbf{H}. \tag{B.11}$$

For the (m,k)-th sample, the variance of Doppler estimate is

$$\sigma_{m,k}^2 = \frac{2f_s^2\sigma^2}{N^3 A_{m,k}^2} \cdot r(\beta_{m,k}). \tag{B.12}$$

The partial derivative of $\sigma_{m,k}^2$ with respect to $\boldsymbol{\theta}$ is

$$\frac{\partial \sigma_{m,k}^2}{\partial \boldsymbol{\theta}} = \frac{2f_s^2\sigma^2}{N^3 A_{m,k}^2} \cdot \frac{dr}{d\beta_{m,k}} \cdot \frac{\partial \beta_{m,k}}{\partial \boldsymbol{\theta}} = \frac{2f_s\sigma^2}{N^2 A_{m,k}^2} \cdot \frac{dr}{d\beta_{m,k}} \cdot \frac{\partial f_{m,k}(\boldsymbol{\theta})}{\partial \boldsymbol{\theta}}. \tag{B.13}$$

$dr/d\beta$ is given by

$$\frac{dr}{d\beta} = \begin{cases} \left[a_1(\beta) cos^2(\beta\pi) + b_1(\beta)\pi \sin(2\beta\pi)\right] \pi^2 / \cos^4(\beta\pi) & \beta \in [0, 0.25) \\ \left[a_2(\beta) \sin^2(\beta\pi) + b_2(\beta)\pi \sin(2\beta\pi)\right] \pi^2 / \sin^4(\beta\pi) & \beta \in (0.25, 0.75) \\ \left[a_3(\beta) \cos^2(\beta\pi) + b_3(\beta)\pi \sin(2\beta\pi)\right] \pi^2 / \cos^4(\beta\pi) & \beta \in (0.75, 1). \end{cases} \tag{B.14}$$

where we have

$$
\begin{aligned}
a_1(\beta) &= (2\beta^2 - 0.5)(6\beta^3 + 0.5\beta) \\
b_1(\beta) &= (\beta^2 - 0.25)^2(2\beta^2 + 0.5) \\
a_2(\beta) &= 2(1-2\beta)(3\beta^2 - 3\beta + 1)\beta(1-\beta) \\
b_2(\beta) &= -(2\beta^2 - 2\beta + 1)(\beta^2 - \beta)^2 \\
a_3(\beta) &= (\beta - 1)(2\beta^2 - 4\beta + 1.5)(6\beta^2 - 12\beta + 6.5) \\
b_3(\beta) &= (\beta^2 - 2\beta + 0.75)^2(2\beta^2 - 4\beta + 3.25).
\end{aligned}
\tag{B.15}
$$

Because

$$
\beta_{m,k} = (f_c + f_D^{(m,k)})N/f_s - \lfloor (f_c + f_D^{(m,k)})N/f_s \rfloor, \tag{B.16}
$$

we have

$$
\frac{\partial \beta_{m,k}}{\partial \boldsymbol{\theta}} = \frac{N}{f_s} \cdot \frac{\partial f_{m,k}(\boldsymbol{\theta})}{\partial \boldsymbol{\theta}}. \tag{B.17}
$$

Let $\mathbf{p} = [\mathbf{p}_1^T, \mathbf{p}_2^T, \cdots, \mathbf{p}_M^T]^T$, and the k-th element of $\mathbf{p}_m$ is given as

$$
\mathbf{p}_m[k] = \frac{2f_s\sigma^2}{N^2 A_{m,k}^2} \cdot \frac{dr}{d\beta_{m,k}}. \tag{B.18}
$$

Then, we can organize the results and conclude

$$
\frac{\partial \boldsymbol{\sigma}}{\partial \boldsymbol{\theta}} = \mathbf{PH}. \tag{B.19}
$$

where $\mathbf{P} = \mathrm{diag}(\mathbf{p})$.

Appendix C

Appendix for the FrFT-Based Signal Analysis

C.1 FrFT and MLE

In this section, we will show that finding the MLE of f_0 and k is equivalent to finding the peak in the FrFT of $r(t)$.

The maximum likelihood estimate of f_0 and k should be

$$[\hat{f}_0, \hat{k}, \hat{A}] = \arg\min_{\bar{f}_0, \bar{k}, \bar{A}} \int_{t=0}^{T} \left| r(t) - \bar{A} e^{j(2\pi \bar{f}_0 + \bar{k}\pi t^2)} \right|^2 dt. \tag{C.1}$$

The component inside the can be expanded as

$$\begin{aligned} &|r(t) - \bar{A} e^{j(2\pi \bar{f}_0 + \bar{k}\pi t^2)}|^2 \\ =&|r(t)|^2 + |\bar{A}|^2 - 2\Re\left\{ \bar{A}^* r(t) e^{-j\left(2\pi \bar{f}_0 + \bar{k}\pi t^2\right)} \right\}. \end{aligned} \tag{C.2}$$

Define Δ as

$$\Delta = \int_{t=0}^{T} r(t) e^{-j\left(2\pi \bar{f}_0 + \bar{k}\pi t^2\right)} dt, \tag{C.3}$$

and we have

$$
\begin{aligned}
[\hat{f}_0, \hat{k}, \hat{A}] &= \arg\min_{\bar{f}_0, \bar{k}, \bar{A}} \int_{t=0}^{T} |r(t)|^2 dt + |\bar{A}|^2 T - 2\Re\{\bar{A}^* \Delta\} \\
&= \arg\min_{\bar{f}_0, \bar{k}, \bar{A}} |\bar{A}|^2 T - 2\Re\{(\bar{A}_r - i\bar{A}_i)(\Delta_r + i\Delta_i)\} \\
&= \arg\min_{\bar{f}_0, \bar{k}, \bar{a}} T\bar{A}_r^2 + T\bar{A}_i^2 - 2(\Delta_r \bar{A}_r + \Delta_i \bar{A}_i).
\end{aligned}
\tag{C.4}
$$

Here, we have

$$
\begin{aligned}
\bar{A}_r &= \Re\{\bar{A}\}, \quad \bar{A}_i = \Im\{\bar{A}\}, \\
\Delta_r &= \Re\{\Delta\}, \quad \Delta_i = \Im\{\Delta\}.
\end{aligned}
\tag{C.5}
$$

Apparently, for an arbitrary given Δ, to minimize the target function, we should have

$$
\bar{A}_r = \Delta_r / T \text{ and } \bar{A}_i = \Delta_i / T, \tag{C.6}
$$

leading to

$$
\begin{aligned}
&\min_{\bar{f}_0, \bar{k}, \bar{A}} \int_0^T |r(t)|^2 dt + |\bar{A}|^2 T - 2\Re\{\bar{A}^* \Delta\} \\
&= \int_0^T |r(t)|^2 dt + \min_{\bar{f}_0, \bar{k}, \bar{A}} T\bar{A}_r^2 + T\bar{A}_i^2 - 2(\Delta_r \bar{A}_r + \Delta_i \bar{A}_i) \\
&= \int_0^T |r(t)|^2 dt + \min_{\bar{f}_0, \bar{k}} |\Delta|^2 / T - 2|\Delta|^2 / T \\
&= \int_0^T |r(t)|^2 dt + \min_{\bar{f}_0, \bar{k}} -|\Delta|^2 / T.
\end{aligned}
\tag{C.7}
$$

Therefore, the MLE of f_0 and k can be obtained by

$$
\begin{aligned}
[\hat{f}_0, \hat{k}] &= \arg\min_{\bar{f}_0, \bar{k}} -|\Delta|^2 / T \\
&= \arg\max_{\bar{f}_0, \bar{k}} \left| \int_{t=0}^{T} r(t) e^{-j\left(2\pi \bar{f}_0 t + \bar{k}\pi t^2\right)} dt \right|.
\end{aligned}
\tag{C.8}
$$

Now we can safely conclude that the MLE of the initial frequency and frequency rate is equivalent to finding the peak in the spectrum of the LMF signal contaminated by white Gaussian noise.

Appendix D

Appendix for the Pilot Decontamination Scheme

D.1 Proof of the Upper Bound of the Residual Error

In this section, we will justify the upper bound of the residual error in (2.22). To begin with, we have

$$|\alpha_{mod_M(l+1-r)}|^2 \leq \frac{1}{4(\beta-1+r)^2}, \tag{D.1}$$

where we use the inequality

$$1 \geq \sin^2 x \geq \frac{4}{\pi^2}x^2 \ (|x| \leq \pi/2). \tag{D.2}$$

Similarly, we have

$$|\alpha_{mod_M(l+r)}|^2 \leq \frac{1}{4(r-\beta)^2}. \tag{D.3}$$

Then, define

$$\beta_r = |\alpha_{mod_M(l+1-r)}|^2 + |\alpha_{mod_M(l+r)}|^2 \tag{D.4}$$

and

$$f(\beta) = \frac{1}{(r-\beta)^2} + \frac{1}{(r-1+\beta)^2}. \tag{D.5}$$

We can prove that $f(\beta)$ decreases with β, leading to $f(\beta) < f(0)$ and

$$\beta_r \leq \frac{1}{4}\left(\frac{1}{r^2} + \frac{1}{(r-1)^2}\right). \tag{D.6}$$

When $M = 2F$, we have

$$Res[\,R\,] = 1 - \sum_{r=1}^{R} \beta_r = \sum_{r=R+1}^{F} \beta_r. \tag{D.7}$$

Given that M is very large, we can obtain the following inequality:

$$\begin{aligned} Res[\,R\,] &= \lim_{M\to\infty} \sum_{r=R+1}^{F} \beta_r \\ &\leq \frac{1}{4}\left[\lim_{M\to\infty} \sum_{r=R+1}^{F} \frac{1}{r^2} + \lim_{M\to\infty} \sum_{r=R+1}^{F} \frac{1}{(r-1)^2}\right] \\ &= \frac{\pi^2}{12} + \frac{1}{4R^2} - \sum_{r=1}^{R} \frac{1}{2r^2}, \end{aligned} \tag{D.8}$$

in which we employed the well acknowledged limit

$$\lim_{M\to\infty} \sum_{r=1}^{M} 1/r^2 = \frac{\pi^2}{6}. \tag{D.9}$$

When $M = 2F + 1$, we have

$$Res[\,R\,] = \sum_{r=R+1}^{F} \beta_r + |\alpha_{mod_M(l-F)}|^2, \tag{D.10}$$

where $|\alpha_{mod_M(l-F)}|^2 \leq 1/F^2$. When M approaches infinity, this component is negligible and the result is identical to that of $M = 2F$.

As a result, regardless of whether M is odd or even, if we take the closest $2R$ components to re-establish $\mathbf{e}\,[\omega]$, the upper bound of the residual error can be given by (2.22).

D.2 Justification to the Distribution of $\lambda_m^{(l,k)}$

Here, we justify the results concerning the distributions of $\lambda_m^{(l,k)}$ in (7.10) and (7.11).

When $DS_m = 0$ and $PC_m = 0$, $\left|f(\omega_b^{(l_i,k)} - m\omega_0)\right|$ and $\left|f(\omega_b^{(l,k)} - m\omega_0)\right|$ will be very small because $\left|\omega_b^{(l_i,k)} - m\omega_0\right| > \omega_0$ and $\left|\omega_b^{(l,k)} - m\omega_0\right| > \omega_0$ hold for any given i and b. Therefore, the absolute value of $\mathbf{h}_{S,P}^{(l,k)}[m]$ will be very small in this case, and we have $\lambda_m^{(l,k)} \approx |\tilde{\mathbf{n}}_k[m]|^2$. Then, we can conclude that $\lambda_m^{(l,k)}$ follows the exponential distribution as

$$f_0\left(\lambda_m^{(l,k)}\right) = 1/\sigma_o^2 \cdot \exp\left(-\lambda_m^{(l,k)}/\sigma_o^2\right), \tag{D.11}$$

where $\sigma_o^2 = E\left\{|\tilde{\mathbf{n}}_k[m]|^2\right\}$.

On the other hand, when $DS_m = 1$ or $PC_m = 1$, $\left|\mathbf{h}_{S,P}^{(l,k)}[m]\right|$ cannot be neglected, and $\lambda_m^{(l,k)}$ can be approximated by

$$\lambda_m^{(l,k)} = \left|\mathbf{h}_{S,P}^{(l,k)}[m]\right|^2 + 2\Re\left\{\mathbf{h}_{S,P}^{(l,k)}[m] \cdot \tilde{\mathbf{n}}_k[m]^*\right\} + |\tilde{\mathbf{n}}_k[m]|^2. \tag{D.12}$$

Given that signal is much stronger than the noise, $|\tilde{\mathbf{n}}_k[m]|^2$ can be neglected and we have

$$\lambda_m^{(l,k)} \approx \left|\mathbf{h}_{S,P}^{(l,k)}[m]\right|^2 + 2\left(\Re\left\{\mathbf{h}_{S,P}^{(l,k)}[m]\right\} \cdot \Re\{\tilde{\mathbf{n}}_k[m]\} + \Im\left\{\mathbf{h}_{S,P}^{(l,k)}[m]\right\} \cdot \Im\{\tilde{\mathbf{n}}_k[m]\}\right). \tag{D.13}$$

In (D.13), the first part is a constant for a given realization of the channel, while the second part follows a zero-mean Gaussian distribution. Therefore, the PDF of $\lambda_m^{(l,k)}$ in this scenario is given in (7.11).

In our case, λ_{th} is chosen to minimize the sum of false alarm and miss rates, which means $f_0(\lambda_{th}) = f_1(\lambda_{th})$. Define

$$SNR_o = \left|\mathbf{h}_{S,P}^{(l,k)}[m]\right|^2 / \sigma_o^2, \tag{D.14}$$

and λ_{th} can be given as (7.13). The false alarm rate will be

$$R_{FA} = \int_{\lambda_{th}}^{\infty} f_0(\lambda) d\lambda = \mathrm{e}^{-\lambda_{th}/\sigma_o^2}, \tag{D.15}$$

while the miss rate is

$$R_M = \int_{-\infty}^{\lambda_{th}} f_1(\lambda) d\lambda. \tag{D.16}$$

Replace λ with $t = \frac{\lambda - (SNR_o+1)\sigma_o^2}{2\sqrt{SNR_o}\sigma_o^2}$, and we have (7.15a).

D.3 Proof of Theorem 2

Given that a strong component of the desired signals exists on $m\omega_0$, the probability that a strong pilot contamination component coexists is bounded by

$$Pr(PC_m = 1 | DS_m = 1) = 1 - \left(1 - \frac{2}{M}\right)^{6B}, \tag{D.17}$$

and the right hand side can be expanded as

$$\begin{aligned} 1 - \left(1 - \frac{2}{M}\right)^{6B} &= \frac{12B}{M} + \sum_{i=1}^{3B} \left[\binom{6B}{2i+1} \left(\frac{2}{M}\right)^{2i+1} - \binom{6B}{2i} \left(\frac{2}{M}\right)^{2i} \right] - \left(\frac{2}{M}\right)^{6B} \\ &= \frac{12B}{M} + \sum_{i=1}^{3B} \binom{6B}{2i} \left(\frac{2}{M}\right)^{2i} \left(\frac{2(6B-2i-1)}{(2i+1)M} - 1 \right) - \left(\frac{2}{M}\right)^{6B}. \end{aligned} \tag{D.18}$$

In (D.18), $\frac{2(6B-2i-1)}{(2i+1)M} - 1$ decreases monotonically with i for $1 \le i \le 3B-1$, which gives

$$\frac{2}{(6B-1)M} \le \frac{2(2i+1)}{(6B-2i-1)M} \le \frac{4B-2}{M} \ll 1. \tag{D.19}$$

Therefore, we can decide that

$$Pr(PC_m = 1 | DS_m = 1) < \frac{12B}{M}. \tag{D.20}$$

Similarly, we can obtain

$$Pr(PC_m = 1 | DS_m = 1) > \frac{12B}{M} \left(1 - \frac{6B-1}{M}\right). \tag{D.21}$$

Following similar procedure, we can prove that $Pr(PC_m = 1|DS_m = 1)$ is bounded by

$$\frac{2B}{M}\left(1 - \frac{B-1}{M}\right) < Pr(DS_m = 1|PC_m = 1) < \frac{2B}{M}. \tag{D.22}$$

Hence, Theorem 2 is proven.

D.4 Conditional PDF of $\phi_m^{(l,k)}$

Based on (7.22), we define a random variable y as

$$y = \phi_m^{(l,k)} 2|r_{pc}|^2/\sigma_{proc}^2 = \left|\frac{\Re\{r_{pc}\} + \Re\left\{\tilde{\mathbf{n}}_{proc}[m]s_{l_i,k}^*\right\}}{\sigma_{proc}/\sqrt{2}}\right|^2 + \left|\frac{\Im\{r_{pc}\} + \Im\left\{\tilde{\mathbf{n}}_{proc}[m]s_{l_i,k}^*\right\}}{\sigma_{proc}/\sqrt{2}}\right|^2 \tag{D.23}$$

The PDF of $\tilde{\mathbf{n}}_{proc}[m]s_{l_i,k}$ is identical to $\tilde{\mathbf{n}}_{proc}[m]$. Therefore, the right hand side of (D.23) follows a non-central chi-square distribution given by

$$f_Y(y) = \frac{1}{2}\exp\left(-\frac{y+\eta}{2}\right) I_0\left(\sqrt{\eta y}\right), \tag{D.24}$$

where $\eta = 2|r_{pc}|^2/\sigma_{proc}^2$, and $I_0(\cdot)$ is given in (7.25). The PDF of $\phi_m^{(l,k)}$ will be

$$f_{pc}(\phi_m^{(l,k)}) = \eta f_Y(\eta\phi_m^{(l,k)}). \tag{D.25}$$